Processing and properties of a Zr-Co-Al BMG for biomedical applications

Eliott Guerin

THÈSE

Pour obtenir le grade de

DOCTEUR DE L'UNIVERSITE GRENOBLE ALPES

Spécialité : **Matériaux, Mécanique, Génie Civil, Electrochimie**

Arrêté ministériel : 25 mai 2016

Présentée par

Eliott GUERIN

Thèse dirigée par **Jean-Jacques Blandin, DR, Grenoble INP**,
et co-encadrée par **Rémi DAUDIN, CR, CNRS**

Préparée au sein du **Laboratoire SIMaP**
dans **l'École Doctorale IMEP-2**

Processing and properties of a Zr-Co-Al bulk metallic glass for biomedical applications

Elaboration et propriétés d'un verre métallique massif Zr-Co-Al pour des applications biomédicales

Thèse soutenue publiquement le **« 08/03/2022 »**,
devant le jury composé de :

Dr Mariana CALIN
Professeur, IFW Dresden, rapporteuse
Dr Jean-Christophe SANGLEBOEUF
Professeur, IPR, Université de Rennes, rapporteur
Dr Éric BEAUGNON
Professeur, LNCMI, Université Grenoble Alpes, examinateur, président
Dr Stéphane GORSSE
Maître de conférences, ICMCB, Université de Bordeaux, examinateur
Dr Jean-Jacques BLANDIN
Directeur de recherche CNRS, SIMaP, Université Grenoble Alpes, directeur de thèse
Dr Rémi DAUDIN
Chargé de recherche CNRS, SIMaP, Université Grenoble Alpes, co-encadrant de thèse
Dr Damien FABREGUE
Professeur, MATEIS, INSA Lyon, invité
Dr Nicolas COURTOIS
Directeur recherche et affaires cliniques, Anthogyr SAS, invité
Dr Alexis LENAIN
Manager R&D matériaux, Vulkam Inc, invité

Table of content

« En essayant continuellement, on finit par réussir. Donc plus ça rate, plus on a de chances que ça marche »

Jacques Rouxel, les Shadoks

A mes grands parents…

Remerciements

Le manuscrit qui suit est une œuvre collective. C'est le fruit d'innombrables heures de travail, de discussion, avec de nombreuses personnes qui ont toujours pris de leur temps pour faire avancer ces recherches, sans rien attendre en retour. Ce n'est en rien un travail individuel et de ce fait, de nombreuses personnes doivent être remerciées.

Je me dois forcément de commencer par le duo de choc qui a constitué mon encadrement le plus proche : Jean-Jacques Blandin et Rémi Daudin. Un binôme de mentors qui a parfaitement fonctionné à mon sens. Bien que ce fut ta première thèse encadrée, Rémi, tu as toujours répondu présent et je ne compte plus les fois où j'ai traversé le couloir pour entrer dans ton bureau (toujours porte ouverte) poser une question (pas forcément claire) ou discuter d'un résultat (pas forcément clair). Je te remercie infiniment pour ta motivation et ta vision toujours positive des choses. « Quel est le message ? » « Comment capitaliser sur ces résultats ? » C'est deux petites phrases peuvent permettre à bon nombre de doctorant de te reconnaître Jean-Jacques ! Merci beaucoup d'avoir mis toute ton expérience au service de cette thèse. Tu m'as souvent aidé à prendre du recul, quand je pouvais avoir tendance à foncer tête baissée. Toi et Rémi m'avez poussé pendant ces trois ans (et un peu plus) à me dépasser et à aller chercher toujours plus loin. Il est clair que je ne serai pas allé aussi loin sans votre détermination. Il est clair pour moi que vous avez très à cœur ce « devoir de formation » qui fait partie intégrante de la thèse. Au-delà des résultats scientifiques purs, il est indéniable que j'ai énormément appris durant ces trois ans et c'est pour moi le plus grand des résultats car il me suivra toujours. Vous m'avez appris une vraie méthode scientifique. Ce duo d'encadrant « made in SIMaP » est en réalité un trio. A toi aussi Georges, je tiens à dire merci. Bien que tu ne sois pas de l'encadrement « officiel » de cette thèse, tu y as participé très activement, que ce soit au niveau des expérimentations mais aussi des points hebdomadaires. Mon travail a été fortement alimenté par le tien, que je trouve extrêmement intéressant et j'espère qu'à mon tour, les quelques résultats de cette thèse pourront te faire avancer.

Ce projet, AMA-MED, fait converger de nombreux acteur. Au côté du laboratoire SIMaP, j'ai pu collaborer avec le laboratoire MATEIS, de l'INSA Lyon, représenté par Damien Fabregue. Merci énormément Damien pour ton soutien et tes idées. Tu as toujours su me challenger lors de nos réunions, ce qui était toujours intéressant. Mais tu n'as pas été le seul de ton laboratoire à m'apporter ton soutien et je voudrai adresser un remerciement général à tout ce laboratoire qui m'a accueilli à bras ouvert et m'a beaucoup formé. Je voudrai particulièrement remercier Benoit Ter-Ovanessian. Je suis venu te solliciter pour les investigations concernant la corrosion en début de première année, tu t'es beaucoup investi dans le projet et j'en suis très heureux. Cette nouvelle collaboration va se poursuivre après la thèse, notamment avec Rémi. Merci pour ta motivation et ta pédagogie. Merci également à Jean Marc Pelletier pour avoir réalisé ces expériences de DMA et qui ne font qu'attiser un peu plus notre curiosité.

Au côté de ces deux laboratoires, deux entreprises ont été particulièrement investies dans ce projet. Tout d'abord Anthogyr, fabricant français de dispositifs médicaux. Merci à Nicolas Courtois et Anne-Lise Chopard Lallier pour leur engagement tout au long de la thèse. Merci de m'avoir apporté votre vision de professionnels du secteur médical, ce qui a permis de fermement ancrer cette thèse dans son contexte. Merci notamment pour tous les essais suivant des normes spécifiques du médical ainsi que votre analyse critique de ces derniers. Merci également à toi Nicolas d'avoir pris le temps de discuter de mon projet professionnel.

Et « last but not least » merci infiniment à toute la famille Vulkam. Quand je suis arrivé, vous n'étiez que quatre, Alexis Lenain, Nassim Mendil, Sébastien Gravier et Xavier Cerutti. Aujourd'hui vous êtes plus d'une vingtaine et ça a été un immense plaisir de vous voir évoluer et de faire partie en quelques sorte de l'aventure. Je dis quatre à l'origine, mais c'est bien sûr sans compter les stagiaires, et notamment

Sarah !! Merci à Alexis et Sébastien pour leur participation active dans les réunions de travail. Vous avez toujours su apporter de nouveaux axes de travail, anticiper les éventuels points bloquants et contribuer aux questionnements scientifiques par votre vaste connaissance des verres. Merci aussi à Alexis pour avoir fait partie de mon jury de thèse. Depuis 2018, la famille Vulkam s'est largement agrandie c'est certain !! Difficile de remercier chacun tant vous formez un groupe compact avançant vers un but commun. Merci à Tiphaine et Johan de m'avoir permis de participer aux travaux sur la qualité, plus particulièrement pour le médical. Merci à toutes les mains de la « team moulage » pour ces centaines de pièces injectées. C'est un travail colossal et qui a grandement influencé le cours de cette thèse. Enfin, merci à Damien et Léna, de la « team matériaux » pour leurs conseils et avoir toujours pris le temps de partager leur expérience. Je suis très heureux de vous rejoindre prochainement pour poursuivre l'aventure !

Cette thèse a inclus une grande part de travaux expérimentaux. Aucuns de ceux-ci n'auraient été réalisable sans l'aide de plusieurs personnes que je tiens à remercier. Merci à Charles Josserond, Cyril Rajon, Xavier Bataillon et Franck Pelloux, les rouages indispensables du GPM2, qui tous les jours réalisent des merveilles pour nous permettre de réaliser nos projets ou de réparer nos bêtises. Je souhaite également adresser de chaleureux remerciement à Patricia Donnadieu, Frederic De Geuser et Alexander Pisch pour le temps qu'ils m'ont consacré et les dispositifs expérimentaux qu'ils m'ont permis d'utiliser. Merci également à Thierry Encinas et Stéphane Coindeau, qui sont les deux seuls humains capables de réaliser une DRX plus vite qu'il ne faut de temps pour l'épeler. Merci aussi à Elisabeth Lussi et Khadija Rassouli, pour leur bienveillance et leur disponibilité.

Et puis merci au SIMaP, au GPM2. Bien sûr, je n'ai connu qu'un seul laboratoire, donc difficile d'être objectif, mais je pense que je peux quand même affirmer que j'ai eu beaucoup de chance d'effectuer ma thèse au sein de celui-ci. Un merci tout particulier à tous les membres du GPM2 pour tout ce temps passé chez vous. Ce fut trois années magnifiques. Merci pour les (innombrables) pauses café (même si je dois maintenant traiter une addiction), les barbecues ou tout simplement les mots échangés en se croisant dans les couloirs. J'ai particulièrement apprécié l'esprit du laboratoire, ou les portes sont toujours ouvertes et la hiérarchie est peu marquée, ce pourquoi on n'hésite jamais à venir demander de l'aide ou un avis. Un remerciement un peu spécial à Guilhem Martin, qui m'a suivi depuis Polytech, sans qui je pense que je ne serai jamais arrivé jusqu'ici. Tu m'as donné le gout de la recherche, merci beaucoup pour ça. Merci aussi d'avoir été là pour me booster dans la dernière ligne droite ! Mention spéciale également à Arthur Després, je te souhaite plein de réussite et de succès dans ta future vie d'enseignant-chercheur.

Le GPM2 ne serait certainement pas ce qu'il est sans sa fine équipe de doctorants (au moins pour préparer le café) ! J'ai eu la chance d'intégrer ce qui est indéniablement la meilleur salle (aka la salle blanche). J'ai tout d'abord une pensée pour l'équipe qui constituait la salle lors de mon arrivée, Jessica, Guillaume, Mathilde et Zoé. Merci de m'avoir intégré comme vous l'avez fait. Merci pour ces pauses thés et les moments potins. Mathilde, quand tu veux pour retourner promener des chiens à la SPA !! Peut-être même que tu y rencontreras ton futur toutou… Guillaume, même si tu fais maintenant partie du CEA, j'espère que tu continues la fabrication de cookies (virtuels). Mathilde et Guillaume C., merci également pour vos conseils sur la gestion de la thèse et les nombreuses bières partagées. L'équipe a évolué au cours du temps, avec l'arrivée de Bruno ! Merci d'avoir ramené ton amour de la charcuterie et du sport avec toi. Melek tu étais discrète au début, mais j'ai beaucoup apprécié apprendre à te connaître au fil des ans ! Avec Guillaume H. et Nicolas, nous avons constitué notre « génération de thésards » et c'était vraiment chouette de partager ce temps et cette aventure avec vous. Nicolas… j'ai peut-être perdu la course de l'écriture du manuscrit, mais je pense avoir gagné un bon pote ! Merci pour ta bonne humeur légendaire ! J'ai toujours aimé discuter avec toi, de tous sujet. Alors en effet, avec Guillaume H., vous ne faites pas partie de la salle blanche… comme quoi il existe des thésards sympas ailleurs ! Mathis par exemple, beau spécimen barbu, merci de m'avoir fait découvrir le pub des copains. Pas mon bar préféré, mais le fromage

y est bon. Merci également à Alexandre pour ces parties de Times Bomb endiablées ! Tu t'exprimes sur ton sujet avec des étoiles dans les yeux et c'est toujours intéressant de discuter avec toi. Au banc des passionnés, comment ne pas mentionner Maxence. Spécimen rare, je pense unique au laboratoire, tu es animé d'une véritable flamme pour ton sujet et je suis persuadé que cela te portera très loin. Merci également à Julien, spécialiste du 10km et du polissage. Je n'ai pas l'espoir de t'égaler dans aucun de ces deux domaines ! Mais revenons plutôt à la salle blanche… Milles mercis à Loïcia. Définitivement meilleure pâtissière du GPM2 dans la catégorie cookies (réels), merci pour tous ces moments passer à discuter, à évacuer la frustration quand ça n'allait pas, mais aussi à parler de tout et de rien, ou simplement à analyser les avancées (plutôt lentes) des travaux de Ecomarch. Bon courage pour la fin de la thèse, je t'attends de l'autre côté, d'où j'écris ces mots, et tu vas voir c'est très sympa. Je te prie de transmettre mes amitiés à Ruby. Enfin pour terminer avec les ptits nouveaux, Fabrice, rentre vite de Belgique pour gérer Paul s'il te plait, il est en passe de finir *Le Bon Coin*. Plus sérieusement, merci à tous les deux pour ces sorties ski ou VTT, et surtout à très bientôt pour de nouvelles j'espère.

Enfin je voudrai adresser un énorme merci à tous ceux qui, à côté de ma vie de laboratoire, m'ont soutenu et encouragé. Merci à tous mes amis : Astrid, Allan, Bryan, Estelle, Guillaume, Gaëlle, Maxime, Noémie, Quentin, Robin, Thomas… Merci d'avoir toujours répondu présent et d'avoir continué à toujours m'intégrer, même quand je refusais plus d'invitations que je n'en acceptais. Merci également à Julius ! Une des belles rencontres de ces trois années ! Même si c'est toujours compliqué de trouver à se voir, les moments passés ensembles sont toujours très sympa. Merci à mon meilleur ami, Martin. Ça fait un sacré bout de chemin depuis Cranfield où je discutais de mes doutes sur le fait d'entamer une thèse. Tu as toujours su être là pour me motiver, me tenir concentré ou au contraire me permettre de décompresser. Tu m'as accompagné tout au long de cette aventure, et maintenant c'est à mon tour de t'accompagner dans la grande aventure qui t'attend. Je sais que tu vas réussir.

Pour finir je tiens à remercier ma famille. Merci à Lucie !! Merci d'avoir été à mes côtés avec douceur, quand ça allait et quand ça n'allait pas. Merci de m'avoir permis de ne jamais lâcher, même quand l'envie s'en faisait sentir ! Merci également d'avoir traversé le confinement avec moi. Et merci à toute la famille Tauvron pour votre accueil. Merci à mes parents, vous qui m'avez soutenu depuis toujours. Merci maman de ta patience et de ton investissement sans limite. Cette réussite est aussi la tienne. Merci Papa, d'avoir été là pour m'écouter et me guider, j'ai d'ailleurs bien appliqué tes conseils pour la rédaction ! Merci également à mes beau-parents. Et merci à mes petites sœurs, vous qui m'avez poussé à me dépasser et à être le meilleur exemple possible, même si je n'ai pas toujours pu être aussi présent que je l'aurai voulu. Merci à Laurence et Isabelle, mes super tatas, vous avez beaucoup influencé mon parcours scolaire ! Et enfin merci à mes grands-parents, pour les valeurs que vous m'avez transmis.

Ça fait 61 « merci », mais il en faudrait une infinité pour exprimer ma reconnaissance d'en être arrivé là. Alors j'en rajoute un dernier.

Merci.

Introduction

The *small* implantable devices market and the thesis context

With the continuous improvement of living standards and the progressive ageing of the population, the demand for biomaterials is growing. Furthermore, the rapid improvement of surgical procedures and the increasing level of safety standards call for the development of safer and higher quality biomaterials (both for mechanical and biomedical properties). Anthogyr is a French manufacturer of dental implants and surgical tools. In an effort of innovation, it is continuously working toward new solutions. Figure 1 illustrates the Axiom® Multi Level® suite, which highlights several components of a dental replacement solution. The materials involved in the fabrication of such devices are exposed to high and repeated loading-unloading cycles (because of the mastication), temperature changes (from drinking hot tea to eating ice cream) and are constantly immersed in a corrosive environment (buccal environment). In addition to all the challenging operating conditions they have to face, the materials used must be perfectly harmless for the human organism. For the realisation of such devices, metallic materials, as well as ceramics, are often used. One of the main metallic materials used by Anthogyr is the TA6V (Ti-6Al-4V) grade V-ELI. Stainless steel (316 L SS) and CoCrMo alloys are also used.

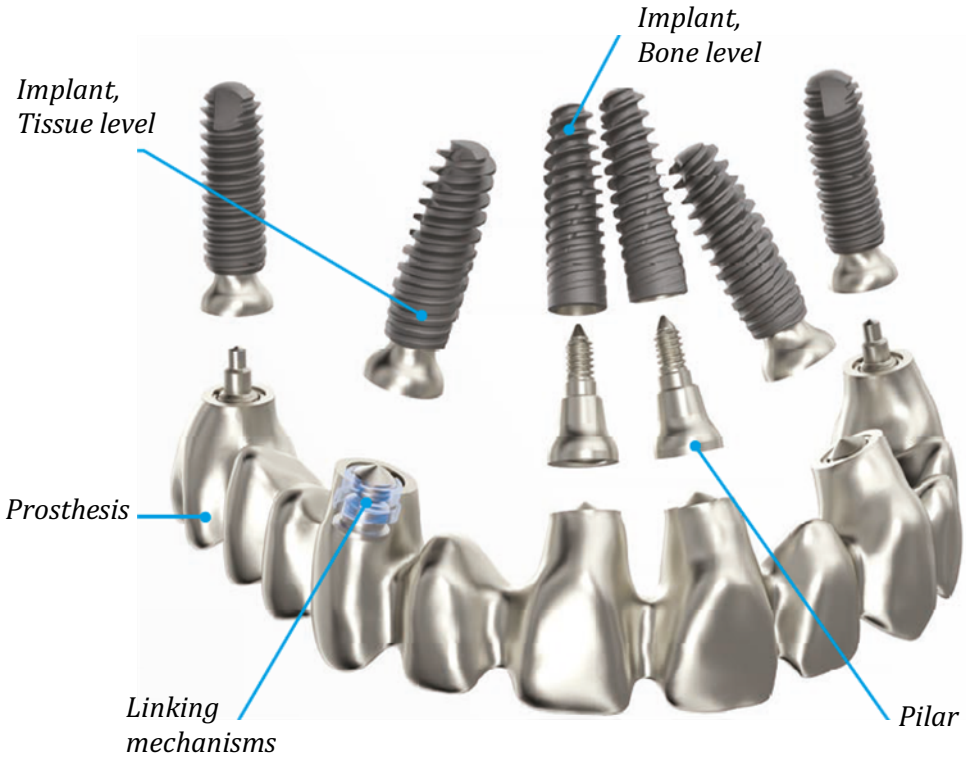

Figure 1: 3D illustration of the Axiom® Multi Level® suite developed by Anthogyr. The implant is the part anchoring the device in the bone. The pilar makes the link between the anchor (the implant) and the prosthesis. The pilar is connected to the prosthesis by a special linking mechanism. The prosthesis is the end part, ensuring the function role of the human organ it is replacing.

One of the main challenges of Anthogyr is the miniaturisation of their devices, allowing for less invasive surgeries. Even though the TA6V V-ELI is one of the most advanced metallic materials on the market, it is reaching its limits in terms of mechanical resistance and is one of the limiting factors when designing news implants. Anthogyr is therefore looking for new, high resistance, biocompatible materials which can unlock new design possibilities.

Objectives and requirements

After internal studies, Anthogyr started a partnership with two laboratories and a start-up from the metallurgical industry. The partnership took the form of a thesis project. The SIMaP laboratory and the MATEIS laboratory are two material research-oriented labs. The SIMaP Laboratory is a lab specialized in the design and study of architectured materials (materials designed to exhibit specific properties). Metallic glasses have been long studied at SIMaP Lab. and MATEIS Lab. which has a speciality in the biocompatibility of materials, which is complementary to the mechanical aspect brought by SIMaP Lab. while designing biomaterials. Vulkam is a start-up created by former SIMaP researchers and focuses on the development of new innovative amorphous alloys and high precision casting. The overall objective of the collaboration (based at SIMaP laboratory) is to explore new metallurgical solutions by using all the skills of the four actors of the project to find a new material that could potentially replace TA6V V-ELI, 316L SS or CoCrMo alloys. Table 1 lists the mechanical properties of the three alloys. Table 1 also reports the mechanical properties of the cortical bone.

Material	Yield stress (MPa)	Elastic strain (%)	Plastic strain (%)	Density ($g.cm^{-3}$)	Hardness (HV)	Young's modulus (GPa)	Ref
316L SS	190-690	0.34	12-40	7.9	365	193-210	[1]
TA6V	760-1050	0.67	8-15	4.4	320	101-125	[1]
CoCrMo	450-1030	0.18	8-28	8.3	345-390	210-255	[1]
Cortical Bone	130-150	1	2	0.7-1.85	63-75	3-50	[1]

Table 1: Mechanical specifications of the 316L SS, TA6V and CoCrMo alloys, along with the mechanical properties of the cortical bone.

It is important to minimize the "stress shielding effect", resulting in the deterioration of the bone at the implant contact which is caused by a great gap between the bone and the implant material Young's modulus E. Therefore, the Young's modulus of the implant should be as close as possible to the one of the cortical bone. Based on mechanical characteristics, a good replacement candidate should exhibit superior yield stress (at least twice the one of TA6V), low density to maximise specific strength (yield stress divided by density) and a low Young's modulus. Finally, the material should of course be biocompatible. This property is evaluated by applying testing protocols described in several ISO standards (ISO 10271,

ISO 10993, ISO 22674, ISO 14801…) which concerns the evaluation of mechanical properties specifically for medical applications, but also corrosion resistance and cytotoxicity. Therefore, the developed material should respect these international standards.

The biocompatible aspect also means that the composition of the developed alloy should not present any threats to the human organism. In this sense, the **E**uropean **CH**emical **A**gency (ECHA) is classifying all chemicals through the REACH (**R**egistration, **E**valuation, **A**uthorisation and **R**estriction of **C**hemicals) benchmark since 2007. All elements are classified depending on their level of risk in several categories (fertility damage, carcinogenic potential, genetics alteration). The class is 1A if the harmful potential is proven, 1B if it is supposed, and 2 if it is suspected. This is to be completed with the new European regulation on medical devices (DM) UE 2017/745 which states that any medical device that is invasive and is in direct contact with the human body can not contain more than 0.1 wt% of a substance classified 1A or 1B. The legislation is illustrated in Figure 2.

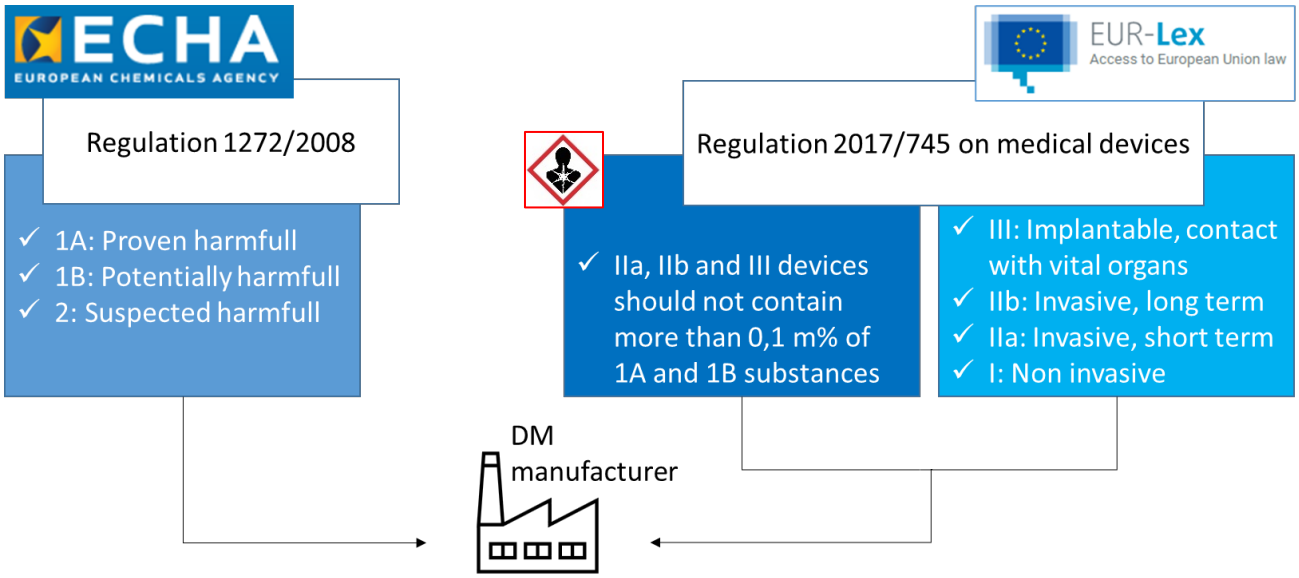

Figure 2 : Schematic illustration of the European legislation on the conception of medical devices

The reader should be informed at this point that the alloy studied in the thesis is bearing cobalt (Co). Cobalt was reclassified during the present PhD work as "may cause cancer" (carcinogenic 1B). In the present state, it will no longer be possible to produce implants bearing more than 0.1 wt% of cobalt by 2024. The authors are not experts in toxicology and are not qualified to express any judgment about the harmful potential of cobalt. However, it is to be noted that the classification given by the REACH committee is based on the submission by individuals or entities of toxicological reports. These toxicological reports are often based on a single exposure mode, which in the case of cobalt, concerns mostly the inhalation of cobalt powder. A recent meta-study showed that there is no correlation between cancer occurrence and exposure to cobalt-bearing implants [2]. From a material point of view, the nature

of the compound bearing Co and the exposure route should be considered. Also, depending on the alloy structure and the Co integration in the structure, the exposure level of cobalt release in the body can vary.

Metallic glasses as potential biomedical materials

Metallic Glasses (MG) are metallic alloys that do not exhibit long-range, periodical order like crystalline metallic alloys. By combining compositions with slow crystallisation kinetic upon cooling and fast quenching, the metallic glass formers can bypass crystallisation during solidification and keep an amorphous structure inherited from the liquid state. They are yet limited in size because of the high cooling rates required. MGs with characteristic sizes over 1 mm (in diameter often) are referred to as Bulk Metallic Glasses (BMGs). MG remained quite a small field of metallurgy for about twenty years but attracted strong interest and have seen their development accelerate from the early 90s' with the development of new alloy systems and fast quenching techniques. Because of their unique structure, they exhibit unique combinations of properties. Properties are highly dependent on composition and many glass-forming systems have been developed over the years. Yet, among their *general* properties, one can name their high hardness, low Young's modulus, extended elastic strain (several %), superior strength, ability to be thermoformed, or good corrosion resistance. The most famous metallic glass to date is the Vitreloy 1: $Zr_{41,2}Ti_{13,8}Cu_{12,5}Ni_{10}Be_{22,5}$ [3], as it is one of the first metallic glass to be commercialized.

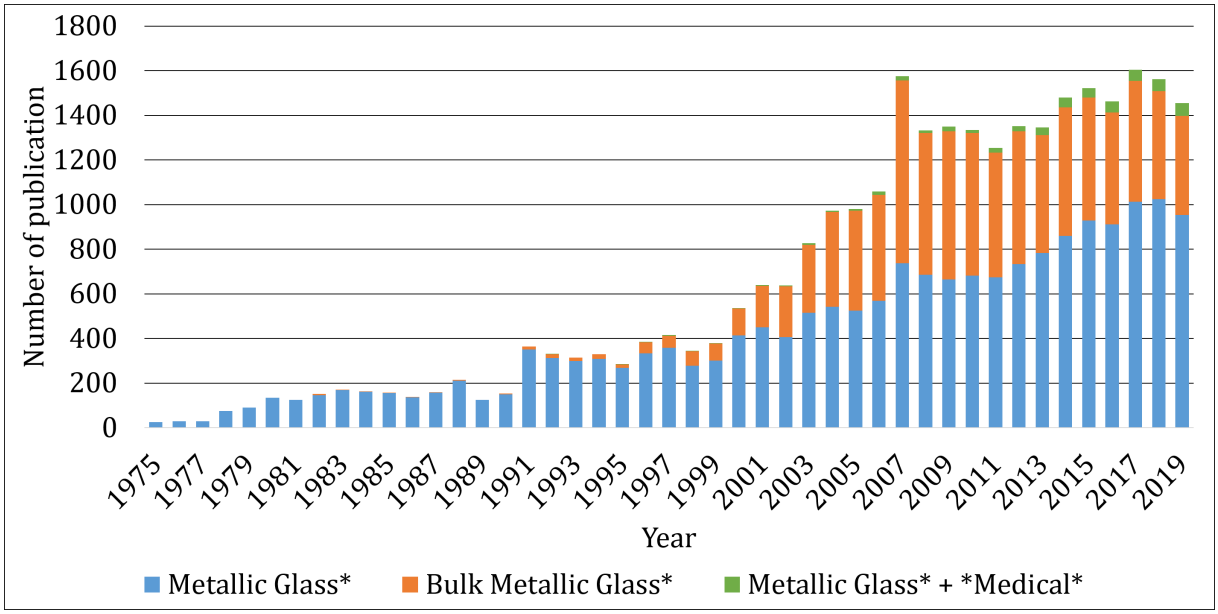

Figure 3: Bar chart of the number of publications registered in Web of Science's core collection database for several key words as topic from 1975 to 2019

Because of all these properties, metallic glasses are particularly interesting for structural applications. Because they combine both high strengths, low Young's modulus and good corrosion resistance, they are also very appealing for biomedical applications (tooling and implants). The growing interest in metallic glasses can be illustrated by the number of publications including the keywords "Metallic Glass", "Bulk Metallic Glass" or "Metallic glass + Medical" as a topic in the Web of Science's core

collection database. In Figure 3, one can observe a great increase in the number of publications starting in 1990. The proportion of publications dedicated to bulk metallic glasses and metallic glasses for medical application gradually increase over the years.

The start-up Vulkam Inc. is specialized in the design of glass-forming compositions and the casting of small parts. They are currently developing the technology to bring the production of metallic glasses to the industrial scale and take full advantage of their superior mechanical properties by casting micro-parts for high-end applications. Figure 4 exhibits some application examples for MGs: (a) and (b) are examples of miniaturization using the superior mechanical strength of MGs, (c) are implants' pilar replicate directly cast as near-net shapes, (d) is an example of surface thermo-plastic forming on an MG and (e) is a tool for eye surgery, machined from an MG.

Although MGs are very promising, they represent quite a young field of metallurgy. More precisely, the link between their unique structure and their mechanical properties is still unclear. The main goal of this thesis is therefore to study the relationship between the structure and the properties (mechanical mainly) of MG, to be able to tune the properties to meet the biomedical's market requirements.

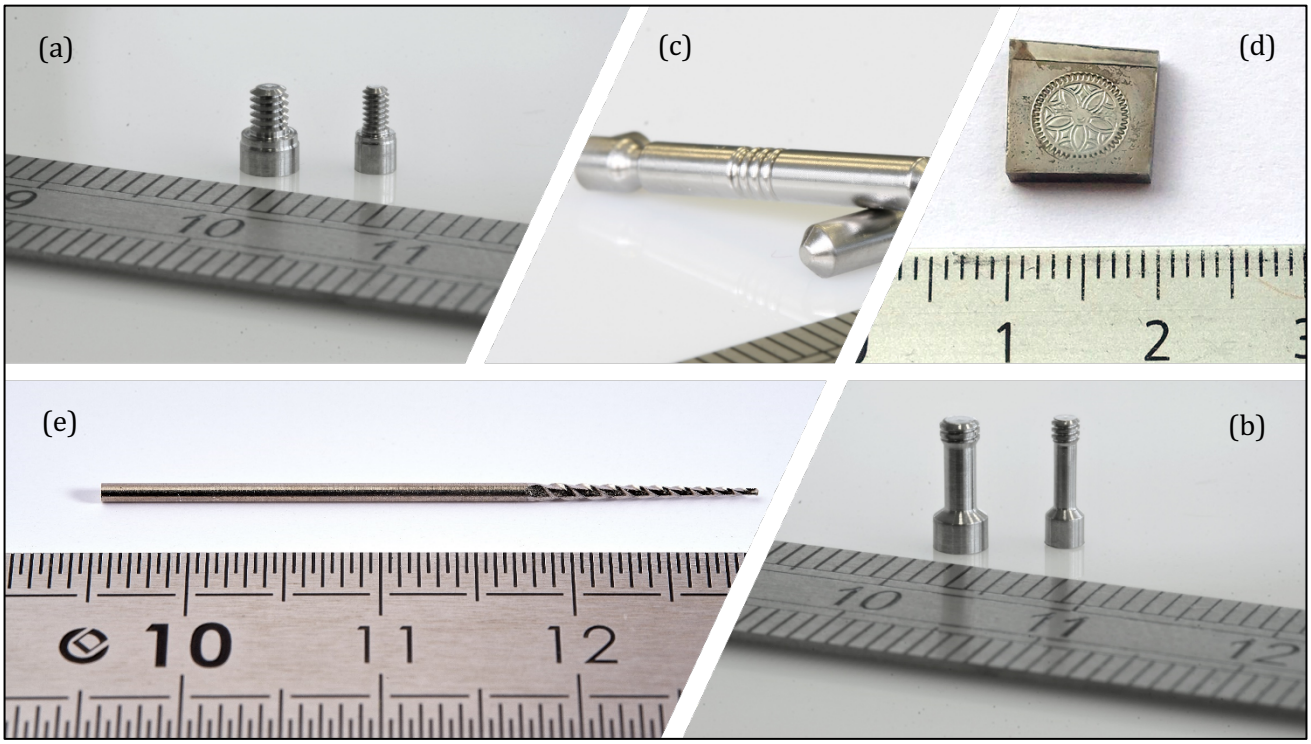

Figure 4: Pictures showing examples of some bulk metallic parts: (a) and (b) are miniaturized screws (on the left is TA6V, on the right is BMG, both having equivalent mechanical resistance); (c) are implant's pilar replicates for mechanical testing, directly casted to this shape; (d) is an example of thermoforming on a BMG and (e) is a surgical tool machined from a BMG rod.

Chapter I:

State of the art review

I. State of the art review

This chapter is dedicated to the review of the state of the art regarding bulk metallic glasses. The main objective of this chapter is to give a robust background on glass formation, thermodynamic, and structure. After a rather general background presentation, a particular focus is made on the glass structure. This review of different concepts of the glass structure will help us to understand the important idea that metallic glasses are disorganized solids only when considering long-range order and that they exhibit an ordered structure to some extent. This will be discussed later on in chapter III.

The mechanical properties of metallic glasses are deeply related to their structure. As the superior mechanical resistance of BMGs is of primary interest for potential application, it will be thoroughly discussed in this review of the literature. The concept exposed in this chapter, notably on deformation under compressive stress and fatigue resistance, will feed the discussion and help us to understand the behaviours observed in chapters III, IV and V.

With the understanding of the mechanical behaviour of metallic glasses, the focus will be made on possible strategies to improve mechanical resistance. This will be the closing part of this review regarding mechanical properties and will be used as a starting point for the work presented in chapters IV and V.

Finally, as exposed in the introduction, the main applications of the bulk metallic glasses studied in this work are small-sized structural implants and surgical tools for micro-surgery. This review presents several key properties mandatory for biomedical materials, besides mechanical resistance. This will help us to identify the key experiments that need to be performed to validate the relevance of our alloys for medical applications.

This chapter is concluded by a review of the bulk metallic glass compositions already reported for biomedical applications. This will be used as a starting point for identifying the alloy composition that will be used as the base of study in chapter III.

I.1. Background about amorphous alloys

What is usually referred to as "glass" is the transparent solid, composed of around 70% of silicon dioxide, also called silica (this type of glass account for around 90% of manufactured glass) [4]. Although it is not clear when, where and how mankind learned to make glass, it is accepted among the historic research community that the first manufactured glass vessels were produced about 3000 before Christ [5]. Glasses exhibit an amorphous structure, like organic polymers. This means that the atomic structure does not show long-range periodic order, unlike crystalline materials. Atoms in crystalline solids are arranged periodically in three dimensions (not necessarily with the same periodicity in all dimensions). This means that by knowing the position of an atom, and the periodicity in the three dimensions, one can predict the position of every other atom. There is a limited number of arrangements because of symmetry constraints: 7 crystal systems and 14 Bravais lattices [6]. Any solid where a long-range periodicity is absent is considered as "amorphous". "Non-crystalline" or "glassy" (as the reference to the amorphous state of glass) are also used to describe the absence of atomic organisation. Solid materials can therefore be divided into two categories: crystalline and amorphous. In 1984, Shechtman *et al.* pointed out a third category [7]. The quasicrystals do not possess either long-range translational symmetry or the absence of long-range order. Shechtman was attributed with a Nobel prize for this discovery in 2011.

II.1.1. What is an amorphous metallic alloy?

A new kind of glass was first reported by Duwez *et al.* in 1960 in the Au-Si system [8, 9]. Metallic glasses exhibit the same amorphous structure and absence of long-range order as silica glasses and are also obtained through rapid solidification/fast quenching techniques but with larger cooling rates. During conventional cooling, atomic reorganisation takes place in crystalline alloys, to minimize the energy of the system. Those atomic movements result in crystal formation. If the cooling rate during solidification is high enough, the atoms ordering and the nucleation of crystals can be bypassed. This competition between the quenching kinetic and the crystallisation kinetic is illustrated by Figure I-1 [10].

Curves 1 and 2 indicate two different solidification rates. If the liquid alloy is cooled down, from above the liquidus temperature (T_l), at rate 1, solidification will start at temperature T_1 and time t_1. The atomic reorganization will take place and will result in crystal formation. However, if the liquid alloy is cooled down at rate 2 (higher than rate 1), the alloy will remain in the liquid state far under T_l (undercooled liquid). Once the undercooled liquid reaches the glass transition temperature (T_g), it will be "frozen" as an amorphous solid.

It is important to mention that the metallic glass state is a metastable state (out of equilibrium), which will be more or less relaxed, depending on the applied cooling rate. The unique combination of the amorphous structure and metallic bonds (instead of Van Der Waals bonds in polymers) give metallic

glasses unique properties, keeping in mind that Van der Walls bonds are at least one order of magnitude below the force of a metallic bond.

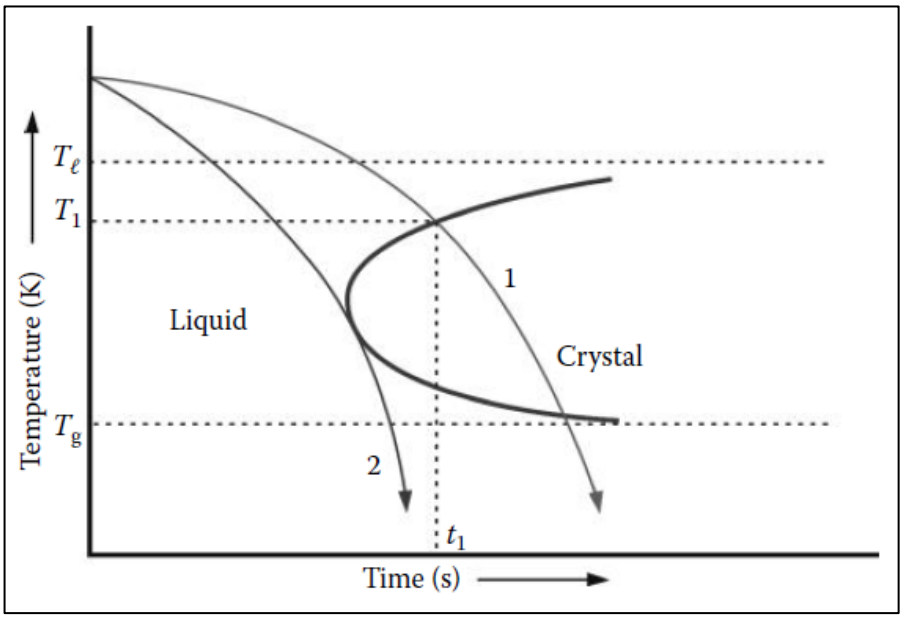

Figure I-1: Schematic time-temperature-transformation (TTT) diagram for an hypothetic alloy system. Two solidification paths are represented: (1) is crossing the crystallisation nose, resulting in a crystalline alloy, (2) is cooled rapidly enough to avoid the crystallization nose, resulting in an amorphous alloy. [10]

I.1.1. How to obtain a glass?

As mentioned earlier, metallic glasses are obtained through fast quenching techniques. The main goal is to achieve the critical cooling rate (R_c) to bypass the nucleation phenomenon and prevent crystallization. The volume fraction of the solid crystalline phase can be calculated using the equation [11, 12]:

$$X(T) = \frac{4\pi}{3R^4}\int_{Tl}^{Tg} I(T')\left[\int_{Tl}^{Tg} U(T'')dT''\right]^3 dT'$$

I-1

where X is the volume fraction of the crystalline phase, T is the temperature, R is the cooling rate and I and U is the steady-state nucleation frequency and the crystal growth rate, respectively. It is commonly accepted that for volume fractions under 10^{-6}, crystals are not detectable, hence the solid is considered as "amorphous". If we use this value as the volume fraction in our equation, we can calculate R_c with the following expression:

$$R_c{}^4 = \frac{4\pi}{3\times 10^{-6}}\int_{Tl}^{Tg} I(T')\left[\int_{Tl}^{Tg} U(T'')dT''\right]^3 dT'$$

I-2

As I and U depend on many parameters, such as the viscosity of the liquid (η) and the entropy of fusion ΔS_f, R_c will decrease with increasing η or decreasing liquidus temperature (through deep eutectics for instance). However, using this equation could lead to a false estimate of the critical cooling rate as it

is valid only on isothermal processes. Other equations have been adapted for continuous cooling conditions [13, 14]. Lin and Johnson brought another equation that includes the geometry of the casted sample [15]:

$$R_c = \frac{10}{d^2}$$

I-3

where *d* is the sample typical dimension (diameter or thickness). One can note that this equation was derived using a difference between the melting temperature and the glass transition temperature of 400 K, the thermal conductivity of 0,1 W/cm s^{-1} K^{-1} and a heat capacity per unit volume of 4 J/cm^3K^{-1}. Those values are rather typical for molten metallic alloys.

Lin and Johnson proposed a plot linking the maximum thickness of a glass phase (D_c, critical diameter) and the critical cooling rate of several alloys (Figure I-2, from [15]).

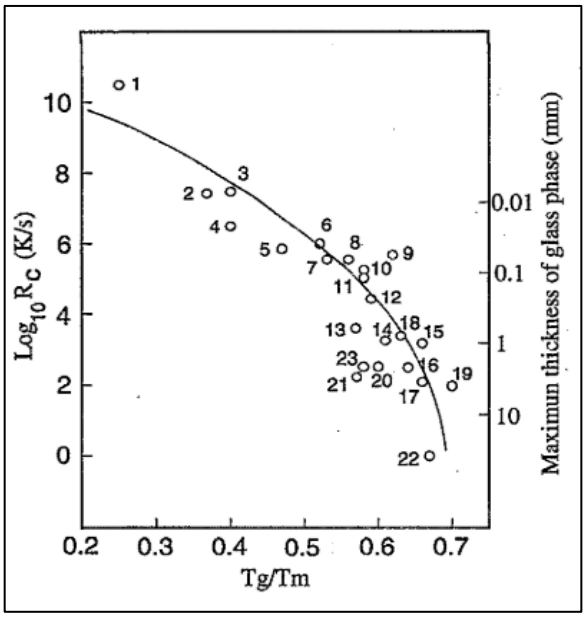

Figure I-2: Critical cooling rates for glass formation and corresponding maximum thickness of glass phase. [15]

(1) Ni

(2) $Fe_{91}B_9$

(3) $Fe_{89}B_{11}$

(6) $Fe_{83}B_{17}$

(7) $Fe_{79}Si_{10}B_{11}$

(22) $Zr_{41,2}Ti_{13,8}Cu_{12,5}Ni_{10}Be_{22,5}$ (Vit1)

(23) $Ti_{34}Zr_{11}Cu_{47}Ni_8$

It can be seen that pure metals, for instance Ni, have a very low critical diameter as they require a very high critical cooling rate. However multicomponent systems require lower R_c. This tendency will be detailed in both the GFA and Inoue Criteria sub-sections. By looking at the R_c for several compositions of the binary Fe-B alloys, we can note that the higher B(at%)/Fe(at%), the lower the cooling rate. Finally, we can note that Vitreloy 1 (Vit1) has an R_c two decades lower than the alloy number 23 (same base elements, without Be). A particular focus was given to the development of alloys with lower R_c, to achieve higher critical diameters. We understand that even though at the long-range order (LRO), amorphous alloys exhibit the absence of organization, they will exhibit different structures on the atomic level, depending on the composition or other factors. A robust understanding of the structure of the amorphous alloy, mandatory to understand their properties, is the subject of many research works over the years and will be discussed later on.

I.1.2. Thermal stability and Glass Forming Ability (GFA)

I.1.2.1. Thermal stability of metallic glasses

The glassy state is metastable. Therefore, the system will tend to a state of lower energy over time [16]. There are two possibilities here:

- The system stays amorphous but reduces its energy. This phenomenon is called structural relaxation, or physical ageing. Structural relaxation can happen naturally over time but can be catalysed by thermal or mechanical solicitations. The relaxation state will directly affect the mechanical properties of the alloy. Qiao *et al.* proposed in 2019 a very well documented review on the matter [17].
- The material can crystallize. When exposed to elevated temperatures, atoms can gather enough energy to overcome the crystallization energy barrier and reorganize themselves into more stable configurations.

As other amorphous materials (such as polymers), bulk metallic glasses exhibit a glass transition temperature (T_g) and crystallization temperatures (T_x). They also exhibit liquidus temperature (Tl). They are usually measured through differential scanning calorimetry (DSC) or differential thermal analysis (DTA) as glass transition is an endothermic event and crystallization an exothermic one. This is illustrated in Figure I-3 (a) [18]. It is important to note that the values obtained through DSC are strongly influenced by the kinetic. Therefore, for higher heating rates, characteristic temperatures such as T_g and T_x will shift to higher values. Crystallization will happen quickly once the material reaches T_x and above. It is not always a single-step process and several phases may form [16]. The primary crystallization may be followed by different transformations (*i.e.* multiple peaks can be observed on DSC measurements. Crystallization can also occur under T_x. Above T_g, the viscosity of the material dramatically decreases and may provide enough atomic movement to allow crystallization. Crystallization kinetics can also be observed through isothermal measurements, such as in Figure I-3 (b) [19].

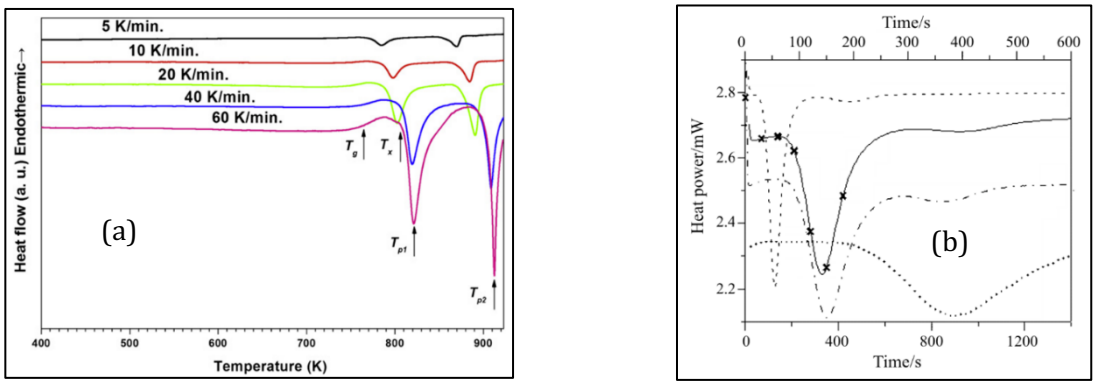

Figure I-3 : (a) Isochronal DSC curves of the as-cast $Zr_{56}Co_{28}Al_{16}$ BMGs measured at heating rates of 5, 10, 20, 40 and 60 K/min [18]. (b) Isothermal DSC crystallization curves at various temperatures Ta of the as-quenched glassy $Fe_{75}Si_{15}B_{10}$ ribbon. For --- Ta=803K and -° Ta=793K the upper time scale holds. For -°- Ta=783K and °°° Ta=773K the bottom time scale holds [19].

I.1.2.2. Glass forming ability of metallic glasses (GFA)

The Glass Forming Ability (GFA) describes the ability for a certain composition to be synthesized as an amorphous solid. Many criteria were proposed over the years to describe and compare the GFA of newly developed compositions. The first criteria to be used were based on the thermal stability of the alloys (more precisely of the supercooled liquid region), using the specific temperatures mentioned in the latter section: T_g, T_x, T_l [10]. The reduced glass transition temperature (T_{rg}) was first introduced by Turnbull *et al.* [20].

$$T_{rg} = \frac{T_g}{T_l}$$

I-4

This parameter is generally high for all glass-forming alloys, with values often above 0.6. A strong correlation was observed by Lu *et al.* between T_{rg} and R_c [21]. The higher the T_{rg}, the lower the R_c could be and therefore the easier it is to obtain metallic glass. This led to investigating potential BMG composition at or near deep eutectics. A second criterion widely used is the width of the supercooled liquid region upon heating [22].

$$\Delta T_x = T_x - T_g$$

I-5

The higher ΔT is, the more stable the supercooled liquid is and therefore the later crystallization will happen upon heating. The observation has been made by Inoue *et al.* for several compositions that the higher ΔT is, the lower R_c is [6]. Nevertheless, with the rapidly growing number of metallic glasses discovered over the years, some exceptions to this criterion appeared. This criterion should be kept for evaluation of the thermal stability but not the GFA. New criteria have been developed since. Some of them are reported in Table I-1.

Criteria	Formula	Ideal value	Ref
γ	$\frac{T_x}{T_g + T_l}$	0.5	[23]
γ_m	$\frac{2T_x - T_g}{T_l}$	1	[24]
α	$\frac{T_x}{T_l}$	1	[25]
β	$\frac{T_x}{T_g} + \frac{T_g}{T_l}$	2	[25]
δ	$\frac{T_x}{T_l - T_g}$	∞	[26]

Table I-1: Summary of the main parameters proposed to assess GFA based on transformation temperatures and their ideal value.

With such a wide range of parameters, it is rather hard to know which one to choose. Suryanarayana *et al.* collected data up until 2007 and calculated the correlation factor R^2 value for $\log(D_c)$ and the results can be found in Table I-2 [27]. The "All" row includes data for Au, Ca, Ce, Co, Cu, Fe, La, Mg, Nd, Ni, Pd, Pr, Pt, Ti and Zr as base elements.

Base	T_{rg}	ΔT	α	β	γ	γ_m	δ
Au	0.820	0.575	0.988	0.988	0.979	0.958	0.957
Cu	0.266	0.274	0.458	0.458	0.447	0.433	0.398
Ti	0.394	0.01	0.432	0.432	0.413	0.392	0.419
Zr	**0.001**	**0.007**	**0.021**	**0.006**	**0.005**	**0.001**	**0.009**
All	0.112	0.184	0.295	0.295	0.349	0.354	0.207

Table I-2: Statistical correlation factors R^2 between D_c and "GFA parameters" for several families of alloys (defined by their base metal) [27].

One can note that Zr-based metallic glasses exhibit very low correlation while precious metals, with Au for instance, exhibit very high correlation.

The experimental critical diameter (D_c), *i.e.* the maximum diameter that can be used for the alloy to be cast fully amorphous is the most commonly used parameter to describe the Glass Forming Ability (GFA) on a specific composition. This may be the only parameter with relevance for application-oriented studies. It is important to keep in mind that the maximum diameter that can be obtained is dependent on the sample composition but also on the processing technique. For instance, copper-mould casting will provide higher cooling rates than water quenching. The critical diameter should always be linked to a production technique.

All the above parameters are usually derived from experimental data. To obtain those, one must first be able to synthesize the alloy in a glassy state. For this reason, a lot of studies have been dedicated to predicting the GFA. Predictive approaches such as thermodynamic modelling (*e.g.* heat of mixing or other thermodynamic parameters), computational modelling (*e.g.* CALPHAD approach), or approaches based on structural and topological parameters (*e.g.* Egami's atomistic approach, Miracle's topological criterion…) have been proposed.

I.1.3. Inoue's criteria for glass-forming alloys

Based on the experimental data concerning the synthesis of bulk metallic glasses, Inoue proposed three empirical criteria for the formation of bulk metallic glasses [22, 28–30]:

- "The alloy must contain at least 3 components. The formation of glass becomes easier with increasing number of components in the system"

- "A significant atomic size difference should exist among the constituent elements in the alloy. It is suggested that the atomic size difference should be above about 12% among the main constituent elements."
- "There should be negative heat of mixing among the (major) constituent elements in the alloy system."

The first criterion is based on thermodynamic and kinetic aspects. It is however to be nuanced as binary glasses can be produced (such as Zr-Cu). The second is based on topological aspects (atomic packing). Along with the first criterion, it is expected to result in the efficient packing of atoms and an increase in the density of the supercooled liquid. The third criterion promotes the mixing of atoms and the formation of a homogeneous glassy phase. It is also to be nuanced as two-phased glasses exist. These criteria can be simply understood. To avoid crystallization, one should try to disfavour atomic rearrangement. This is realised by bringing so-called "confusion" to the liquid structure. When atomic rearrangement is slowed down, crystallization does not happen before solidification, upon quenching.

I.1.4. (Bulk) metallic glasses elaboration techniques.

Metallic glasses are obtained through rapid solidification from the liquid state. To achieve rapid solidification, fast quenching techniques are required [31]. The point of any metallic glass production method is to extract as much heat from the supercooled liquid metal as fast as possible. The first metallic glasses produced by Duwez *et al.* [9] was obtained in the form of very thin Au-Si ribbons using a technique called melt spinning. This consists of pouring the alloy on a rapidly rotating wheel. The wheel is made of a good thermal conductor, which most of the time is copper. The cooling rate applied to obtain the $Au_{75}Si_{25}$ metallic glass was of the order of 10^6 $K.s^{-1}$. A breakthrough for the production methods came with the apparition of bulk metallic glasses (BMG). With their improved stability and superior glass-forming ability, BMG requires much lower critical cooling rates (R_c), only about 1 $K.s^{-1}$. With lower critical cooling rates required, BMG processing progressively transitioned from quenching methods to more traditional casting methods, such as the copper mould casting method. In 1990, Inoue and his group were the first to successfully cast a bulk metallic glass in a copper mould [32]. Today the range of cooling rates spans from 10^{-1} to 10^7 $K.s^{-1}$. This gives access to bulk metallic glasses of various sizes, as illustrated in Figure I-4 (scale 1:1).

Many production techniques have been reported to date. They can be divided into three main categories: vapour state process, liquid state process and solid-state process [33]. Among them, we can cite physical and chemical vapour deposition, injection casting, suction casting, tilt casting, twin-roller casting, warm rolling and pressing [34, 35]. Injection casting and suction casting are the two most popular production methods. They are the two technics used in this work and will be detailed in the material and methods section (Chapter II). The improvement of synthesis methods, along with the development of

new alloy compositions, with a lower critical cooling rate, offered the possibility to dramatically increase the critical thicknesses over the year [36–38], see Figure I-4 and Table I-3 for some examples.

Base metal	Composition	Maximum diameter	Production method	Year	Ref
Pd	$Pd_{40}Ni_{40}P_{20}$	10	Fluxing	1984	[39]
	$Pd_{42,5}Cu_{30}Ni_{7,5}P_{20}$	80	Copper mold casting	2012	[40]
Zr	$Zr_{65}Al_{7,5}Ni_{10}Cu_{17,5}$	16	Water quenching	1993	[41]
	$Zr_{46}Cu_{30,14}Ag_{8,36}Al_{8}Be_{7,5}$	73	Copper mold casting	2011	[42]
Ti	$Ti_{40}Zr_{25}Cu_{12}Ni_{3}Be_{20}$	14	Copper mold casting	2005	[43]
	$Ti_{32,8}Zr_{30,2}Be_{26,6}Ni_{5,3}Cu_{9}$	50	Water quenching	2010	[44]
Mg	$Mg_{65}Cu_{7,5}Ni_{7,5}Zn_{5}Ag_{5}Y_{5}Gd_{5}$	25	Copper mold casting	2005	[45]
	$Mg_{59,5}Cu_{22,9}Ag_{6,6}Gd_{11}$	27	Copper mold casting	2007	[46]
Pt	$Pt_{42,5}Cu_{27}Ni_{9,5}P_{21}$	20	Water quenching	2004	[47]
Ni	$Ni_{50}Pd_{30}P_{20}$	21	Water quenching	2009	[48]
Fe	$Fe_{48}Cr_{15}Mo_{14}Er_{2}C_{15}B_{6}$	12	Copper mold casting	2004	[49]
	$Fe_{41}Co_{7}Cr_{15}Mo_{14}C_{15}B_{6}Er_{2}$	16	Copper mold casting	2005	[50]
Ca	$Ca_{50}Mg_{22,5}Cu_{27,5}$	10	Copper mold casting	2006	[51]
	$Ca_{65}Mg_{15}Zn_{20}$	15	Copper mold casting	2004	[52]
Cu	$Cu_{46}Zr_{42}Al_{7}Y_{5}$	10	Copper mold casting	2004	[53]
	$Cu_{49}Hf_{42}Al_{9}$	10	Copper mold casting	2006	[54]
Co	$Co_{48}Cr_{15}Mo_{14}C_{15}B_{6}Er_{2}$	10	Copper mold casting	2004	[55]
Y	$Y_{36}Sc_{20}Al_{24}Co_{20}$	25	Water quenching	2003	[56]
Nd	$Nd_{70}Fe_{10}A_{20}$	12	Copper mold casting	1997	[57]
La	$La_{65}Al_{14}(Cu_{5/6}Ag_{1/6})_{11}Ni_{5}Co_{5}$	30	Copper mold casting	2007	[58]

Table I-3: Summary of some BMG with critical diameter over 10mm and the year they were first reported

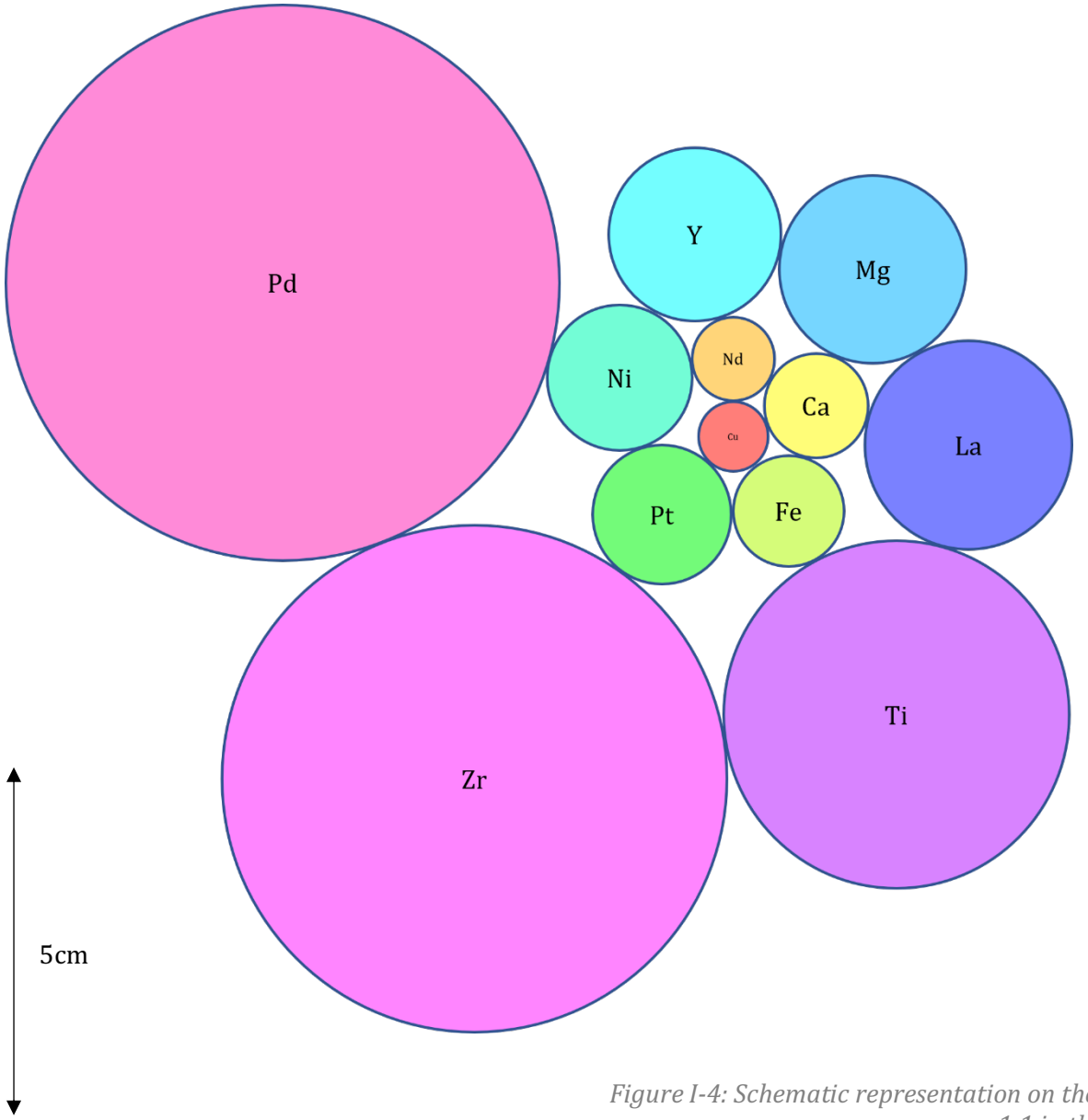

Base	D_c (mm)	Year
Pd-Cu-Ni-P	80	2012
Zr-Cu-Ag-Al-Be	73	2011
Ti-Zr-Be-Ni-Cu	50	2010
La-Al-Cu-Ag-Ni-Co	30	2007
Mg-Cu-Ag-Gd	27	2007
Y-Sc-Al-Co	25	2003
Ni-Pd-P	21	2009
Pt-Cu-Ni-P	20	2004
Fe-Co-Cr-Mo-C-B-Er	16	2005
Ca-Mg-Zn	15	2004
Nd-Fe-Al	12	1997
Cu-Zr-Al-Y & Co-Cr-Mo-C-B-Er	10	2004

Figure I-4: Schematic representation on the critical diameters achieved in metallic glasses. Scale is 1:1 in the A4 printed version.

I.2. Structure of metallic glasses

A detailed review of the development of structure model in Metallic Glasses has been written by X. Yue, A. Inoue, C.T. Tsuna and C. Fan in 2017 [59]. Understanding the structure of metallic glasses is one of the oldest topics concerning this kind of metallic material. We can quote X. Yue *et al.:* "*Understanding the structure-property correlations at the atomic level on amorphous alloys is one of the most interesting topics and also might be one of the hardest fields to finish".* There are two major approaches while developing models to describe the amorphous structure of metallic glasses. The first approach consists in describing the entire structure, at the atomic scale. The second approach, which came approximately 10 years later, describes the structures based not on lone atoms but on groups of atoms, called clusters. We will first review the most used models of the atomistic approach, before moving on to the cluster approach. More recently, electronic structural models were also proposed. A rapid review will be proposed in the second part of this section Structural information can be obtained by two means: experimental or simulation. The first mean consists of all experiments based on particle diffraction imaging (X-ray diffraction [60], small-angle X-ray scattering, high-resolution transmission electron microscope, neutron scattering etc.). The second mean consists of all computer simulations, such as molecular dynamics [61] or Monte Carlo simulation [62].

I.2.1. Atomic structure models

I.2.1.1. Atomistic approach

In 1959, Bernal [63] proposed a model called the random dense packing model (RDM). This model was improved a year later also by Bernal to become the hard-sphere random dense packing model (HSRDPM) [64, 65]. This model is based on three main assumptions: (1) the liquid is homogeneous (2) all the atoms are rigid balls stacked randomly and there is no void of the size of an atom (3) the atoms are incompressible. The pair distribution function (PDF) is commonly used to describe amorphous structures. It gives the probability of finding the centre of a particle at a given distance from the centre of another particle[66]. This model is useful to understand amorphous alloys but has some drawbacks which are mainly based on the fact that atoms are considered as hard spheres. It is however accepted that the radius of atoms will change due to atomic interactions. Therefore, a "soft sphere" random dense packing model is more powerful. Nevertheless, the HSRDPM will be relatively accurate for alloys with atoms with comparable atomic sizes and limited chemical short-range interactions.

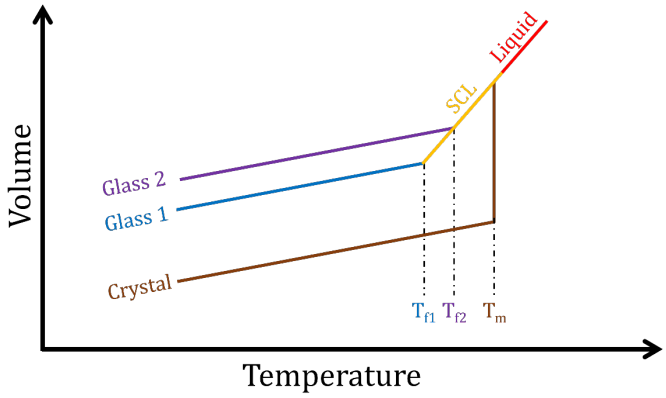

Figure I-6: Schematic representation of the decrease in enthalpy/volume of a glass-forming liquid upon cooling. T_m is the melting temperature, T_{f1} and T_{f2} are solidifications temperatures for two different glasses.

A very famous model called the Free volume model was first published by Cohen and Turnbull, in the early '70s [67, 68], to describe self-diffusion in liquids. It was later on used by Spaepen for the understanding of the deformation mechanisms in metallic glasses [69, 70]. During cooling, atoms rearrange, forming ordered networks, crystals. This ordering process is concomitant to a shrinking of the total volume of the system. However, during rapid solidification of liquids, the rearrangement of atoms is bypassed and there is less volume shrinkage. As a result, there is a gap between the volume of the amorphous solid and the volume of the corresponding crystalline solid. This excess of volume is called the free volume. The evolution of the volume with temperature is illustrated in Figure I-6 [71]. The three stages of glass-formation are represented: liquid, super-cooled liquid (SCL) and glass. Depending on the cooling rate, the structure of the glass will be different, exhibiting more or less free volume V_f. This model has been of great importance to explain mechanical behaviour (plastic flow, fracture, shear band…[72]). In this model, atoms can jump from their original position to free space in any direction if the free space is large enough to accommodate its volume. This phenomenon is illustrated in Figure I-5 from [69]. Under applied stress, jumps in a certain direction are predominant, resulting in a forward flux of atoms, creating the flow. Under applied stress, the atom can be squeezed into a space smaller than its volume, creating a certain amount of free volume. Even though this model is quite powerful for high-temperature behaviour, it is not very accurate for low-temperature studies (under T_g). A.S. Argon [73] proposed a theory of the shear transformation, where the flow is the result of the movement of a group of atoms and not of a single atom. This was later on developed by Falk and Langer [74, 75] with the Shear Transformation Zone (STZ) which will be the subject of the next section. This model is more robust than the free-volume model at low temperatures.

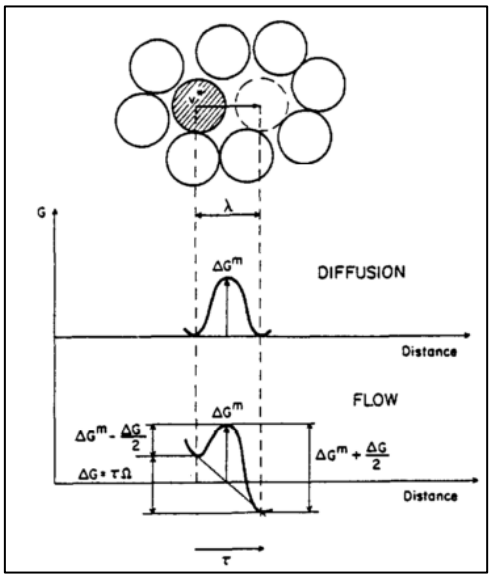

Figure I-5: Free Volume model atomic jump description. [69]

I.2.1.2. Cluster approach

With the cluster approach, the basic unit grows from the atom to a group of atoms, named a cluster. There are two predominant models: the *dense packing of the atomic cluster model* and the *flow unit model*.

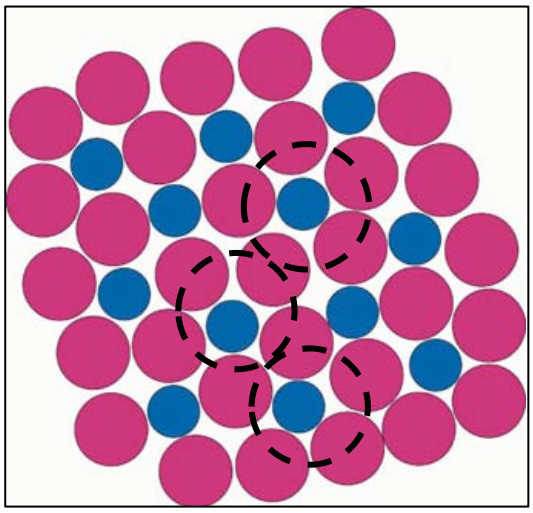

Figure I-7: Two dimensional schematic of efficient cluster packing model for binary glass. [80]

Bernal's model (RDM) failed to describe metallic glasses with strong chemical short-range order (SRO, first coordination shell). In 1978, Gaskell proposed a model for transition metal-metalloid glasses [76]. This model first introduced the idea of a basic structural unit of a scale larger than the atom. However, this model could never accommodate the medium-range order (MRO, a few structural motifs) [77]. One year later, Wang [78] proposed that amorphous metals have a crystal-like short-range order, composed of various types of polyhedrons (being the basic unit). A breakthrough was made by Miracle [79], using the MRO to explain the connection between clusters (SRO) in a model called the efficient cluster packing (ECP) model. According to this model, clusters are formed around solute atoms (minority). They are called solute-centred clusters and the solvent (majority) is efficiently packed around the solute atom. Among the most discussed polyhedrons are the icosahedral, which form icosahedral-like clusters of very high density. Clusters are connected by sharing solvent atoms but the order cannot extend beyond a few cluster diameters. With this model, both SRO, MRO and absence of long-range order are linked. The model is illustrated in Figure I-7 [80]. It underlines major features: the solute-centred clusters (blue atoms), the overlapping neighbour clusters sharing solvent atoms (dashed line) and the randomly placed clusters. This model was later improved, for instance, to fit ternary alloys [81, 82]. This is the most successful model in recent years.

The last model presented here will be the flow unit model. More models exist but they are less used. The flow unit model considers that metallic glasses are a combination of liquid-like regions and solid-like regions [83]. Liquid-like regions are unstable while solid-like regions have lower entropy. Liquid-like regions are the minority and are included in a solid-like glass matrix [84]. Liquid-like regions are of lower density and viscoelasticity and are defined as "flow units". In this model, the flow unit governs the mechanical behaviour.

This is not to be mistaken with the conceptual model based on the ECP model that refers to high-density clusters as icosahedral-like or liquid-like clusters and low-density clusters as crystal-like or FCC-

like clusters [85]. In the ECP model, based on their lower conformation/density, crystal-like clusters will act as the flow unit.

I.2.2. Electronic structure models

Electronic structural models differ from the atomic structural models as they are aiming to explain glass stabilization rather than solving atomic arrangements [86]. Nagel and Tauc introduced the nearly-free electron model in 1975 [87]. The nearly-free electron model accounts for the electronic structure of the constituent atoms and states that the glass is stabilized when there is a local minimum in energy at the Fermi level. C. Dong *et al.* presented that the nearly-free electron model can be used to explain many binary and ternary BMGs-forming compositions. Dong *et al.* proposed in 2007 a hybrid model, the cluster-plus-glue-atom model [86]. This model is based on the possible existence of molecule-like structural units. Clusters are all isolated and matched together with so-called "glue-atoms", forming molecular like-structural units, reaching MRO. In this model, the solute atom is therefore surrounded by a first shell of nearest-neighbour on top of which is a shell of outer-shell glue atoms, as illustrated in Figure I-8.

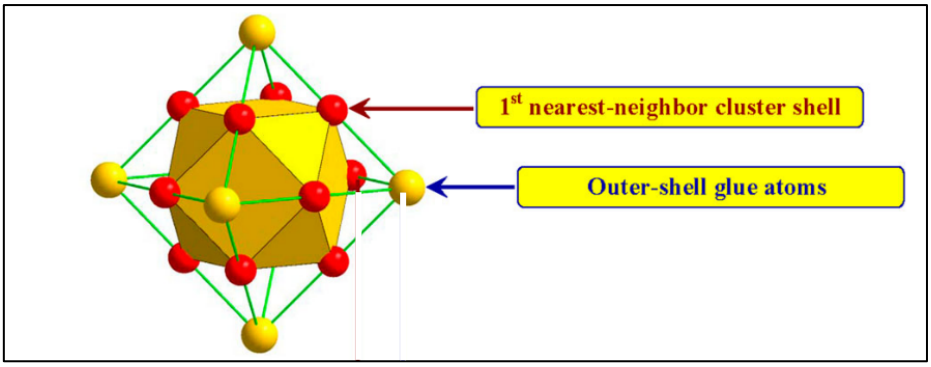

Figure I-8: Schematic representation of the cluster-plus-glue-atom basic unit, presenting the nearest-neighbour cluster shell and the outer-shell (glue atoms). [86]

Like other materials, such as crystalline metallic alloys, the structure of glass will ultimately dictate its properties. It has now been clearly exposed that metallic glasses are amorphous, meaning that they lack periodicity, but only at the long-range order (LRO). They do exhibit structural order, but only at medium and small ranges (the distance of a few atoms and the first neighbour shell, respectively). In the next section, we will review metallic glasses properties and bring a particular focus on their mechanical properties.

I.3. Mechanical properties of bulk metallic glasses

I.3.1. A brief overview of the general properties of BMGs.

Metallic glasses and more recently bulk metallic glasses have drawn considerable attention since their discovery because of their broad range of interesting properties. Because they lack crystalline order

and traditional metallic alloys microstructure, they are also free of all the crystallographic defects, such as point defect (vacancy, interstitial, anti-site) and line defect (dislocations) but also planar defect (grain boundaries, stacking faults). When there is no order, nothing is out of place. All of those defects are limiting some properties of crystalline alloys. M.F. Ashby and A.L. Greer [88] proposed a review of metallic glasses properties for potential applications as structural materials, which is resumed in Table I-4.

Attributes	Attractive	Unattractive
Mechanical	• High hardness, good wear resistance • High mechanical resistance (yield stress) • High elastic deformation	• Severe localization of deformation at room temperature, impeding ductility • Fracture toughness can be very low
Corrosion	• Low corrosion rates due to the lack of grain boundaries and secondary phases	
Biocompatibility	• Some compositions are free of potentially harmful elements • May be biodegradable (Mg-based BMGs)	• Composition free of potentially harmful elements may often have very low GFA
Processing	• Low solidification shrinkage, easier to cast near-net shape products • High viscosity and thermal stability allow thermoforming	• Cost of components and processing • Need for vacuum or controlled atmosphere casting, slowing down production rates
Magnetic	• High magnetic permeability • Resistivity nearly independent of temperature	
Aesthetic	• Lack of grain boundaries allows a very high polish • High wear and corrosion resistance increase durability	

Table I-4: Summary of the main properties of metallic glasses, adapter from M.F Ashby et al. (2006) [88] and the thesis of A. Lenain (2016)

I.3.2. Deformation mechanisms

Among all the properties exhibited by metallic glasses, their mechanical properties "*have been a subject of fascination for scientists and engineers*" [72]. Over the years, many review papers have been published to gather and organize all the ongoing works and theories about the mechanical properties and deformation mechanisms of metallic glasses [17, 72, 82, 89–93]. In the following sub-sections, we will

review bulk metallic glasses deformation mechanisms, from the elastic deformation to the fracture. Note that this review is only interested in deformation behaviour at room temperature.

I.3.2.1. Elastic deformation

Metallic glasses are particularly attractive because of their very high yield stress, combined with a rather low Young's modulus. Figure I-9 shows the yield stress σ_y as a function of Young's modulus E for numerous metals, alloys, composites and metallic glasses [88]. Note the logarithmic scale on both axes. One can see from this figure that for identical E values, BMGs have higher yield stress values. One can also observe that among the metallic materials presented here, the metallic glasses are closer to the theoretical strength (E/10) [88].

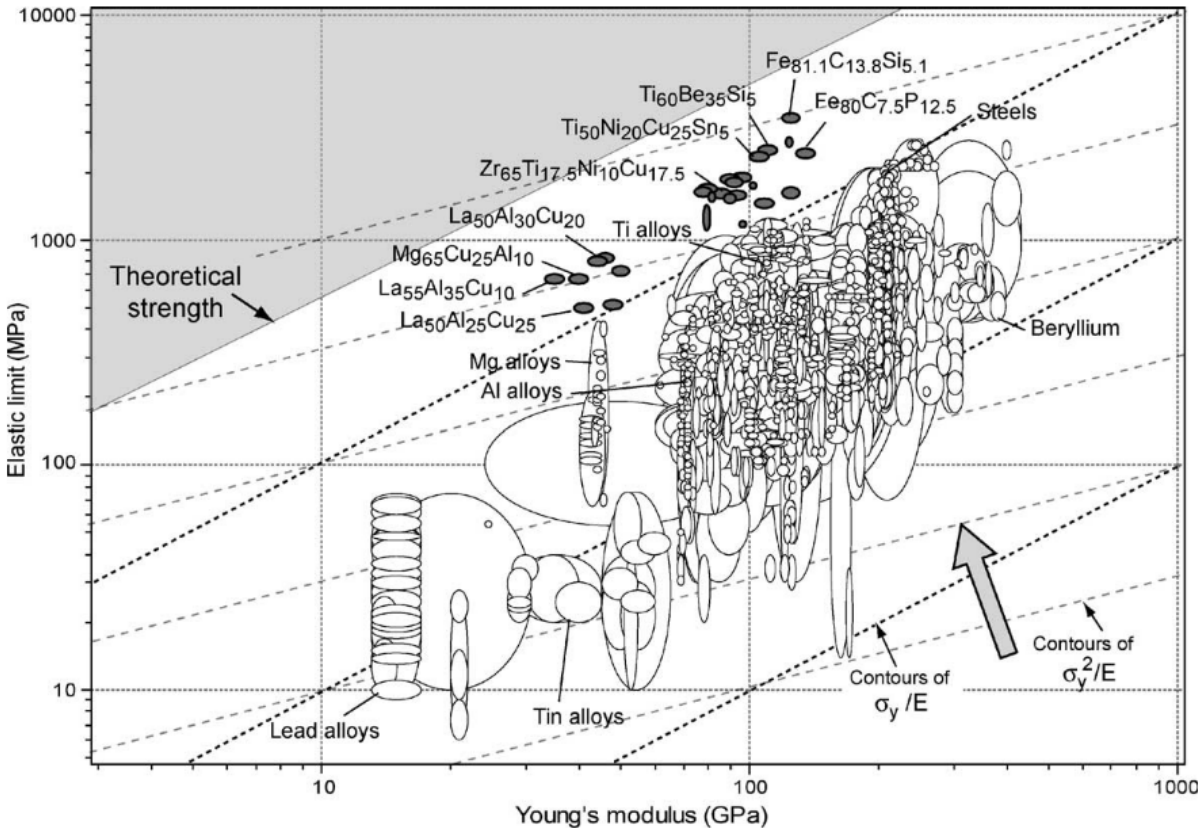

Figure I-9: elastic limit σ_y plotted against the Young's modulus E for 1507 metals, alloys, metal matrix composites and metallic glasses. The contours show the yield strain (σ_y/E) and the resilience (σ^2_y/E) [88].

The following presentation of bulk metallic glasses elastic properties is based on three main reviews: the review from Egami *et al.* (2013) [89], the overview article from Hufnagel *et al.* (2016) [91] and the review from Wang (2012) [94]. In conventional crystalline alloys, a homogeneous strain will result in a homogeneous deformation in simple crystals. At low strain in crystals ($\varepsilon < 0.2\%$), deformation is fully reversible and follows Hook's law (affine deformation). The elastic deformation for a continuum body can be written as:

$$r' = (1 + \bar{\bar{\varepsilon}}).r$$

I-6

where r and r' are atomic positions respectively before and after deformation and $\bar{\bar{\varepsilon}}$ is the strain tensor following Hook's law. However, at the atomic level, an amorphous solid is not a continuum and each atom has a different surrounding environment, meaning a different strain tensor for each atom. The elastic deformation can therefore be re-written as:

$$r_i' = (1 + \bar{\bar{\varepsilon}}_i).r_i$$

I-7

where the suffix i refers to each atom of the system. The highly important takeaway message from these equations is that the strain field for metallic glasses under stress will be highly heterogeneous at the MRO scale. Because stress can be higher than the elastic limit at local scales while applying stress lower than the elastic limit at a macroscopic scale, the glass will locally undergo anelastic deformation and non-linear (non-affine) deformation. The deviation from Hook's law has been widely studied in simulation for a broad variety of systems. It appears that the strain shows a strong dependence on the length scale of measurement. Typically, the deviation from Hook's law is very pronounced on short length but the response becomes homogeneous and linear at longer length scales. This highlights the several scales which must be considered while conceptualizing metallic glasses structure, namely short-, medium- and long-range order (SRO, MRO and LRO). An additional reflection of the disordered structure of BMGs lies in their high compliance. Indeed, it has long been recognized that metallic glasses have lower stiffness than crystalline counterparts of similar compositions.

I.3.2.2. Shear banding and plastic deformation

In addition to the several reviews mentioned earlier, this part will be based on the extensive review published by A.L. Greer, Y.Q Cheng and E. Ma in 2013 [90].

I.3.2.2.1.Shear Transition Zones (STZs)

It is now clear that the deformation of bulk metallic glasses will not be controlled by dislocation displacement, as in conventional crystalline materials, as they do not possess such defects. Nevertheless, some metallic glasses are capable of plastic deformation (usually in compression). As Hufnagel *et al.* [91] pointed out, it is helpful to be familiar with the concept of potential energy landscape to understand the connection between structure and deformation mechanisms in amorphous materials. Figure I-10 is a schematic one-dimensional potential energy landscape (reproduced from [91]).

The glass in the as-cast state will find itself in one of the basins, inside a metabasin, as represented in Figure I-10 (a). Applying shear stress to the glass will affect its potential energy landscape. Shear deformation can cause basin (energy minima) to disappear, forcing the system to move in a more favourable (of lower energy) inherent state, as shown in Figure I-10 (b). Simulations suggested that 10 to 50 atoms or more could be involved in such rearrangement. This kind of instability has been conceptualized by Argon *et al.* under the name of "shear transformation". Movements of the atoms involved in the shear transformation are of a higher magnitude than the surrounding atoms. The zone including the atoms involved in the shear transformation is termed as a "Shear Transformation Zone" (STZ). It is important to emphasize that STZ are not defaults embedded in the glass matrix but nucleate under external stimuli. It is however controversial if the sites for the nucleation of STZs are encoded in the glass structure.

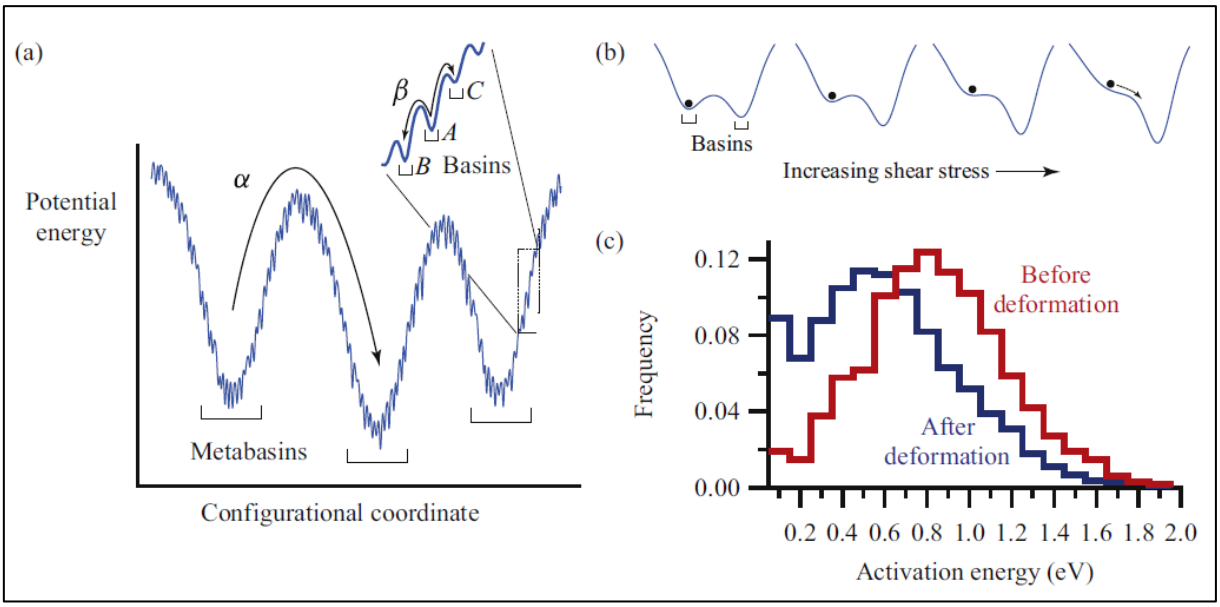

Figure I-10: (a) Schematic potential energy landscape for a glass. Upon cooling from the liquid, the system will find itself in one of the basins (A in the inset.) The β relaxation corresponds to a thermally-activated transition to a neighbouring basin (A/B) but a glass does not have enough thermal energy to transition to another metabasin by a series of uphill jumps (A/C). An evolution to another metabasin requires sufficient thermal energy to activate the α transition - that is, the glass must be heated through the glass transition to become a supercooled liquid again. (b) Applying a shear stress changes the shape of the potential energy landscape, possibly rendering some stable configurations unstable by eliminating the barrier to a neighbouring configuration. (c) Distribution of activation energies in a simulated metallic glass before and after plastic deformation. [91]

As seen from the previous sub-section, stress tensors are very heterogeneous in the glass matrix. Therefore, shear transformation occurs not only in the plastic regime but could occur very early in the elastic regime, in a very localized manner. The rest of the glass matrix can elastically accommodate for the change in the shape of the STZ. This results in an overall macroscopic strain, which will itself influence the potential energy landscape, and the nucleation of new STZs. The STZs size and activation energies are very central questions that focused research in the past years. As reported by Hufnagel *et al.*, recent

analysis using DMA (Dynamical Mechanical Analysis) revealed distinct activations energies correlated to STZs of discrete sizes [91]. This gives us a concept of the STZs were at a specific strain, part of the STZs nucleate and are triggered, while some other STZs needs higher stress/strain to be activated and lead to atomic rearrangement.

Other studies suggested that STZs are more likely to be found in regions presenting more structural disorders which commonly contain larger free volume content [90]. We can connect this to the structural models detailed earlier in this presentation (section I.2): in the ECP model, favourable regions for STZs nucleation will be the clusters of lower coordination number (CN) and compacity which will favour shear transformation. To quote Hufnagel *et al.* [91] "it is an open question to whether these soft spots are STZs or whether it is better to think of them simply as "fertile regions" that give rise to shear transformation". Nomoto *et al.* proposed very recently that FCC-like clusters extending over MRO act as STZs and are responsible for the softening of the BMG [85]. Conversely, icosahedral-like clusters at MRO are not favourable for STZs nucleation because of their high CN and compacity.

I.3.2.2.2.Shear Banding

If we consider that each potential STZ is associated with an activation energy depending on its size, increasing loading on the metallic glass will provoke the activation of more and more STZs. Once the stress reaches a critical value, *i.e.,* the yield stress σ_y, yielding occurs and macroscopic irreversible change appears. Yielding is accompanied by the initiation of at least one shear band. "Shear banding" is the phenomenon describing the localisation of a large amount of strain in a thin band, called a "shear band". The relation between shear bands and STZs is debated and three main options are discussed:

- When a sufficient number of STZs are activated, they will exceed a "percolation limit", forming a deformation band into which the strain will be concentrated. This is the initiation of the shear band. With this concept, a shear band develops homogeneously across the material. This is coherent with the vision presented by Nomoto *et al.* as described in Figure I-11 [85]. In this scenario, there is no propagation of shear bands. Nomoto *et al.* went further by proposing a model where the effective yield stress of the glass is related to the volume fraction of softer clusters:

$$\sigma_y = \sigma_y^m - \sqrt{3}E^m(1-\beta)\gamma_{pl}^{MRO}\phi$$

I-8

with σ_y^m being the yield stress of the harder BMG matrix (than the average), E^m the elastic modulus of the BMG matrix, γ_{pl}^{MRO} the plastic strain of the softer clusters at the point of overall composite yielding, β is the material constant of Eshelby's S-tensor for spherical inclusions (depending on the BMG matrix Poisson's ratio) and finally, ϕ is the volume

fraction of softer clusters [85]. From this, we understand that yield is controlled by the softer cluster. But this model does not account for clusters size and repartition.

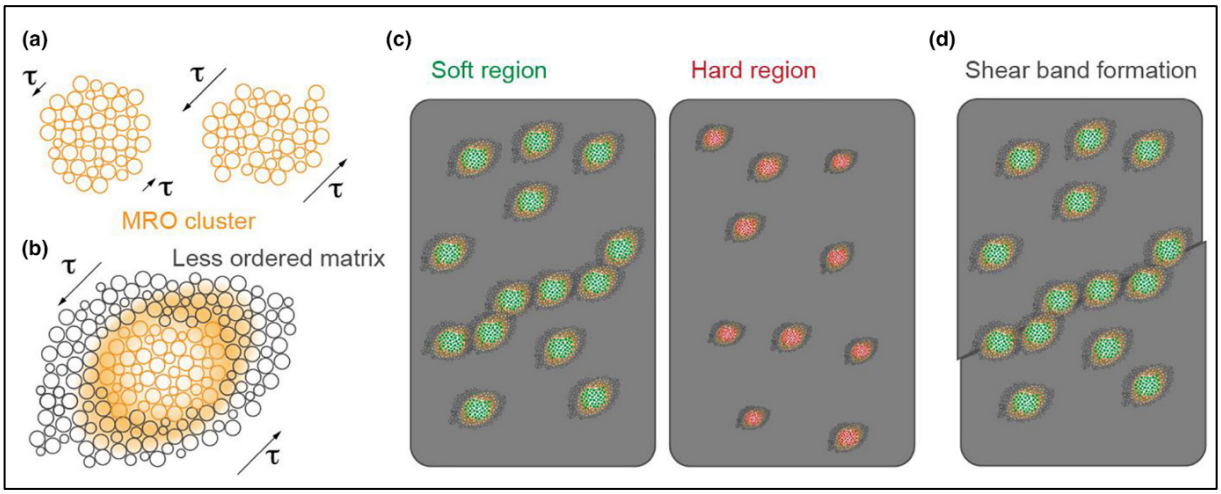

Figure I-11: Schematic illustration of the role medium range order clusters play in BMG deformation. (a) FCC crystal-like MRO cluster acting as a shear transformation zone (STZ) nucleus. (b) Transfer of structural perturbations to the less ordered glassy matrix surrounding the MRO cluster. (c) Percolation of the structural perturbations is easier in the soft regions with larger and more MRO clusters. (d) The linking of MRO clusters to form a shear band nucleus. [85]

- Casting defects (such as voids, surface notches…) will concentrate the stress. The stress concentration will locally activate a group of STZs around the defect creating an embryonic shear band. Once this shear band reaches a critical size, it will develop into a mature shear band that will propagate. Such shear bands will exhibit a "spearhead-like hierarchy". This specific propagation concept is described as proposed by Shimizu and Ogata in Figure I-12 [90]. Unlike the first scenario, this scenario considers shear bands as moving entities, which propagate along a direction in the glass.

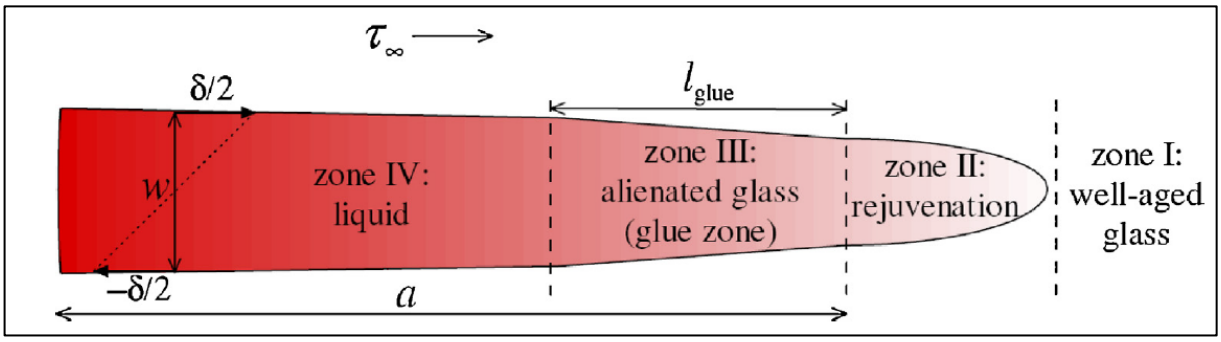

Figure I-12: The propagation front of shear band as modelled by Shimizu and Ogata. [90]

- The third and last scenario considers shear band formation as a two-stage process. The first step is the creation of a "pre-band" by activation of STZ along a band so that the structure becomes looser and more disordered. The STZs activation resembles scenario two as it propagates heterogeneously from the stress concentrators and across the material (Figure I-13 (a), (b) and (c)). Yet it is not considered as a shear band as strain is

small. Once this softer, more mobile path is created, sliding will happen along the STZ plane, creating the shear band (Figure I-13 (d)). As sliding increases, the temperature will rise, activating other STZs and thickening the shear band. This third scenario is illustrated in Figure I-13 (reproduced from [90]).

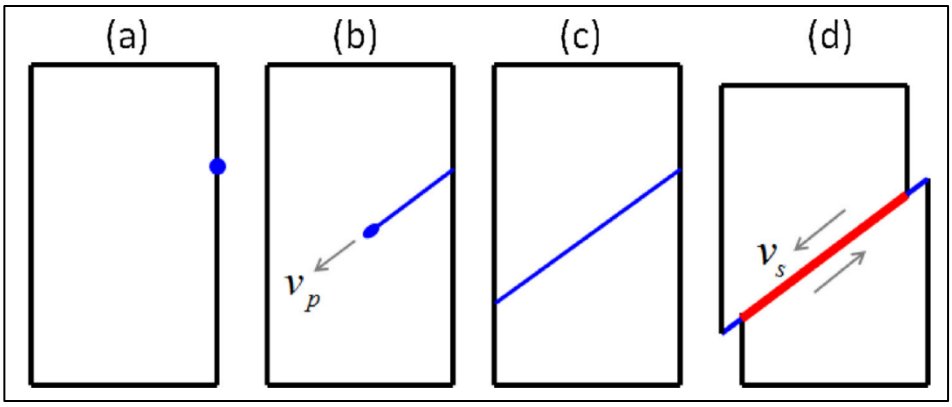

Figure I-13: Schematics showing how a shear band forms in a metallic glass under compression. (a) A stress concentrator (e.g. flaw or surface notch) leads to higher local stress. (b) Structural disordering propagates at a velocity (vp) (c) The propagating front reaches the other end of the sample, leaving a plane of lower stability than the rest of the matrix. At this moment, the strain in the band and the shear offset are small, and the band is cold. (d) Cooperative shearing/sliding and growth of the shear offset on both ends. Depending on the sample size and loading conditions, the shearing can be stable or unstable, the band can remain cold or become hot, and the shear velocity (vs, the velocity of one side of the shear band relative to the other) can either follow accelerate–decelerate cycles or increase monotonically. [90]

No matter the effective scenario, once the sliding increases inside the shear band, the temperature increases rapidly, locally up to the melting temperature. For this reason, it is common to observe drops on the fracture surfaces, as residual signs of the temperature elevation inside the shear band. The shear banding process is a precursor of the fracture of BMGs. Once a shear band are initiated, it will propagate. Once the displacement reaches a specific strain threshold inside a shear band, a crack forms in the band, rapidly leading to fracture.

I.3.2.3. Fracture of bulk metallic glasses

Several fracture modes can be observed depending on the loading mode and the brittleness of the glass [92]. In uniaxial compression or tension loading, the “shear fracture mode” is the most observed. Facture angles are generally of the order of 45° compared to the loading axes for compression loading and above 45° for tensile loading. For instance, $Zr_{55}Cu_{30}Al_{10}Ni_5$ BMG is reported to fracture with an ingle of 53° in tensile failure and 41° in compressive failure. Figure I-14 (a) and (b) are SEM side-views of a $Pd_{40}Ni_{40}P_{20}$ BMGs for failure in tensile and compression loading.

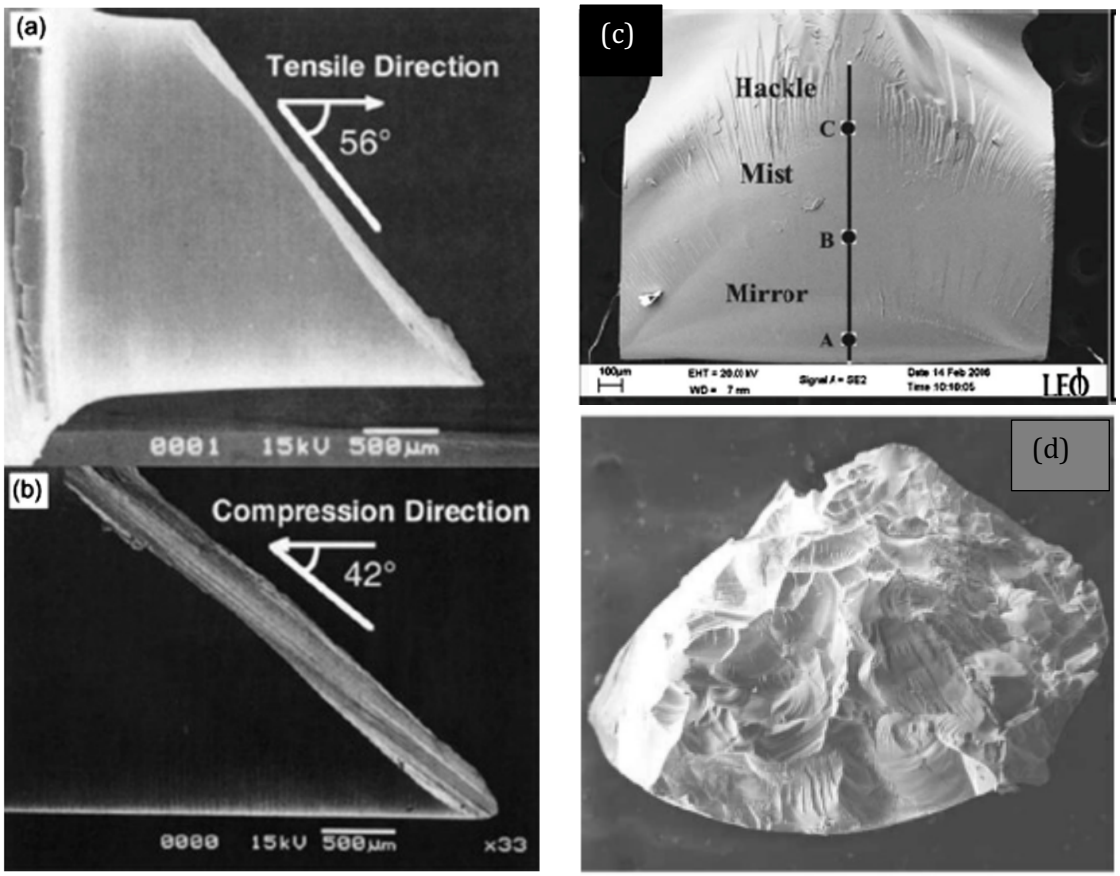

Figure I-14: (a) and (b) are side-views of a PdNiP BMG after shear fracture in tension and compression, respectively. (c) SEM view of a typical cleavage fracture surface for a Fe-based BMG. (d) Picture of a fracture surface particle after fragmentation. [92]

Another mode called the "cleavage mode" can be observed, where the fracture plane is perpendicular to the loading axes. This fracture mode is mostly observed in bending. An example of the fracture surface resulting from this fracture mode is given in Figure I-14 (c) for a Fe-based BMG. Here the very characteristic fracture surface can be divided into 3 regions, the mirror, mist and hackle regions. These differences in the surface roughness along the fracture planes are related to the increasing crack propagation velocity. A third fracture mode is the" fragmentation mode" which is common for the compression failure of very brittle BMGs, such as Co-based BMGs. Such fracture mode is characterised by the division of the sample into many fine particles. This fracture mode can be approximated as a variety of cleavage modes happening simultaneously in a single sample. A fragment of a Co-based BMG which failed through the fragmentation mode is reported in Figure I-14 (d).

The study of the fractures patterns can give valuable indications on the dynamic of the fracture process and other fracture properties [92]. Depending on the material properties and the fracture mode, several patterns can be observed on fracture surfaces

The vein pattern or dimple pattern is commonly observed for the fracture of ductile materials. Figure I-15 is an SEM image of the fracture surface of a Zr-Co-Al BMG on which one can observe the typical vein pattern.

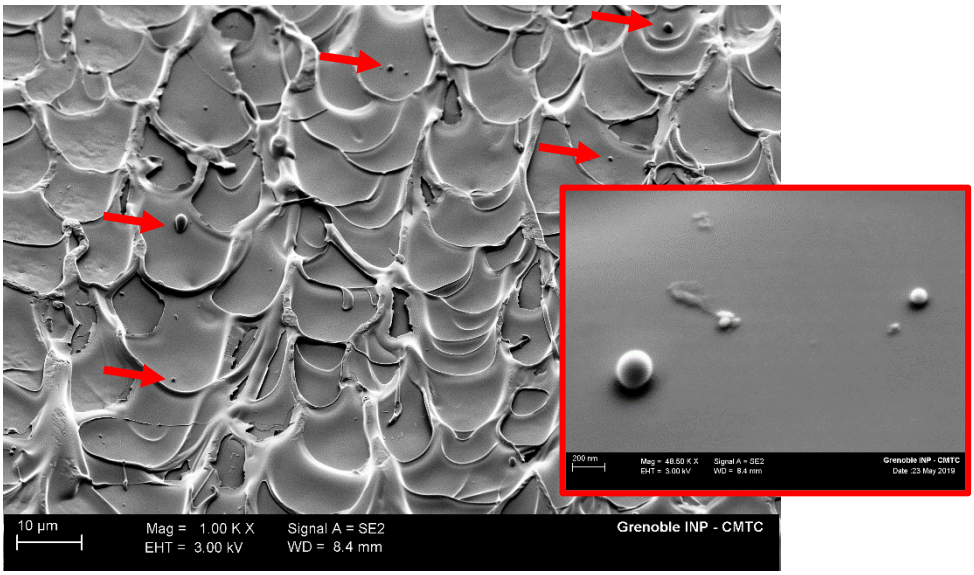

Figure I-15: SEM picture of the vein pattern on the fracture surface of a Zr-based BMG.

This pattern is similar to the pattern left by the separation of a layer of grease between two solid plates of material [92]. It is believed that this pattern is resulting from the softening of the bulk metallic glass inside of the shear band (see I.3.2.2.2). This could be assimilated to a thin viscous layer between two solids, like in the analogy with the grease and the two solid plates. The softening is associated with a temperature rise and actual signs of liquid state can be observed on the fracture surface, such as droplets (see arrows on Figure I-15 and inset).

A correlation between the fracture toughness and the plastic zone size (average dimple size) is illustrated in Figure I-16 from [95]. From this observation, an empiric law was deduced:

$$w = \frac{1}{6\pi}\left(\frac{K_{IC}}{\sigma_y}\right)$$

I-9

with w being the average dimple size, K_{IC} the fracture toughness and σ_y the yield stress. Other patterns can be observed on the fracture surface of BMGs. Brittle (less tough) BMGs exhibit finer patterns than vein-like patterns, suggesting that the softening mechanisms happen at a much smaller scale [92]. Vein pattern analysis should be performed with caution. We can observe strong disparities between several vein pattern zones on a single fracture surface. For this reason, quantitative study of the vein pattern should rely on statistical analysis, as performed for instance by O. Baulin [96].

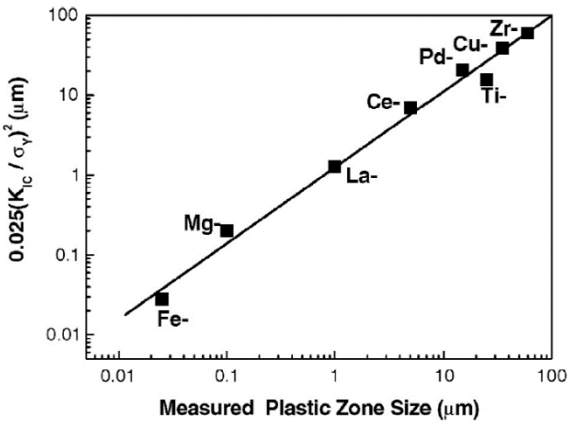

Figure I-16: Correlation between plastic zone size and fracture toughness. [95]

We reviewed the general theory of the deformation of metallic glasses. This was important especially to introduce the concepts of the shear transformation zone (STZ) and the shear band (SB). We will now move on to the mechanical behaviour of metallic glasses under some specific loading modes, such as compressive loading and cyclic loading (fatigue).

I.3.3. Compression and fatigue resistance

I.3.3.1. Compression resistance

BMGs are often reported to exhibit very brittle behaviour, with no plasticity, under tensile loading, while they can exhibit plasticity in compression loading. Q. He *et al.* showed this phenomenon for a $Zr_{61}Tu_2Cu_{25}Al_{12}$ BMG as illustrated in Figure I-17 (a) and (b) [97]. Ignoring the fact that they used different casting diameters for tensile and compression testing, they demonstrated that no plasticity was achieved in 3mm-diameter samples in tensile loading while the same alloy with similar geometry exhibited up to 4% of plastic deformation (for 3mm-diameter samples). Interestingly, yield stress in compression testing is measured at 1688 ± 18 MPa and fracture stress in tension testing is measured at 1600 ± 36 MPa, which is rather close. Similarly, the elastic strain limit is of the same magnitude: around 2%.

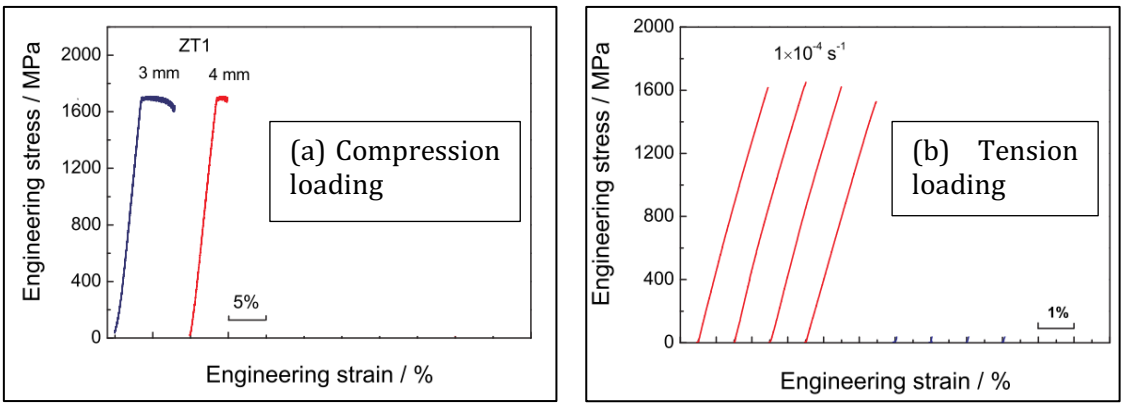

Figure I-17: Stress/Strain response for a $Zr_{61}Ti_2Cu_{25}Al_{12}$ (ZT1) alloy for several loading modes: (a) compressive engineering stress-strain curves at strain rate of $1x10^{-4}$ s^{-1} ; (b) Tensile engineering stress-strain curves at strain rate of $1x10^{-4}$ s^{-1}. Samples for compression testing are machined from 3mm- and 4mm-diameter rods, while samples for tension testing are machined from 6mm-diamter rods. [97]

The same behaviour has been reported in other published papers such as [98]. In tension loading, the shear band can propagate without constraining. There is no confinement of the defects such as in compressive loading. Because of this, catastrophic failure will happen quite early when all the shear deformation is concentrated in a primary shear plane, resulting in zero tensile ductility.

However, under constrained loading such as compressive loading, the shear banding process can be quite different. In theory, materials are not supposed to fracture under compressive loading as there is no opening stress to initiate a crack [92]. The shear banding in the case of the compressive loading can exhibit a stable serrated flow [99–111], as it can be observed in crystalline materials with the "Portevin Le Chatelier" effect. A serration is composed firstly of a loading part, where effective deformation of the speed of the shear band is inferior to the external loading rate. Then, once the stress reaches a critical value, the shear band propagation velocity increase and becomes superior to the external loading rate and a sudden stress drop occurs. This two-stage phenomenon is illustrated in Figure I-18 adapted from [103]. This illustrates that the stress drop happens over a much shorter time frame than the elastic loading.

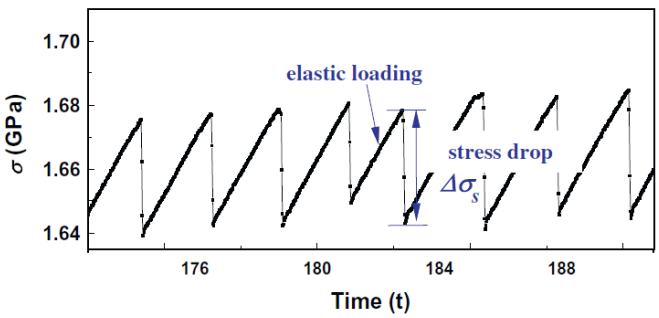

Figure I-18: (a) example of serrations taken from the compression stress/strain curve of a $Zr_{65}Cu_{15}Ni_{10}Al_{10}$ BMG at $2x10^{-4}$ s^{-1}; (b)The absolute derivative of the stress to the time from (a). t_e is the incubation time and t_p is the unloading time. [103]

The detailed study of the serrated flow during the deformation of BMGs can give very valuable insight into the shear banding process. The serrated flow corresponds to the intermittent shear of a shear band along the shear plane or a random shear band emission. In 2010, B.A. Sun *et al.* demonstrated that there is a correlation between the dynamic behaviour of serrated flow and the plasticity of metallic glasses [108]. Looking at the repartition of the stress drops during the serrated flow of MGs, two regimes are highlighted: the chaotic regime and the self-organized criticality (SOC) regime.

- The chaotic regime is defined where no specific order is detected in the stress drop repartition. This is the signature of weak to inexistent interactions between shear bands and of the localisation of the strain in a single shear band.
- Inversely, the SOC regime is defined by a power-law distribution of the stress drop magnitude. This regime is the signature of the dissipation of any external impact throughout a complex

network of participants. This suggests that when the SOC regime is detected, it is the signature of shear band interactions during the deformation of BMGs.

The two serration regimes are illustrated in Figure I-19 for Vit 105 (a) and $Cu_{47.5}Zr_{47.5}Al_5$ (b). Relative mechanical properties in compressive loading are shown in Table I-5. All data and figures are extracted from [108].

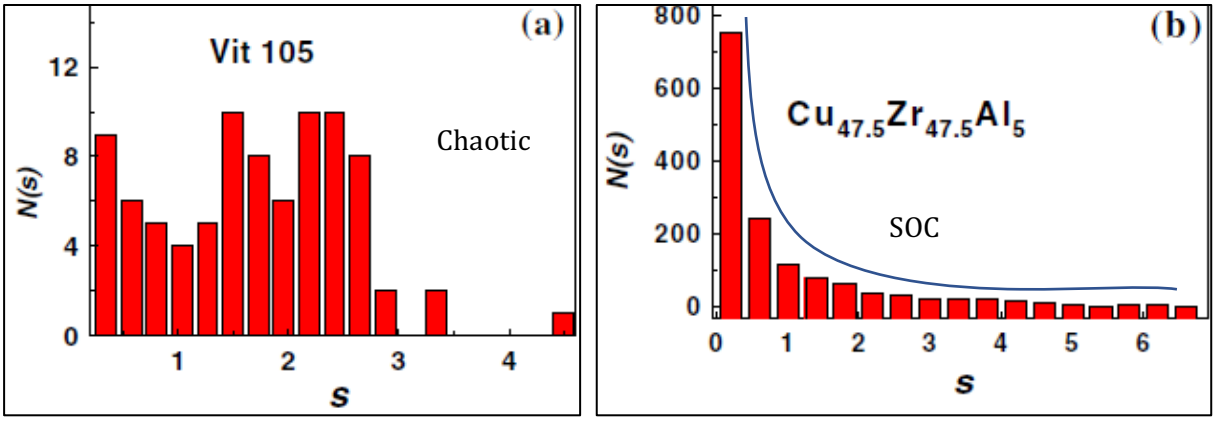

Figure I-19: Number of stress drops N(s) vs the normalized stress drop magnitude s for (a) Vit 105 and (b) $Cu_{47.5}Zr_{47.5}Al_5$. [108]

MG	σ_y (MPa)	ε_p (%)	Dynamics of serrated flow
$Zr_{52.5}Ti_5Cu_{17.9}Ni_{14.6}Al_{10}$ (Vit 105)	1740	2.26	Chaos
$Cu_{47.5}Zr_{47.5}Al_5$	1810	10.9	SOC

Table I-5: Mechanical properties of Vit105 and a Cu-Zr-Al BMGs under compression loading at a strain rate pf $1x10^{-4}$ s^{-1} strain rate.

This analysis was applied by L.H. Liu *et al.* to characterize the serrated flow behaviour of a unique alloy ($Zr_{55}Cu_{30}Ni_5Al_{10}$) but with several heterogeneities content, mainly free volume [105]. They observed that the alloy with the highest heterogeneity content had the highest ductility. By analysing the serrated flow during plastic deformation, they showed that the most ductile BMG displayed a SOC-type serrated flow while the most brittle BMG displayed a chaotic-type serrated flow. Finally, on samples surfaces, they observed much more shear bands on the most ductile BMG while the most brittle BMG presented a much lower shear band concentration. This leads to the following conclusion:

A glass with a higher heterogeneity content will develop more shear bands. A higher density of shear bands will allow for a better repartition of the external stresses, leading to a higher achievable ultimate plastic strain. In the statistical analysis of the serrated flow, one can find that a sign of the collective motion of the shear bands is observed when the stress drop statistical repartition exhibits a power-law distribution (SOC).

I.3.3.2. Fatigue resistance

For structural applications, fatigue resistance is a very important property, as ninety per cent of all service failures due to mechanical causes are associated with fatigue [112]. Fatigue-failure can be described as a three-stage or five-stage process [112, 113]:

- (1) Crack initiation
  - Cyclic plastic deformation before fatigue-crack initiation
  - Initiation of one or more microcracks
- (2) Stable crack growth
  - Propagation from microcracks to macrocracks
  - Propagation of macrocracks
- (3) Fast fracture

The study of the fatigue limit of BMGs has drawn particular attention for the past years, along with the fast-growing critical diameters achievable [112–114]. An extensive review of the fatigue limit of BMGs and BMGs composites has been published by H. Jia *et al.* in 2018 [112]. With the increasing number of studies, it is now clear that BMGs exhibit a wide range of resistances, with fatigue limits ranging from less than 10 % to more than 50 % of their respective fracture strength. The fatigue ratio is given as the fatigue limit over the fracture strength. It should not be mistaken with the R-ratio, which is the minimum load over the maximum load in a loading cycle. Most of the fatigue tests available in the literature are performed with an R-ratio of 0.1, meaning that during the unloading phase of a cycle, the load decreases down to 10% of the maximum load.

Numerous factors can influence the fatigue resistances of BMGs. They can be extrinsic, such as the loading mode, the environment, the stress ratio or the primary alloy quality. They could also be directly related to the glass structure, such as the free-volume content. To grasp mechanisms influencing fatigue resistance of BMGs, X.D. Wang *et al.* compared the fatigue behaviour of the Vit 105 ($Zr_{52.5}Cu_{17.9}Ni_{14.6}Al_{10}Ti_5$) containing different amounts of free-volume [115]. Interestingly, to obtain two distinct free-volume contents in the Vit 105, they only had to have the material processed by two different operators. This once again highlights the sensibility of BMGs to the processing conditions. They used the well-established correlation between the exothermic event before the glass transition, corresponding to relaxation, and the free volume concentration [116]:

$$\Delta H = \beta . \Delta v_f$$

I-10

As a preamble, they correlate the reduction of the free-volume content to a reduction of the ductility of the glass. Both DSC measurements for free-volume evaluation and compression tests are shown in Figure I-20.

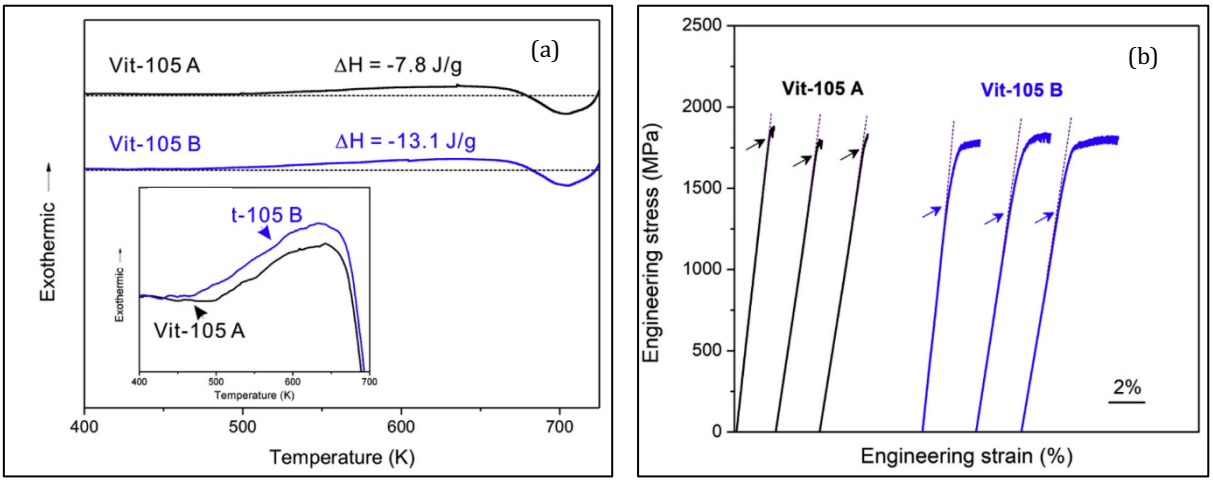

Figure I-20: (a) DSC curves for Vit 105A and Vit 105B, the inset is en enlargement of the region of interest, showing signals before glass transition; (b) compressive engineering stress-strain curves of Vit 105A and Vit105B [115].

From Figure I-20, we can see that the Vit 105A has a lower free-volume content associated with a smaller plastic deformation before fracture in compression testing. In agreement with what is exposed in section I.3.3.1, they observed smaller and numerous serrations in the plastic flow of alloy Vit 105B, which is more ductile compared to Vit 105A. In addition, they showed that Vit 105A had a better fatigue endurance limit than Vit 105B, as illustrated in Figure I-21. From the post-mortem sample surface study, they also noticed that Vit 105B had developed numerous shear bands, while Vit 105A had no sign of shear bands on the surface. Therefore, it is concluded that by suppressing shear band nucleation, one could increase fatigue resistance.

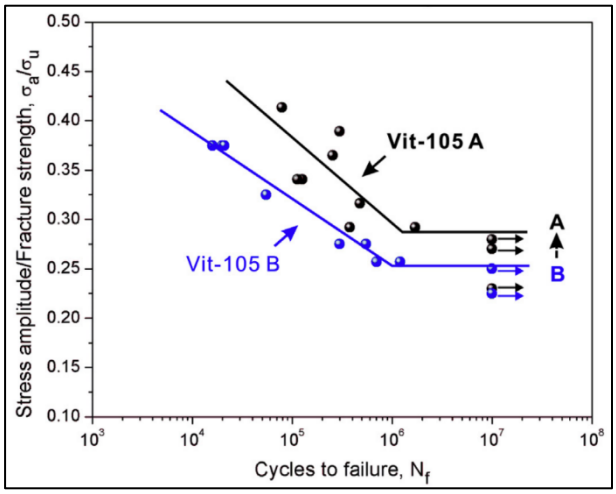

Figure I-21: Applied stress amplitude normalized by the compressive fracture strength, as a function of the cycles to failure, N_f. The alloy is a $Zr_{52.5}Cu_{17.9}Ni_{14.9}Al_{10}Ti_5$. [115]

As mentioned in section I.3.2.2, inelastic deformation can happen way below the effective compressive yield stress. This is for instance practically illustrated by X.D. Wang *et al.* who observed shear band development during compression-compression cyclic deformation of a Vit 105 BMG sample under

its yield stress (Figure I-22 (a)) [115]. They also observed softening during the solicitation, as new shear bands developed after 1900 cycles compared to 1000 cycles (Figure I-22 (a) and (b)). In other words, cyclic compression at stresses below the quasi-static compression the yield stress promoted free-volume creation, reducing energy barrier for the emergence of new shear bands.

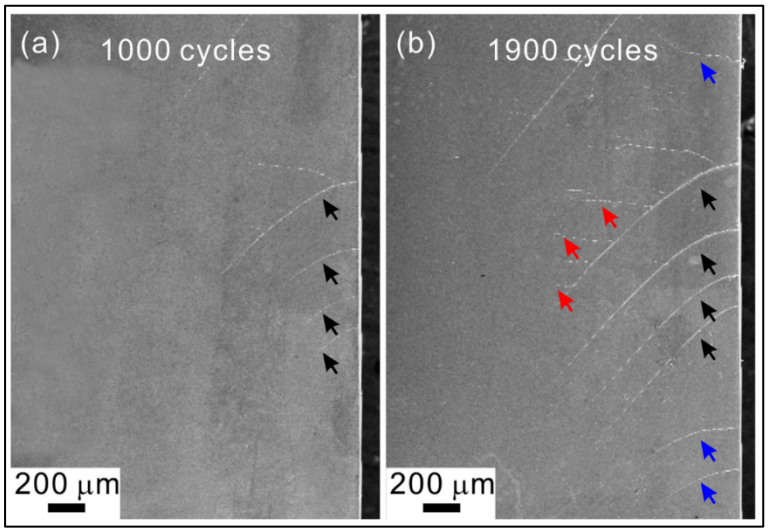

Figure I-22: Shear banding features of Vit 105 BMG after (a) 1000 cycles and (b) 1900 cycles. Between the two stages, shears bands increased in length and number (arrows). [115]

More recent studies provided additional insight into the mechanisms governing fatigue resistance [114, 117, 118]. Fatigue resistance is mainly controlled by two factors related to the three-stage process evocated earlier: the ability to delay crack initiation (stage 1) and the ability to slow down crack propagation (stage 2). The higher the toughness of the glass, the slower the crack will propagate [118], which is rather easy to understand. The crack formation or even shear banding at stresses lower than the yield stress is maybe harder to understand and focuses some current studies of the fatigue resistance of BMGs. We have just mentioned that under cyclic loading, BMGs can exhibit softening (free-volume creation), promoting shear banding. However, this statement does not encounter consensus among the scientific community. X.D. Wang *et al.* [115] proposed a very detailed and comprehensive review of several theories regarding the influence of cyclic loading on glass microstructure, and concluded with three main outcomes: no influence, softening and hardening [115].

The three theories are supported by experiments and simulations which highlight two competing phenomena: creation and annihilation of free volume. When the two phenomena are balanced, there are no structural changes detected. However, when the creation rate is higher than the annihilation rate, the induced free volume creation leads to softening of the glass. On the contrary, when the annihilation rate of free volume is the dominating process, the hardening of the glass is observed. The predominance of one factor over the other is very much related to the stress amplitude applied. It was reported that low-stress amplitude favours relaxation (hardening) while high-stress amplitude favours free volume creation (softening). X.D. Wang *et al.* [115] mentioned that high stress will induce the breaking of the tightly bonded clusters (such as icosahedral-like clusters) into loosely bonded clusters. Accordingly, increasing the number of cycles may promote relaxation.

Structural changes will have a lower impact on crack propagation than on crack initiation in the light of fatigue endurance. As for shear band propagation, constraint concentration of the tip of the crack will induce free volume creation, reducing the sensibility to the initial state of the glass.

We have now seen that mechanical properties in metallic glasses are deeply linked to their structures. Also, we have seen that, even though metallic glasses are by nature amorphous, they can access a wide range of atomic configurations, with for instance different free volume contents. The structural evolution in metallic glasses can be induced by deformation but the glass structure can also be tuned before intended solicitation, to alter mechanical properties. Alteration of the mechanical properties of glasses by structural changes is discussed in the next section.

I.3.4. Mechanical properties alteration

The influence of the BMG structure on the fatigue endurance limit is a very good example of a structure/property relationship. By understanding mechanisms governing mechanical properties, one will be able to tune those properties by tailoring the glass microstructure. This is the subject of this section. Three main categories can be highlighted when looking at structure tailoring:

- Post-casting thermal or mechanical treatments of the amorphous alloy. This is the modification of the glass structure but the preservation of the fully amorphous state. It can go two ways: relaxation toward a more stable state, closer to the equilibrium, or rejuvenation towards a higher energy state [119, 120].
- Alloying of the original glass composition by addition of small atomic fraction of other pure elements. This is often referred to as micro-alloying but atomic fractions can go up to more than 10 at%. [121]
- Post-casting thermal or mechanical treatment of the alloy to induce partial crystallization. [122]

These three categories will be detailed in the following parts. Other routes such as strain-induced crystallization, nano-glass or dual phases glass are currently emerging. They will not be developed in the present presentation.

I.3.4.1. Relaxation and rejuvenation

As mentioned previously in this chapter, metallic glasses are metastable materials. Because of this, they will have a strong tendency for structural relaxation, *i.e.*, to evolve toward lower energy or equilibrium states. This process will happen naturally over time, *i.e.* ageing. Because metallic glasses contain a certain amount of free volume, resulting from the rapid solidification during cooling, the relaxation process is driven by the reduction of the free volume content and the densification of the glass.

As seen in the previous chapter, a reduction of the free volume level, may increase yield stress and reduce plasticity [123].

Very interestingly, S. Zhang *et al.* have studied the mechanical behaviour of a $Zr_{64.13}Cu_{15.75}Ni_{10.12}Al_{10}$ naturally aged for 6, 6.5 and 8 years [123]. According to the authors, this glass has the particularity to exhibit as-cast super plasticity at room temperature. It was reported by the same group that plastic deformation up to 80% in compression testing was obtained for this as-cast glass [124]. After 6 and 6.5 years, it appears that plasticity was reduced to 27.3%. For the sample aged 8 years, the observation is even more striking, as plasticity is reduced to almost 0%.

Relaxation can be accelerated by sub-T_g thermal annealing or mechanical treatments. B. A. Sun *et al.* studied the influence of annealing on the elastic properties of various MGs [109]. For instance, they looked at the bulk modulus K, the shear modulus G, the Young's modulus E and the Poisson's ratio ν of the Vit 105 during annealing at 600K (sub-T_g). The results are illustrated in Figure I-23.

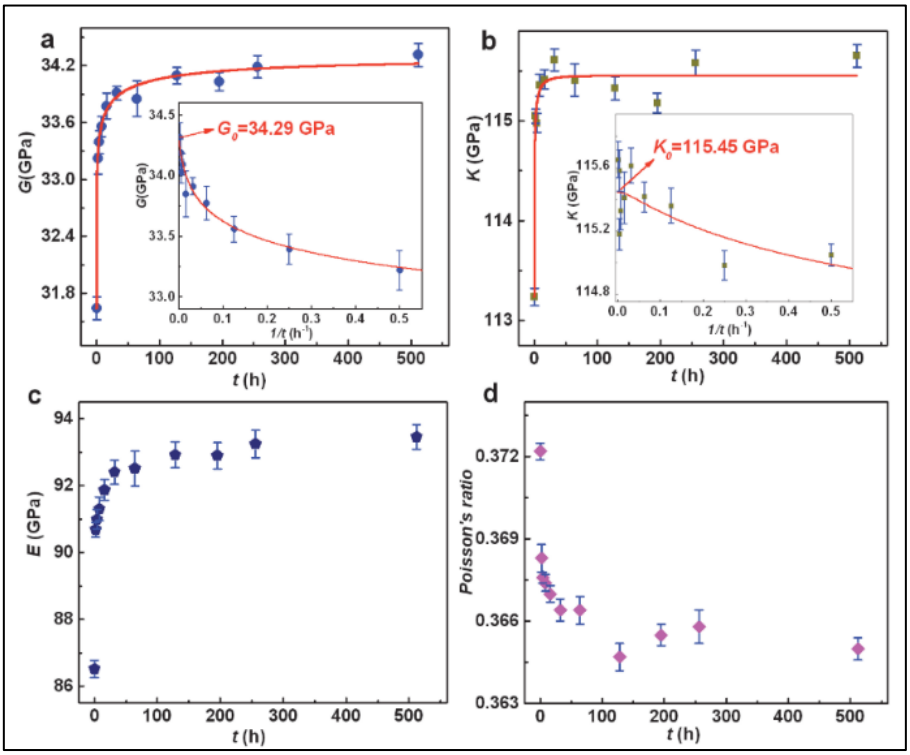

Figure I-23: Evolution of the measured elastic constants versus the annealing time t at 600K, for the Vit105 MG: (a) shear modulus G, (b) bulk modulus K, (c) Young's modulus E, (d) Poisson's ratio ν. The inset shows variations of K and G as a function of the inverse of time. [109]

Figure I-23 shows that with increasing annealing time below T_g, G, K and E increase rapidly until reaching a plateau whereas the Poisson ratio ν decreases until it also reaches a plateau. The authors used theoretical modelling to illustrate the structure variation during relaxation. They proposed that with the increase of the shear modulus G, the volume fraction of flow units is reduced (see Figure I-24 for illustration). J. J. Lewandowski and A. Greer proposed a correlation between the Poisson's ratio and shear-banding mediated plasticity [125]. They proposed that a high Poisson's ratio is correlated with high

ductility. X. L. Bian *et al.* confirmed the relation between the volume fraction of free volume and the ductility by manipulating free volumes with Xe-ions radiations [126]. They argued that the increase of the free volume is manifested by a lower yield strength and higher ductility.

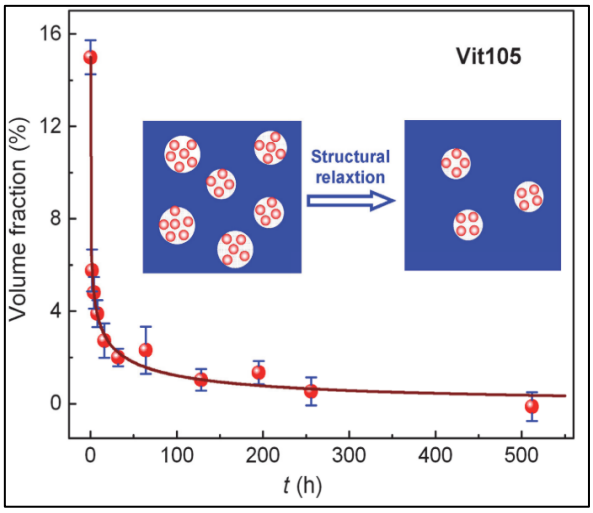

Figure I-24: Calculated volume fraction of flow units with the annealing time for Vit 105 based on G. The inset schematic diagrams illustrate the evolution of the flow units with time during structural relaxation. [109]

Relaxation can also be achieved by applying mechanical stress, suggesting that temperature and stress can have equivalent effects on the dynamic of BMGs [127]. M. Zhang *et al.* demonstrated that elastostatic compression loading at ambient temperature for 48h leads to an increase in the density of the glass. In detail, they loaded a $Zr_{35}Ti_{30}Be_{27.5}Cu_{7.5}$ MG at 50% and 70% of its yield stress (σ_y = 1687 MPa) for 48h [127]. After unloading, they performed residual strain and density measurements, differential scanning calorimetry and compression testing. They found that:

- The sample loaded at $0.7\sigma_y$ exhibited residual strain up to 0.2%.
- The value of the exothermic heat flux associated with the structural relaxation upon heating was reduced. However, no change of the crystallization enthalpy or the glass and crystallization temperatures are observed.
- The density was increased by almost 1% (respectively 0.7%) for the sample loaded at $0.7\sigma_y$ (respectively 0.5 σ_y).
- The yield stress increases from 1687 MPa to 1706 MPa and 1753 MPa for the samples loaded at $0.5\sigma_y$ and $0.7\sigma_y$, respectively.

By measuring the apparition of the first pop-in (serration) in the load-displacement curve acquired by nano-indentation, M. Zhang *et al.* showed that the shear banding process was delayed in the relaxed samples [127]. Interestingly, they showed that by further increasing the stress during the elastostatic loading ($0.9\sigma_y$), there was a transition from relaxation to rejuvenation. Experimental results brought by M. Zhang *et al.* are reported in Figure I-25 (from [127]).

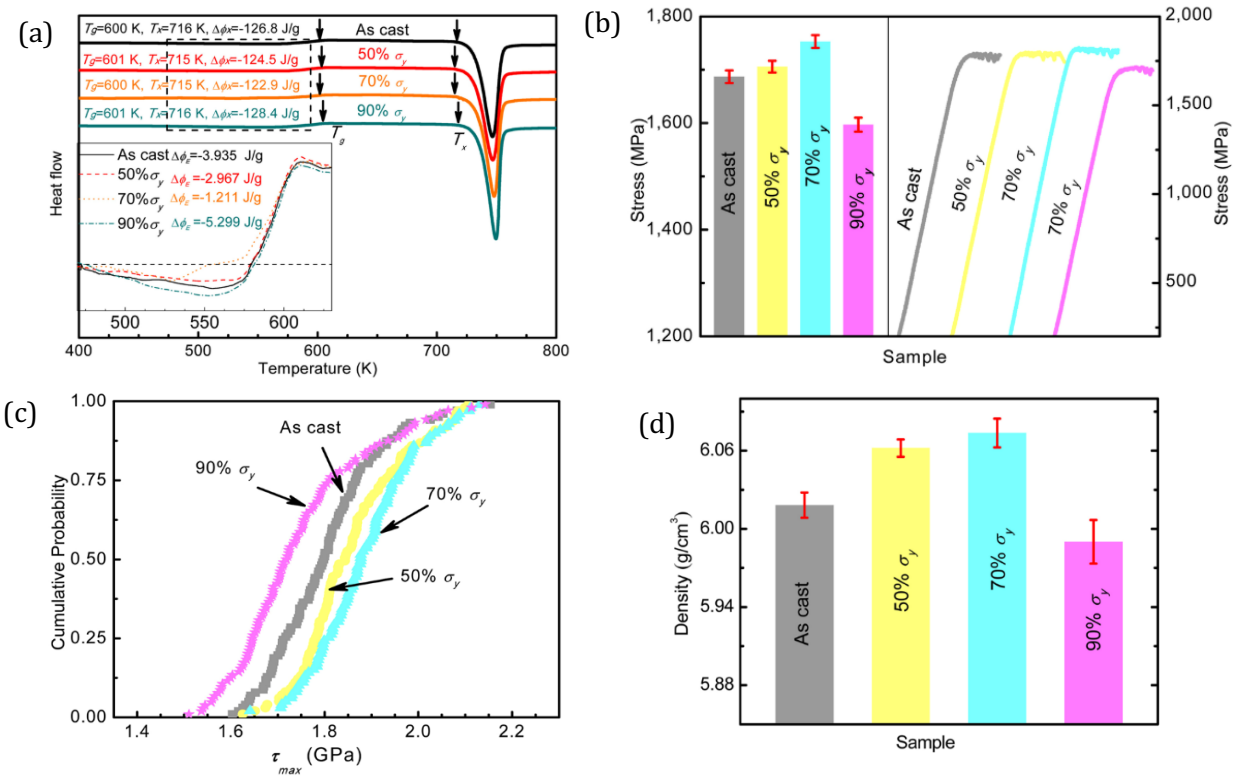

Figure I-25: Influence of the elastostatic loading at 0.5, 0.7 and 0.9σ_y for 48h. (a) DSC curves, inset shows a close-up of the relaxation enthalpy. (b) yield stress of the as-cast and post-elastostatic compression and stress-strain curves. (c) the shear stress at the burst of the first pop-in event in nanoindentation. (d) density of the as-cast and post-elastostatic compression specimens. [127]

As it is exposed in Figure I-25, increasing the stress from 0.7σ_y to 0.9σ_y increases free volume content and decreases the density, the value of the shear stress at the first pop-in as well as the yield stress. However, no major change is observed in the plastic deformation. While the sample is driven to a lower energy state at 0.5σ_y and 0.7σ_y, it appears to be driven at a higher energy state at 0.9σ_y. This reminds us of the load influence during cyclic solicitation (fatigue loading), where X.D. Wang *et al.* proposed that there is a threshold above which a transition from a relaxation dynamic to a rejuvenation dynamic can occur [115].

From this, we understand that there is a sort of continuum of states between relaxation and rejuvenation. A glass can access a continuum of energy states, from the most stable to the most unstable. This continuum is defined as the potential energy landscape. This idea can be illustrated as presented in Figure I-26 (from [96]).

There are many reported ways to rejuvenate a metallic glass [96, 123]. We just mentioned elastostatic loading [123, 128], but severe plastic deformation (such as cold-rolling) [129–132] has also been employed, as well as cryogenic cycling [106, 133] and ion irradiation [126]. All of the rejuvenation technics are based on the same principle: inducing structural changes in some way to create free volume and lower the atomic packing density. From there, shear bands can be initiated at lower stresses which

favours their nucleation and ultimately leads to a better homogenization of the deformation, and hence better deformability.

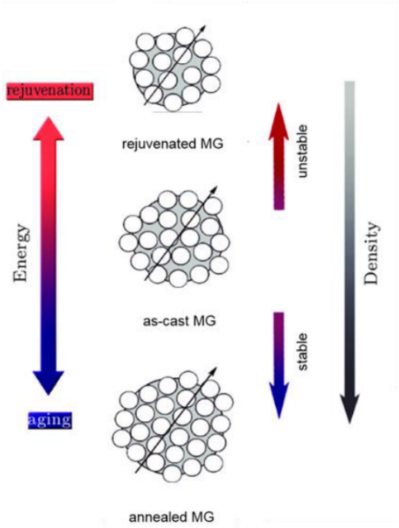

Figure I-26: Schematic representation of amorphous structures differences between structural relaxation and rejuvenation. [96]

Even though rejuvenation is raising growing attention, one rejuvenation technic received too little attention in the past few years. All of the previously mentioned mechanical technics for rejuvenation are based on geometry modification and are to this extend destructive. Cyclic loading for a limited number of cycles has been investigated by C.E. Packard to induce hardening [134, 135]. The effect of a high number of cycles has already been discussed in the section dedicated to fatigue and in some published work [136]. Here we are focusing on a low number of cycles, between 1 and 40. C. E. Packard *et al.* demonstrated that a small number of cycles (nanoindentation) could induce strain hardening (recently confirmed by C. M. Meylan and A. L. Greer [137]). They also showed that the effect was increasing with the number of cycles until it reaches a plateau. Finally, they demonstrated that the effect was also composition dependent. Interestingly, they also pointed out a threshold below which no change appears (see Figure I-27). But surprisingly, over this threshold, the material is hardened and not softened as seen in the elastostatic loading for instance. The effect of a low cyclic loading in the elastic regime for rejuvenation purposes has only been studied in computational work [138, 139] and the thesis of Oriane Baulin [96] to the best of our knowledge.

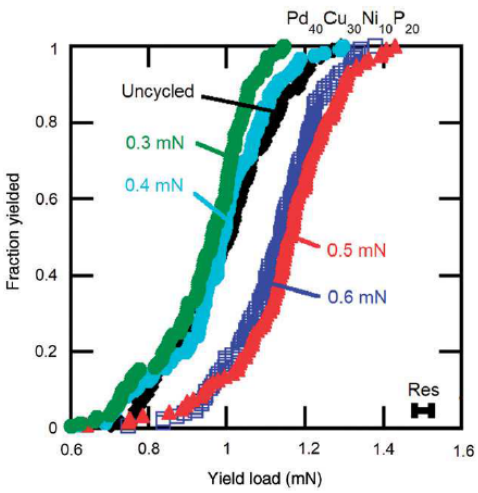

Figure I-27: Effect of the applied cycling amplitude on the apparent hardening, as observed in the cumulative yield load distribution (data for 5 cycles). [134]

I.3.4.2. Alloying

Minor addition or micro-alloying has been widely used in more conventional metallurgy, on crystalline alloys [140–143]. It also plays an important role in the design of properties of BMGs such as glass-forming ability, crystallization, thermal stability or mechanical or corrosion properties [144]. W. H. Wang wrote an extensive review of the roles of minor additions in the formation and properties of bulk metallic glasses. He listed the functions of the minor addition in metallic glasses [144]:

- Enhancing GFA
- Explore new BMGs
- Deteriorate GFA
- Scavenging the oxygen in elements and processing
- Purify the elements during melting and improve castability
- Induce the formation of BMG-based composites (see I.3.4.3)
- Strengthen the BMG
- Enhance ductility
- Improve magnetic properties
- Tune certain physical properties (see I.4.1 and I.4.2 for the influence of alloying on corrosion resistance and general biocompatibility)

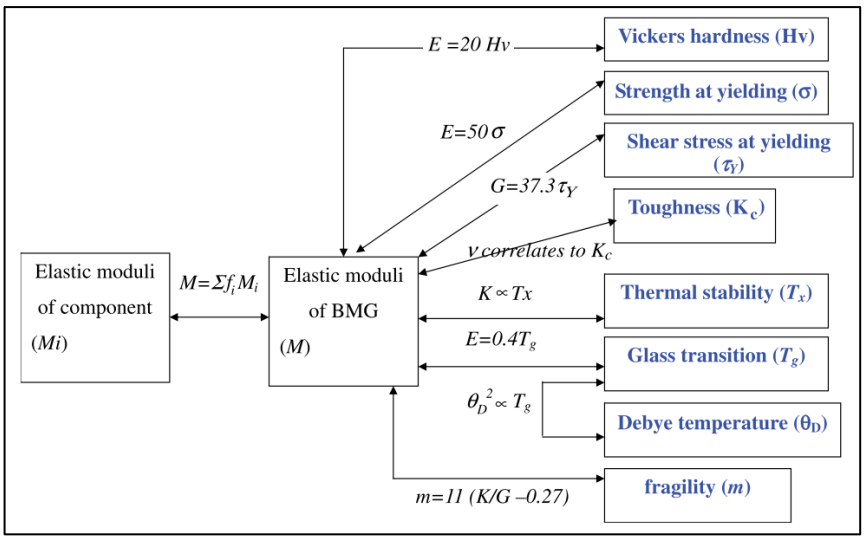

Figure I-28: Schematic diagram showing how the properties of the metallic glasses can be improved or tailored by a proper selection of adding component with suitable elastic moduli (M_i). [144]

Of course, it is hard to alter only the behaviour of a BMG in one of these categories without altering its behaviour in another or more. All of these properties are ultimately linked to the glass structure and are therefore interconnected. In this subchapter, we will mainly focus on the alteration of mechanical properties. W. H. Wang proposed an empirical rule to enhance mechanical properties of the BMG based on the elastic moduli of the elemental constituents (M_i), as the elastic moduli (M or E) of the BMG scales

with the M_i of its constituents [144]. Experimental data revealed a correlation between the elastic moduli and numerous properties (Figure I-28 [144]). For instance, Q. He and J. Xu studied the Zr-Cu-(Ti)-Al glass-forming system and exhibited a correlation between the elastic (Young's) modulus and the glass transition temperature [97] as illustrated in Figure I-29. They argued that a higher T_g value reflects a stronger atomic bonding, hence a higher Young's modulus. Even though some correlation could be made for specific glass-forming systems, the process of enhancing mechanical properties through minor alloying still relies heavily on the trial-and-error process.

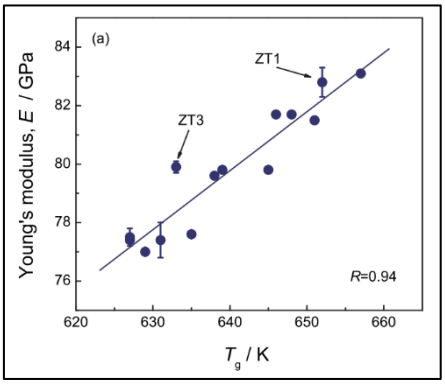

Figure I-29: Plot of the glass transition (Tg) against Young's modulus (E) for Zr-Ti-Cu-Al BMGs: ZT1 = $Zr_{60.9}Ti_{2.1}Cu_{25}Al_{12}$ and ZT3 = $Zr_{61.6}Ti_{4.4}Cu_{24}Al_{10}$. [97]

In 2013, M. Calin *et al.* published a detailed review of their method to perform micro-alloying on a Ti-based BMG [145]. Among the atomic features of each component, they were interested in the enthalpy of mixing with the main constituent (here Ti), and the difference in atomic radius, also compared to the main constitutive element. They also considered the biological safety of each element. From this study, many alloying elements were highlighted, such as B, Si, P, and In. The same study can be reproduced with Zr as the main constitutive element. Figure I-30 is a reproduction of the figure proposed by M. Calin *et al.* but adapted, using Zr as the main constitutive element.

Based on the criterion retained by M. Calin *et al.* (to enhance GFA), several elements are highlighted: B, Si, P, Pt, Au. We can note noble elements such as Pt and Au have already been studied as alloying elements in a $Zr_{53}Co_{31}Al_{16}$ [121]. They confirmed that the alloying elements enhanced the GFA of the ternary alloy. The question that needs to be addressed is "what are the properties to enhance?", which will determine how to select the alloying element. To enhance GFA, following Inoue's empirical rules (see Chapter I.1.3), M. Calin *et al.* chose elements with negative heat of mixing (NHM) and atomic radii mismatch over 12%.

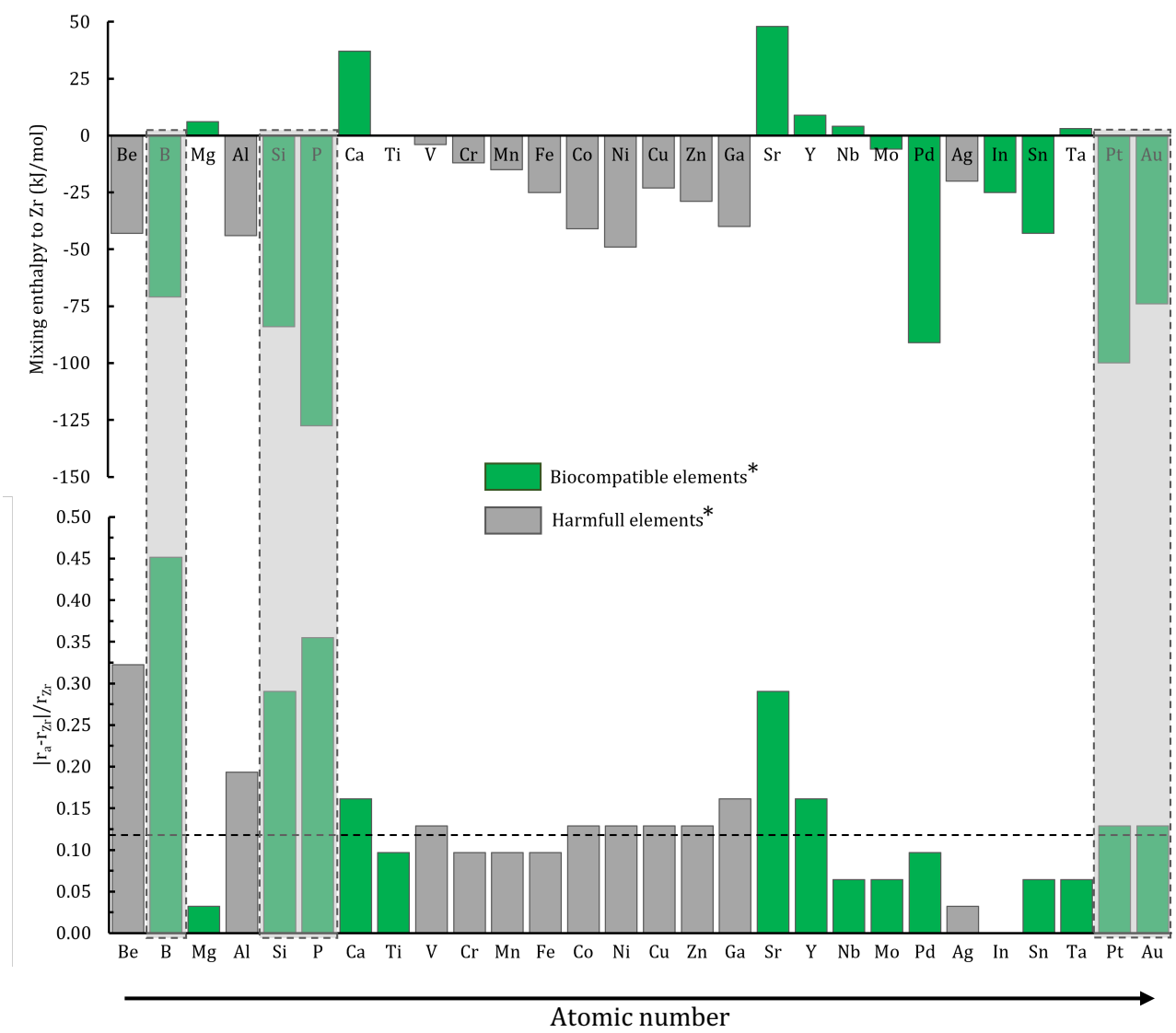

*Figure I-30: Mixing enthalpy of possible alloying elements with Zr and atomic radius mismatch of these elements, also with Zr. *The biological safety of each element is based on M. Calin et al. classification. [145]*

On the contrary, D. Cao *et al.* recently proposed a detailed study of the influence of alloying with elements having positive heat of mixing with Cu on the plasticity and GFA of a $Cu_{48}Zr_{48}Al_4$ BMG [146]. Inoue's empirical criterion (see I.1.3) tells us that one needs to mix elements with negative heat of mixing to achieve the best GFA. Here the authors showed that GFA could be enhanced otherwise: they brought the critical diameter of the $Zr_{48}Cu_{48}Al_4$ from 2mm to 9mm by the substitution of 8 at% of Cu by Ag. Following a standardised procedure, they located the best glass former composition with several alloying elements: Ag (8 at%), Ga (3 at%), Nb (1,5 at%), Ni (0,5 at%), V (0,5 at%), Co (0,3 at%), Cr (0,5 at%), Fe (0,5 at%), Mo (0,3 at%), W (0,3 at%). From this analysis, they showed that only alloying elements with small positive heat of mixing (PHM) and high radiuses significantly enhanced GFA (Ag, Nb, Ga). Interestingly, they demonstrated that plasticity was enhanced by the elements having the greater positive heat of mixing ΔH_{mic} (see Figure I-31 (a) and (b)). From these results, they concluded that alloying

elements with PHM favoured the formation of flow units, favouring plastic deformation (see I.3.2.2) and that inversely, elements with low PHM favoured denser and more stable glass.

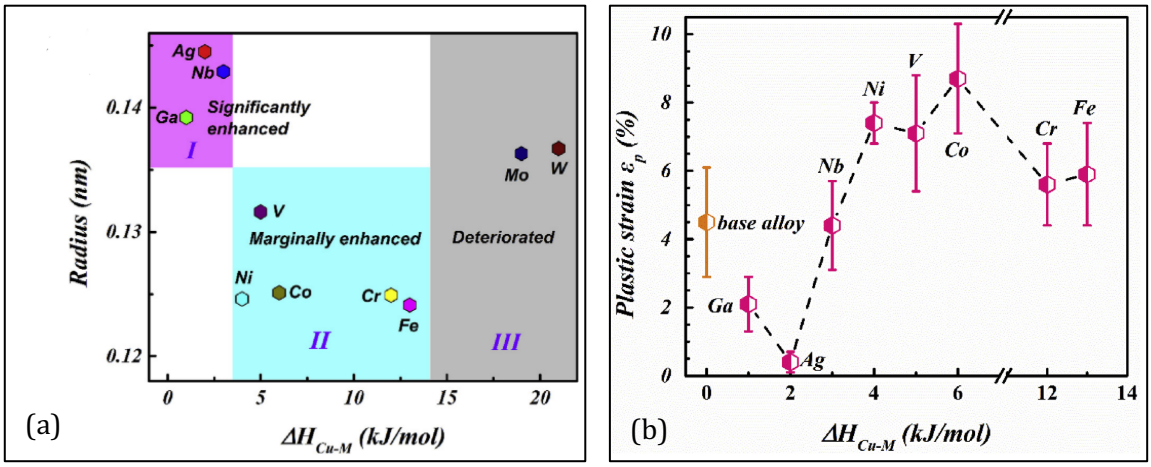

Figure I-31: (a) Dependence of GFA on the atomic radius and $\Delta H_{Cu\text{-}M}$ and (b) plastic strain for the best glass formers in the Cu-Zr-Al-M (M: the positive heat of mixing elements) BMGs as a function of $\Delta H_{Cu\text{-}M}$. [146]

Z.W. Zhu *et al.* studied the influence of Nb addition on the SRO of a Zr-Cu-Ni-Al BMG [147]. They concluded that by substituting Zr with Nb, the quantity of icosahedral short-range order (ISRO) in the glass increased. Accordingly, T_g rises and so does the yield stress. Minor addition of Nb is still actually extensively studied in the BMG field mostly for plasticity and/or corrosion resistance enhancement [148–159]. S.S. Wang *et al.* studied Nb addition to a Zr-Cu-Fe-Al BMG [160]. They found that the addition of 1.5 at% of Nb considerably increased the deformability of the alloy. This is attributed to a decrease of Young's modulus E and shear modulus G, favouring shear band nucleation. However, T_g increases with Nb addition, contrasting with the empirical rule proposed earlier. G. Cao *et al.* investigated the addition of Nb to the $Zr_{47}Cu_{44}Al_9$ BMG [149]. They did not substitute Nb to a specific element: $(Zr_{47}Cu_{44}Al_9)_{100\text{-}x}Nb_x$. The results of the compression tests are gathered in Figure I-32. It is mentioned that the value of 0.5% compressive plasticity at room temperature is reported in the literature. With 1 at% and 2 at% of Nb, the compressive plasticity increases to respectively 7% and 13.2%. With further increasing the Nb content (3 at% and 5 at%), no plastic strain is detectable, implying a dramatic change in the local atomic configuration. Yield stress is progressively decreased with increasing Nb content. It is concluded that Nb addition, considering its PHM with other constituents, induces more local heterogeneities favouring shear banding. Similarly, B. Guan *et al.* demonstrated that Co substitution by Nb in the $Zr_{56}Co_{28}Al_{16}$ alloy increased plasticity [157]. It is controversial whether $Zr_{56}Co_{28}Al_{16}$ possess compressive plasticity as-cast. It might be related to processing parameters and is discussed in chapter III. Oppositely, S. Pang *et al.* reported no change in the compressive behaviour $Zr_{55}Co_{25}Al_{20}$ when Nb is added by substitution to Al [150].

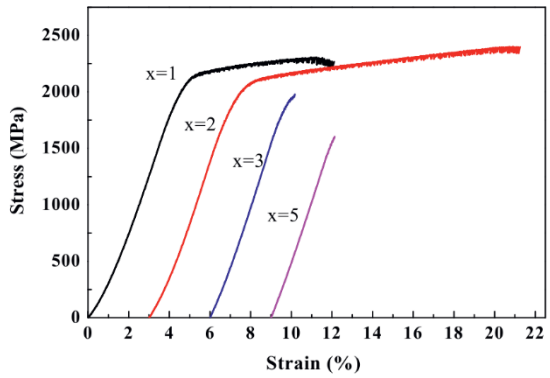

Figure I-32:

Stress/Strain curves of $(Zr_{47}Cu_{44}Al_9)_{100-x}Nb_x$ amorphous samples of 2 mm in diameter. [149]

From this analysis, one should keep that:

- Plasticity enhancement mechanisms are rather well identified (increasing local heterogeneity level). To increase plastic deformation by microalloying, one should try to add elements to increase the local disordering. The heat of mixing (mixing enthalpy) is to be considered.
- The effect of a specific element addition (for instance Nb) is very dependent on the base alloy and the substitution strategy. Moreover, the link between favouring local structuring (ISRO) and heterogeneity content is still unclear.
- Altering plasticity will alter other properties such as GFA as they are connected through the BMG and liquid structure. This might apply to a lower extent for surface properties such as corrosion resistance (see I.4.1).

I.3.4.3. Glass and crystal composites

The issue of the low ductility and tendency to strain softening in the deformation behaviour of BMGs have been tackled by some researchers by the addition of ductile crystalline phases in the glass matrix, to form glass/crystal composites. This idea is particularly interesting as it takes advantage of the qualities of the two metallic materials: the high strength of the metallic glasses and the ductility of the crystalline alloys [36].

There are several ways to obtain metallic glass matrix composites (MGMCs):

In-Situ MGMCs: the point here is to form crystalline phases from the considered alloy. There are two ways to obtain in-situ composites: directly from the liquid alloy during quenching (as-quenched composites) and by post-casting thermal treatment (annealing induced crystallization). Among the many possible crystalline phases that one could try to add to a BMG, the B2 crystalline phase has attracted considerable attention [161–164]. This phase is particularly interesting as it will transform from the B2 austenite phase to a martensite phase (B33 for ZrCo, B19' for ZrCu) under appropriate stress (TRIP effect, transformation induced plasticity) [162, 165]. Among the many systems studied for as-quenched composite formation, we will focus on Zr-Cu-Al and Zr-Co-Al systems.

- As-quenched composites: Y. Wu *et al.* studied the $(Zr_{0.5}Cu_{0.5})_{100-x}Al_x$ system for the formation of as-quenched B2-ZrCu particles in a glass matrix [165]. They showed that the obtained microstructure had a strong dependence on both the Al content and the casting diameter as illustrated in Figure I-33 (a). From this figure one can also see that depending on the cooling rate (here the casting diameter), other phases may appear. Figure I-33 (b) shows the tensile stress-strain curves for the $Zr_{48}Cu_{48}Al_4$ alloy. The 2-mm diameter sample is fully amorphous and exhibits no plasticity. The 3-mm diameter and 4-mm diameter samples have B2-ZrCu crystalline phases embedded in the glass matrix. They exhibit plasticity, indicating that the addition of the B2 phase to the glass matrix confers plasticity to the sample. However, the size of the crystalline particles has also an influence: if the growth of the crystalline phases is too important, the plasticity is reduced. This explains the plasticity difference between 3-mm diameter and 4-mm diameter samples. One should therefore try to promote nucleation and limit growth. With further lowering of the cooling rate, other crystalline phases appear (Al_2Zr here) which appears to be detrimental to plasticity. C. Li *et al.* [166, 167], W. C. Kim *et al.* [163] and Chen *et al.* [162] proposed analogue studies for the formation of as-quenched B2-ZrCo phases in the Zr-Co-Al glass former system. The study showed that the forming of a B2-ZrCo phase is beneficial to the deformability of the glass. However, one should try to prevent the formation of other phases, such as the eutectic phase Zr_6CoAl_2 which significantly decrease the work hardening effect.

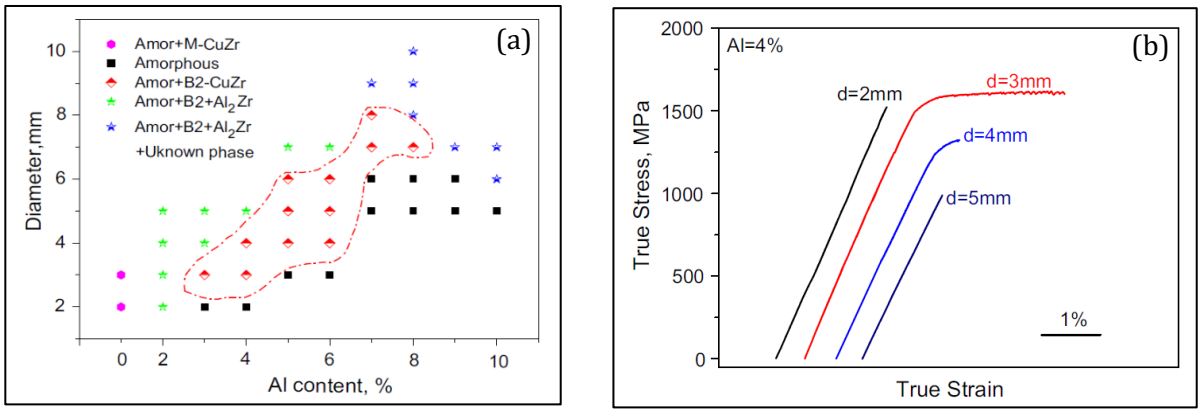

Figure I-33: (a) Microstructure dependence on Al content and cooling rate in $(Zr_{0.5}Cu_{0.5})_{100-x}Al_x$ alloy system. (b) Tensile true stress-strain curves of $Zr_{48}Cu_{48}Al_4$ alloy with different casting diameters. [165]

- Annealing induced crystallization: the obtention of as-quenched MGMCs is challenging as one can hardly control the crystalline phase volume fraction. As is it linked to the cooling rate, for each new geometry, one will have to go again through the iterative trial-and-error process to find the right processing parameters. In this regard, partial devitrification of the glass by annealing seems more controllable as temperature and holding time can be easily monitored. For the $Zr_{56}Co_{28}Al_{16}$, Tan *et al.* [18] studied the influence of the temperature over the phase precipitation mechanisms. They performed three different annealing treatments: heating above the first transformation

event and immediately cooling down, heating above the first transformation event and holding for 100 min before cooling down and heating after the second transformation event. They showed that for an increase in the annealing temperature, the formation of B2-ZrCo was promoted over the formation of Zr_6CoAl_2 and ZrCoAl. Chen *et al.* proposed detailed studies of the Zr-Co-Al crystallization behaviour, through conventional and flash annealing [122, 161, 162]. They came to several conclusions:

- GFA decreases with decreasing Al at% and B2-ZrCo but also Zr_6CoAl_2, Zr_2Co and Zr_2Al crystalline phases are formed.
- Annealing under T_g results in glass relaxation and minimal crystal fraction formation, while a large volume fraction of crystalline phase (up to full crystallization) appears while annealing above the first DSC exothermic peak.
- Lower Al content seems to enhance B2-ZrCo phase formation, as well as higher annealing temperatures.
- Higher heating rates (flash annealing) preserve a large amount of amorphous matrix and promotes B2-ZrCo formation while suppressing the intermetallic phases.
- Flash annealing preserve the quality of the amorphous matrix, which can still exhibit ductility while conventional annealing often results in embrittlement of the amorphous matrix
- B2 phase formation is promoted by a Zr/Co or Zr/Cu ratio close to 1. Because of that, as ZrCuAl ternary glass formers exhibit Zr/Cu ratio closer to 1, they exhibit a better tendency for B2 phase formation.

A solution to bypass the complicated trial-and-error process to nucleate and grow favourable crystals in a glass matrix is to add crystalline particles to an amorphous alloy.

Ex-Situ MGMCs: the point here is to add crystalline particles to the metallic glass alloy [36]. This can be done for instance by incorporating crystalline particles with very high melting points, such as tungsten carbides (WC) or tantalum (Ta) inside the alloy, which will not melt during the casting process. The major drawback is the lack of control one have over the distribution of the particles. Moreover, the choice of suitable particles is limited because of the required high melting point.

I.4. Metallic glasses as materials for biomedical applications

It was mentioned through the introduction and this chapter that BMGs have several properties very attractive for applications in the biomedical sector. Metallic materials have been employed for centuries as biomaterials, for instance in orthopaedic for implant realisation or in the surgical sector for specific tooling. But, with the improvement of medical technics, notably with a rapidly growing interest for miniaturization, targeted therapy and less invasive surgeries, conventional crystalline alloys exhibit

several limitations. For the majority of them, they exhibit high Young's modulus. While looking at implantable devices directly in contact with bones, a large mismatch between Young's modulus can cause stress shielding to the bone, creating bone resorption. Moreover, the corrosion resistance of several crystalline alloys is not optimal because of the presence of structural defects such as grain boundaries. Finally, the limited mechanical resistance greatly slows down the effort made for miniaturization.

MGs are very promising candidates for biomedical applications as they have very good physical and chemical properties. However, to combine sufficient GFA and pertinent properties (corrosion and mechanical resistance), glass-forming alloys are often bearing high costs or toxic elements. This part will review BMGs through the prism of medical applications. In the first part, specific properties (*i.e.,* corrosion resistance and cytotoxicity) will be detailed. In a second part, several compositions will be presented to propose a brief overview of the state of the art of BMGs for medical applications.

I.4.1. The corrosion resistance of BMGs

Compared to the very extensive research on the mechanical behaviour of BMGs, their corrosion resistance has been more moderately studied even if, with a growing interest in BMGs from the medical field, this topic received many contributions in the past years. In this thesis work, we will consider corrosion resistance through the number of ions released during extended immersion test and the anodic polarization behaviour.

It is accepted that the corrosion resistance of a material is dictated by its microstructure and the constitutive elements [168]. The corrosion resistance of conventional crystalline materials is often limited by the defects in the material structures, like grain boundaries or secondary phases. Bulk metallic glasses, that exhibit virtually no defects in their structure (*emphasis "virtually"*) are therefore good candidates to have superior corrosion resistance even if we have seen that BMGs are not free of heterogeneities. From 2007, researchers got interested in the impact of the free volume content on the corrosion behaviour of a $Zr_{52.5}Cu_{17.9}Ni_{14.6}Al_{10}Ti_5$ BMG [169]. They compared the glass in the as-cast state, the relaxed state (thermal annealing) and a rejuvenated state (cold-rolling). The changes in free volume content were evaluated using the quantification of the energy released before T_g. Electrochemical cyclic-anodic-polarization tests were performed on the three states.

Figure I-34 shows the cyclic polarization curves for the as-cast, rolled and relaxed samples. The corrosion potential (E_{corr}) is the potential from which the BMG starts to be passivated. No change is observed in E_{corr} with the free volume content. By calculating the corrosion penetration rate (CPR) at the corrosion potential, one can see that the less free volume, the more resistance the BMG to general corrosion. The deformed sample exhibit a CPR of 74 µm/yr while the as-cast sample revealed a CPR of 54 µm/yr and the relaxed sample a CPR of 23 µm/yr (so approximately 1/3 of the deformed sample). However, it is important to moderate this result as the authors calculated the CPR by using Tafel's

approach which is not totally suitable for passive material. All three samples are vulnerable to localized corrosion (pitting) which is detectable by a rapid increase of the current density. It happens at the potential marked as E_{pit}. One can see that the reduction of the free volume content is correlated with a reduction of E_{pit} which goes from 64 mV/SCE and 54 mV/SCE respectively for the deformed and as-cast samples to -43 mV/SCE to the relaxed sample. This is detrimental to the corrosion resistance as it reduces the width of the passivation domain ($E_{pit} - E_{corr}$). This value reflects the pitting initiation resistance. The lower it is, the lower the pitting resistance is. The authors performed cyclic-anodic polarisation, meaning that after pitting, they reduced the potential to observe the re-passivation of the BMGs. The protection potential (E_{pp}) is the potential where the BMGs is protected again. $E_{pp} - E_{corr}$ is another important value as it quantifies the pit propagation resistance. The higher this value is, the higher the resistance is. One can observe that E_{pp} increases with the increasing free volume content (-236 mV/SCE, -216 mV/SCE and -193 mV/SCE for the deformed, as-cast and relaxed samples, respectively).

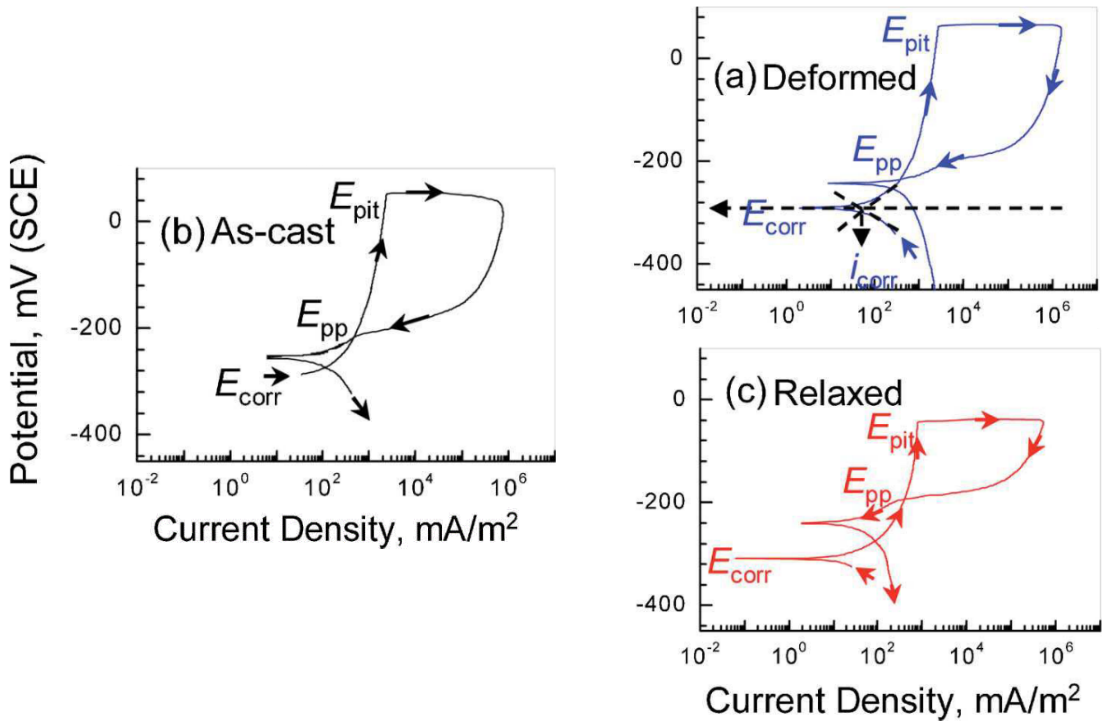

Figure I-34: Cyclic-anodic-polarization curves of the BMGs at various conditions (a) deformed, (b) as cast and (c) relaxed in 0.6M NaCl. [169]

From this, one can conclude that with the decreasing free-volume content, the pit initiation increases and the pit propagation decreases. Finally, the area of the loop is also a quantitative indicator of the severity of the pitting. The smaller it is the more limited the pitting corrosion will be. Post-mortem analysis of the sample surfaces revealed that from deformed to relaxed samples, the number of pitting sites increases but their size decreases, which is coherent with a higher initiation rate and a lower propagation rate. Jiang *et al.* [169] attributed the pit propagation resistance of the relaxed sample to

smaller average interatomic distances and better glass stability. They attributed the increase in the pit initiation rate to more sensitive clusters that could be formed during annealing.

Along with the structure of a specific glass, the influence of alloying elements on the corrosion resistance of the BMGs was also reported. The addition of alloying elements will of course change the structure of the glass, but will also change its chemical composition, in the way that it can change the nature of the passivation layer. Zhang *et al.* studied the influence of replacing Ni by Co in a $Zr_{65}Cu_{17.5}Al_{7.5}Ni_{10}$ BMG on its corrosion behaviour in chloride solution (NaCl 3.5%) at room temperature [170]. They demonstrated that the substitution of Ni by Co reduced the corrosion current (i_{corr}), increased E_{pit} and significantly increased the passivation plateau ($E_{pit} - E_{corr}$). Using energy-dispersive x-ray spectroscopy (EDS), they showed that for the pristine alloy ($Zr_{65}Cu_{17.5}Al_{7.5}Ni_{10}$) pitting sites exhibit higher Cu concentrations, around 30 at%. This could indicate that pits usually initiate and propagate on the BMG surface where the Cu content is enriched. These Cu-enriched zones may originate from local chemical heterogeneity within the glass or selective dissolution during the first step of corrosion (Cu is not oxidized while Zr and Al are preferentially oxidized to form the passive layer). Similar behaviours were reported for other alloys, such as Ti-based alloys [171]. In a Zr-Cu-Ni-Al BMG, the pitting dynamic is reduced with Co addition, meaning that Co addition could reduce the formation of the Cu-rich zone on the BMG surface and promote a uniform distribution of Zr and Al, which form more stable oxides [170]. Zhang *et al.* demonstrated that in the BMG with 6 at% of Co, the passivation layer was mostly composed of ZrO_2 oxides and a small amount of AlO_2 oxides. Similar results have been achieved with other alloying elements, such as Sn or Si by A. Liens *et al.* [171]. They exhibited that the corrosion resistance of a Ti-Zr-Cu-Pd alloy was limited by the presence of two types of defects: Cu rich zones and crystalline inclusions (spherulite). Figure I-35 illustrate the surface reactivity depending on the presence of Si or Sn. Sn addition reduces the presence of Cu-rich zones while adding both Sn and Si reduces the presence of Cu-rich zones and the formation of spherulites.

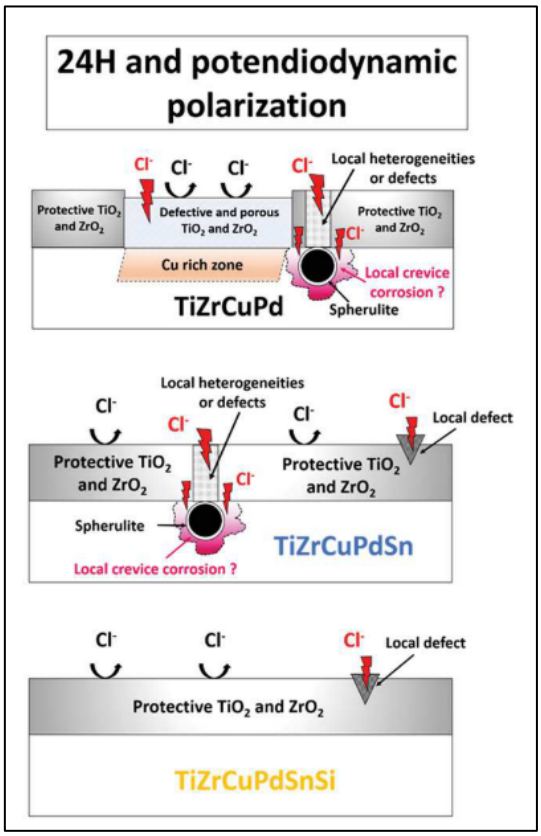

Figure I-35: schematic illustration of the surface reactivity of Ti-Zr-Cu-Pd-(Sn)-(Si) after the potentiodynamic measurement in 0.9% NaCl. [171]

In the Zr-Co-Al ternary system, Hua *et al.* showed that the addition of noble elements (Pt, Pd or Au), increase the BMG corrosion resistance in PBS solution, by increasing E_{pit} [121]. They showed that

the addition of those noble elements promoted the formation of Zr-oxide which is more stable than Al-oxides in chloride solution. Interestingly, they showed that Co was less concentrated in the surface than in the target composition. Pang *et al.* studied the influence of Nb addition in the Zr-Co-Al ternary base on its corrosion resistance in NaCl 3 w% and 1 M H_2SO_4 [150]. They concluded that Al substitution by Nb increased the corrosion resistance in NaCl. Accordingly, W. K. Le *et al.* demonstrated that Nb addition to Zr-Co-Al ternary base was beneficial to its corrosion resistance in Hank's solution [172]. Other researchers reported that the addition of Nb, when substituted to the entire Zr-Co-Al ternary base or a single element (Co or Al), was beneficial to corrosion resistance in various mediums [157, 159, 173]. Nevertheless, the mechanism promoting Zr-oxides other Al-oxides by Nb addition is still discussed. Comparable work was proposed by N. Hua *et al.* on the addition of Ag to the ZrCoAl glass-forming system by substituting Co. They showed that Ag addition increases corrosion resistance in PBS solution [174]. It is also interesting to mention that Ag has anti-bacterial properties, which can be a great asset for the development of surgical tools, preventing bacterial infections.

To conclude on this topic, we can state that there are two possibilities to enhance the corrosion resistance of a metallic glass. On one hand, one can try to enhance the passive film stability. This will have the effect to increase the resistance to pitting initiation. On the other hand, one can try to eliminate pitting propagation, for instance by controlling the local chemical composition and suppressing Cu rich zones in Cu-bearing glasses.

I.4.2. Cytotoxicity of BMGs and hydroxyapatite formation

When considering a new material for biomedical applications, assessing the corrosion resistance is only the first step to evaluate biocompatibility. Being promising candidates for biomedical applications, many BMGs have been tested for cytotoxicity and hydroxyapatite (HA) formation [175]. The apatite-forming ability on the surface of the biomaterial is of critical importance as hydroxyapatite will enhance the bonding between material and tissues, to ensure strong fixation [176, 177]. K. Han *et al.* studied the cytotoxicity of the $Zr_{60.5}Hf_3Al_9Fe_{4.5}Cu_{23}$ BMG [178]. They showed that the cell viability after 24h of incubation was much better on the BMG sample than on a TA6V sample (see Figure I-36 from [178]). S.

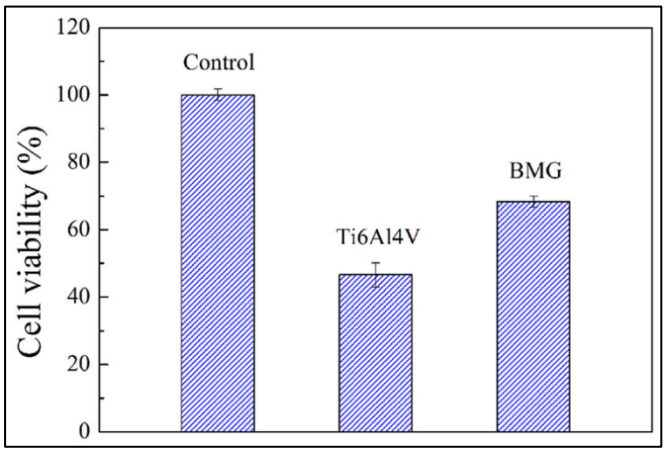

Figure I-36: the cell viability of CDD-986sk cells after 24h incubation on Zr-Hf-Al-Fe-Cu BMG and TA6V alloy. [178]

Buzzi *et al.* studied the cytotoxicity of a BMG in the Zr-Cu-Fe-Al system [179]. They showed that the Zr-oxide (zirconia) layer forming on the metallic glass protects the cells from the cytotoxic metal in the alloy (Cu). However, when this surface layer is damaged, the alloys allowed only minimal or no cell growth. In their conclusion, they advised the development of Cu- or Ni-free Zr-based metallic glass, such as glass formers in the Zr-Co-Al system. N. Hua studied the $Zr_{53}Co_{31}Al_{16}$ base, with Co for Ag substitution up to 7.75 at% [174]. They showed that cell proliferation with and without Ag addition was comparable to the cell proliferation observed on TA6V (see Figure I-37 right [174]). B. Guan *et al.* demonstrated that Nb addition to Zr-Co-Al BMG was beneficial for cell viability when substituted to Co (see Figure I-37 left [157]).

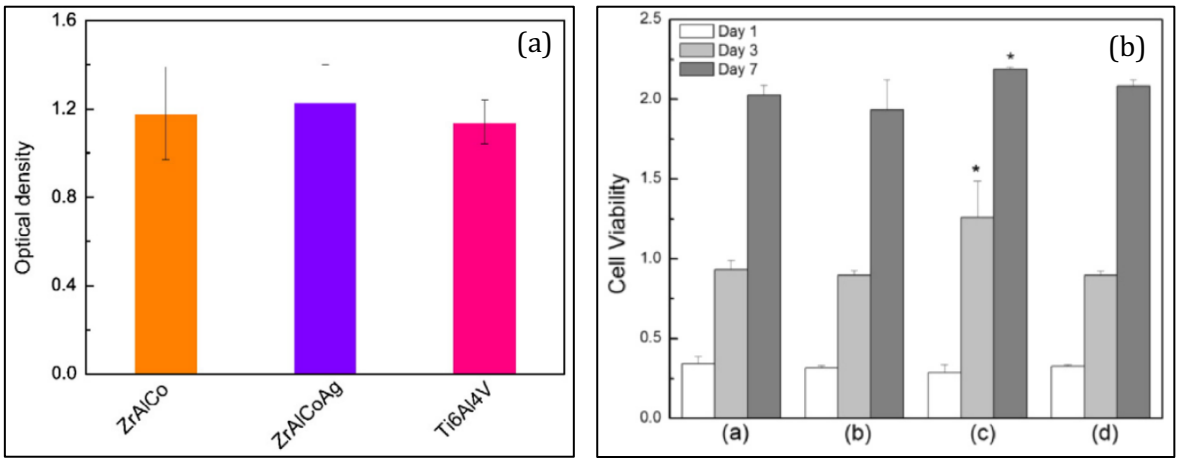

Figure I-37: (a) Optical cell density of $Zr_{53}Co_{31}Al_{16}$ and $Zr_{53}(Co_{0.75}Ag_{0.25})_{31}Al_{16}$ BMGs and TA6V after 7 days of MC3T3-E1 cells proliferation. [174] (b) Cell viability after different incubation times on the surface of (a) $Zr_{56}Co_{27}Al_{16}Nb_{1}$, (b) $Zr_{56}Co_{25}Al_{16}Nb_{3}$, (c)$Zr_{56}Co_{23}Al_{16}Nb_{51}$ ribbon samples and pure Ti (d). [157]

Wada *et al.* studied the HA formation of the $Zr_{56}Co_{28}Al_{16}$ BMG. In simulated body fluid solution (HBBS), they showed that $Zr_{56}Co_{28}Al_{16}$ exhibited spontaneous formation of HA, which demonstrates its bioactive nature [176]. They even made the hypothesis that Co was favouring HA formation, following the same mechanism from which Ti favours HA formation. Interestingly, they also showed that Co releasing rates were lower during immersion in HBBS for the $Zr_{56}Co_{28}Al_{16}$ BMG (0.3 ng/mm^2) compared to Co-Cr-Mo crystalline alloys (5.8 ng/mm^2), suggesting that the amorphous structure could impact releasing rates.

I.4.3. Mg- and Ca-based BMGs

Among biomedical oriented BMGs is a special group composed of the BMGs intended for temporary implantable devices. Biodegradable bulk metallic glasses are particularly interesting as they could be used temporarily and without additional surgical procedures to be removed after they served their purpose. Among those are Mg- and Ca-based BMGs [180]. From the review published by H.F. Li *et al.*, we learn that many Ca-Mg-Zn and Mg-Zn-Ca alloys with critical diameters larger than a millimetre have been developed [181]. Interestingly, they exhibit slower degradation rates than conventional

biodegradable crystalline metallic alloys. Biodegradable BMGs will not be more detailed in this review as we are targeting applications as permanent, structural implants or reusable surgical tooling.

I.4.4. Ti-based BMGs

In a paper published in 2016, P. Gong *et al.* proposed a review of the state of the art of Ti-based BMGs [181]. Titanium as a metallic element is very attractive as it possesses many superior properties: ultra-high specific strength (combination of its low density and high mechanical resistance), high corrosion resistance and good biocompatibility. Consequently, crystalline alloy TA6V (89 w% Ti, 6 w% Al, 4 w% V and 1 w% of other alloying elements) is one of the most used metallic alloys in the biomedical industry [182].

Comp. (at%)	Preparation method	D_c (mm)	σ_f (MPa)	E	Vickers hardness (H_v)
$Ti_{40}Zr_{10}Cu_{36}Pd_{14}$	AM + CMC	6	1950	82	-
$Ti_{60}Zr_{10}Si_{15}Nb_{15}$	AM + CMC	ribbons	> 2000	-	660
$Ti_{45}Zr_{10}Cu_{31}Pd_{10}Sn_4$	SPS	15	2060	-	-
$Ti_{45}Zr_{10}Cu_{31}Pd_{10}Sn_4$	AM + CMC	4	1970	95	650
$Ti_{40}Zr_{10}Cu_{32}Pd_{14}Sn_4$	AM + CMC	10	2000-2150	-	-
$Ti_{41.5}Zr_{2.5}Hf_5Cu_{37.5}Ni_{7.5}Si_1Sn_5$	AM + CMC	6	2000	80	600
$Ti_{45}Ni_{15}Cu_{25}Sn_3Be_7Zr_5$	AM + CMC	5	2480	-	715
$Ti_{41.3}Cu_{43.7}Hf_{13.9}Si_{1.1}$	AM + CMC	3	1685	95	-

Table I-6: Summary of several Ti-based BMGs reported for biomedical applications from [181] along with some key properties. AM = Arc Melting, CMC = Copper-Mould-Casting, SPS = Spark Plasma Sintering. D_c is the critical diameter, σ_y is the compression fracture strength and E is the Young's Modulus [181].

From this review and other published articles, one can first see that many of the Ti-based BMGs explored are palladium bearing [171, 177, 183]. Palladium (Pd) is not of concern in terms of biocompatibility but is a very high-cost material. In May 2021, a kilogram of palladium was reported to cost near 70,000 €. Moreover, its high density (12.02 $g.cm^{-3}$), greatly impedes the specific strength of the alloy. For this reason, we do not believe that Pd-bearing BMGs are truly suitable for biomedical application and mass production, even though they exhibit exceptional properties.

In addition, several Ti-based BMGs bear beryllium (Be), which is a known harmful element [184]. It is reported in the C&L (Classification and Labelling) as "causing skin irritation", "causes serious eye irritation" and "may cause cancer by inhalation". The entire C&L classification for Beryllium and other materials of interest is reported in supplementary material A. Ti-based BMG without any harmful elements or high-cost elements is so far achieving poor critical diameters (<10 mm).

Even though Ti-based BMGs exhibit several flaws, it is important to highlight their strength. Studies have revealed that the corrosion resistance of Ti-based BMGs in several fluids (phosphate-buffered solution PBS, simulated body fluid SBF, 1 w% lactic acid…) is very good. In detail, corrosion rates are low, susceptibility to pitting corrosion is limited and Ti-based BMGs appear to promote the formation of hydroxyapatite, which is one of the main components of human bone and teeth [181]. This was for instance illustrated by the alloy developed by M. Calin *et al.* $Ti_{60}Nb_{15}Zr_{10}Si_{15}$ [168]. In this work, they demonstrated corrosion behaviour close to pure Ti in Ringer's solution at 310 K. They also showed remarkable strength over 2000 MPa which is twice as much as the best commercial TA6V available. It appears that Ti-based BMGs, from a biocompatibility point of view, behaves somehow like pure Ti, which has excellent biocompatibility. Therefore, even though composition development is still needed for Ti-based BMGs, mainly to remove harmful or high-cost elements and improve GFA, they are very promising for future medical applications. They could also be considered for coating, which bypasses the issue of the limited critical diameter and still takes advantage of the high wear resistance and biocompatibility of the BMG for instance.

I.4.5. Zr-Based BMGs

Aside from Ti-based BMGs, the Zr-based BMG system is one of the most studied metallic glass former system [185]. Along with their review of Ti-based BMGs for biomedical applications, H.F. Li *et al.* have proposed of review of Zr-based BMGs [181]. Some Zr-based compositions presented for medical applications are summarized up in Table I-7 with some key features.

Comp. (at%)	Preparation method	D_c (mm)	σ_f (MPa)	E (GPa)	Vickers hardness (H_v)
$Zr_{52.5}Al_{10}Ti_5Cu_{17.9}Ni_{14.6}$	AM + CMC	7	1700*	90	590
$Zr_{61}Cu_{17.5}Ni_{10}Al_{7.5}Si_4$	MS	ribbons	1800	-	510
$Zr_{60}Ti_6Cu_{19}Fe_5Al_{10}$	AM + CMC	-	1652	70	-
$(Zr_{72.5}Cu_{27.5})_{80}(Fe_{40}Al_{60})_{20}$	AM + CMC	13	1560-1690	95	521-563
$Zr_{46}(Cu_{5/6}Ag_{1/6})_{47}Al_7$	AM + CMC	20	1916	-	-
$Zr_{56}Co_{28}Al_{16}$	AM + CMC	18	2070-2300	92-110	-
$Zr_{60.14}Cu_{22.31}Fe_{4.85}Al_{9.7}Ag_3$	AM + CMC	10	1720	82	-
$Zr_{62.5}Al_{10}Fe_5Cu_{22.5}$	AM + CMC	6	1700	80	459

*Table I-7: Summary of several Zr-based BMGs reported for biomedical applications from [181] along with some key properties. AM = Arc Melting, CMC = Copper-Mould-Casting, MS = Melt Spinning. D_c is the critical diameter, σ_y is the compression fracture strength and E is the Young's Modulus. *tensile fracture strength [181].*

Compared to Ti-based BMGs, Zr-based are of a relatively lower hardness and fracture strength. Ti-based BMGs generally exhibit hardness between 600 and 700 HV while Zr-based BMGs range between

500 and 600 HV. Similarly, Ti-based BMGs have compression fracture strength mostly above 2000 MPa while most of the Zr-based BMGs have compression fracture strengths between 1600 MPa and 2000 MPa.

Nonetheless, Zr-based BMGs have some advantages compared to Ti-based BMGs. For instance, Zr-based BMGs tend to have higher critical diameters compared to Ti-based BMGs and have been achieved without toxic elements such as Be or high costs elements such as Pd. Looking back at stress shielding, Zr-based BMGs have lower Young's modulus (70-95 GPa) than Ti-based BMGs. This is lower than Young's modulus of 316 L stainless steel (about 200 GPa) or TA6V (110-120 GPa)[182]. As for Ti-based BMGs, the corrosion resistance of Zr-based BMGs has been investigated in various physiological solutions. Zr-based BMGs have the particularity of forming ZrO_2 passive films, which gives them good corrosion resistance. As for Ti-based BMGs, developing BMGs without any controversial elements (including but not only Cu or Al) is very challenging. It appears that Al addition to Zr-based BMGs usually greatly improve the critical diameter. O. Baulin *et al.* focused on the development of a Ni-, Cr-, Be-, Cu- and Al-free Zr-based glass-forming alloy [186]. Three glass-forming compositions were proposed: $Zr_{56}Co_{28}Ga_{16}$, $Zr_{56}Co_{28}Ga_{14}Si_2$ and $Zr_{56}Co_{28}Ga_{14}Sn_2$. As expected, the three alloys appear biocompatible based on cell proliferation tests. It is interesting to note that Si- and Sn-bearing alloys exhibited higher cells proliferation than $Zr_{56}Co_{28}Ga_{16}$. Unfortunately, glasses were only produced as ribbons, showing how challenging it is to achieve large critical diameters using only risk-free elements.

Among the many Zr-based BMGs developed, the ternary Zr-Co-Al stood out and is now one of the most studied Zr-based ternary bases. It was firstly introduced in 2002 by T. Zhang and A. Inoue [187] who proposed four Zr-Co-Al ternary BMGs with several Zr/Co ratios. In supplementary material B, the reader will find several tables summarizing data available for Zr-Co-Al BMGs. Three main categories of data are considered: thermal data (T_g, T_x…), mechanical data (σ_y, $\varepsilon_{...}$) and polarisation data (corrosion potential, pitting potential…).

- Table B-1 and B-2 summarize the data on Zr-Co-Al ternary alloys.
- Table B-3 summarizes the data on Zr-Co-(Cu, Fe)-Al quaternary alloys.
- Table B-4 and Table B-5 summarize the data on Zr-Co-Al-(Nb, Ag, Y, Au, Pt, Pd) quaternary alloys.

This ternary base still attract research in 2021, mostly for the formation of glass-crystal composites [122, 156, 161, 162]. This work will focus on Zr-Co-Al ternary base and more precisely the $Z_{56}Co_{28}Al_{16}$ composition. A detailed study of this ternary base and this specific alloy will be presented as part of the results in Chapter III.

I.5. Conclusion

It appears that metallic glasses are unique in the large variety of alloy systems in the even larger family of metallic materials. They differentiate by their specific atomic organisation, or more specifically in this case, disorganisation. Thanks to their amorphous nature (and lack of defects associated with the crystalline organisation), they exhibit remarkable properties. Among these, one can name their ability to reach very high mechanical properties: high yield stresses (several GPa), high elastic strain (around 2%) and high ultimate strains. They are also usually associated with good corrosion resistance, high hardness, wear resistance, thermoplastic forming and so on… Because of their unique combination of properties, they are particularly promising for the fabrication of micro-devices for the medical field, such as precision surgical tools and small implantable devices.

The properties of a metallic glass (mechanical or else) are strongly related to its structure. Depending on the base elements of the alloy and alloying elements, properties can exhibit strong variations. Two main fields of study ensue from this observation. First, the relation between the glass composition and its structure is still under intense investigation. Even if metallic glasses have no long-range order, they do exhibit an organisation at medium and short-range. Second, the way the glass structure dictates its properties is still arousing significant attention. A better understanding of these two relations could be a real breakthrough for the industrialisation of metallic glasses. Nowadays, their production is still often relying on the trial-and-error method, which is very time and money consuming.

The glass structure, and by extension its properties, can be tuned in several ways. Relaxation and rejuvenation are two post-casting methods currently employed to alter a glass structure and tune its properties. A better understanding of these processes could lead to major improvement of glass properties and processing methods. There is also a lot of work on the minor alloying of bulk metallic glasses. The addition of the appropriate element can dramatically influence the glass properties. However, as with most of the work regarding metallic glasses, minor addition to improving properties often rely on intense experimental work. The influence of specific elements is too rarely related to the alloying method used and the influence on the glass structure.

This thesis work aims to evaluate the potential of a specific ternary glass-forming base (Zr-Co-Al) to produce medical devices. The selection of the ternary base, its detailed characterisation and the comparison to the literature will be presented in Chapter III. To further enhance our understanding of the glass structure, and its relation to mechanical properties, the relaxation and the rejuvenation of the present Zr-Co-Al alloy are the topics of Chapter IV. Finally, Chapter V is dedicated to the study of minor-alloying, with Nb. A particular focus is made on the influence of the alloying method, as too often, only the introduction of the alloying element is considered while how it is introduced is also of prime importance.

Chapter II:

Experimental procedures

II. Experimental procedures

This chapter is dedicated to the technical means and experimental procedures used to synthesize and characterize the amorphous alloys and their properties. This thesis is a collaboration between several partners, productions and characterization means are distributed among every partner. Data from a piece of specific equipment were always acquired by the same operator to minimize the operator's related variability. First will be described alloys preparation technics from raw materials and metallic glass casting. Then amorphous nature validation and glass structure characterisation procedures will be presented. Mechanical properties characterisation will be detailed before moving on to the way biocompatibility-related properties are studied.

II.1. Processing of metallic amorphous alloys

II.1.2. Processing procedures

This sub-section is dedicated to the amorphous alloys preparation processes, where a primary alloy is cast into the desired shape.

II.1.2.1. Primary alloy preparation by arc-melting

Primary alloys are always prepared using arc melting, no matter the subsequent casting process, to form calibrated (in mass and composition) ingots. Ingots are obtained by melting pure raw materials (purity > 99.99%) weighted at the desired composition (in atomic %). Each constitutive element is weighted with a precision balance. A tolerance of 0.05 at% on the composition of the primary alloy is accepted. An example is given for 10 g of $Zr_{56}Co_{28}Al_{16}$ alloy in Table II-1.

	Zr	Co	Al
Atomic fraction (at%)	56	28	16
Mass fraction (m%)	71.0	22.9	6.0
Total mass (g)	7.1047	2.2949	0.6004
Error: ± 0.05 %	*0.0018*	*0.0032*	*0.0018*
Min. acceptable mass (g)	7.1029	2.2918	0.5986
Max. acceptable mass (g)	7.1065	2.2981	0.6022

Table II-1: Example of tolerance for weighing 10 g of $Zr_{56}Co_{28}Al_{16}$ primary alloy.

Pure elements are mixed by fusion using plasma into water-cooled copper crucibles under a high-purity argon atmosphere (99,999%). The plasma arc current is set to 220 A for pre-alloys fusion. The mass of the ingots is calibrated to reach the volume required for casting. Figure II-1 illustrates the raw materials and the resulting calibrated primary alloy ingots.

Figure II-1: Picture illustrating the raw metals (on the right) and the calibrated primary alloy ingots (on the left)

II.1.2.2. Suction casting

The suction casting process is integrated within the same device as the arc melting. This device was designed at the SIMaP laboratory. Ingots are melted using plasma above a water-cooled copper mould. Once fusion is reached, the alloy is pushed inside the mould by applying a pressure difference (ΔP) between the arc chamber and the mould chamber. ΔP usually varies from 50 to 150 mbar. Shapes like plates or rods, with various thicknesses and diameters, can be obtained by changing moulds. One can also vary the arc current, but for this thesis, it was chosen to keep it constant (200 A). The current is slightly lower, to minimize a bit the thermal gradient within the ingot. The thermal gradient can sometimes cause strains high enough to break the ingot during heating.

II.1.2.3. Injection casting performed at Vulkam

The injection casting process relies on the same ingots of primary alloy as the suction casting process. Ingots are melted by induction under high vacuum. Once the ingot reaches fusion, it is pushed inside the mould cavity by a plunger. Mould temperature, plunger speed and applied pressure are controlled. This technic is developed by Vulkam. Figure II-2 (a) and (b) illustrate respectively the suction casting process and the injection casting process.

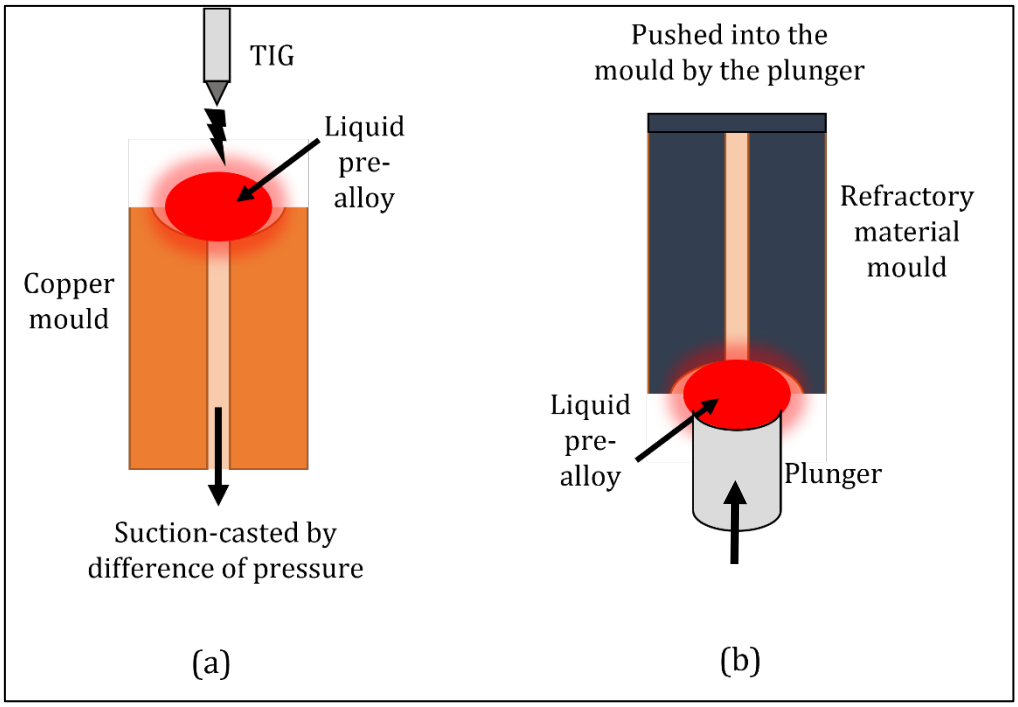

Figure II-2: (a) schematic representation of the suction casting process, (b) schematic representation of the injection casting process.

II.1.3. Processing issues

Key issues can be encountered while synthesizing bulk metallic glasses. Metallic glasses possess a metastable structure very sensitive to processing conditions. For this reason, the processing is always made under controlled atmosphere (argon atmosphere for suction casting or vacuum for injection casting). Moreover, in the arc melting/suction casting process, the atmosphere is Ti-gettered to trap the remaining oxygen. Crystals germination is favoured by impurities presence, with act as nucleation sites. Raw metal purity is therefore of primary importance. Purity is controlled by manufacturers but light element quantification is always tricky. Potential pollution can be detected after fusion when a lot of dirt is found in the crucible.

The chemical affinity (i.e. mixing enthalpy) is also a factor that can potentially degrade homogeneity. Zr has a large negative heat of mixing with Al (ΔH_{mix} = -44 kJ/mol) and Co (ΔH_{mix} = -41 kJ/mol), meaning a strong chemical affinity. Silver (Ag) for instance has a positive heat of mixing with Co (ΔH_{mix} = +19 kJ/mol), Fe (ΔH_{mix} = +28 kJ/mol) or Nb (ΔH_{mix} = +16 kJ/mol). Ag will then be hard to mix with those elements, with a greater tendency to segregation.

One other issue lies in the homogenization of the primary alloy. Constituent metallic elements present different fusion temperatures which can be a challenge. The temperature of the melt bath is limited by constitutive elements, and therefore, might not reach temperatures high enough to melt every element. In our alloy system, Zr and Nb have the highest melting temperatures, with respectively 2128

and 2750 K. Al and Co have lower melting temperatures with respectively 933 and 1768 K. To raise the melt temperature, a first ingot is prepared with only Zr and Nb. This strategy is backed up by the Zr-Nb binary diagram, which shows a minimum around 20 at% of Nb. At this point, the melting temperature is lowered around 2000 K (Figure II-3).

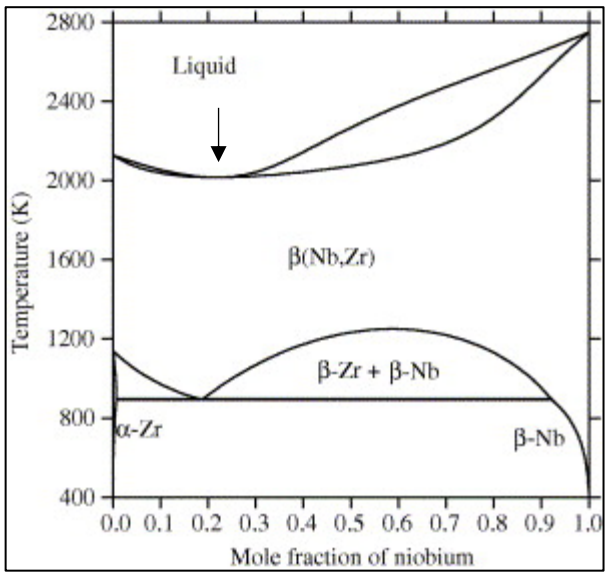

Figure II-3: Binary phase diagram Zr-Nb

II.2. Structural characterisation of bulk metallic glasses

II.2.1. Structure analysis

II.2.1.1. Optical observation

To validate the amorphous nature of the produced alloys, one has to perform structural characterizations. To discriminate samples with high degrees of crystallization, optical observation is

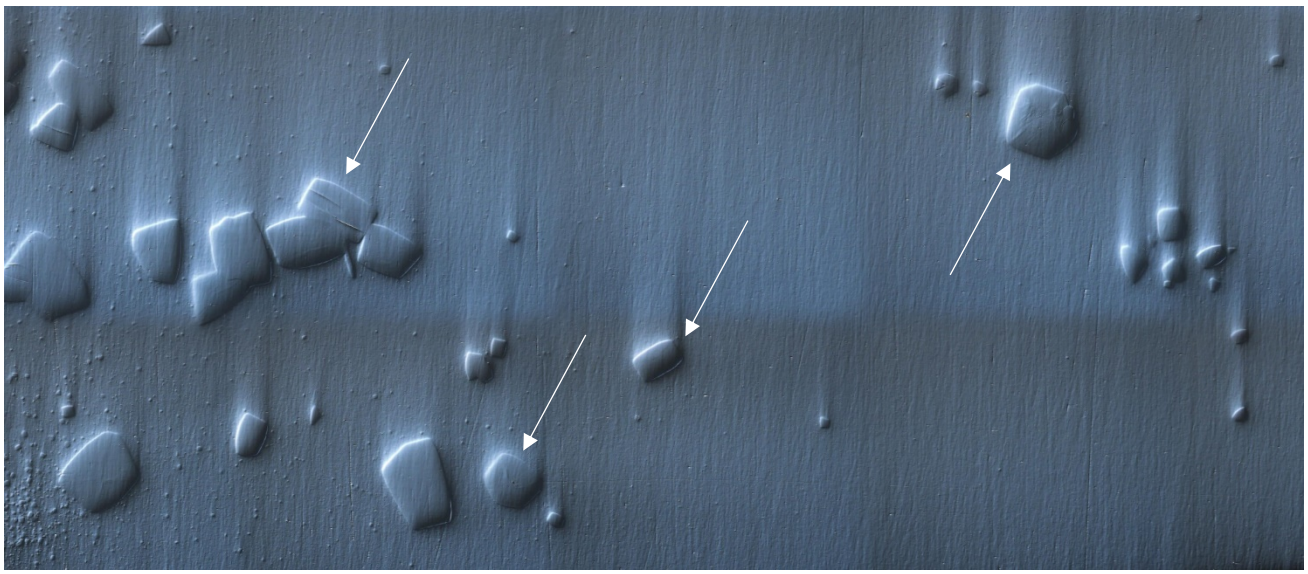

Figure II-4: Optical observation of a Zr-Cu-Fe-Al sample, with embedded crystalline phases (arrows).

enough. Cross-sections of samples (plates and rods) were polished down to 0.03 µm and observed using an Olympus optical microscope DSX 500. This microscope proposes a differential interference contrast mode (DIC) which produce a pseudo-3D shadow image. Crystalline phases and amorphous phases can present different hardness and fine polishing create height differences, which are better revealed with DIC mode. Crystallization may manifest itself as dendrites, surface crystallization (see chapter III) or spherules (Figure II-4).

II.2.1.2. XRD measurement

X-ray diffraction (XRD) measures are also performed to validate the amorphous state. They are realized using a PANalytical diffractometer using Cu-Kα radiation (1.5419 Å). If there is no long-range atomic order in the material, there will be no predominant inter-atomic distance, hence no intense sharp peak on the diffraction pattern. Crystalline phases need to be large enough to be detected (> 20 nm). This technique can differentiate amorphous (only a broad diffraction bump, see Figure II-6), partially crystallized (some peaks are visible, but the broad diffraction bump is still visible, Figure II-5 (a)) and crystalline samples (no broad diffraction bump observed, Figure II-5 (b)). In this work, it will be considered that samples are amorphous when no crystals are detected on the XRD pattern.

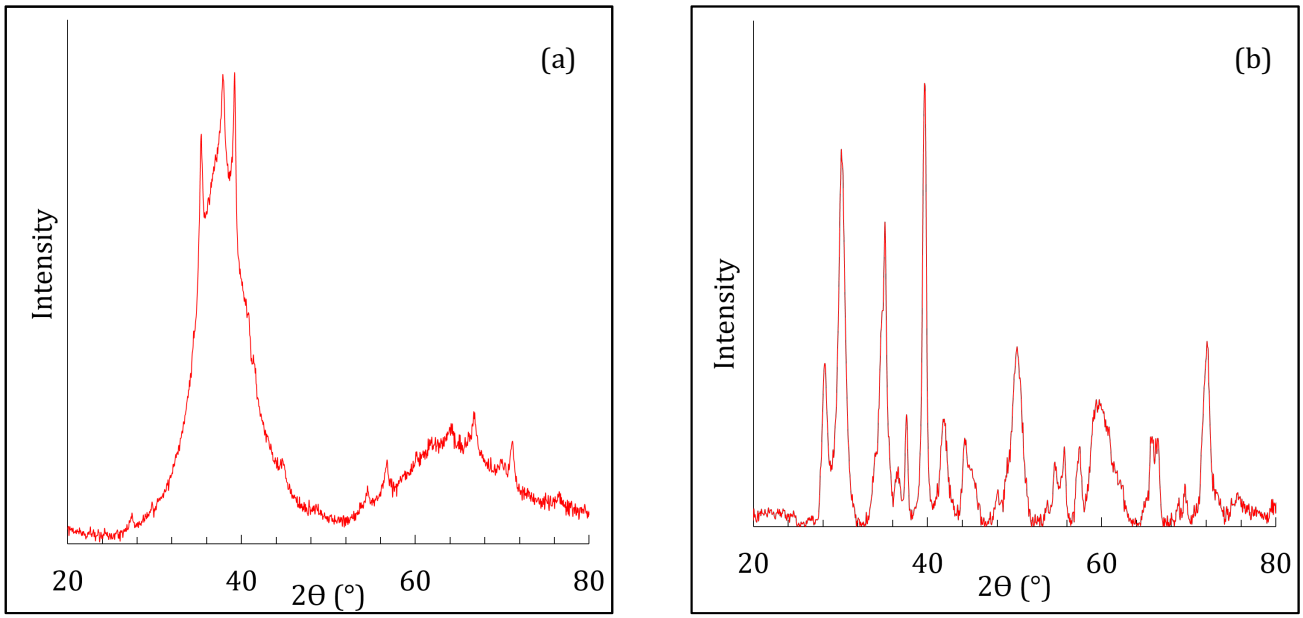

Figure II-5: XRD patterns for a partially crystallized sample (a) and a fully crystallized sample (b). Alloy is Zr-Co-Al.

Additional information can be obtained by fitting the amorphous-related XRD with a Lorentz's function:

$$f(x) = y_0 + \frac{A \times \sqrt{\frac{2}{\pi}}}{w} \times e^{\left[-2\times\left(\frac{x-x_c}{w}\right)^2\right]}$$

II-1

where A is the area under the fit, x_c the broad peak position, w the width and y_0 the offset (Figure II-6). To compare XRD fits, acquisitions were always performed on samples with the same geometry, the same radiation source and the same exposition time. Fits are realized with QtiPlot software.

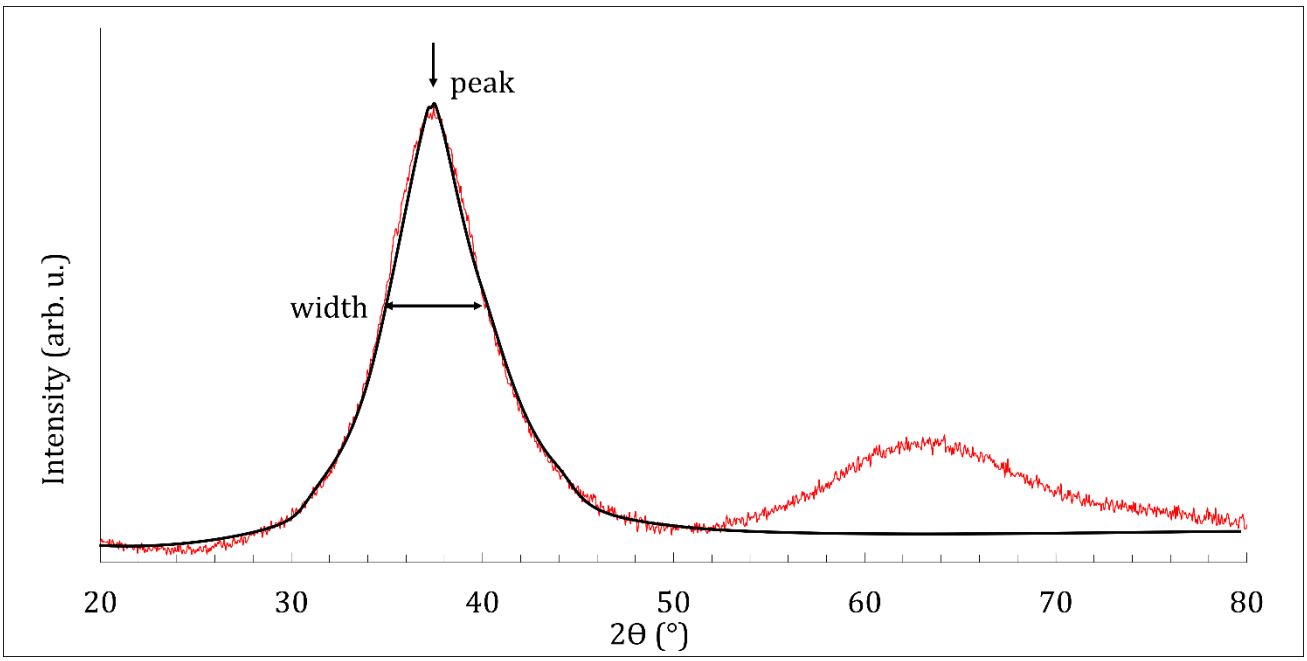

Figure II-6: Schematical example of a Lorenztian fit onto a XRD pattern.

II.2.2. Critical diameter evaluation

Critical diameter evaluation is a useful tool. Rather than measuring the critical cooling rate, the ability to form a metallic glass can be evaluated in terms of critical diameter. Yet, the achievable critical diameter or thickness is very dependent on the processing parameters (alloy temperature, mould temperature, mould shape, melt flow…). This parameter should therefore be considered with all due precautions. A common technic is to cast cones. With the increasing diameter along the revolution axis, a gradient of cooling rates is achieved. When the cooling rate becomes lower than the critical cooling rate, the crystallization starts. The critical diameter can then be measured. To assess glass formation ability, it was chosen to use 5mm diameter rods produced via arc melting and suction casting in a water-cooled copper mould. If the XRD on cross-sections of such rods reveals an amorphous state, the glass formability is declared satisfying.

II.3. Properties measurement

II.3.1. Thermal stability analysis

Metallic glasses behaviour upon heating was studied using a Mettler Toledo DSC setup. Graphene crucibles were used and sample weight was calibrated to be between 10 and 15 mg. Measurements were performed under azote atmosphere. To quantify relaxation, glass transition and crystallization, a heating rate of 20 K/min was used. T_g is measured at the inflexion point, located on the endothermic event

associated with the glass transition (Tg_i on Figure II-7). Other specific points such as the onset (T_{go}) are sometimes used in the literature. Other heating rates have been used to calculate activation energies with Kissinger's plot method (see Chapt. III). The acquisition was always realized in two steps: first, a heating ramp up to 973 K (700°C) followed by cooling down to room temperature; then a second heating ramp, on the same temperature range, to acquire a baseline which is then subtracted to the first ramp signal.

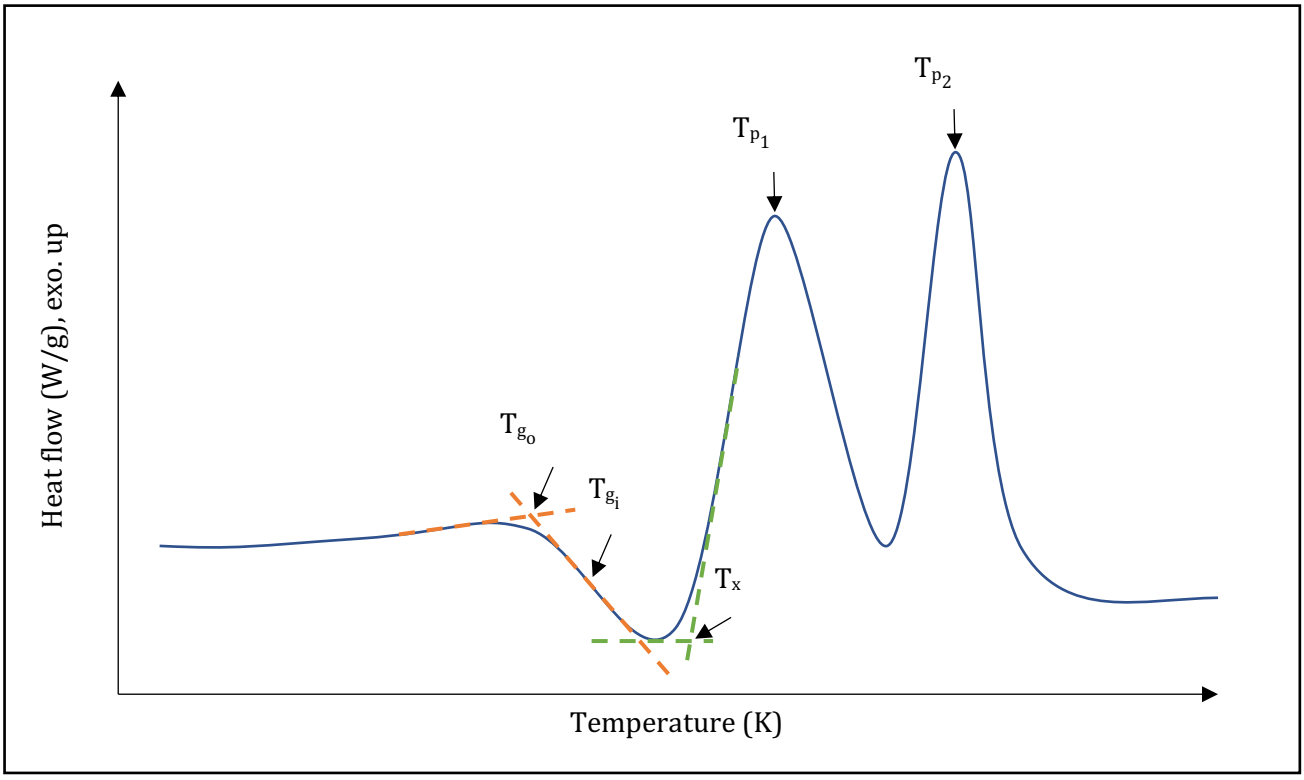

Figure II-7: Typical DSC signal with position of characteristic temperatures (T_g = glass transition, T_x = crystallization temperature and T_p = crystallization peak temperature).

II.3.2. Density measurements

Density is measured using Archimedes' principle. The balance used is a Mettler Toledo ML304T, with a precision of 0.1 mg. It is equipped with a standard density kit from Mettler Toledo. Every sample is firstly weighted in the air and then in a solvent (ethanol). The volumetric mass density is then obtained with:

$$\rho = \frac{m_{air}}{m_{air} - m_{ehtanol}} \times (\rho_{ethanol} - \rho_{air}) + \rho_{air}$$

II-2

where ρ_i and m_i are respectively the volumetric mass density ($g.cm^{-3}$) and the mass of the sample in fluid i (g). For this measurement, rod-shaped samples with a diameter of 2 mm and a weight of approximately 0.8 g were used. The ethanol used for the measurement was kept in the measurement room for several

hours before measurement to ensure thermal stability. Both ethanol and air temperatures were measured before measuring to adjust densities.

II.3.3. Mechanical characterization

II.3.3.1. Young's modulus

Young's modulus is determined by Impulse Excitation of Vibration. The system used is a GrindoSonic MK7 from GrindoSonic BVBA. Samples used were rod-shaped with a 2 mm-diameter and a length of approximately 45 mm. The longitudinal mode was used and the procedure followed ASTM standard E 1876 – 01. The sample is hit at its extremity with an impulser, which is composed of a flexible polymer rod at the end of which is attached a steel ball. The fundamental longitudinal frequency is measured with a microphone at the opposite extremity (see Figure II-8). A low-pass filter and a high-pass filter are used to isolate a frequency range coherent with expected Young's modulus values for Zr-based bulk metallic glasses.

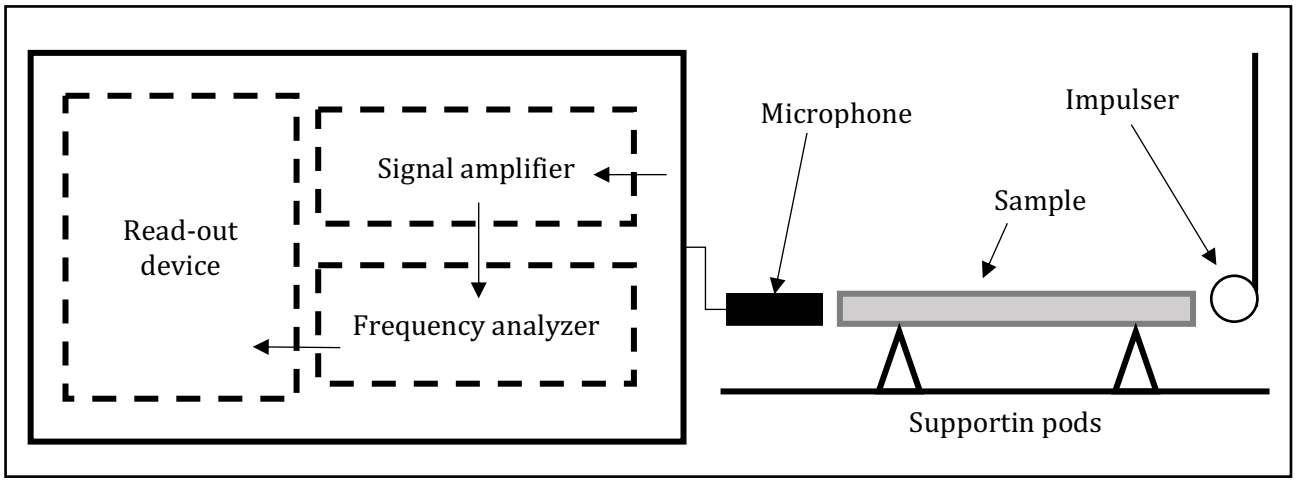

Figure II-8: Grindosonic experimental set-up

In longitudinal mode, Young's modulus can be calculated using the following equation:

$$E = 16m \times f_1^2 \left[\frac{L}{\pi \times D^2 \times K}\right]$$

II-3

where m is the mass of the bar (g) f_1 is the fundamental longitudinal frequency of the sample (Hz), L is the length of the bar (mm), D is the diameter of the bar (mm) and K is a correction factor to account for the finite diameter-to-length ration and Poisson's ratio (μ) such as:

$$K = 1 - \left[\frac{\pi^2 \times \mu^2 \times D^2}{8L^2}\right]$$

II-4

This is a very powerful, non-destructive method to measure elastic constants. It is however very sensitive to the sample geometry. Therefore, only carefully prepared 2 mm diameter rods were used.

II.3.3.2. Hardness

Vickers hardness was chosen to measure micro-hardness. Indentation was realized on a Presi MMT-X7 micro hardness instrument. A load of 1000 g.f was applied with a dwell time of 10 s. Vickers hardness was calculated from the measure of the diagonals length of the indent:

$$HV = \frac{2F \times \sin\frac{136}{2}}{9.80665 \times d^2}$$

II-5

where F is the applied load (1 kg.f = 9.80665 N) and d is the average length of the two diagonal lengths.

For more precision, each indent was observed using the Olympus optical microscope DSX 500. The optical microscope presented give access to greater magnification, hence a better resolution. Each indent size was measured with the ImageJ software.

II.3.3.3. Nano-hardness

The device used for nano-hardness mapping is an Anton Paar TriTec Micro Indentation Tester, with a Berkovich's diamond tip. Mapping of at least 100 indents was realized on polished samples (down to 1 µm). The indentation maximum load was determined by a calibration test. The hardness tends to increase with the indentation depth until it plateaus. The hardness was therefore measured while increasing the indentation depth (proportional to the applied load) to reach a depth where it stabilizes. The corresponding load is subsequently used for the mapping.

Nano-hardness is measured on the same principle as micro-hardness, meaning calculating the ratio of the applied force on the contact area. The hardness can be calculated as followed:

$$H = \frac{F_m}{A_c}$$

II-6

where F_m *is* the maximum applied load and A_c is the projected contact area.

$$A_c = 24{,}5 \times h_c^2$$

II-7

with h_c being the height of contact.

However, an issue can lie in the miss-estimation of the contact area. The ideal case is where the indenter perfectly penetrates the sample surface, without any deflection of the surface. But a deflection of the sample surface can be observed (sink-in effect). The opposite phenomenon is a rise of the sample surface at the edge of the indent, called a pile-up effect.

	Indenter cross-section	Projected contact area	Contact height h_c
Sink-in	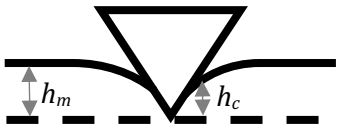		$h_c < h_m$
No deflection	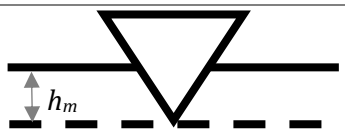		h_m
Pile-up	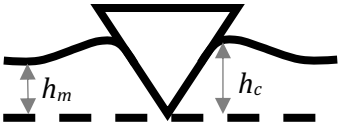		$h_c > h_m$

Table II-2: Surface deflection scenarios in nano-indentation

A sink-in effect leads to an overestimation of the contact area, therefore underestimating the hardness. A pile-up effect leads to an underestimation of the contact area, therefore overestimating the hardness. The surface deflection phenomenon has to be checked while performing nano-indentation tests.

II.3.3.4. Compression

For uniaxial compression testing at room temperature, an MTS 4/M with a 20 kN load cell and an acquisition frequency of 10 Hz was used. The displacement was measured using an extensometer, mounted on the compression platens. Small tungsten carbides discs were placed between samples and compression platen to avoid any indentation of the compression platen surface. Samples were obtained from 2mm-diameter rods processed via injection casting resulting in fewer porosities than the suction casting process. To ensure consistency, rods were machined into compression cylindrical specimens through computer-controlled machining by Anthogyr. A 2:1 height to diameter ratio was chosen. Ultimately, the used samples were 3.7 mm in height and 1.85 mm in diameter. The diameter was reduced from 2 mm to 1.85 mm to suppress any surface defects. After machining, samples are controlled with X-Ray Tomography (device RX Solution EasyTom XL). Compression tests were performed at constant strain rate, which was set at 2.5 10^{-4} s^{-1}. The machine compliance was corrected during data treatment. Machine deformation mainly impacts the elastic deformation of the sample because the stress is rapidly rising during the elastic regime. Stress/strain curves are corrected using Young's modulus measured by Impulse Excitation of Vibration (see II.3.3.1 Young's modulus). Figure II-9 shows a typical stress/strain

curve, before and after correction. One can see that because Young's modulus was underestimated in the raw data, the ultimate deformation was overestimated.

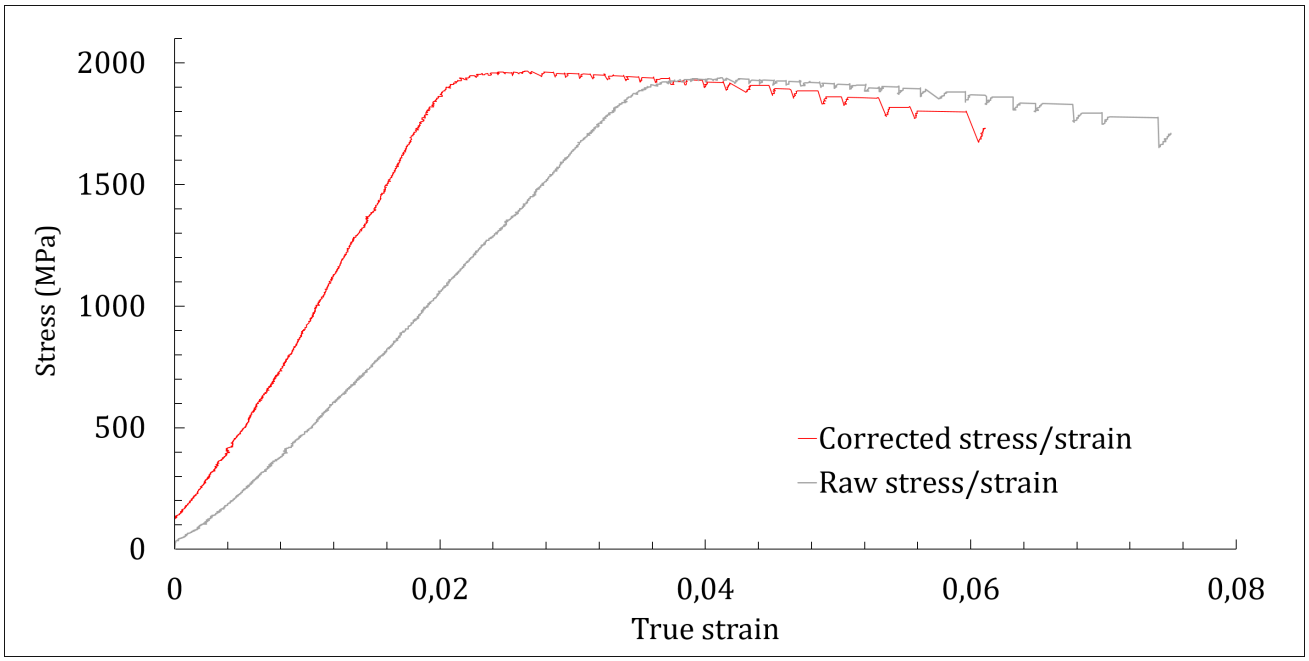

Figure II-9: Raw and corrected strain/stress curves

II.3.3.5. Fatigue testing performed at Anthogyr

Fatigue resistance is investigated following the procedure described in the ISO standard 14801 – 2016. Samples are machined into a specific geometry to mimic a dental implant pillar. Samples are also controlled via X-Ray Tomography to check for porosities, as illustrated in Figure II-10 (a). The red circle highlights a porosity. When such a defect is detected, the sample is not used for mechanical testing. The load is applied with an angle of 30°± 2° to the pillar rotation axis as illustrated in Figure II-10 (b), from ISO 14801 - 2016. The load is applied as a cycle of loading and unloading, hence the fatigue testing. The load ranges from 10% to 100% of the maximal applied load. Frequency is set at 15Hz (15 cycles per second) and tests are performed in the air at room temperature. If the sample reaches 5 000 000 cycles, the test is interrupted, the load is increased by 20N and the test is launched again for 5 000 000. This procedure is repeated until the failure of the sample. This is called staircase testing. This experimental setup makes it hard to calculate effective constraints. Sections reductions induce stress concentration, and the angle between the sample and the loading direction induces a shift of the neutral fibre (between compression and traction). Nonetheless, this test is appropriate to evaluate the fatigue resistance of a material for biomedical applications.

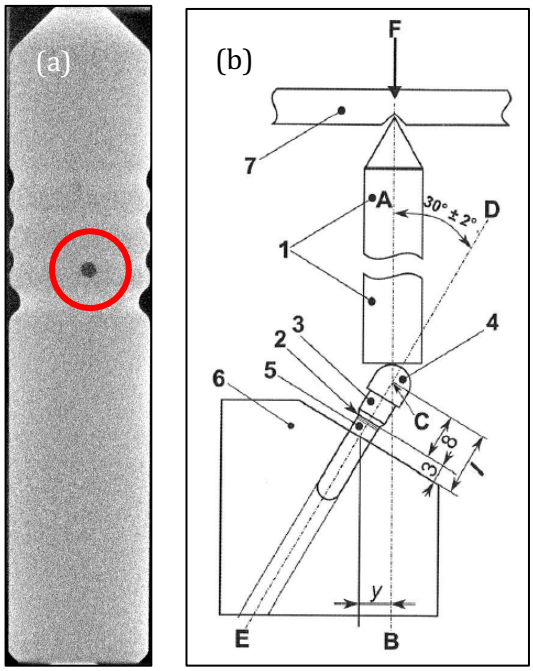

Figure II-10: Dynamic loading testing for dental implants.

(a) Tomography imaging of a fatigue sample

Red circle: porosity

(b) Schematic of the fatigue experimental device

1-Loading device, 2-Nominal height level of the bone, 3-Dental implant pillar, 4-Hemespheric cap for load application, 5-Implant body, 6-Sample holder, 7-Load applicator

[AB] – Loading axis, [DE] – Implant axis, C – loading and implant axis intersection.

II.3.3.6. Dynamical Mechanical Analysis performed at MATEIS

To measure the dynamical mechanical properties of the studied metallic glasses, mechanical spectrometry, also known as Dynamical Mechanical Analysis (DMA) was performed. Generally speaking, this technic consists of the application of a sinusoidal constraint onto the samples and the measurements of deformation phase shift δ.

Stress is applied with a frequency f and an amplitude σ_0. It can be written as:

$$\sigma = \sigma_0 \cos(\omega t)$$

II-8

with $\omega = 2 \times \pi \times f$

Strain resulting from the applied stress is then expressed as:

$$\varepsilon = \varepsilon_0 \cos(\omega t - \delta)$$

II-9

With δ being the phase delay (see Figure II-11) and ε_0 the amplitude.

Energy loss during a cycle ΔW can be expressed as:

$$\frac{\Delta W}{W} = 2 \times \pi \times \tan \delta$$

II-10

With W being the elastic work per volume unit. To perform this analysis, an inverted torsion pendulum is used. It applies shear stress and shear modulus G can be calculated:

$$G = \frac{\sigma}{\varepsilon} = G' + iG"$$

II-11

G' is the part of the modulus corresponding to the elastic response and G" is related to the viscoelastic response.

$$G' = \frac{\sigma_0}{\varepsilon_0} \times \cos\delta$$

II-12

$$G" = \frac{\sigma_0}{\varepsilon_0} \times \sin\delta$$

II-13

$$\tan\delta = \frac{G"}{G'}$$

II-14

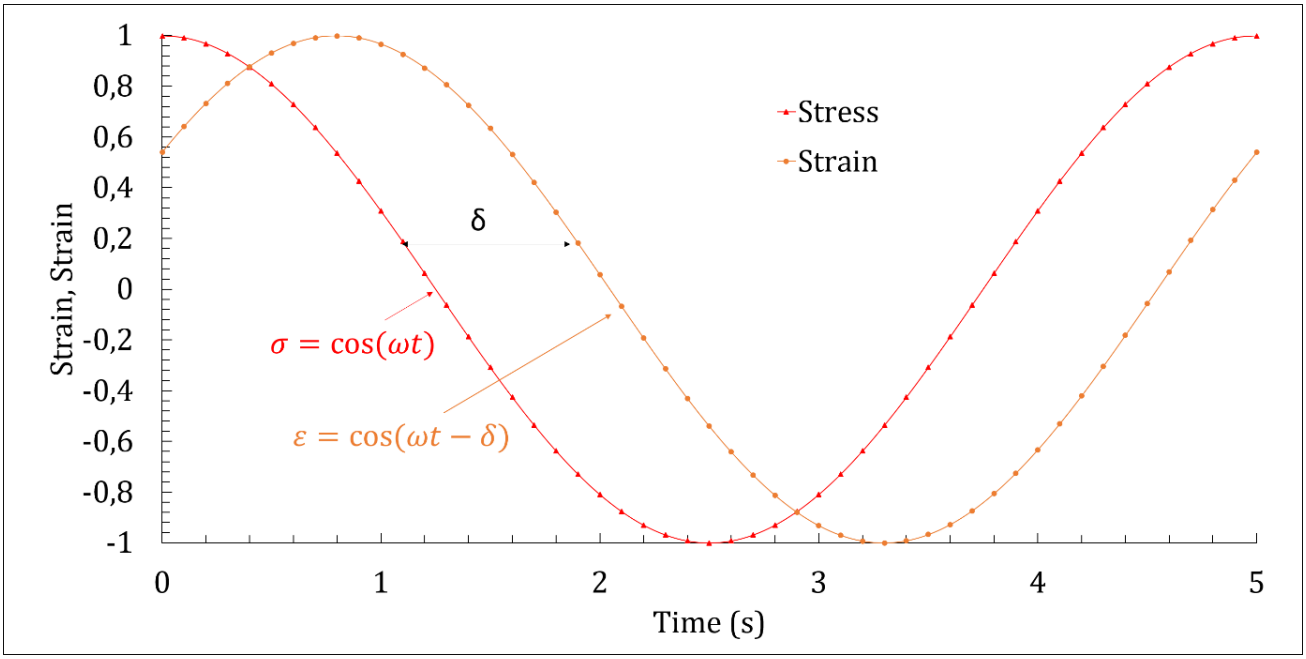

Figure II-11: Stress applied and strain measured in a DMA experiment, as function of time

For this specific device, designed at INSA Lyon, parallelepipeds samples with dimensions 30 mm x 2.25 mm x 0.9 mm are used. Samples are held between a fixed jaw (lower part) and a mobile jaw (upper part) which is applying the torsion. Deformation angle is measured using Poggendorff's method. Tests are realized under high vacuum. Two types of measurements can be realized: fixed frequency (0,3 Hz)

and ramping temperature (3K/min) or isothermal measurements and varying frequency. In the varying frequency mode, 24 frequencies are used. The starting frequency is 2Hz and frequency is multiplied by 0.8 for each step, down to 0.01 Hz. This procedure is repeated for several temperatures from 550K to 760K. For the work presented in this manuscript, we only used the fixed frequency mode.

II.3.4. Biocompatibility assessment

II.3.4.1. Corrosion resistance performed at MATEIS

Corrosion tests have been performed on several alloy compositions. Tests were initially based on the ISO 10271 standard but the procedure was then modified to be more discriminatory. The experiment took place in a temperature-controlled, 3 electrodes glass cell. A Biologic reference SP300 was used for voltage control and current measurement. The working electrode was the metallic glass, the counter electrode was graphene, and the reference electrode (Ref.) was an Ag/AgCl electrode (+0.222 V to standard hydrogen electrode, SHE). The working solution was a NaCl solution, with a concentration of 9 g/L, maintained at 310 K. These conditions are specifically designed to mimic the buccal environment. Unlike recommended in the ISO 10271, tests were realized in open-air solutions. The exposed area was 5.31 cm^2 and was delimited by a rubber gasket. The test protocol is described below:

- Open-circuit potential (OCP) measurement for 24 hours.
- Polarization curves during scanning in potential from 200mV under the value of the OCP at 24h to 1000 mV vs Ref. The scanning rate is set at 1 mV/s. A limit is also set at a measured corrosion current of 1 mA to detect pitting. Once this current is reached, the potential decreases at the same speed (-1 mV/s) until re-passivation is observed.

Samples are suction-casting plates with a thickness of 2 mm. Surfaces are polished with SiC papers down to P4000 grain size. OCP measurements and polarization curves are complementary measures as OCP will allow for the study of the alloy stability without any current, and the polarization measurement will give us access to the corrosion potential, the passive current and the pitting potential.

II.3.4.2. Immersion resistance performed at MATEIS

Immersion resistance testing is performed as proposed in ISO standard 10271. In this test, the studied samples are immersed in a thermostatically controlled (body temperature) solution for 7 days. After 7 days (±1h), the solution is replaced by a fresh one and the old one is analysed via inductively coupled plasma mass spectrometry (ICP-MS) to quantify released metallic elements. Solution pH, as well as mass loss, are also measured after immersion. Samples are ultimately immersed for 4 weeks. The immersion solution is prepared at 0.1 mol/L of lactic acid and 0.1 mol/L of sodium chloride. Water is used as a solvent and the pH is balanced at 2.3. The solution is maintained at 310 K and is homogenized through agitation (50 rpm) in a New Brunswick Innova 40/40R oven. Samples have a surface of 14.2 cm^2

and are polished down to grain size P1200. Because of available experimental material, the material's surface to solution's volume ratio is 0.62 instead of 1 as recommended in the ISO standard. Containers are sealed to avoid evaporation. Figure II-12 shows pictures of the samples inside the containers before being sealed and the incubator. Two kinds of tests are performed: on the one hand, the studied metallic glass alone is in the solution. On the other hand, the metallic glass is immerged in contact with a conventional metallic material for medical application, such as TA6V-ELI, 316 L Stainless Steel or Co-Cr-W. The metallic glass and the conventional crystalline materials have the same working surface area. This second kind of test intends to evaluate the potential for multi-material implants design. If the two materials have very different potentials, galvanic corrosion could happen and degrade the less noble material.

Figure II-12: Immserion experimental set-up. On the left are the glass-containers with inside the samples. On the right is the incubator where the samples were kept for four weeks.

II.4. Geometries and associated characterization

Table II-3 is a summary of the different geometry produced via suction casting used in this work, with corresponding characterisations. The reported dimensions are the casting dimensions and not the dimensions of the tested samples. Samples dimensions can be found in the related sections.

Use	Geometry	Dimensions	Casting method
XRD	Rod	5 mm diameter	Suction
Hardness	Rod	5 mm diameter	Suction
Nano-hardness	Rod	5 mm diameter	Suction

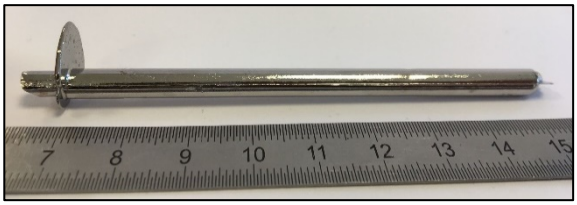

Figure II-13: picture of a 5 mm-diameter rod as-cast from the suction casting device

Fatigue – ZrCoAl	Rod	5 mm diameter	Suction

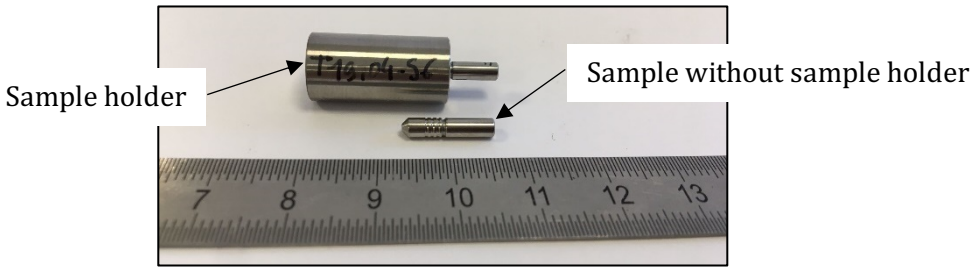

Figure II-14: picture of the sample machined from a 5 mm-diameter rod for fatigue testing.

OCP + Polarization	Plate	2 mm thickness	Suction
Immersion	Plate	2 mm thickness	Suction

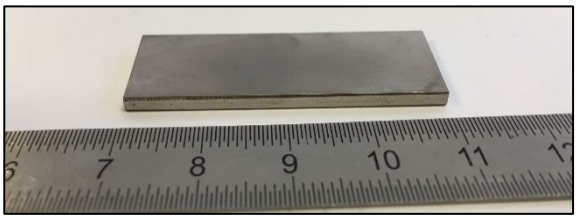

Figure II-15: picture of a 2 mm-thick plate produced via suction casting for surface properties testing

Table II-3: Correspondence cast geometry/performed characterisation

Table II-4 sums up the several geometries produced via injection casting.

Use	Geometry	Dimensions	Casting method
Young's modulus	Rod	2 mm diameter	Injection
Compression	Rod	2 mm diameter	Injection

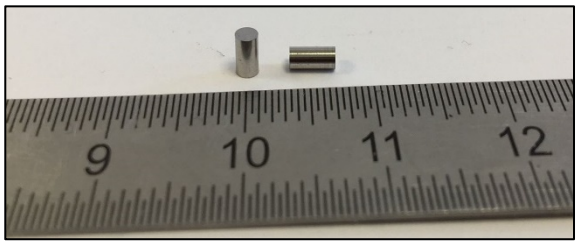

Figure II-16: picture of two compression samples, machined from a 2 mm-diameter rod produced via injection casting

DMA	Plate	1 mm thickness	Injection

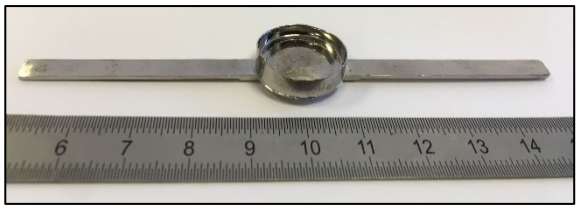

Figure II-17: picture of the 1 mm-thick plates produced via injection casting. Two plates are produced with each injection (left and right from the injection sprue). DMA samples are machined from those plates

Table II-4: Correspondence cast geometry/performed characterisation

II.5. Conclusion

In this part, all the experimental techniques for processing and characterisation are explained.

First, the primary alloy obtention is discussed. In this thesis work, we chose arc melting and kept this means for all the elaboration. Bulk metallic glasses could be very influenced in their properties by the processing techniques. Therefore, keeping the same primary alloy elaboration technics throughout the entire work ensure consistency. The casting technique is also very important. Thanks to the context of the thesis, we had the opportunity to explore two casting techniques. The most conventional casting technique used is arc melting. This technique is commonly used to produce BMGs in the research community, the process is stable and reliable, but it also possesses flaws. Casting times are long as one can only cast one part at a time, with important pumping times between each casting. Also, flows can be erratic and samples with high form factor (one long direction, such as rods) often exhibit porosities (at least for Zr-Co-Al), very detrimental for mechanical resistance. Samples exhibiting porosities were not used for mechanical testing. The injection casting technique, currently developed by Vulkam Inc. is very powerful as it increases mould conformation (melt/mould contact) and suppresses porosities. This technique was progressively developed with the design of new machines during this thesis. Along with the improvement of the mould filling, this machine considerably improves production times as it can realise several injections in a raw. However, as this process is under development, the machines are less available, and the influence of the injection casting compared to the suction casting is not well understood. Most of the samples for mechanical testing were realised using injection casting to prevent porosities issues. One should keep in mind those aspects while comparing results obtained with different casting techniques, but a specific characterisation was always performed using the same casting technique and therefore results can easily be compared.

Second, the various characterisation techniques used in the PhD thesis are described. Three major categories can be outlined:

- The structure and thermal experiment, including XRD measurements, density tests, DSC experiments and transmission electron microscopy (TEM).
- The mechanical characterisation, including compression testing, fatigue testing, hardness (micro and nano) and dynamical mechanical analysis
- The biocompatibility-related characterisation, with the corrosion and the immersion testing.

This set of characterisations gives a broad picture of the thesis scope. This work was mainly focused on the structure/mechanical properties relationships but always had in mind the potential biomedical applications.

Chapter III:

Properties and thermal stability connection with the specific structure of the as-cast Zr-Co-Al BMG

III. Mechanical properties and thermal stability connection with the specific structure of the as-cast Zr-Co-Al BMG

In the first part of this chapter, the main Zr-based ternary compositions on the Zr-TM-Al model (TM= transition metal, such as Zr-Cu-Al, Zr-Co-Al, Zr-Ni-Al and Zr-Fe-Al) will be compared based on data gathered from the literature, to understand the influence of the selected TM. In this work, the Zr-Co-Al ternary base is chosen for its combination of superior GFA, corrosion resistance and mechanical properties. Several compositions for this ternary alloy are also explored and the composition $Zr_{56}Co_{28}Al_{16}$ is ultimately chosen.

In a second part, the alloy is thoroughly characterised, and measured properties are compared to the available data in the literature. As surface properties are of primary importance for biomedical applications, the influence of the casting process on the surface properties of the $Zr_{56}Co_{28}Al_{16}$ is studied. The aim is to tackle the issue of surface crystallization, which is preventing the production of near-net-shape parts. The thermal properties of the alloy are characterised through DSC and DTA measurements. The potential for biomedical applications is evaluated through immersion and polarisation tests. All tests related to biocompatibility are performed following ISO standards or protocols inspired by ISO standards. Mechanical properties are explored through compression testing, dynamical mechanical analysis, and fatigue resistance.

In the final part, a particular focus is brought on the alloy structure and its influence on properties of interest. All along with this chapter, comparisons are made with Zr-Cu-Al BMGs, using data gathered in the available literature, to try to grasp the influence of the late transition metal (TM) in the Zr-TM-Al BMGs formability and properties.

This chapter is concluded with potential optimization axes, which will be developed in the following chapters. Two main leads are considered for properties alteration: the glass structure alteration post-casting, through thermal or mechanical solicitation (Chapter IV), and the glass composition modification using micro-alloying with a fourth compound (Chapter V).

III.1. Amorphous alloy selection for medical application

III.1.1. Zr-TM-Al Bulk Metallic Glasses (BMG)

As mentioned in Chapter I (state of the art review), bulk metallic glasses exhibit very attractive properties for medical devices production. Among the many compositions developed, Ti-based, and Zr-based metallic glasses may be the more promising for surgical tools and permanent implants development. Yet, even though several Ti-based BMG have excellent corrosion and mechanical resistance, ones with sufficient critical diameter (D_c) are often Pd-bearing [188, 189], which considerably raises production costs. Moreover, they are also often containing allergenic or toxic elements like nickel and beryllium [190, 191] (see Chapter I.4.4). These metals are known to release harmful ions. Ni-, Be- and Pd-free Ti-based metallic glasses do not exhibit sufficient critical diameter to this day [168, 192]. Also, ternary Ti-based glass formers are rare, and they do not exhibit sufficient critical diameters to be used in structural implants such as the one we are focusing on here.

Ternary Zr-based bulk metallic glasses exhibit very promising properties coupled with large GFA. A. Takeuchi and A. Inoue [193] proposed a BMGs classification in 2005, based on constitutive elements. Most of the reported Zr-based ternary metallic glasses fall in the first group (group I) which is composed of an early transition metal (ETM, groups IIIA to VIIA in the periodic table), a late transition metal (LTM, groups VIII to VIIB) and Al. The specific role of the Al is in the glass structure is still not clear to us but it appears that it greatly improves the thermal stability of Zr-Cu binary glass [194] and increase Zr-Co-Al alloys GFA as Zr-Co-Al ternary glasses with low Al amount are crystallized [166]. In this configuration, zirconium is the early transition metal (group IV A in the periodic table) and among reported alloys, four main late transition metals are used: Fe, Co, Ni (all of them being in group VII in the periodic table) and Cu (group IB in the periodic table).

It is then of interest to compare these four bases and their constitutive elements. Numerous BMGs with critical diameters >1mm are extracted from a systematic study of the literature [18, 60, 121, 129, 150, 159, 165, 176, 187, 195–217] and are plotted in Figure III-1. The list of all compositions used is available in supplementary material C.

From Figure III-1, reported BMGs compositions for each Zr-(Cu, Co, Fe, Ni)-Al barely overlaps. In this figure and the following discussion, the late transition metals will be referred to as transition metals. Zr-Cu-Al BMGs present low Al content and high TM content, resulting in a lower Zr/TM ratio. Zr-Cu-Al is the only Zr-TM-Al ternary system showing bulk glass former close to the equimolar Zr/Cu ratio. Moreover, many binary Zr-Cu glass formers are reported [218], which is not the case for Zr-Co binary systems for instance. With slightly higher Al content, Zr-Ni-Al BMGs exhibit the lower TM content (and therefore high Zr/TM ratio). Zr-Ni-Al BMGs reported spawn from a little less than 10 at% of Al to more

than 20 at% and TM content between 20 at% and 30 at%. Finally, Zr-Co-Al BMGs combine high Al content and high TM content.

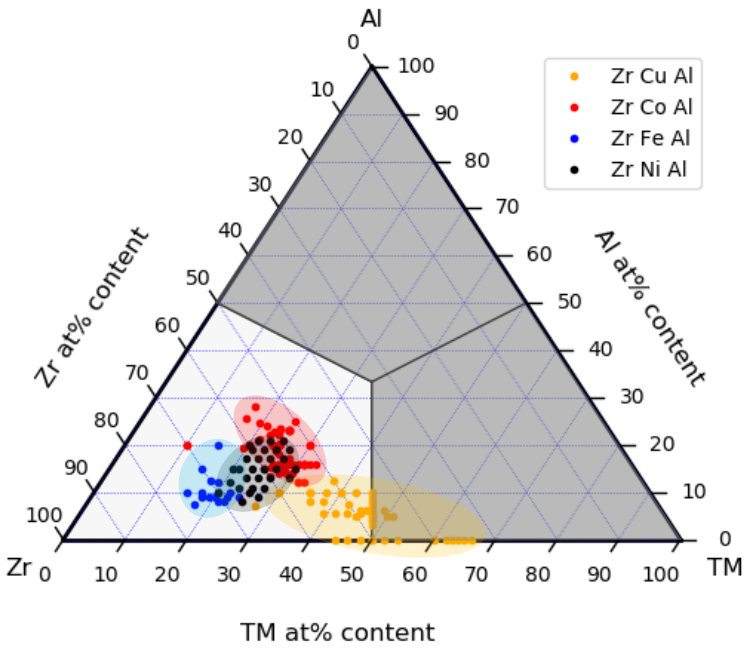

Figure III-1: Zr-TM-Al ternary diagram with several Zr-TM-Al BMGs showing critical diameter over 1mm. Data extracted from a systematic review of the literature.

From the data gathered in the extensive literature available, one can directly conclude that TM cannot easily be swapped in the Zr-TM-Al system to produce BMGs. In other words, simply switching Cu for Co at the sample atomic composition may not produce glass with the same GFA or may not produce glass at all. There is therefore a need to highlight each transition metals specificities and its influence on the Zr-TM-Al BMGs. Glass formers are often considered based on their chemical mixing enthalpy (ΔH_{chem}). This parameter, mainly used after being introduced in Inoue empirical rules for glass formers, can be calculated using the following formula [219]:

$$\Delta H_{chem} = \sum_{i=1,\, i\neq j}^{4} \Omega_{ij} c_i c_j$$

III-1

$$\Omega_{ij} = 4 \times \Delta H_{mix}^{ij}$$

with ΔH_{mix}^{ij} being the mixing enthalpy of elements i and j, and c_i being the atomic fraction of element i.

Mixing enthalpies for considered atomic pairs are reported in the following Table III-1, data are extracted from Takeuchi and Inoue [219]:

Values in (kJ/mol)	13 Al	26 Fe	27 Co	28 Ni	29 Cu	40 Zr	41 Nb
Al		-11	-19	-22	-1	-44	-18
Fe	-11		-1	-2	13	-25	-16
Co	-19	-1		0	6	-41	-25
Ni	-22	-2	0		4	-49	-30
Cu	-1	13	6	4		-23	3
Zr	-44	-25	-41	-49	-23		4
Nb	-18	-16	-25	-30	3	4	

Table III-1: Atomic pairs mixing enthalpies in kJ.mol^{-1}.

According to Inoue's empirical rules (see I.1.3), the lower the mixing enthalpy of the system, the more stable the glass-forming liquid and ultimately the higher the GFA. Mixing enthalpies are presented under the form of ternary diagrams and compositions from the literature in the Zr-TM-Al system are plotted as dots (Figure III-2). Based on the mixing enthalpies, the four ternary bases can be divided into

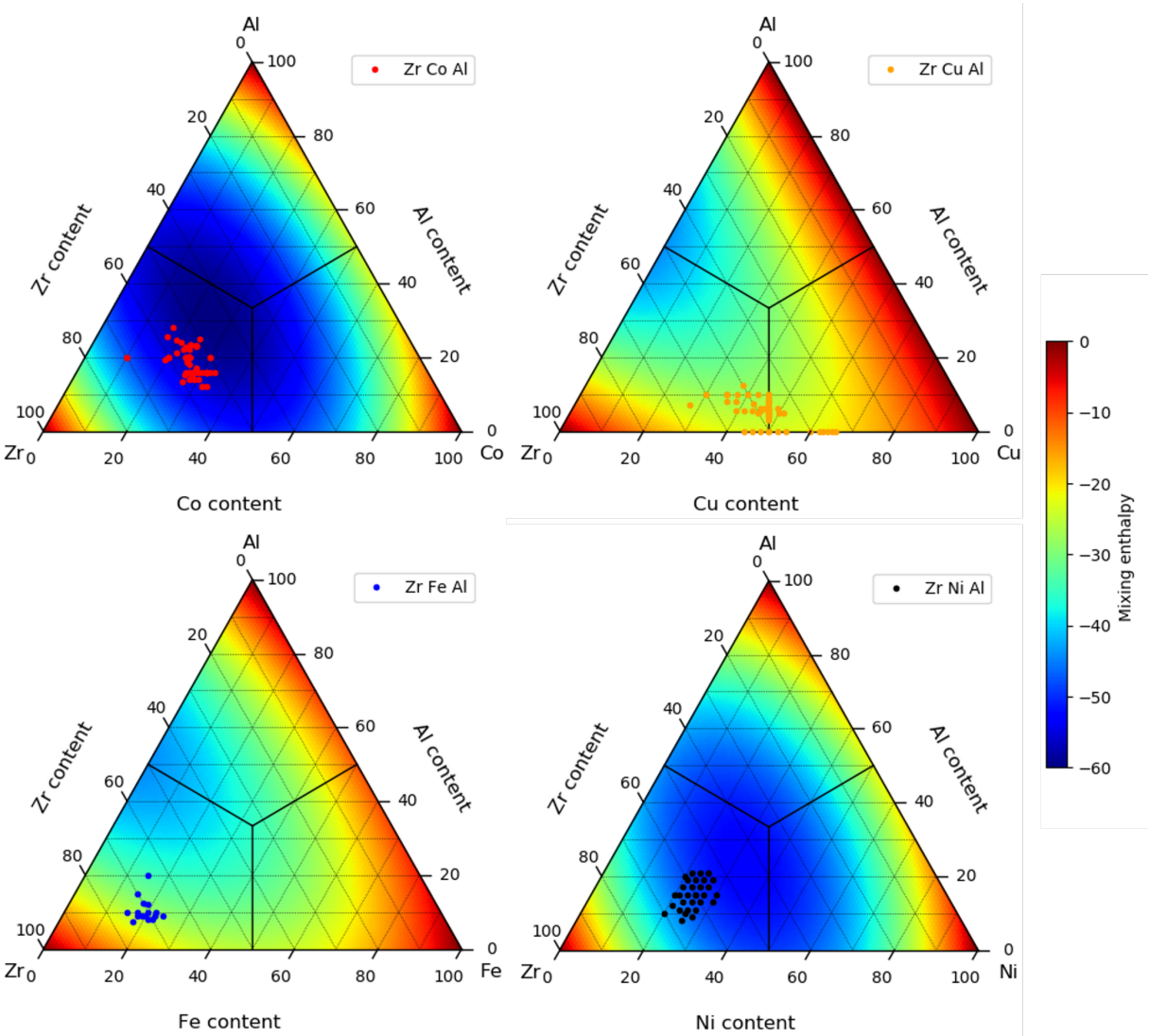

Figure III-2: Ternary diagrams representing calculated mixing enthalpies (kJ.mol^{-1}) for Zr-Co-Al , Zr-Cu-Al, Zr-Fe-Al and Zr-Ni-Al alloys systems. Several compositions reported in the literature are reported as dots.

two groups: on the one hand Zr-Co-Al and Zr-Ni-Al, with lower mixing enthalpies (between -35 and -55 kJ/mol) and on the other hand Zr-Cu-Al and Zr-Fe-Al with higher mixing enthalpies (between -20 to -35 kJ/mol). Co and Ni have very close mixing enthalpies with Zr and Al. Similarly, Fe and Cu have comparable mixing enthalpies with Zr. It is interesting to note that the mixing enthalpy of Cu/Al is almost null (-1 kJ/mol) while it reaches -19 kJ/mol for Co/Al. We also note that reported glass formers are not found in the zones of the lowest mixing enthalpy. This indicates that the mixing enthalpy is not the only parameter to consider while assessing glass forming ability.

In addition to the mixing enthalpy, which is a chemical criterion, a topological criterion is also often used: the mismatch entropy (Figure III-3). It aims to qualitatively evaluate the disorder induces by atoms of several diameters. This also echoes one of Inoue's principles for glass formation which is to aim for more than 12% differences in atomic radii of the constitutive elements. This parameter has also been introduced by Takeuchi and Inoue in 2000 [219]. The parameter is based on atomic radii of constitutive

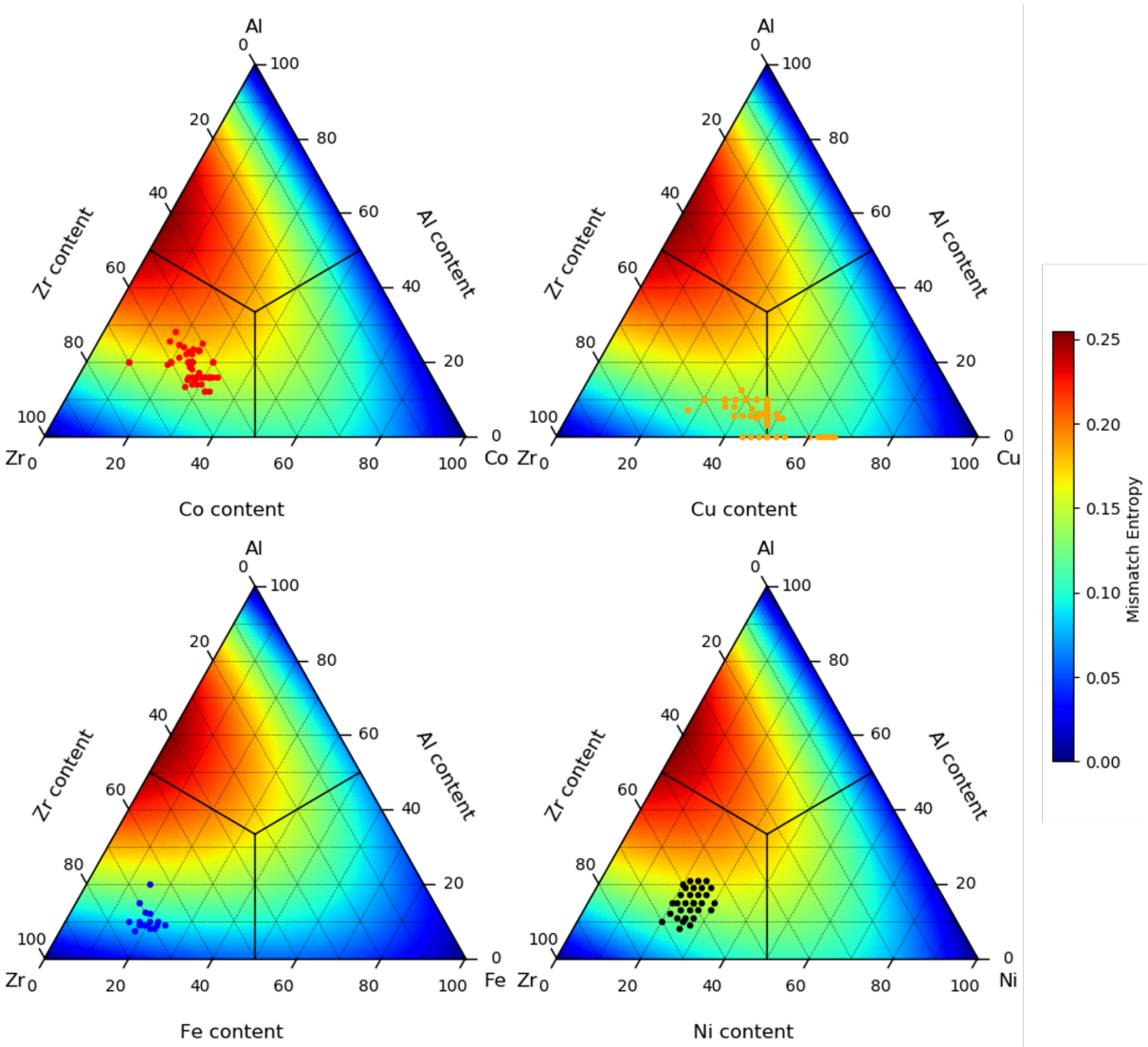

Figure III-3: Normalized mismatch entropy calculated for Zr-Co-Al, Zr-Cu-Al, Zr-Fe-Al and Zr-Ni-Al

elements and their respective concentrations in the alloy. The detail of the calculation is given in supplementary material D.

An increase of the mismatch entropy parameter usually indicates an increase of the GFA, as it is related to an increasing degree of disorder in the liquid state. This parameter is often expressed normalized by the Boltzmann's constant. From Figure III-3, we can observe that reported Zr-rich Zr-Co-Al and Zr-Ni-Al have the highest mismatch entropies, up to 0.2. Zr-Cu-Al exhibits mismatch entropies between 0.1 and 0.15 while Zr-Fe-Al has the lowest mismatch entropy values, below 0.1.

Combining the chemical parameter (mixing enthalpy) and the topological parameter (mismatch entropy) we can understand GFA differences among these four ternary systems. On the one hand, Zr-Cu-Al and Zr-Fe-Al exhibit lower GFA, which can be attributed to their higher mixing enthalpy and lower mismatch entropy. In addition, the Zr-Cu-Al ternary base exhibit very low corrosion resistance [220], which is very detrimental for biomedical applications. On the other hand, Zr-Co-Al and Zr-Ni-Al have the largest D_c (up to 18 mm for $Zr_{56}Co_{28}Al_{16}$ [176]), which is coherent with their largely negative mixing enthalpy and their rather high mismatch entropy. The Zr-Co-Al ternary base was chosen as the glass-forming base of this study. This base also has the advantage of being Ni-free, as Ni is a common allergen. In the next section, the Zr-Co-Al ternary base will be reviewed in light of the available literature to converge to the composition that will be used as the base of our study. Also, along with this introductive part, we have shown that there exist major differences between the Zr-based ternary BMG, depending on the TM used. We will be discussing these differences by regularly comparing the results obtained on the Zr-Co-Al elaborated in this work with results on the Zr-Cu-Al ternary base gathered in the literature. This will help us to better grasp the specific role of the cobalt in the Zr-Co-Al ternary base.

III.1.2. Overview of the Zr-Co-Al base

The Zr-Co-Al ternary base for bulk metallic glass formation was first introduced by T. Zhang and A. Inoue in 2002[202]. From this point, increasing work has been published on the subject and research on this specific base is still ongoing [161, 162, 212, 221]. The influence of the Zr/Co ratio, as well as the Al/Co ratio on glass-forming ability and mechanical properties, were studied [222]. Increasing the Zr/Co ratio appears to reduce Tg and increase plasticity and glass-forming ability [205]. Looking at thermal stability, Zr-Co-Al ternary alloys are quite particular as most of the explored compositions exhibit two intense exothermic peaks in the DSC measurement. They are usually associated with structural transformation, such as crystallization. To the best of our knowledge, the presence of two peaks is rarely observed for other Zr-based ternary bulk metallic glasses and the presence of two distinct transformation events, for Zr-Co-Al alloys, which are composition dependant, is not discussed in the literature. Moreover, an increase of the Al/Co ratio reduces the gap between the two transformation events, as illustrated in Figure III-4 [222]. As T_g is barely changing, ΔT increases. While the first exothermic peak appears at higher temperatures with increasing Al/Co ratio, the second exothermic peak shifts toward lower temperatures. With further reducing the Al/Co ratio, one can even see the two peaks merge into one. A lowering of the gap between the two exothermic events has also been observed while decreasing the Zr/Co ratio [202, 205, 223]. The same behaviour is observed while lowering the Zr/Al ratio [212]. It seems that reducing the Al content favours the increase of the temperature gap between the two exothermic peaks. This is interesting as the Zr-Cu-Al glass formers with lower Al content usually exhibit only one exothermic peak [124, 195, 201]. These changes in the crystallisation dynamics of the alloys must be related to their structure stability, but no dedicated study completely explains this phenomenon to the best of our knowledge.

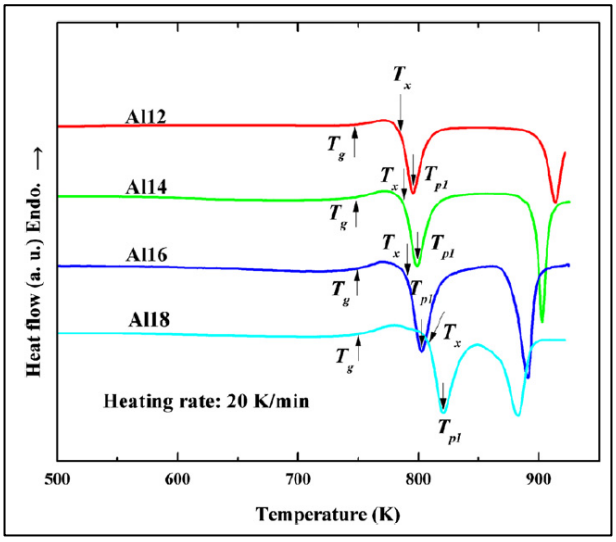

Figure III-4: DSC curves for several Al/Co ratio for the $Zr_{56}Co_{44-x}Al_x$ alloy. Increasing Al at% results in the reduction of the temperature gap between the two exothermic peaks. [222]

Among all compositions reported, $Zr_{56}Co_{28}Al_{16}$ [176] and $Zr_{55}Co_{25}Al_{20}$ appear as the two most promising for several reasons. Firstly, because of their glass-forming ability, with critical diameters reported being respectively 18 mm and 10 mm. Secondly, the two alloys also exhibit yield stress around 1900 MPa. Unfortunately, $Zr_{55}Co_{25}Al_{20}$ possesses very limited plasticity (<1 %) according to the literature. As this parameter is critical for the application, $Zr_{56}Co_{28}Al_{16}$ has been chosen for this study.

In the following sections of this chapter, we will be reviewing the $Zr_{56}Co_{28}Al_{16}$ properties having in mind the requirements of the biomedical field. We will also see how the alloy processed in this work compares to reported data available in the literature. We will try to have a critical discussion of glass properties' variability. Finally, we discuss links between the observed properties and the glass atomic structure.

III.2. Processing and characterisation of the $Zr_{56}Co_{28}Al_{16}$ BMG

III.2.1. Processing of the $Zr_{56}Co_{28}Al_{16}$ and influence of the casting method

We started by processing the $Zr_{56}Co_{28}Al_{16}$ using arc melting and suction casting, which is the usual set-up used to produce samples for experimental purposes. SIMaP laboratory produces bulk metallic glasses using arc melting and suction casting, as explained in Chapter II. Vulkam Inc. developed an injection casting process also described in Chapter II. Suction casting can present several issues, such as a lack of conformation (quality of contact between the melt and the mould), porosities due to chaotic flow, or surface crystallization [224, 225]. Samples are systematically checked for porosities and samples containing porosities are systematically discarded. Conformation should also be mastered to ensure industrial production. Good conformation is mandatory to produce near-net-shape parts.

Figure III-5 (a) and (b) shows the XRD patterns for as-cast $Zr_{56}Co_{28}Al_{16}$ and the optical image of the cross-section of a sample processed by suction casting. From this, we see that a part produced via suction casting exhibit crystallization when studied as-cast, as the XRD pattern shows intense, sharp peaks. The observed peaks correspond to two phases, the ZrCo and Zr_6CoAl_2, which are usually identified in Zr-Co-Al crystallized alloys. The crystallized layer is observed in optical imaging.

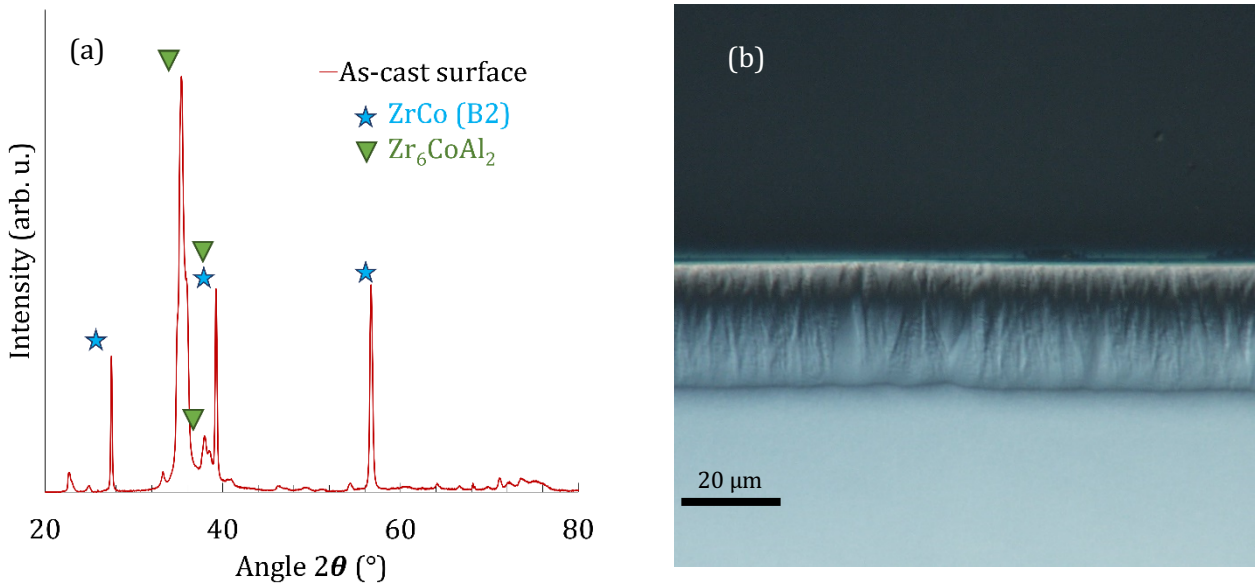

Figure III-5: (a) XRD pattern for as-cast $Zr_{56}Co_{28}Al_{16}$ and (b) optical image of the cross-section near edge the same $Zr_{56}Co_{28}Al_{16}$ part produced via suction casting. The as-cast surface shows clear signs of crystallization (intense, sharps peaks).

But by removing approximately 40 µm of the outer surface, we see that the glass underneath is amorphous as no more peaks are observed on the diffraction pattern in Figure III-6. This means in this case that crystallization is only localized on the surface of the produced part.

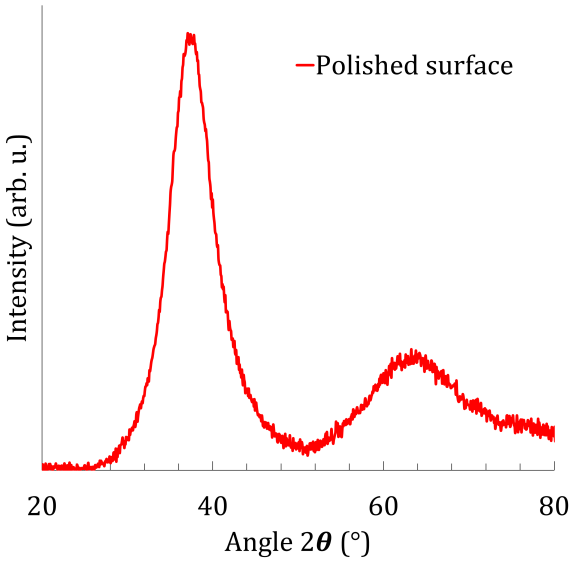

Figure III-6: XRD pattern of a $Zr_{56}Co_{28}Al_{16}$ after removing crystallized outer layer.

Surface crystallisation is often overlooked in published works focusing on corrosion resistance, where samples are simply polished before corrosion testing [170]. We showed that surface crystallization deteriorates corrosion resistance, which is a key property for biomedical applications [226]. We investigated the origin of surface crystallization, which appears as counterintuitive as surface sample surface is where the highest cooling rates are achieved. By systematic testing, we refuted any other possible causes such as pollution from the injection chamber environment, pollution from mould material or mould temperature. We demonstrated that surface crystallization in suction casting comes from a lack of conformation between the melt and the mould surfaces. For this reason, the injection casting process developed by Vulkam Inc. suppresses surface crystallization. All these findings are grouped up and detailed in the published article, available in the supplementary material E. This result is important for further work on the industrialisation of casting and micro-casting of BMG parts. It is of great importance to be able to cast near net shape parts with an excellent surface finish. It would be a big step forward on the path to bringing BMGs to the market. The importance of conformation also needs to be considered when casting complex shapes, for which the level of conformation may vary depending on the geometry.

We performed transmission electron microscopy (TEM) imaging on our alloy as cast, to validate the amorphous nature at a smaller scale. Figure III-7 shows a TEM bright-field image acquired on our $Zr_{56}Co_{28}Al_{16}$ glass in the as-cast state. The absence of contrast in the image confirms the absence of signs of crystallization. Moreover, the diffraction pattern acquired on the same sample is not showing any

diffraction peaks (represented as dots). This confirms that the glass elaborated can be considered as fully amorphous in the as-cast state.

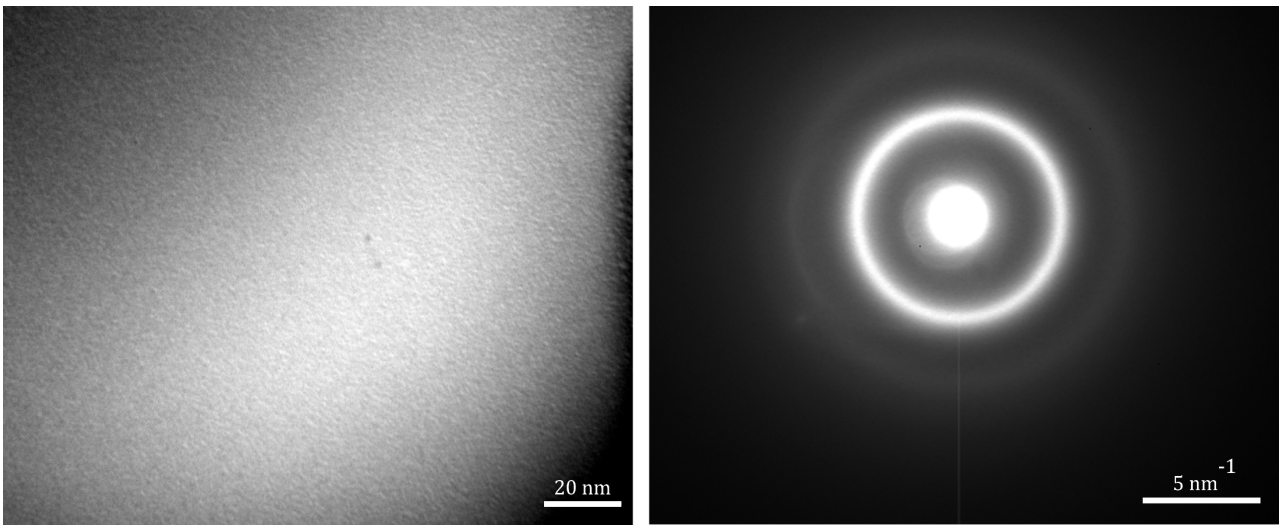

Figure III-7: TEM bright field image of the as-cast $Zr_{56}Co_{28}Al_{16}$ and the associated diffraction pattern.

Based on the XRD measurements, we did not measure differences among the several geometries that were processed, either by suction casting or injection casting.

III.2.2. Thermal stability of the $Zr_{56}Co_{28}Al_{16}$ processed at SIMaP Laboratory

Characteristic temperatures are measured through DSC experiment at 20 K/min up to 970 K (for relaxation, Tg, Tx and Tp). Figure III-8 shows the DSC curve for a sample of BMG cut from a 5mm diameter rod. On the acquired signal, the glass transition (endothermic) along with the two characteristic transformation/crystallisation events (exothermic) mentioned earlier can be seen. Tg is measured at 751 K, which is close to values reported in the literature (Table III-2). The onset of transformation is measured at 784 K and the two exothermic events respectively at 796 K and 880 K.

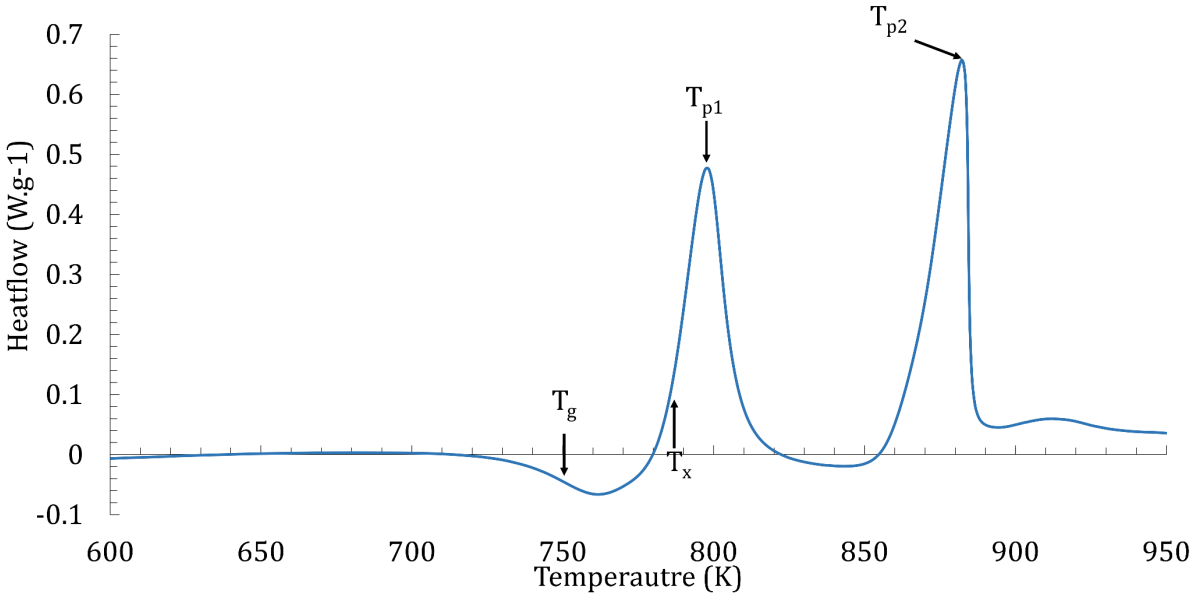

Figure III-8: DSC curve of a 5-mm diameter rod of $Zr_{56}Co_{28}Al_{16}$ BMGs alloy.

Heating rate (K/min)	T_g	T_x	T_{p1}	T_{p2}	T_m	T_l	ΔT_x	T_g/T_m	T_{rg}	γ	ΔT_l	ΔT_g	Ref.
5	745	770	783	862	-	-	25	-	-	-	-	-	This work
5 (DTA)	-	-			1210	1270	-	0.616	0.587	0.382	500	525	
20	751	784	795	878	-	-	33	-	-	-	-	-	This work
20	749	791	803	891	-	-	42	-	-	-	-	-	[18]
20	749	794	806	888	-	-	45	-	-	-	-	-	[214]
20	738	793	-	-	-	-	55	-	-	-	-	-	[206]
20	743	792	-	-	1191	1258	49	-	0.591	0.396	466	515	[205]
20	760	810	-	-	1226	1247	50		0.609	0.403	437	487	[227]
20	753	802	818	878	-	-	49	-	-	-	-	-	[228]
20	753	797	-	-	-	1208	44	-	0.623	0.406	411	455	[176]

Table III-2: Characteristic temperature (in K) for $Zr_{56}Co_{28}Al_{16}$ alloy measured in this work via DSC and values from the literature. The GFA-assessment parameters are detailed in Chapter I.1.2.2 except $\Delta T_l = T_l - T_x$ and $\Delta T_g = T_l - T_g$.

It appears that the measured temperature for the glass transition agrees with values from the literature, fluctuating around 750 K. It is interesting to note that values are ranging from 738 K to 760 K, implying a delta of 22 K, which is consequent. This could come from the position chosen for T_g measurement. T_g variations could also come from the way the alloy is produced. We chose the inflexion point of the endothermic event as this is the only value that is not influenced by the user. The way T_g is measured and if the onset of the inflexion point is chosen is rarely detailed in the literature. The measured crystallisation temperature (onset of the first exothermic transformation event) is measured at 784 K which is slightly lower than values reported in the literature (ranging from 791 to 810 K). This results in a lower measured ΔT_x of 33 K, while other reported ΔT_x ranges from 45 to 55 K. This offset of around 10 K is also measured on the peak position of the two intense exothermic events.

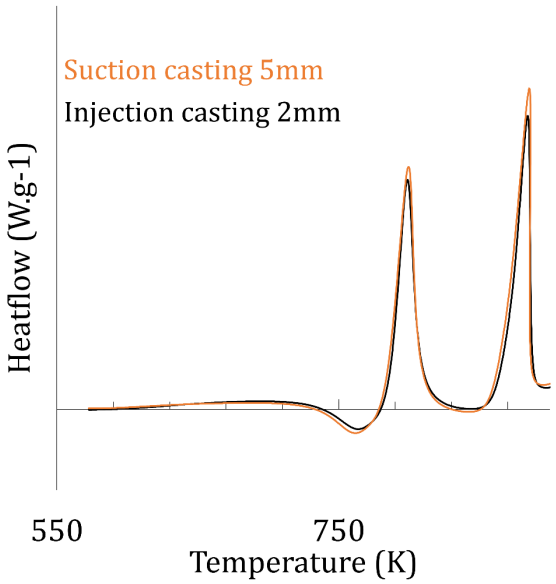

Figure III-9: DSC curves acquired on 2-mm diameter sample (injection casting) and 5-mm diameter sample (suction casting).

We can infer that depending on the processing techniques, the melt dynamic could be different, influencing the glass-forming ability. Therefore, from one setup to another, parameters like T_{rg} or ΔT_x can vary. Between several casting geometries, it is interesting to mention that we do not observe variations in characteristic temperatures between geometries. Figure III-9 shows two DSC curves acquired on one sample cast as a 2-mm diameter rod (injection casting) and on one sample cast as a 5-mm diameter rod (suction casting). Once again here we highlight the presence of two intense exothermic events.

Figure III-10 (a) shows the XRD diffraction patterns of a sample of $Zr_{56}Co_{28}Al_{16}$ heat-treated at 850 K (between the two crystallization peaks). The XRD pattern exhibits no intense and sharp peaks, as observed for amorphous materials. One can however observe a small peak around 40°. The absence of significant signs of crystallization after the first exothermic peak is unusual and was not reported in the literature. It is very different from what was reported by Chen *et al.* who annealed the $Zr_{56}Co_{28}Al_{16}$ at 853 K (no holding time) and observed peaks in the XRD patterns, as shown in Figure III-10 (b) [161].

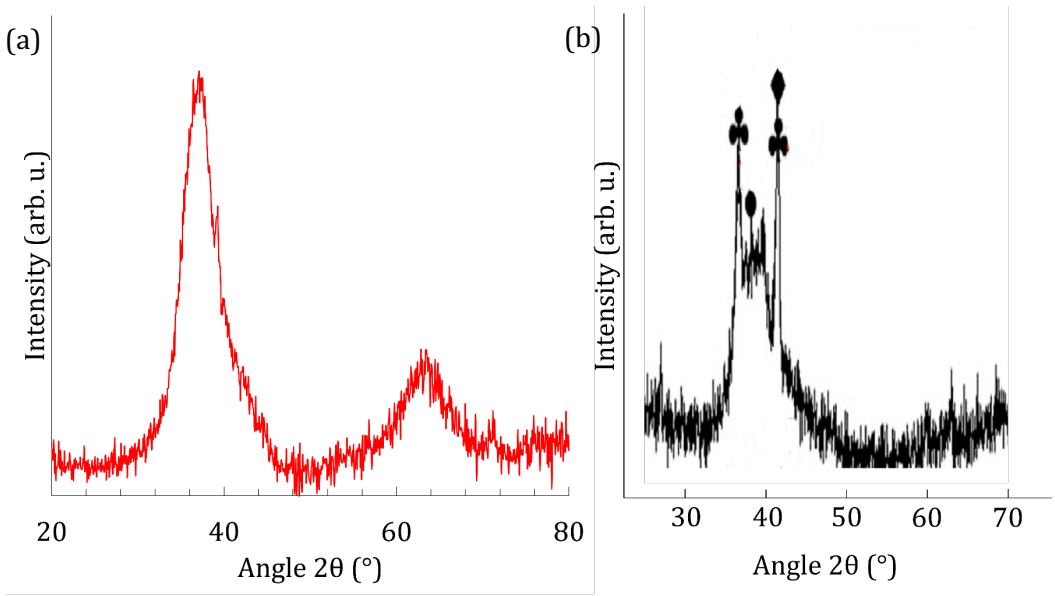

Figure III-10: XRD measurements of (a) a $Zr_{56}Co_{28}Al_{16}$ sample processed at SIMaP and annealed at 850 K and (b) same alloy and same annealing procedure but from Chen *et al. [161]*

TEM was used for further investigation as shown in Figure III-11. TEM bright-field image shows some darks dots, but no diffraction spots can be observed on the associated diffraction pattern. We attribute the first exothermic peak to a reorganisation of the glass structure more than a strong crystallization event. If there is no crystallisation during the first exothermic peak, we could then argue that ΔT is far greater than first thought.

This reinforces this idea that the $Zr_{56}Co_{28}Al_{16}$ that we process is particular and should be studied. A second thesis dedicated to the thermoplastic forming of the Zr-Co-Al and the study of its thermal stability is currently undergoing at the SIMaP laboratory. After heating above the second exothermic

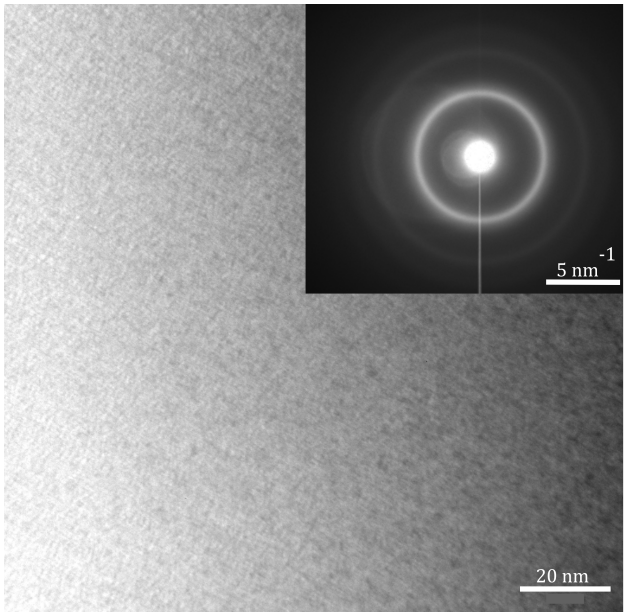

Figure III-11: TEM bright field and diffraction pattern for the $Zr_{56}Co_{28}Al_{16}$ alloy processed at SIMaP and heat treated for 0min at 853K.

event (975 K), intense, sharp peaks are observed with XRD measurement, revealing the fully crystalline nature of the alloy (see Figure III-12). Among the observable phases, we can mention Zr_6CoAl_2, ZrCo (B2) and ZrCoAl. These phases were identified based on the angles matching with available data from the literature on the Zr-Co-Al (more details on the identification process are available in supplementary material F). These three phases have been already reported after crystallization of the $Zr_{56}Co_{28}Al_{16}$ [162].

Note that phase formation upon crystallisation strongly depends on the heating rate as suggested in several publications [162]. Phase formation is also related to the alloy composition. It has been identified that ZrCo (B2) phase formation is promoted by low Al content [161, 162]. This could explain why Zr-Cu-Al ternary alloys are more prone to form the B2 ZrCu phase upon crystallization, as we recall from earlier that they have lower aluminium content. Interestingly, we also note that we observe the

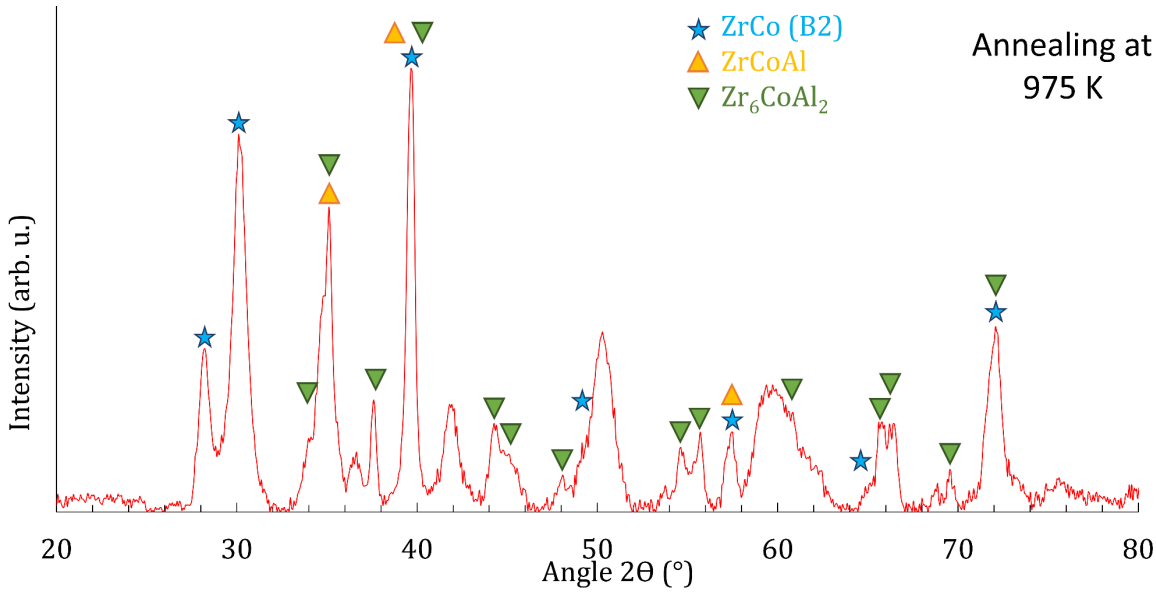

Figure III-12: XRD measurement of a $Zr_{56}Co_{28}Al_{16}$ sample after annealing up to 975 K.

presence of the ZrCoAl phase, which was not detected in the surface crystallization. This could be an insight into the crystallisation sequence. We could think that ZrCo and Zr_6CoAl_2 are crystallized first and then ZrCoAl.

For melting temperature and liquidus temperature, differential thermal analysis (DTA) was used, up to 1370 K as shown in Figure III-13. We were not able to use the DSC set-up as its temperature is limited in achievable temperature at 950 K. DTA analysis shows a first endothermic event around 1185 K, which could correspond to the solidus, or in other words the first drop of liquid forming. There is a much stronger event at 1210 K, indicating complex fusion. The liquidus is located at the invariant at 1270 K (complete solid to liquid transformation, a transition from a two-phase domain to a single-phase domain). From these measurements, usual GFA-assessment parameters (see Chapter I.1.2.2) can be calculated and are shown in Table III-2. We also compare our measured characteristic temperatures to values reported in the literature for the same alloy at the same heating rate. Fewer data are available for liquidus and melting temperature. We appear to be in the same range, as published T_m and T_l range from 1191 to 1226 K and from 1208 to 1258 K respectively.

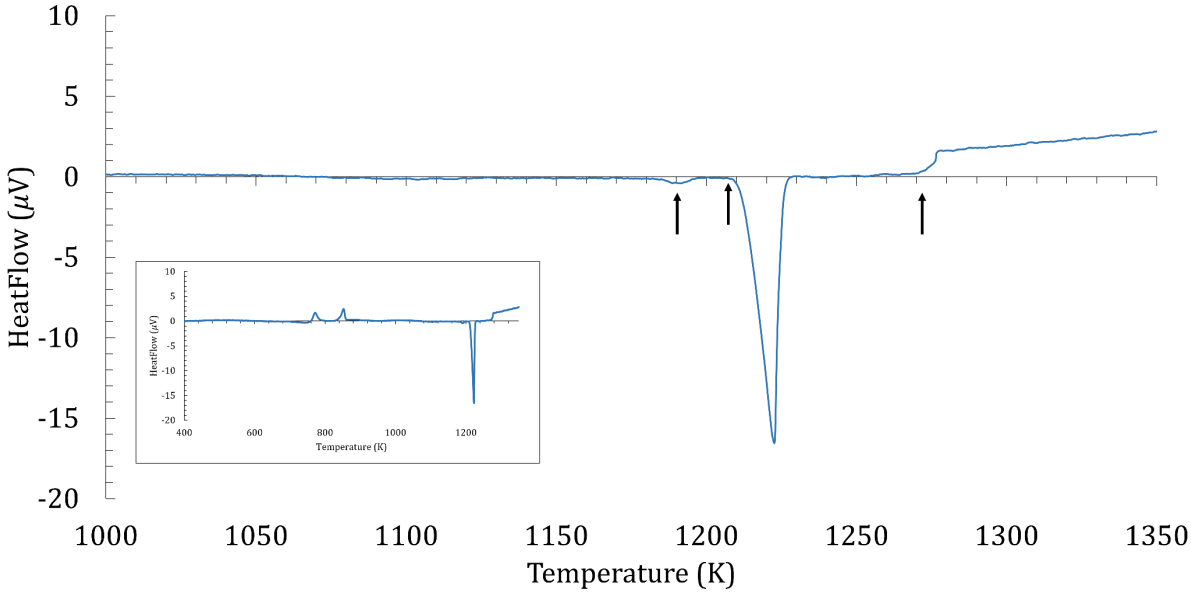

Figure III-13: DTA measurement from a $Zr_{56}Co_{28}Al_{16}$ at 5 K/min. The inset shows the entire scan, from 400 to 1400 K.

Looking at parameters used to assess GFA, we first note that we have a slightly lower T_{rg}. This could be explained by the fact that we have the highest reported T_l. This also applies to the calculated value of γ which is lower than those reported in the literature, as we have a lower T_x together with a higher T_l. We should remind that Surayanarayana *et al.* [27] published a critical analysis of those GFA parameters in 2009, showing a low correlation between calculated parameters and measured experimental D_c for Zr-based metallic glasses ($R^2 < 0.022$). This analysis is detailed in Chapter I (see I.1.2.2). To illustrate this specifically on the Zr-Co-Al base, we can refer to Wada *et al.* work [176] where

they calculated γ and measured critical diameters for several compositions. The alloy with the highest D_c (18mm) is the $Zr_{56}Co_{28}Al_{16}$ with a reported γ of 0.406. The $Zr_{55}Co_{25}Al_{20}$ and $Zr_{58}Al_{14}Co_{28}$ compositions have D_c respectively of 10 and 15 mm but γ of respectively 0.414 and 0.398. From Surayanarayana *et al.* [27] the only reliable correlation seems to be between high GFA, low liquidus temperature and high T_{rg}. Those parameters should be considered for a practical evaluation of characteristic temperatures rather than a reliable evaluation of the GFA. Looking at other systems, we note that Zr-Cu-Al amorphous alloys have also T_{rg} around 0.6. The glass transition temperature is on average lower than for Zr-Co-Al alloys with values ranging from 670 to 720 K [195, 229]. Accordingly, T_l values are also lower which gives a similar T_{rg} value.

Figure III-14 shows the DSC curves acquired on the $Zr_{56}Co_{28}Al_{16}$ at several heating rates. Specific temperatures at all the measured heating rates are summed up in Table III-3. When increasing the heating rate, one is expecting to see all characteristic temperatures shift toward higher temperatures, as these values represent thermally activated processes [212].

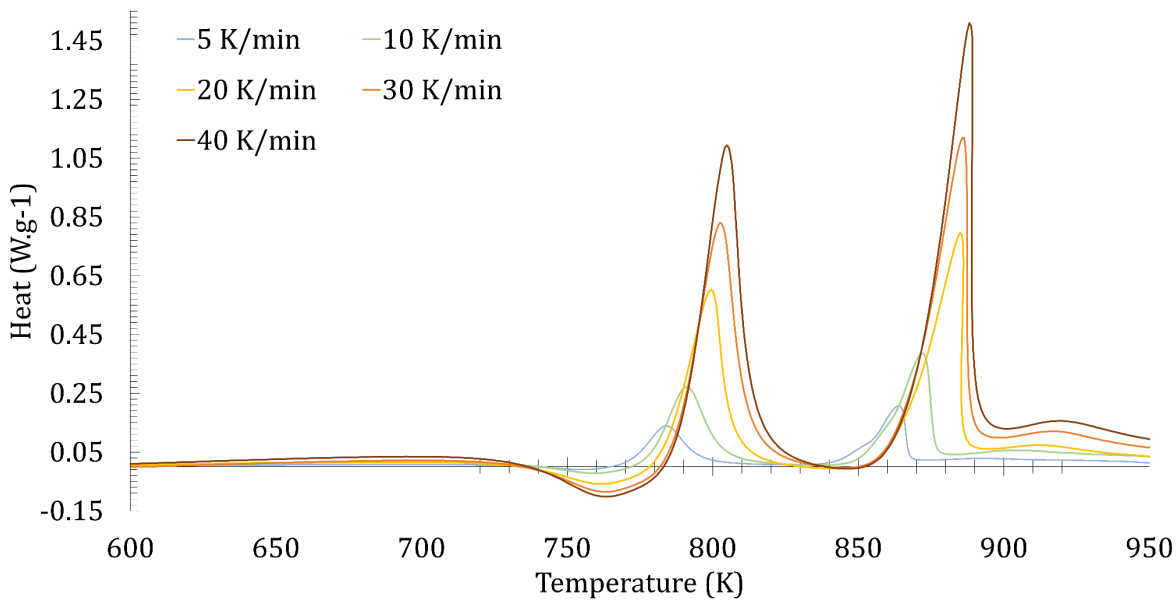

Figure III-14: DSC curves acquired at several heating rates (5, 10, 20, 30 and 40 K/min) for $Zr_{56}Co_{28}Al_{16}$ BMG.

The glass transition does not seem to be very sensitive to the heating rate in our case, as opposed to data reported in the literature (see Table III-3). From heating rates of 10 K/min to 40 K/min, T_g remains at 750K. This observation is rather striking. Measures were repeated several times for each heating rate and two different methods were used for the identification of the glass transition temperature (onset and inflexion point). Samples mass was kept low (between 10 and 15 mg as advised after discussion with the DSC manufacturer) while samples contact surface was kept maximum to limit as much as possible inertia hiding temperature shifts.

Heating rate	T_g	T_x	T_{p1}	T_{p2}	ΔT	Ref.
5	745	770	783	862	25	This work
10	750	777	790	869	27	
20	751	784	795	878	33	
30	751	787	798	880	36	
40	750	788	800	880	38	
5	730	775	785	870	45	Tan *et al.* 2011 [18]
10	741	787	798	884	46	
20	749	791	803	891	42	
40	762	810	820	909	48	
60	766	812	821	912	46	
10	745	790	806	865	45	Mohammadi Rahvard *et al.* 2018 [228]
20	753	802	818	878	49	
30	758	808	824	885	50	
40	763	812	831	892	49	

Table III-3: T_g, T_x, T_{p1}, T_{p2} and ΔT_x measured at several heating rates and data from the literature for comparison

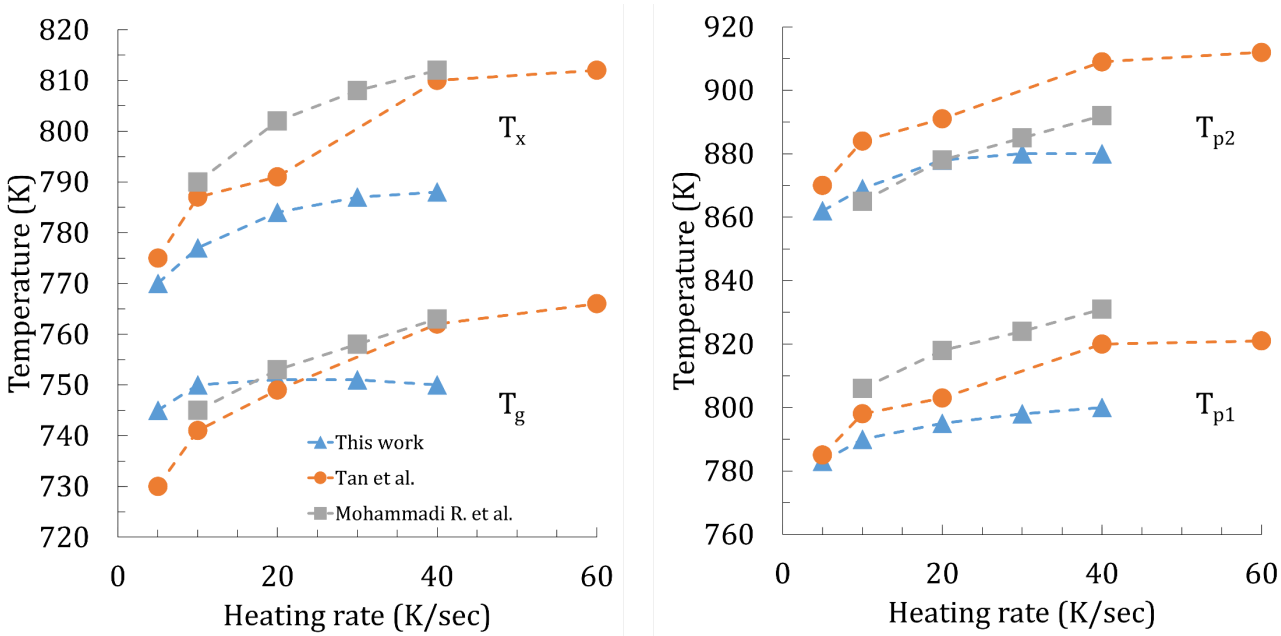

Figure III-15: Evolution of T_g, T_x, T_{p1} and T_{p2} measured during the DSC scans of the $Zr_{56}Co_{28}Al_{16}$ at several heating rates and data from the literature for comparison.

In other words, to activate a transformation process, the atoms need to receive a greater amount of energy than the binding energy of the bonds they share with surrounding atoms. This means that the higher the interaction between atoms is, the higher the activation energy will be. Activations energies of the glass transition (E_g), the onset of crystallisation (E_x), the transformation event (E_{p1}) and the second transformation event (E_{p2}) can be calculated by performing a DSC experiment at several heating rates (Figure III-14) and applying Kissinger equation[230]:

$$ln\left(\frac{\Phi}{T^2}\right) = \left(\frac{E}{RT}\right) + C_1$$

III-2

where Φ is the heating rate in K.min^{-1}, T is the studied characteristic temperature, E is the related activation energy, R is the gas constant (8.314 J.mol^{-1}.K^{-1}) and C_1 is a constant. By plotting $ln\left(\frac{\Phi}{T^2}\right)$ as a function of 1/T, the activations energies can be graphically extracted. Kissinger's plots are represented in Figure III-16 with a linear fitting equation for each transformation.

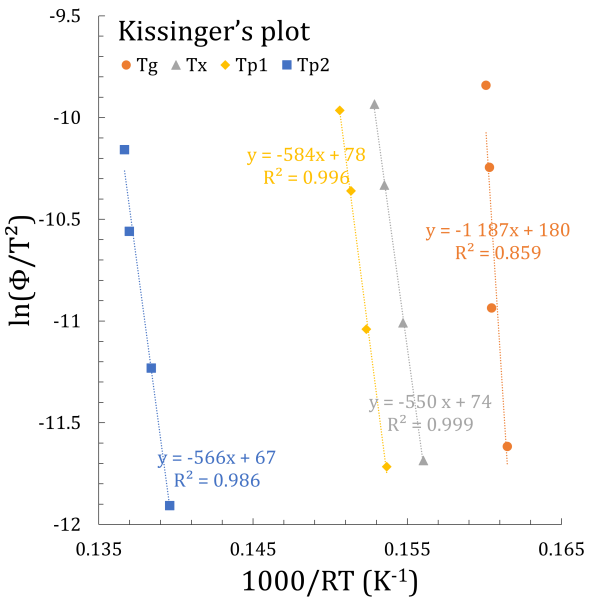

Figure III-16: Kissinger's plots for calculation of activation energies for $Zr_{56}Co_{28}Al_{16}$ BMG.

Fitting of the several T_g temperatures exhibits the lowest R^2 (0.859). The fitting is much more accurate for T_x, T_{p1} and T_{p2} (always above 0.985). All results along with correlation factors are reported in Table III-4, as well as data from the literature for comparison on $Zr_{56}Co_{28}Al_{16}$ and other alloys. The glass transition of our alloy exhibits the highest activation energy. The calculated activation energies of 1187 kJ.mol^{-1} are impressively high and were not reported in the literature. Activations energies E_x, E_{p1} and E_{p2} for our $Zr_{56}Co_{28}Al_{16}$ alloy are calculated to be respectively 550, 584 and 566 kJ.mol^{-1}. Mohammadi Rahvard *et al.* did report that the glass transition has the highest activation energy among all transformations but reported activation energy of 356 kJ.mol^{-1} with Kissinger's method. Interestingly, Dong *et al.* also reported recently high activation energy for Zr-Co-Al BMGs and mainly activation energy of 923 kJ.mol^{-1} for the glass transition of a $Zr_{52}Co_{25}Al_{23}$ amorphous alloy.

From every data available for $Zr_{56}Co_{28}Al_{16}$, we always find Eg > Ex, Ep1 and Ep2. From data available in Table III-4, we show that the tendency for the higher activation energy of the glass transition over the other transformation processes is also true for Zr-Cu-Al BMGs. Data reported for the $Zr_{48}Cu_{48}Al_4$ show an activation energy of 531 kJ/mol for the glass transition and activation energy of 340 kJ/mol for the start of the crystallization.

	E_g	E_x	E_{p1}	E_{p2}	Ref	Alloy
A.E. (kJ/mol)	1187	550	584	566	This work	$Zr_{56}Co_{28}Al_{16}$
R^2	*0.859*	*0.999*	*0.996*	*0.986*		
A.E. (kJ/mol)	356 ± 20	313 ± 15	301 ± 15	319 ± 11	[228]	$Zr_{56}Co_{28}Al_{16}$
A.E. (kJ/mol)	303	316	336	362	[18]	$Zr_{56}Co_{28}Al_{16}$
A.E. (kJ/mol)	340 ± 3	305 ± 8	287 ± 10	-	[161]	$Zr_{56}Co_{28}Al_{16}$
A.E. (kJ/mol)	923 ± 83	352 ± 13	407 ± 13	-	[212]	$Zr_{52}Co_{25}Al_{23}$
A.E. (kJ/mol)	779 ± 102	313 ± 18	322 ± 16	-	[212]	$Zr_{55}Co_{25}Al_{20}$
A.E. (kJ/mol)	531	340	310	-	[231]	$Zr_{48}Cu_{48}Al_4$
A.E. (kJ/mol)	465 ± 7	264 ± 2	270 ± 1	-	[232]	$Zr_{48}Cu_{43}Al_9$

Table III-4: Activation energies derived from Kissinger's equation for $Zr_{56}Co_{28}Al_{16}$ and data collected from the literature for comparison.

From this study, we highlight that the glass transition temperature, and to a lower extent the other characteristic temperatures, appear to be very stable. This stability is characterized by the low dependency on the heating rate. This is unusual and contrasts with data reported on the same composition in the literature. Also, it does not exhibit any signs of crystallization after the first exothermic peak. All these findings suggest the conclusion that this glass possesses a quite specific structure. For some reason, that may be related to the processing, our glass seems different from the other $Zr_{56}Co_{28}Al_{16}$ reported in the literature. This specific behaviour could influence its properties (biocompatibility but also mechanical resistance). Its pronounced stability upon heating makes it an interesting candidate for thermoforming (even though its supercooled liquid region seems rather narrow) and it is studied currently for such applications at SIMaP laboratory.

III.2.3. Biocompatibility investigation

As seen from the literature (Chapter I, section I.4), BMGs are very appealing candidates for biomedical applications. Yet the biocompatibility of alloys needs to be systematically assessed to ensure good performances. In this section, proofs of concept on the biocompatibility of our $Zr_{56}Co_{28}Al_{16}$ BMG are given through several tests generally performed before cytotoxicity and other biological assessments. Corrosion resistance may be the first step in assessing the potential of a given material for biomedical application. In this work, we designed our protocol based on the ISO standard 10271:2011 (now replaced by the ISO 10271:2020). Accordingly, the long-term corrosion behaviour was based on the same ISO standard. This section is thought to give an overview of the alloy capabilities in terms of biocompatibility and not be a deep dive into the complex mechanisms involved in the corrosion of BMGs (which are to be further studied). A discussion is proposed on the biocompatibility of the $Zr_{56}Co_{28}Al_{16}$.

III.2.3.1. Corrosion behaviour

Open circuit potential (OCP) measurements and cyclic-polarisation measurements were performed on the $Zr_{56}Co_{28}Al_{16}$ BMG. The OCP was measured after 24 hours of immersion at -0.195 ± 0.051 V *vs.* Reference (Ag/AgCl). After 24 hours of immersion, the samples exhibited no signs of pitting on their

surfaces. For comparison, the $Zr_{46}Ti_2Cu_{45}Al_7$ BMG was reported to exhibit many pits at its surface after 24h of immersion in 0.6M NaCl aqueous solution [220]. This apparent absence of damage on our alloy surface after 24h is a sign of its ability to be spontaneously passivated in chloride solution.

Figure III-17 illustrates four cyclic-polarisation measurements performed on our alloy. Several tests were performed to ensure reproducibility. During polarisation, all samples exhibited a distinctive passivation region (see Chapter I.4.1 for more details on the cyclic polarization curves). Passivation current i_{pass} and corrosion potential E_{corr} are measured respectively around $5x10^{-5}$ mA.cm^{-2} and -0.2 V vs Ag/AgCl. For our $Zr_{56}Co_{28}Al_{16}$ alloy, the pitting potential E_{pit} was measured at 0.186 ± 0.030 V vs Reference. E_{corr} is a little lower than the OCP, which is coherent with experimental conditions (24h of immersion and a scan from cathodic potential to anodic potential). This result is also consistent with the absence of pitting signs after immersion and confirms the ability of the material to be spontaneously passivated. E_{pit} is greater than the corrosion potential E_{corr}, approximately by 0.386 V. This corresponds to the width of the passivation plateau observed on the cyclic polarisation curve. On this plateau, stable pitting can not take place, metastable pitting may occur but the glass can repair its passive film.

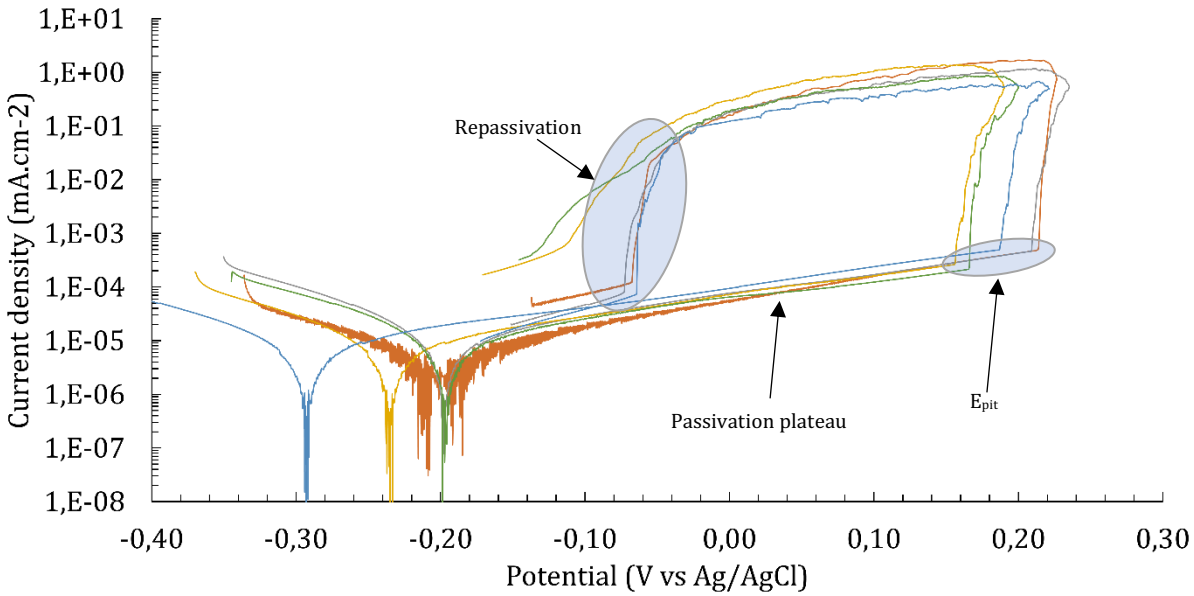

Figure III-17: Polarization curves of $Zr_{56}Co_{28}Al_{16}$ in NaCl electrolyte at 310 K.

Above E_{pit}, pits can reach a state of stable growth. Once the current density reaches 1 mA.cm^{-2}, scan direction was reversed to explore the alloy re-passivation ability which has never been reported in the literature for this specific composition to the best of our knowledge. Re-passivation is observed with lowering the potential (E_{pp}) at a value of -0.075 ± 0.031 V vs Ref. E_{pp} is superior to E_{corr} by approximately 0.125 V. Under $E_{pp,}$ neither metastable nor stable pitting can happen. Between E_{pp} and E_{pit}, metastable pitting can happen, and pre-existing pits can propagate. This result is a marker of the ability of our glass to passivate.

For comparison, one can mention $Zr_{52}Cu_{48}$, which exhibit no detectable passivation in saline solution [233], as well as $Zr_{46}Ti_2Cu_{45}Al_7$ [220]. Conversely, $Zr_{61}Ti_2Cu_{25}Al_{12}$ is reported to exhibit a passivation plateau in saline solution, but at a lower extent than $Zr_{55}Ti_2Co_{28}Al_{16}$ [220]. Figure III-18 shows the polarisation curve of Zr-Cu and Zr-Cu-Ag metallic glasses in saline solution at body temperature (from ref [233]). They do not exhibit any passivation plateau. This highlights the role of the late transition metal in the corrosion behaviour of Zr-TM-Al BMGs in saline solutions.

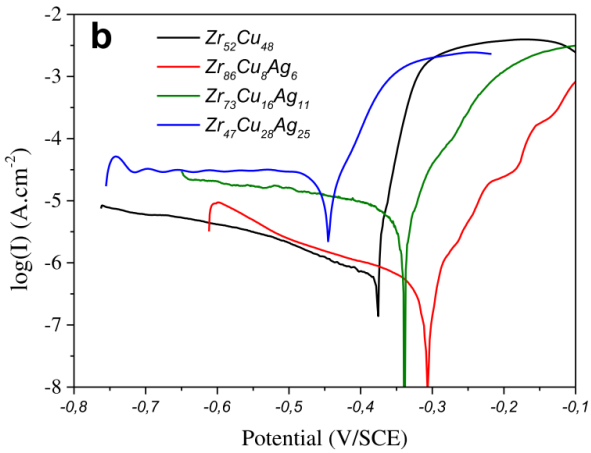

Figure III-18: Polarization curves of the $Zr_{52}Cu_{46}$ and other Zr-Cu-Ag MG in saline solution (0.9% NaCl) [233].

The study of the morphology of the pitting sites can also give valuable information on the pitting mechanism. Figure III-19 shows SEM images of the pitting sites on the $Zr_{56}Co_{28}Al_{16}$ surface.

Appearance inside the pits is lamellar-like, which shows that the pit grew via delamination of the pit surface. Comparable morphologies were observed inside the pits grown on Zr-Ti-Ni-Al and Zr-Ti-Co-Al BMGs [220]. However, the Zr-Ti-Cu-Al pits morphology is more honeycomb-like, with the presence of fine, micro-porous architecture. This is usually a type of morphology observed when a selective dealloying process occurs within the pit. To illustrate this morphology on Cu-bearing BMGs, Figure III-20 is an SEM image showing the pit morphology of a $Zr_{65}Cu_{17.5}Al_{7.5}Ni_8Co_2$ subjected to polarisation in 3.5% NaCl solution exposed to air [170]. Site 3 in Figure III-20 highlights the micro-porous microstructure

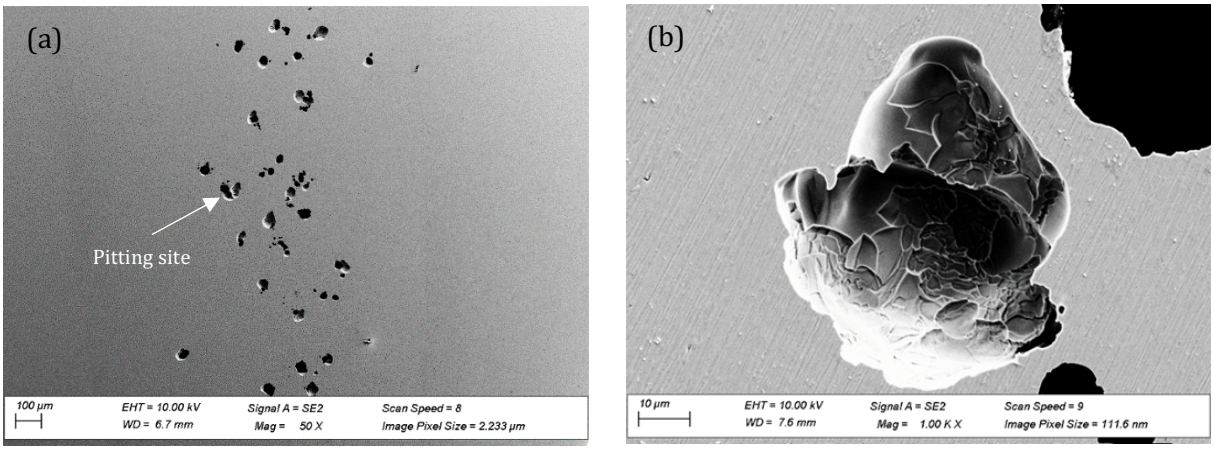

Figure III-19: SEM imaging of the pitting sites at (a) low magnification and (b) high magnification on a $Zr_{56}Co_{28}Al_{16}$ subjected to polarization testing.

resulting from selective dealloying. Chemical composition measurements revealed that this region is twice as less concentrated in Zr than the rest of the matrix and five times less concentrated in Al. We have seen in Chapter I.4.1. that the passivation film of Zr-based BMGs was mainly composed of Zr- and Al-oxides. Yet, Li *et al.* showed that the transition metal has a strong influence on corrosion resistance [220]. Even though the passive films for a Zr-Ni-Ti-Al (similar behaviour to Zr-Co-Ti-Al) and Zr-Cu-Ti-Al are very similar (thickness, kinetic…), the Cu-bearing alloy exhibits a lower corrosion resistance. Pitting initiation could be more favourable with Cu-bearing alloys than Co-bearing alloys. During immersion, in both cases, chloride ions will migrate through the passive film and destabilize it. Once they reach the surface, they will encounter Cu-rich or Co-rich zones, as these elements are less consumed by the passive film than Zr and Al. Generally, Cu-rich zones are more prone to occur. Indeed, as Cu is nobler and stable in 0.9 NaCl solution, Cu neither contribute to the passive film nor dissolve. Co, even if it doesn't participate in the passive film may dissolve at the first stage of passivation as well as Zr and Al. Moreover, Cu will more easily form complexes with Cl- than Co, as exhibited in the Pourbaix's diagrams calculated for Cl^- electrolytes at 0.15 M (see Figure III-21).

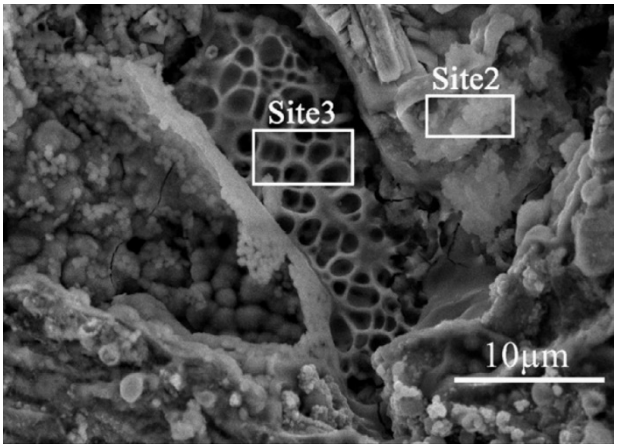

Figure III-20: SEM image of the pit morphology of a Zr-Cu-Al-Ni-Co BMG. Site 2 and 3 highlights corrosion products and micro-porous structure respectively [170].

The formation of these $CuCl_2^-$ complexes at the interface between the metal and the passive film will promote the passive film breakdown. From there, the passive film can be either grow again or pitting can start. Li *et al.* observed that Cu was more concentrated in the pits than in the matrix, unlike Co and Ni

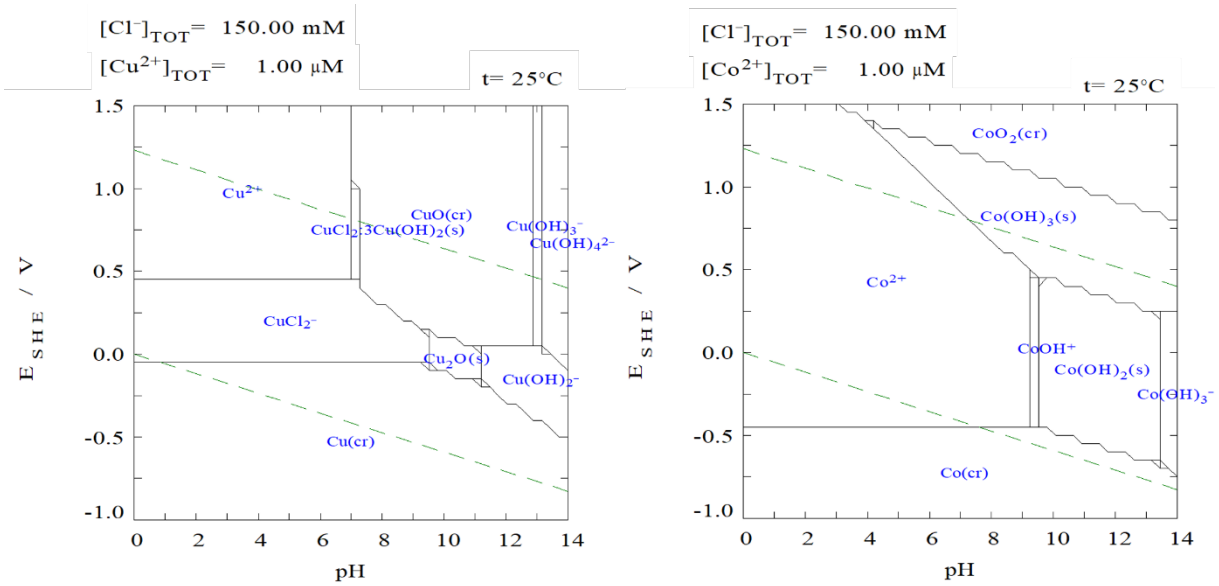

Figure III-21: Pourbaix's diagrams for Cu and Co in Cl^- electrolyte at 150 mM and 298 K (calculated with Hydra and Medusa softwares).

which were as concentrated in the matrix as in the pits. Li *et al.* revealed that Cu enrichment happens during pitting [220]. Because of its higher nobility, selective dissolution of the other constitutive elements happens, leaving Cu-rich zones around the pits. These Cu-rich zones are hardly passivated than the rest of the matrix as they can not form the Zr- and Al-oxides, the main constituent of the passive film. Moreover, as Cu is prone to form complexes with chloride, a salt film could be formed inside the pit, limiting the repassivation phenomenon. This favours stable over metastable pitting processes. Ni has a lesser nobility, which explains why Ni-rich zones are not detected in the paper of Li *et al.* [220]. The same mechanisms could apply with Co instead of Ni as the TM. Because Co has a lesser nobility than Cu, it can be dissolved in conditions that would not induce Cu dissolution. Figure III-22 illustrates the differences in pitting propagation behaviour between Zr-Cu-Al and Zr-Co-Al. It does not include the LTM enrichment under the passive film, as it should be similar for the two ternary glasses. This enrichment comes from the fact that the passive film (in both cases) is mainly composed of Zr and Al oxides.

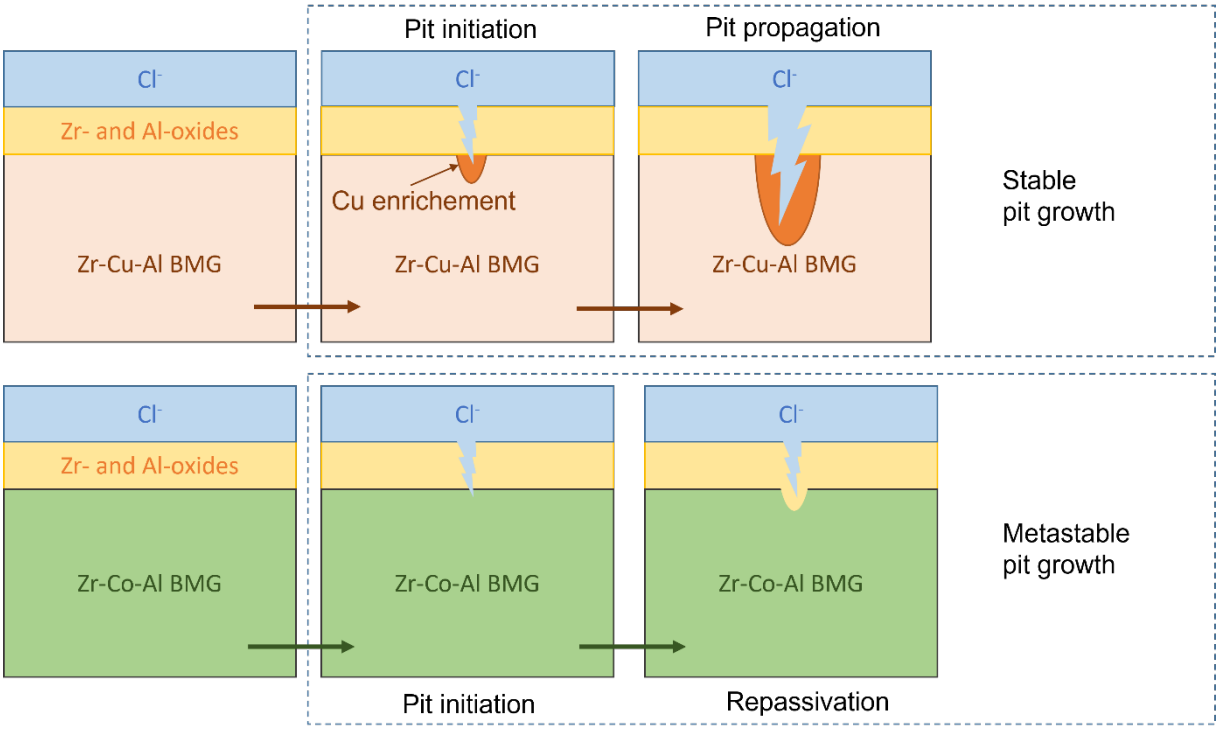

Figure III-22: Illustration of the pitting mechanisms difference between Zr-Cu-Al BMG and Zr-Co-Al BMG.

In this section, we demonstrated that the corrosion resistance of our alloy was very good. It exceeds the corrosion resistance of Cu-bearing ternary Zr-based alloys. To go further into the characterisation of the alloy biocompatibility, we will show and discuss the results of immersion testing in the next section.

III.2.3.2. Immersion tests

Testing of the polarisation resistance gives a good evaluation of the corrosion resistance of the alloy within a short time frame. It is of great interest to also study our material response when immersed

into a corrosive fluid (NaCl + lactic acid, see Chapter II) over an extended period. This fluid is more severe than the one used for polarisation testing. Such testing is particularly relevant when considering potential applications as long-term implants. No data were available in the literature for $Zr_{56}Co_{28}Al_{16}$ BMG static immersion resistance. ISO 10271:2011 proposes an immersion time of a full week (7 days). Based on the good results obtained with the polarisation tests, we choose to extend the immersion time to four weeks, by renewing the immersion solution every week (S1 to S4). In addition to the simple immersion testing of our material, we also perform coupling testing, where our BMG was immersed in contact with a standard material used in the biomedical industry (TA6V, CoCrW, 316L SS). By coupling two different materials with different free potentials, galvanic corrosion can occur. This is of particular interest when thinking of multi-material implants when several metallic materials are in contact. We first tested the solutions from weeks 1 and 4 only for the ions from our glass, i.e., Zr, Co and Al to obtain the insurance that our material was performing well. The results from the ICP measurements are reported in Figure III-23. ISO 22674 specifies that the sum of the metallic products released over 7 days should not exceed 200 µg/cm² of immersed surfaces.

From the reference measurement (a blank solution, without any metallic material, immerged), we can see that we detect roughly 0,1 µg/cm²/7d. This detection level will be attributed to contamination of the equipment used in this experiment. From Figure III-23, we can also observe that our BMG does not exceed 1 µg/cm²/7days which is 200 times less than the official regulation. There is no visible difference in the releasing level between weeks 1 and 4.

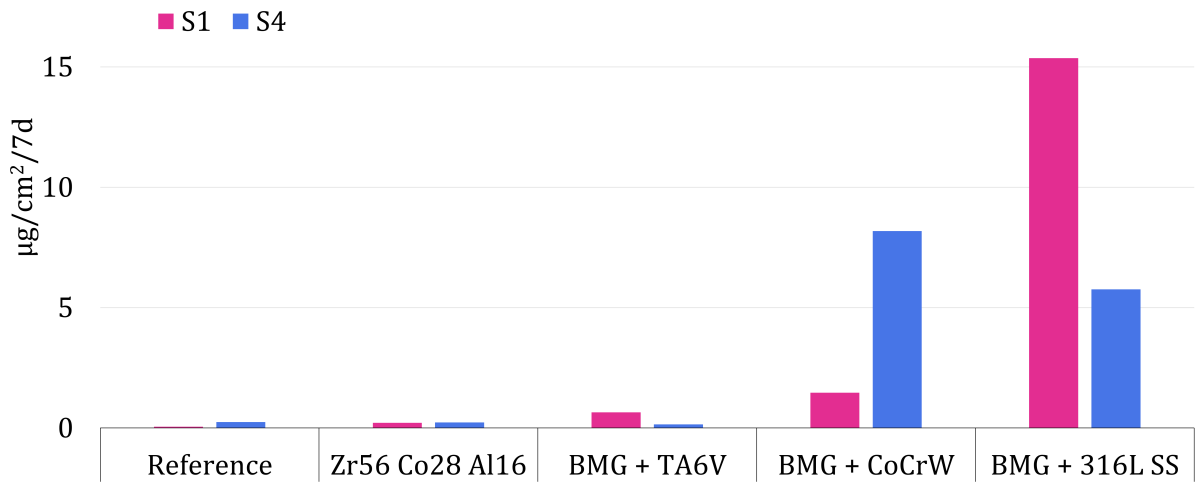

Figure III-23: Quantification of the sum of released products into the immersion solution for weeks 1 (S1) and 4 (S4).

Now looking at coupling tests in Figure III-23, we can first conclude that none of the three couples studied induces important galvanic corrosion, as none of them exhibits high release levels. Coupled with

TA6V, levels of releasing are in the same range compared to the BMG alone. Releasing is slightly higher in the first week compared to the fourth week on immersion. This could imply that passivation films are formed during the first week, which causes slightly higher releasing. Coupling with CoCrW and 316L Stainless Steel (SS), release levels are higher as they exceed 1 µg/cm^2/7days but remains very acceptable as the highest release level measured is near 10 µg/cm^2/7days which is still 20 times less than the ISO limit.

Regular pH measurements showed no change in the pH of the solution (balanced at 2.3) before and after each week of immersion. Weight loss was also measured after 4 weeks of immersion. For comparison, reference materials (TA6V, CoCrW and 316L stainless steel) are also immersed in the same conditions as the BMG and weight loss is measured. No weight loss exceeding 0.03% is measured, which is negligible. This confirms the good stability of our alloy during immersion, alone or coupled to other crystalline materials. This also shows that no significant amount of compounds that were not quantified by ICP are released.

The detail of the quantification of each element is given for weeks 2 and 3 in Figure III-24. For the BMG alone ($Zr_{56}Co_{28}Al_{16}$), released products are mainly Zr and Al. Iron also appears in the quantified products, in weeks 2 and 3. This could be related to the pollution of the equipment. For BMG + TA6V, we can quantify two main constituents, Al (0.05 and 0.06 µg/cm^2 respectively during the first and fourth weeks of immersion) and Ti (0.35 and 0.21 µg/cm^2 respectively during the second and third weeks of immersion). Titanium is coming from the TA6V (Ti content of around 90 wt%). Al could be coming from both TA6V (around 6 wt% of Al) and the BMG. The interesting thing is the higher release of titanium compared to zirconium. This implies that the BMG could have a better immersion resistance compared

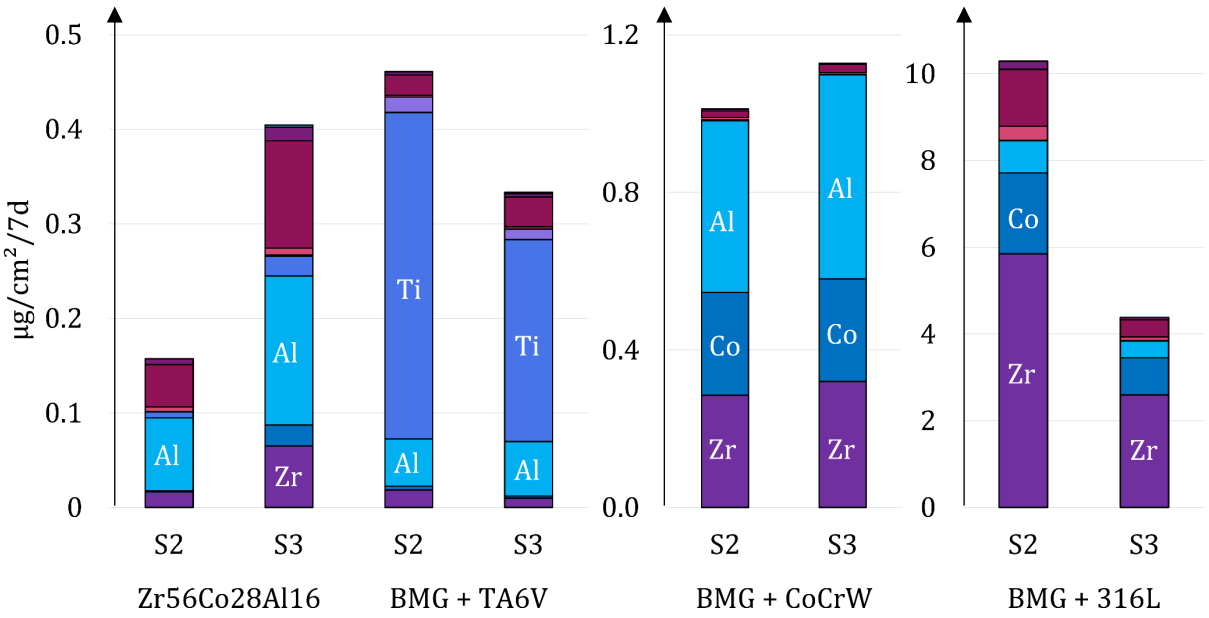

Figure III-24: Quantification of released elements after immersion for weeks 2 (S2) and 3 (S3) in NaCl + lactic acid at 310 K. Quantified elements are Zr, Co, Al, Ti, V, Cr, Fe, Ni and W. In this figure we more specifically highlight Zr, Al, Ti and Co.

to the TA6V when the two materials are tested together. For BMG + CoCrW coupling, we mainly detect Zr, Al and Co (0.32, 0.52 and 0.26 for Zr, Al and Co respectively in the third week of immersion). Zirconium and aluminium should be released from the BMG. Cobalt could come from both the BMG and the crystalline alloy. Finally, the analysis of the BMG + 316L SS solution shows a high content of zirconium along with cobalt (2.6 and 0.85 for Zr and Co respectively in the second week of immersion). The higher iron content in the solution in the second week could come from 316L stainless steel.

From the static immersion testing of the $Zr_{56}Co_{28}Al_{16}$, we can conclude that the immersion resistance of the alloy in a solution of NaCl and the lactic acid at 310 K is excellent. Also, the BMG remains in perfect integrity when coupled to other crystalline materials frequently used in the biomedical sector. Among the three constituents of the alloy, we showed that cobalt has the lowest releasing rate (except for BMG + 316L SS). This is an interesting finding as cobalt is the element of concern in this alloy. This study further confirms the potential of this alloy for biomedical application, as we performed immersion tests following protocols that are more drastic than what the ISO standard suggests.

III.2.4. Mechanical properties

The mechanical properties of the alloy should be assessed while keeping in mind potential biomedical applications. This part presents the results of the different mechanical characterisations that were performed on the BMG. The focus will be made on the compressive resistance of the alloy. A particular interest will be given to the plasticity of the alloy and the variability of the mechanical resistance. As it is of primary importance for application as a structural implant, the fatigue resistance of the $Zr_{56}Co_{28}Al_{16}$ is also tested using a procedure specifically designed for the dental implantology industry.

III.2.4.1. Compressive resistance

Compression testing was performed firstly to assess the mechanical resistance of the alloy. A large amount of data is already available on the compressive resistance of the $Zr_{56}Co_{28}Al_{16}$. Some of those are summed up in Table III-5. From the literature, quite large variations of yield stress and plastic strain are observed. Strain rates are mostly of 2.5 $x10^{-4}$ s^{-1} which does not explain the differences. The yield stress ranges from 1720 to 2010 MPa. Plastic strain ranges from nearly 0 (in the case of the fracture happening before yield [156]) to a little above 10%, which is already an important plastic strain for a bulk metallic glass. The yield strain is stable at 2%. The ultimate compressive strength is also rather stable, between 2100 and 2200 MPa. Therefore, in addition to the simple characterisation of the mechanical resistance of the alloy, its variability is also a subject of interest.

σ_y (MPa)	σ_{max} (MPa)	ε_p (%)	Strain rate (s^{-1})	D (mm)	Density ($g.cm^{-3}$)	HV	E (GPa)	Ref
1720	2100	10	2.5 x10-4	2	-	664	91.9	[234]
1770	2160	6	2.5 x10-4	2	-	678	92.7	[234]
1780	2078	6	1 x10-4	2	-	-	-	[209]
1897	2136	10	-	2	-	-	92	[18]
1920	2125	1	2.5 x10-4	2	6.525	-	-	[215]
1950	2180	2	2.5 x10-4	2	-	687	93.1	[234]
1959	2192	10	2.5 x10-4	2	6.5	-	-	[222]
1959	2190	10	2.5 x10-4	2	-	-	-	[207]
1980	2100	0	2.5 x10-4	2	-	691	93.6	[234]
2010	2300	3	3 x10-4	1,5	6.684	631	-	[227]
-	-	0	2 x10-4	3	-	531	-	[156]
-	-	-	-	-		515 ± 6		[129]

Table III-5: Yield stress, ultimate compressive strain (σ_{max}), plastic strain, density, hardness (Vickers) and Young's modulus extracted from the literature on the compression resistance of the $Zr_{56}Co_{28}Al_{16}$ BMG.

Tan *et al.*[234] showed that depending on the current used for the arc, in the arc melting process, several ultimate plastic strains could be obtained. To minimize any effect of the processing on the ultimate mechanical properties, all primary alloy was prepared following the same protocol. From each primary alloy ingot, 3 rods are cast simultaneously. 6 to 7 compression samples are numerically machined from each rod. Performing a great number of compression tests under the same conditions, on samples originating from the same primary alloy or different primary alloys, allows us to carefully assess the variability in the mechanical resistance of the alloy. More than 20 compression tests were performed in the same conditions. Figure III-25 shows 5 stress/strain curves from the 7 samples machined from the same rod (*i.e.* same primary alloy and same casting parameters). The inset illustrates the method for the

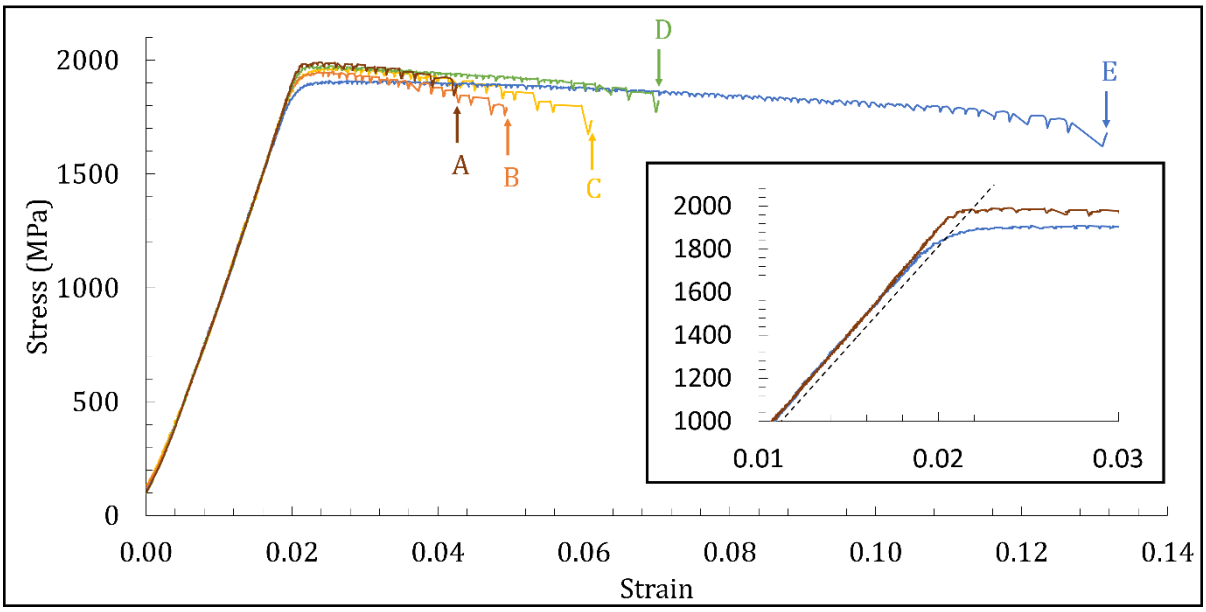

Figure III-25: Compression stress/strain curves for the $Zr_{56}Co_{28}Al_{16}$. Inset is a close-up to highlight of the yield stress measurement.

yield stress definition. The yield stress is taken at the intersection of the stress/strain curve and a straight line parallel to the strain/stress curve elastic domain with an offset of 0.0005.

As mentioned in chapter II.3.3.1, machine compliance is corrected using the material Young's modulus measured at 93 MPa for 2 mm in diameter rods of $Zr_{56}Co_{28}Al_{16}$. Table III-6 shows σ_y, ε_y, σ_{max} and ε_p for the five curves presented in Figure III-25. It also shows the average values and standard deviation for σ_y, ε_y, σ_{max} and ε_p for the 7 samples machined from the considered rod. The stress-strain curves exhibited here are representative of the compressive behaviour of all the as-cast $Zr_{56}Co_{28}Al_{16}$ samples tested in this study. One can first notice that based on the yield stress and the ultimate compressive stress, the compressive behaviour is highly reproductive. Yield stress and Young's modulus are comparable to the values reported in the literature (see Table III-5). However, even though it is very reproducible in our tests, the ultimate compressive stress is lower for our $Zr_{56}Co_{28}Al_{16}$. This is attributed to the pronounced strain-softening observed close after the yield stress in our case. Some compressive tests on the $Zr_{56}Co_{28}Al_{16}$ reported in the literature exhibit strain hardening, mainly when data are expressed using the engineering stress (no correction of the cross-section variation).

From Figure III-25 and Table III-6 we can mainly observe a significant variability on plastic strain ε_p. It ranges from 2.1% for sample A to 11.2% for sample E. σ_y and σ_{max} also exhibit variations (but to a much lesser extent) over the five presented samples: from 1845 MPa to 1980 MPa for σ_y and from 1910 to 1991 for σ_{max}. We do not observe a correlation between yield stress and plasticity. Only sample E stands out with a plastic strain significantly larger (11.2% compared to 4.8% for the second-highest value) and with yield stress significantly lower: 1845 MPa compared to 1915 MPa for the second-lowest value. Generally, it is observed that higher plastic strain is associated with lower yield stress.

Sample	σ_y (MPa)	σ_{max} (MPa)	ε_p (%)	Strain rate (s^{-1})	D (mm)	E (GPa)
A	1980	1991	2.1	2.5 x10^{-4}	1.85	93
B	1920	1971	2.9	2.5 x10^{-4}	1.85	93
C	1915	1967	4.0	2.5 x10^{-4}	1.85	93
D	1965	1976	4.8	2.5 x10^{-4}	1.85	93
E	**1845**	**1910**	**11.2**	**2.5 x10^{-4}**	**1.85**	**93**
Average	1926 ± 44	1963 ± 25	4.9 ± 3			

Table III-6: Compression data from the 5 stress/strain curves shown in Figure III-25 and average and standard deviation calculated over the 7 samples from the selected rod.

The variability on plastic deformation observed in the performed compression tests is of the same magnitude as the variability observed with the data available on the $Zr_{56}Co_{28}Al_{16}$ in the literature. However, we achieved very good reproducibility on the stress levels (yield stress and ultimate stress). All the presented samples here originated from the same primary alloy, and the same injection process,

we can conclude that the variability does not come from a difference in the material sourcing, the processing parameters or the testing setup.

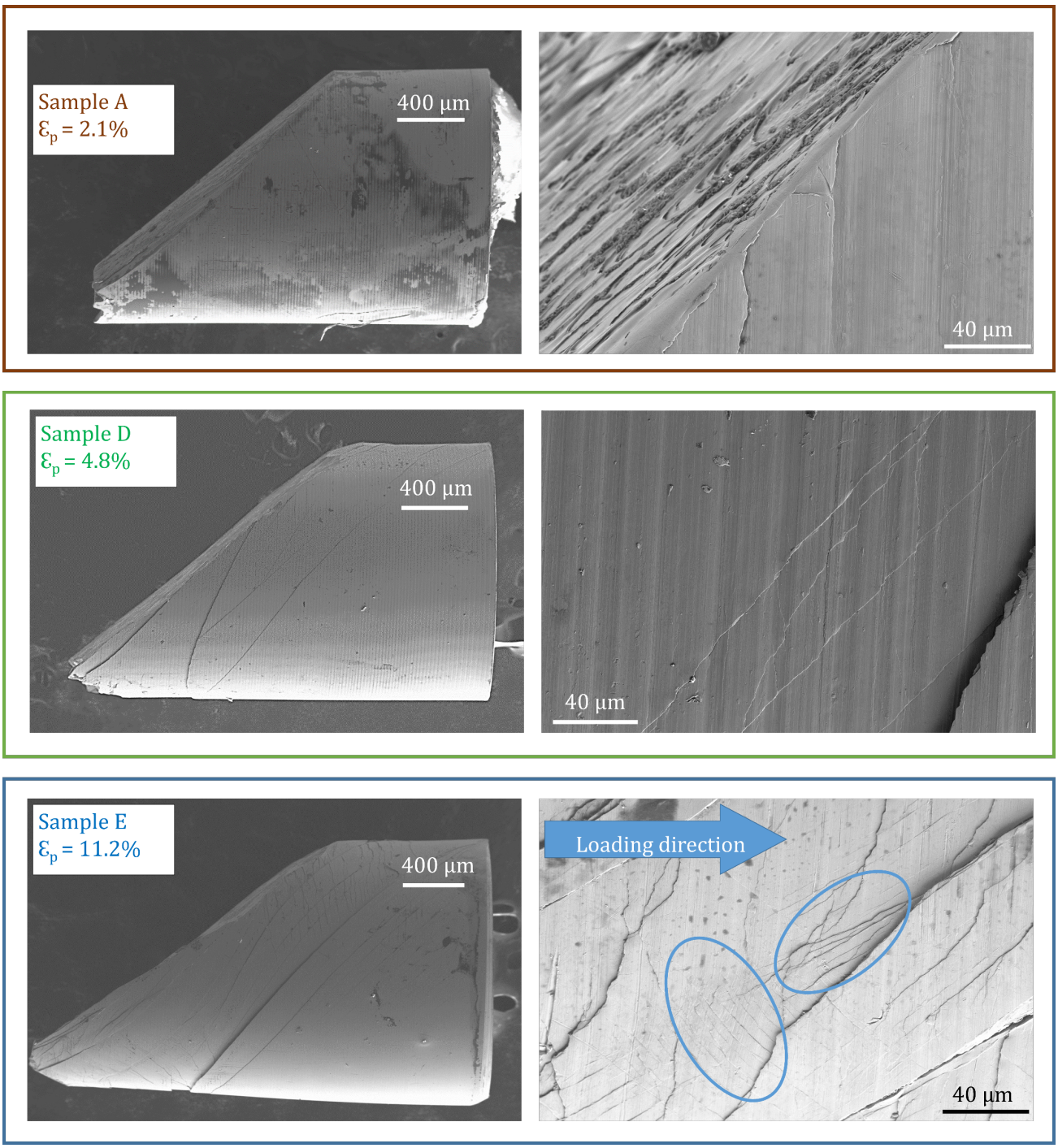

Figure III-26: SEM images of sample A, D and E surfaces after fracture at two magnifications. Only a single shear band can be observed on sample A. Several shear bands are observed on sample D, mostly parallel to the fracture plane (primary shear bands). Numerus shear bands are observed on sample E, parallel to the fracture plane (primary shear bands) and in other direction (secondary shear bands).

To further study the difference of plasticity between these samples, 3 samples are selected: A, D and E. Sample A presents the deformation with the lowest plasticity, while sample E represents the case with the maximum plastic strain. Sample D is selected as an intermediate behaviour. Sample surfaces are

observed using SEM imaging. On sample A surface (see Figure III-26), no other shear band than the one from the fracture plane are visible. This means that the load/deformation was concentrated on a single shear band. Sample D surface (see Figure III-26) shows multiple shear bands, with a majority orientated in the same direction as the fracture plane. The presence of multiple shear bands spreads out the load, which delays the apparition of the main shear band and slows down its propagation, ultimately delaying fracture. Sample E surface (see Figure III-26) exhibits many shear bands. Along with the primary shear bands, secondary shear bands are also visible. Secondary shear bands are shear bands that do not develop in the preferential direction (approximately 45° to the loading axis). These shear bands, therefore, require more energy to propagate. Multiple shear bands can also accommodate a larger deformation than a single shear band. A close-up image of the primary and secondary shear bands of sample E surface is proposed in Figure III-26. In these images, multiple shear bands can be observed, but we can also observe shear bands crossing, stopping or splitting. For better understanding, these phenomena are illustrated in the SEM image presented in Figure III-27. The observation of such events is the footprints of a more homogeneous activation of numerous shear bands with low propagation dynamic which, once again, increase deformability.

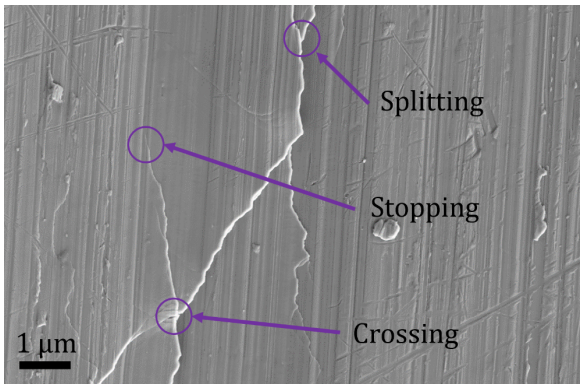

Figure III-27: SEM image of a $Zr_{56}Co_{28}Al_{16}$ sample surface after compressive testing, showing shear band stopping, crossing and splitting.

From the observation of the sample fracture surfaces, no differences are observed. All three samples exhibit the typical vein pattern on their surfaces, as shown in Figure III-28. The vein pattern is typical of the ductile fracture of a BMG. Note that the vein pattern is heterogeneously distributed on the sample fracture surface. It is therefore tricky to define a representative vein pattern for a sample. Analysing vein patterns for quantitative information should be done with much caution, as the statistical analysis proposed by O. Baulin [96].

From the study of the sample surfaces, we show that the difference in deformability is correlated with a difference in the shear band density. With a higher shear bands nucleation rate, failure is delayed as numerous shear bands will be able to accommodate a higher deformation than a single shear band. However, so far, we have only analysed post-deformation features. To better understand what happens during plastic deformation, the study of the serration dynamic must be performed. The serrated behaviour results from a sort of “stick & slip” process during deformation. Each “drop” in the measured stress could correspond to a shear band movement (see Chapter I.3.3.1). The study of the stress drops

emerging from the serration pattern can give very valuable information on the way serrations interact during deformation.

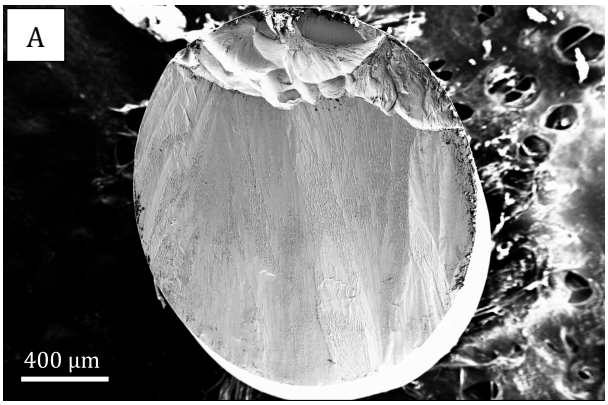

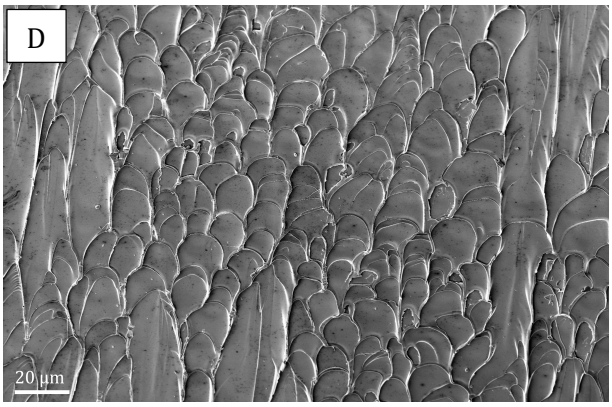

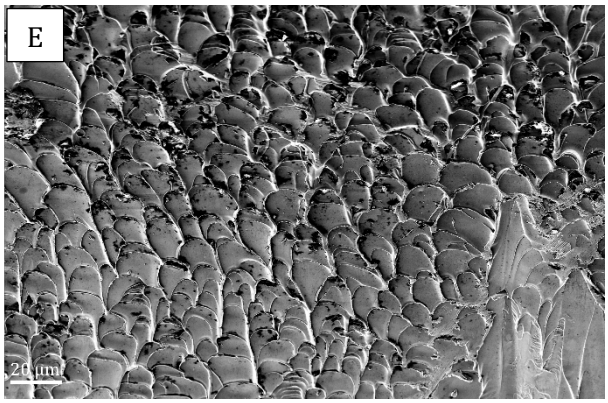

Figure III-28: fracture surfaces for the three studied samples (A, D and E). Each fracture surface exhibit typical vein pattern.

Figure III-29 gives the repartition of the stress drops detected with the strain, measured from sample E. The stress drop detection limit is set at 1 MPa which corresponds approximately to a load drop of 2.7 N based on our geometry. This figure exhibits two regimes in the serration development, based on the magnitude of the stress drops. In the first regime, stress drops are of a rather moderate magnitude corresponding to the steady propagation of multiple shears bands which spreads out stress and strain resulting in the detection of a high density of serration. The time interval between serration is short (less than 800 ms). Stress drop values are fluctuating between 1 MPa and around 25 MPa with a progressive increase of the magnitude of the maximum stress drops. It appears that there may be a stress drop threshold, here around 25 MPa, above which the second regime starts. Comparable stress drop repartition and threshold phenomenon have been reported recently by Louzguine-Luzgin *et al.* [235]. The second regime could correspond to the localization of the strain into a single shear band. In this regime, stress drop magnitude rapidly increases up to the dramatic failure of the sample. In this regime, very few to no small stress drops are detected. The frequency of the drops is reduced with a larger time gap between each event.

Figure III-30 (a) represents each detected stress drop as a function of the strain for the three studied stress/strain curves (samples A, D and E). Figure III-30 (b), (c) and (d) show the stress drop statistical repartition respectively for samples A, D and E. Figure III-30 (a) exhibits the two serration

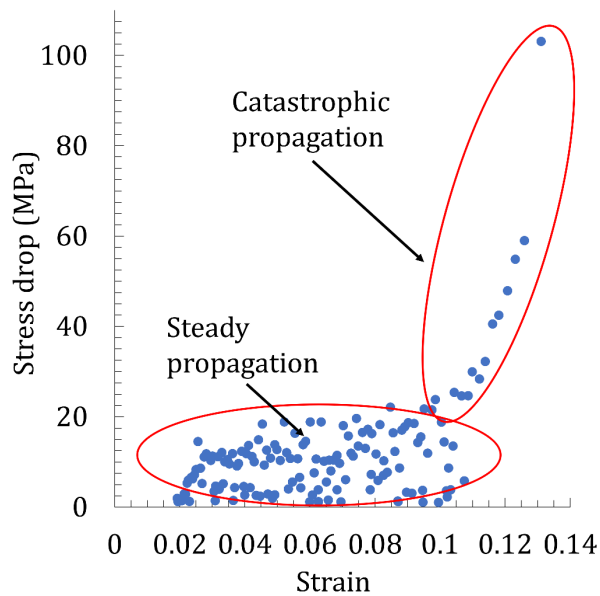

Figure III-29: Illustration of the two regimes in the serration flow. First the steady propagation with low-magnitude stress drops alternating small and medium drops. Second the catastrophic propagation with rapidly increasing stress drops and no small drops.

propagation regimes, as described above, happening during plastic deformation until failure. Based on those two regimes, we can see that sample A (see Figure III-25 and Figure III-30), with the lowest plastic strain, enters the second regime from the start of the plastic deformation. This means that very few shear bands are activated and that deformation is directly concentrated in a limited number of the shear band, leading to early catastrophic failure. This analysis confirms the observations made on the sample surface, which showed only one shear band. Sample D exhibits 6.8% of plastic strain. For this sample, in Figure III-30 (a) the first regime is held up to around 5.5% of absolute strain. Accordingly, its stress drop threshold between the two regimes is lower (maybe just below 20 MPa) than the one of sample E (around 25 MPa). For strain values above 5.5% of strain, the stress drops magnitude starts to increase rapidly, which marks the transition to the second regime. Now looking at sample E, with the highest plastic deformation, the first regime takes place between 0 and 9% of plastic deformation (2 and 11% of absolute strain). This regime exhibits the highest stress drop density, in other words, the highest frequency of serrations. This can be explained by a lot of shear bands sharing the applied stress by being simultaneously activated and interacting. This is coherent with the observations made on sample E surface, where lots of primary and secondary shear bands were detected.

By comparing the behaviours of the three samples in the second regime, we observe that they are rather similar. For instance, we note that the penultimate stress drops for each sample have a magnitude of roughly 60 MPa. This could be interpreted as follows: each sample develops a different density of shear bands; The higher the shear band density, the higher they interact and spread-out load and deformation; The longer the localization of the stress in a single shear band is delayed. Yet once deformation enters the catastrophic stage, the shearing process is similar. Liu *et al.*[105] studied the serration patterns for the compression testing of Zr-Cu-Ni-Al BMGs. They reported that ductility was increased by reducing the casting diameter. But they also proposed that the maximum stress drop magnitude is insensitive to the internal structure. The magnitude of the maximum stress drop for the studied Zr-Cu-Ni-Al BMG is ranging

between 47.1 and 52.5 MPa. This affirmation could be confirmed for our alloy if we disregard the last stress drop for each sample. However, Liu *et al.* [105] data do not show the second regime as we do. Their Zr-Cu-Ni-Al alloy seems to fail straight at the end of the steady propagation regime. In our case, the magnitude of the last stress drop is increasing with the increasing ultimate plastic strain: 78 MPa for sample A, 87 MPa for sample D and 103 MPa for sample E. This could imply that a more ductile glass, in addition to the faculty to develop more shear bands, have the faculty to withstand higher stress drop. This could be confirmed in the present case by the fact that deformation starts to localize in a single shear band (transition from the first to the second regime) at higher stress drop magnitude for the less brittle glass (here sample E).

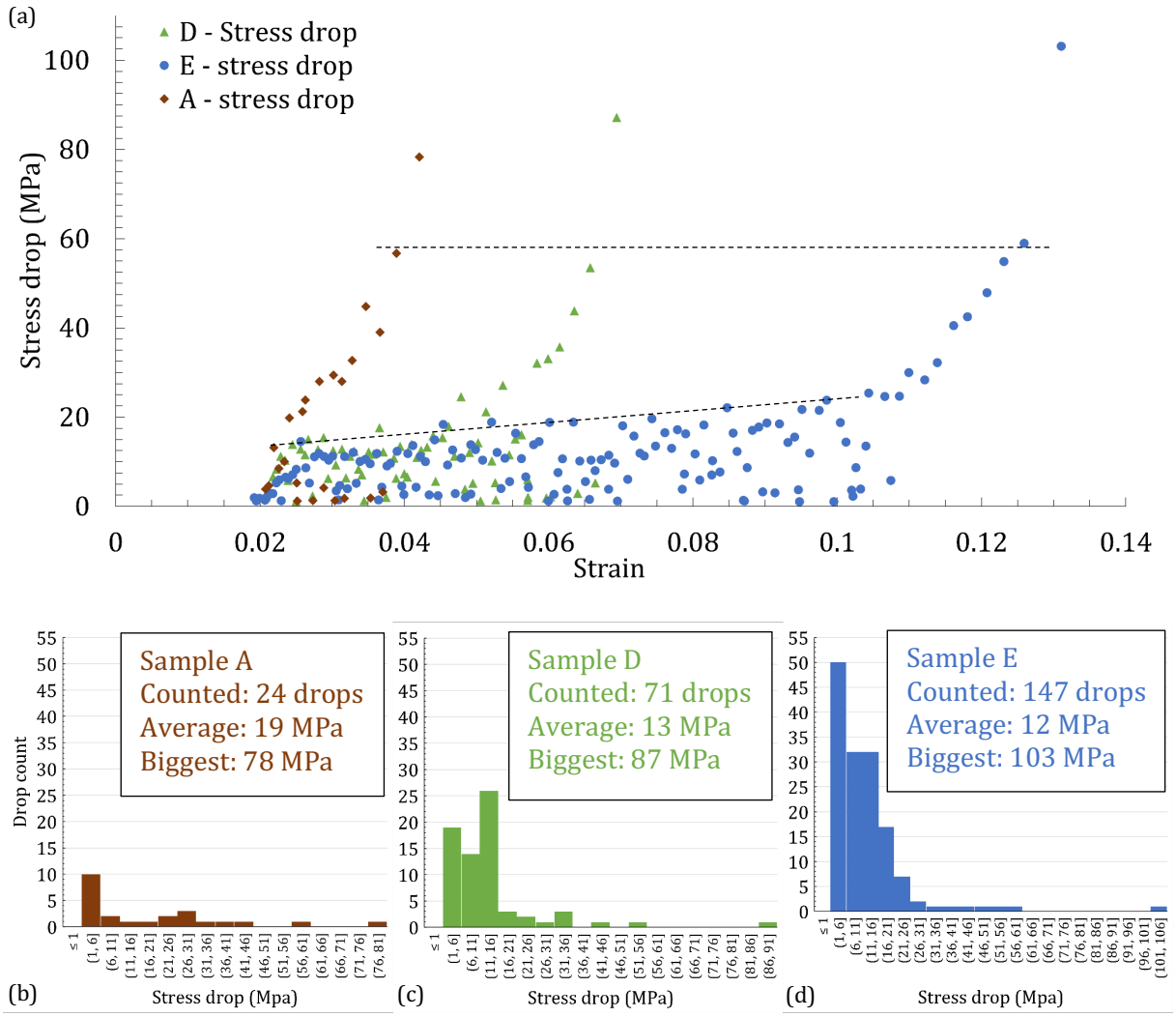

Figure III-30: Serration analysis of the compression stress/strain curves from samples A, D and E. (a) shows the correspondence between each detected stress drop and the deformation for each sample. (b), (c) and (d) detail stress drops repartition based in their magnitude for each curve.

The statistical analysis of the stress drops distribution also gives information on the underlying deformation mechanisms (see Chapter I.3.3.1). The distribution of the stress drops is represented for each sample in Figure III-30 (b), (c) and (d). For sample E, with the highest plastic deformation, the

distribution can be fitted by a power-law distribution with a square exponential decay function. This is an indicator of the self-organized critical (SoC) state in the serration dynamics of MGs. Interestingly, sample D stress drop distribution cannot be fitted by a power-law function. Instead of exhibiting a decreasing probability with the increasing stress drop magnitude, it exhibits a maximum probability for stress drops between 11 and 16 MPa (between 1 and 6 MPa for sample E). This kind of distribution (Gaussian-like) is a typical feature of a chaotic dynamic state. For sample A, there are not enough quantified serrations to precisely evaluate the serration distribution.

From the analysis of the serrated flow of the plastic deformation we have seen:

- With plastic deformation, serration development exhibits two distinctive regimes:
    - First, a steady propagation of the deformation. The load is spread out between multiple shear bands simultaneously. This is characterized by a slowly increasing magnitude of the stress drops (under a threshold different for each sample studied), alternating shear bands of low and medium magnitude.
    - Second, a catastrophic propagation of a single shear band. Once the magnitude of the stress drop reaches a certain value (the threshold mentioned above), there is a transition from steady propagation to catastrophic propagation. Here a single shear band concentrate the entire deformation. Stress drop magnitude increases rapidly until failure.
- The longer the steady propagation is maintained, the higher the deformability of the sample. Sample A which exhibits very low plastic deformation (around 2%) enters directly in the second stage of the serrated flow whereas samples with higher deformability tolerate higher stress drops before transiting from the first to the second stage.
- Catastrophic shear band propagation is comparable for the three samples and does not seem to be correlated with deformability. Only the last stress drops have an increasing magnitude with the increasing deformability. This could imply that a more ductile glass can withstand higher energy release.
- Looking at the statistical distribution of stress drop magnitude, we see that higher deformability is correlated with a power-law distribution with a square exponential decay. Based on the literature, samples exhibiting lower ductility should display a statistical distribution of the stress drop magnitude following a Gaussian distribution.
- From a single injection casting process, we observe major differences in the shear bands development. The conclusions from the serration analysis are backed up by the observation of the sample's surfaces.

At this point, it is clear shear bands mitigate the deformations. Before discussing the glass structure, we will characterize the fatigue resistance of the $Zr_{56}Co_{28}Al_{16}$ BMG processed at SIMaP.

III.2.4.2. Resistance to fatigue following dental cyclic mechanical loading standard

Fatigue resistance, *i.e.* resistance to prolonged cyclic loading under the yield stress, is a key property for materials used in the realisation of structural implants. We tested fatigue resistance using the industrial standard ISO 14801:2016 entitled "Dynamic fatigue test for endo-osseous dental implants". The geometry used for this test is specifically designed to replicate actual dental implant structural parts. This set is not the most appropriate to calculate stress and strain, as one could do with more traditional three-point or four-point bending setups but this setup gives a reliable image of the alloy capabilities for the targeted application. Moreover, we were able to compare the results from the BMG with results obtained on materials currently used in the fabrication of dental implants by Anthogyr.

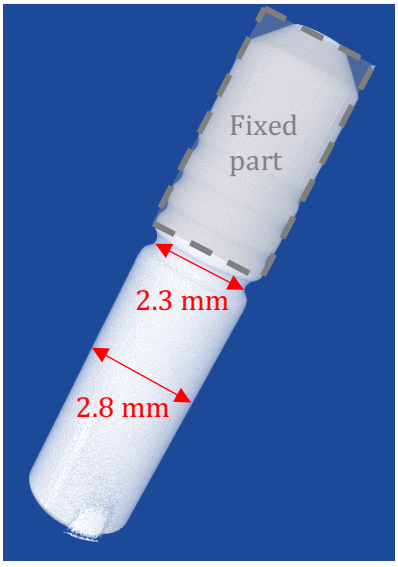

Figure III-31: 3D tomographic image of a sample used for fatigue testing.

The samples used for fatigue testing are cylinders with an outer diameter of 2.8 mm. A groove, with a diameter of 2.3 mm is carved and the sample is inserted and glued in a sample holder up to this groove. This groove will concentrate stress. Figure III-31 shows a 3D image acquired via X-ray tomographic imaging. The sample part which is inserted in the sample holder is marked as "fixed part". Tomographic imaging was used on each sample before testing to check that no porosity is present. Any sample presenting porosities were excluded (see Chapter II.3.3.6).

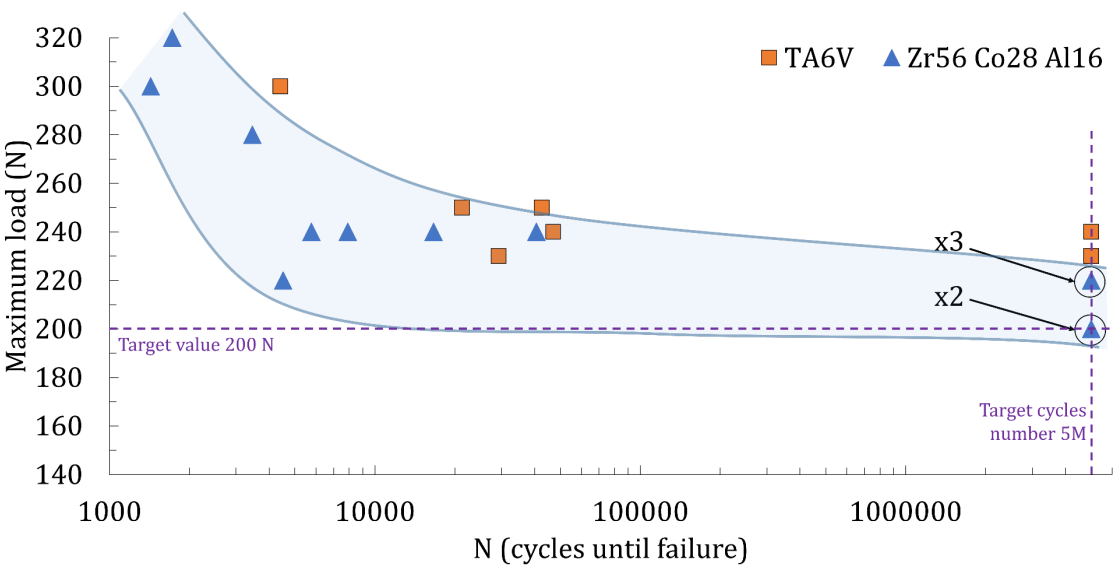

Figure III-32: S-N curve for $Zr_{56}Co_{28}Al_{16}$ BMG and TA6V crystalline alloy, as machined. Data on TA6V are provided by Anthogyr SAS.

Figure III-32 shows the S-N curve (pseudo-Wohler curve), for our BMG ($Zr_{56}Co_{28}Al_{16}$) and TA6V. The targeted cycles number was 5 million and the target load defined by the ISO standard is 200 N. The $Zr_{56}Co_{28}Al_{28}$ matches this requirement. Table III-7 shows the load and number of cycles sustained by each tested bulk metallic glass sample.

Maximum load (N)	Number of cycles	Sample identification
200	5 000 000	S-1
	5 000 000	S-2
220	5 000 000	S-3
	5 000 000	S-4
	5 000 000	S-5
	4 511	S-6
240	40 611	S-7
	16 638	S-8
	7 909	S-9
	5 760	S-10
280	3 451	S-11
300	1 428	S-12
320	1 721	S-13

Table III-7: Number of cycles achieved for each sample tested at specific loads.

The two samples tested at 200 N passed 5 million cycles and did not fail. Out of the four samples tested at 220 N, three passed 5 million cycles without failing and one failed rather early, at 4511 cycles but in this case, fracture surface analysis through SEM imaging revealed the presence of a major spherical inclusion of more than 50 µm in diameter which could have triggered the early failure. The spherical shape of the inclusion let us think that they could be crystals embedded in the glass.

No sample tested reached 5M cycles at 240 N. Still we observe a fairly high dispersion in the number of cycles before failure: sample 13 (S13) reached 40 611 cycles before failing while sample 4 (S4) failed after 5 760 cycles. For higher loads (280 to 300 N), no samples reached more than 3 500 cycles.

From this analysis, several conclusions can be drawn:

- $Zr_{56}Co_{28}Al_{16}$ meets ISO 14801:2016 requirement of 200 N for fatigue resistance in this specific set-up.
- In the condition imposed by ISO 14801:2016, $Zr_{56}Co_{28}Al_{16}$ fatigue resistance lies between 220 and 240 N in terms of maximum load.
- Under a specific load, low variability is observed in the fatigue resistance. In other words, under fatigue solicitation, the majority of the samples tested will exhibit the same behaviour.
- Above the fatigue limit, namely above 240 N of load here, a variability is observed in the fatigue resistance. This variability could be correlated to the variability observed and discussed in the compression resistance chapter (see III.2.4.1).

- Far above the fatigue resistance limit, for loads from 280 to 300 N, less variability is observed as failure happens very quickly, namely before 5 000 cycles.

Figure III-32 also shows the comparison with TA6V. Three samples were tested at 230 N. Out of those three samples, two reached the 5 million cycles target. At 240 N, one sample reached 5 million cycles and one sample failed before 50 000 cycles. TA6V endurance limit is evaluated around 230 N, *i.e.* slightly higher than for $Zr_{56}Co_{28}Al_{16}$. If we compare compressive and fatigue resistances for TA6V and $Zr_{56}Co_{28}Al_{16}$, the yield stress at 0.2% for TA6V is given around 950 MPa[1], while our alloy average is 1926 MPa, hence 2 times the yield stress of TA6V (ISO 5832-3). Yet, the fatigue resistance of the TA6V is of the same order (up to 9% higher if we consider 220 N as our endurance limit). Crystalline materials are considered to exhibit a higher fatigue ratio (fatigue endurance limit divided by the ultimate tensile stress) than bulk metallic glasses [112–114]. It could be challenging to benefit from the impressive yield stress of our BMG as-cast, as any attempt at size reduction could degrade fatigue resistance. It was demonstrated that there is a size effect to the fatigue resistance of BMG (smaller samples have lower fatigue resistance [236]).

Mechanisms favouring fatigue resistance are differing from the one discussed earlier regarding plastic strain in quasi-static compressive loading. During compressive testing of metallic glasses, deformation is controlled by shear band displacements and higher ultimate strain is related to the ability of the material to generate many shear bands. Unlike crystalline alloys, the fatigue resistance of metallic glasses is dependent on crack initiation rather than crack propagation. Moreover, during fatigue, a bulk metallic glass goes through four stages: shear band initiation, shear band propagation, crack initiation and crack propagation [237]. Fatigue cracks are nucleated from shear bands that reach a critical size. In other words, to maximize plastic strain in metallic glasses, one will have to maximize shear band nucleation but, to maximize fatigue resistance, one will have to delay crack initiation and by extension shear band initiation as much as possible. During fatigue solicitation, there is a competition between relaxation and heterogeneities creation. When relaxation is of larger magnitude than free volume creation, the glass tends to harden. Inversely, when free volume creation is higher than free volume annihilation (relaxation), the glass tends to soften. When free volume creation and annihilation are balanced, no structural changes are detected (see Chapter I.3.3.2 for more details).

To study the influence of cycling at low stress on the $Zr_{56}Co_{28}Al_{16}$, we performed staircase fatigue testing. Figure III-33 illustrates S-N curves for 5 samples. Each sample was first solicited at 200 N (samples S-1 and S-2) or 220 N (samples S-3, S-4 and S-5). Once 5 million cycles are reached, the load is increased by 20 N. Table III-8 sums up the load and number of cycles for each sample subjected to staircase testing.

[1] In tensile testing

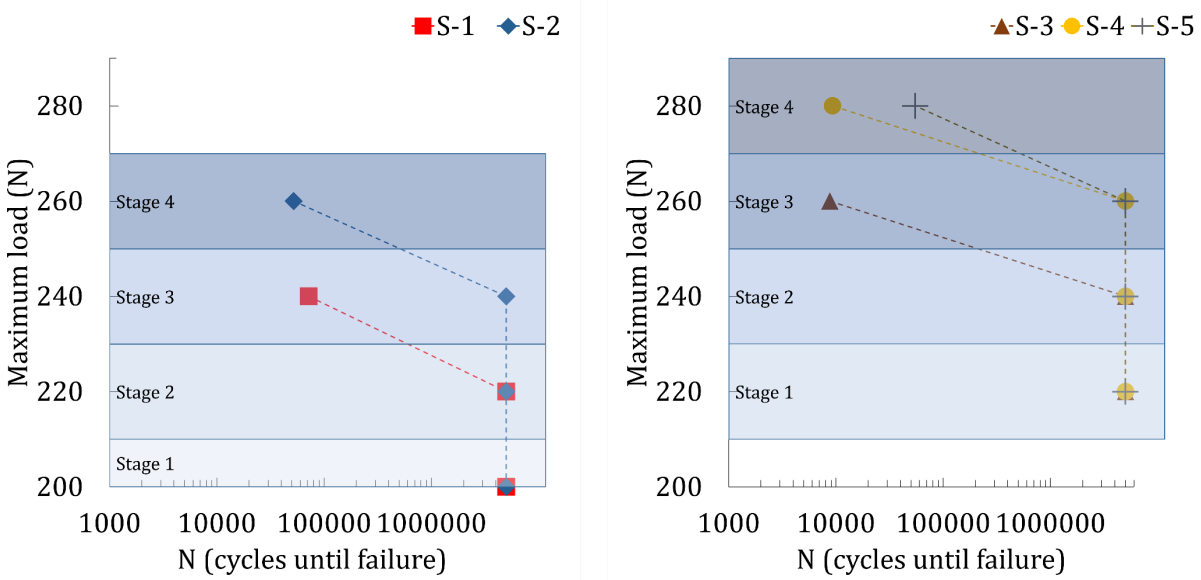

Figure III-33: S-N curve for $Zr_{56}Co_{28}Al_{16}$ BMG under staircase testing: when a sample reaches 5 million cycles, the load is increased by 20 N and the sample undergoes again 5 million cycles again. This procedure is repeated until failure.

Maximum load (N)	Number of cycles	Cumulative number of cycles	Sample identification
200^1	5 000 000	10 072 135	S-1
220^2	5 000 000		
240^3	72 135		
200^1	5 000 000	15 052 053	S-2
220^2	5 000 000		
240^3	5 000 000		
260^4	52 053		
220^1	5 000 000	10 008 791	S-3
240^2	5 000 000		
260^3	8 791		
220^1	5 000 000	15 054 876	S-4
240^2	5 000 000		
260^3	5 000 000		
280^4	9 288		
220^1	5 000 000	15 009 288	S-5
240^2	5 000 000		
260^3	5 000 000		
280^4	54 876		

Table III-8: Load and cycle history for samples subjected to staircase testing. The exponent in the maximum load column indicates the cycling stage.

We have seen from Figure III-32 and Table III-7 that no samples reached 5 million cycles while directly loaded at 240 N. Here we observe that by first loading our sample at 200 N or 220 N for 5 million cycles, a higher fatigue limit can be achieved. Out of the five samples tested, 4 reached 5 million cycles

under 240 N of load. Out of the three samples that started at 220 N, three reached the 5 million cycles target under 260 N of load. In other words, gradually increasing the load seems to delay crack initiation. We have seen that crack initiation originates from shear bands which themselves originate from the percolation of shear transition zones (STZs) (see Chapter I.3.2.2.2). By extension, it is possible that by applying cyclic loading under the fatigue limit of our alloy, we promote relaxation, making it harder for shear bands to nucleate. Therefore, even though we are soliciting our alloy at stresses well below the yield stress, we are probably affecting the glass structure. To our opinion, it is an interesting finding that shows that the glass increases its fatigue resistance under the appropriate solicitation.

While increasing the stress to the fatigue limit (somewhere a little under 240 N), the free-volume annihilation rate may be reduced and the free-volume creation rate may be increased. Above the fatigue limit, the heterogeneity creation phenomenon is predominant and we start to initiate failure mechanisms. This ultimately leads to failure but at stresses far higher than what was achieved without gradually increasing the load.

From the study of the fatigue resistance of the $Zr_{56}Co_{28}Al_{16}$, we can conclude that:

- The studied amorphous alloy meets the requirements from ISO 14801:2016 in terms of fatigue resistance. All the samples tested at 200 N reached the objective of 5 million cycles.
- Using this particular set-up, the $Zr_{56}Co_{28}Al_{16}$ fatigue endurance limit is between 220 N and 240 N, with samples machined from 5 mm rods produced via arc melting. This is of the same order as the TA6V (less than 9% lower).
- Higher fatigue endurance limit is reached when gradually increasing the load. By doing so, the 5 million cycles can be reached at loads up to 260 N (a 30% increase compared to 200 N). This is attributed to the fact that loading at moderate stresses tends to favour the relaxation of the glass. With the relaxation of the glass, part of the embedded heterogeneities is suppressed and it, therefore, requires more energy to activate the shear banding process. The fatigue loading in a staircase fashion of the BMGs is rarely reported. Yet the enhancement of the fatigue resistance with relaxation is discussed in the literature (see Chapter I.3.3.2). This finding is interesting as it means that under the right load, the glass fatigue resistance could be increased under use.

Maximizing plasticity upon quasi-static deformation and maximizing fatigue endurance limit are two processes that do not rely on the same mechanisms. On the one hand, maximizing plastic strain will require high shear band density, which is usually developed in a glass in a high energy state. On the other hand, maximizing fatigue endurance limit will require limiting shear band nucleation. This is usually achieved for glasses in low energy states, which require more energy to activate the shear banding process.

III.2.4.3. Correlating between mechanical properties of the $Zr_{56}Co_{28}Al_{16}$ alloy and its glass structure

We have characterized the mechanical resistance of the $Zr_{56}Co_{28}Al_{16}$ BMG, subjected to quasi-static loading (compression) and high-frequency cyclic-loading (fatigue). In both cases, we have seen that shear bands development is the main factor dictating the mechanical response. Shears bands are nucleated by the percolation of shear transformation zones (STZ), which themselves preferably nucleate at the location of softer volume units (of low density) compared to the average hardness of the glass.

Free volume can be quantified by measuring glass density before and after "full" relaxation. Such density measurements were performed on entire rods as compression samples were too light to give accurate measurements. We performed density measurements as-cast and after relaxation for 48h at 0.9Tg for the $Zr_{56}Co_{28}Al_{16}$ for three 2 mm-diameter rods from which are machined the compression samples. As-cast density is measured at 6.378 g.cm^3 ± 0.031 while relaxed density is measured at 6.511 g.cm^3 ± 0.015. Sample weight has not changed during relaxation, which means that the density increase is purely coming from volume variations more precisely from excess free volume annihilation. Volume reduction is calculated to average 2.09%, which means that during annealing, ≃ 2 vol% of the sample (related to free volume), was suppressed. From this measurement, we exhibit the presence of a fair amount of free volume in the as-cast glass. No data in the literature are available on $Zr_{56}Co_{28}Al_{16}$ for comparison, but we can compare to data proposed by Liu *et al.* [105]. For the $Zr_{55}Cu_{30}Ni_5Al_{10}$ 3-mm rod, they measured a free volume amount of 1.1% using the same technique (volume loss after full relaxation). However, this measurement gives us a global appreciation of the free-volume presence in our material but does not account for spatial distribution.

To probe the local variation of the density, *i.e.*, heterogeneities repartition, nanoindentation was used. Figure III-34 shows the box plots of the normalized micro- and nano-hardness for the $Zr_{56}Co_{28}Al_{16}$ 5 mm-diameter rods. We see in Figure III-34 that the dispersion of the values is lower for micro-hardness than for nano-hardness. The furthest measure from the average for micro-hardness represents a deviation of 3% while it represents a deviation of 13% for nano-hardness. The micro- and nano-hardness are normalized by the mean value calculated from 44 and 100 measurements, respectively. Mean, standard deviation, minimum and maximum values for nano-hardness are reported in Table III-9 and for micro-hardness in Table III-10

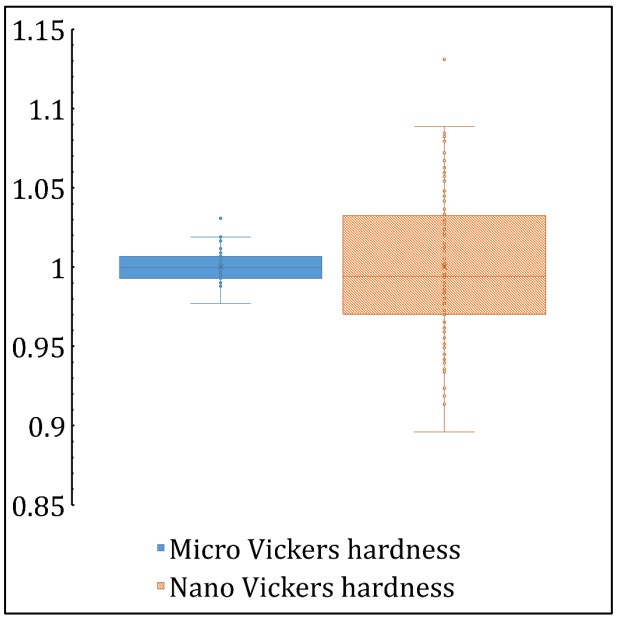

Figure III-34: Box plot from normalized micro-hardness and nano-hardness measurements on $Zr_{56}Co_{28}Al_{16}$ 5 mm-diameter rods.

	Mean	Min.	Deviation of min	Max.	Deviation of max
Normalized nano-hardness	1 ± 0.05	0.90	13%	1.13	13%

Table III-9: Mean, standard deviation, minimum and maximum values from the 100 nano-hardness tests performed on $Zr_{56}Co_{28}Al_{16}$ BMG.

	Mean	Min.	Deviation of min.	Max.	Deviation of max.
Normalized micro-hardness	1 ± 0.01	0.98	2%	1.03	3%

Table III-10: Mean, standard deviation, minimum and maximum values from the 44 micro-hardness tests performed on $Zr_{56}Co_{28}Al_{16}$ BMG.

It is interesting to note that by solicitation of a greater volume, the variability decreases. This gives us a glimpse at the length scale on which the heterogeneity extends. By probing a larger volume (micro-hardness), we are averaging the hardness over a scale at which the density variations are hardly detectable. This highlights that everything in bulk metallic glasses is a matter of scale. At the "micro-hardness scale", our glass is rather homogeneous, while at a "nano-hardness scale", our glass is much more heterogeneous. We will now discuss the influence of the heterogeneities repartition:

Figure III-35 proposes a schematic illustration of heterogeneities (regions in pink) with several volume fractions and repartitions. The upper part represents the heterogeneities in the glass matrix when no load is applied. The lower part represents shear bands development under loading, in the three

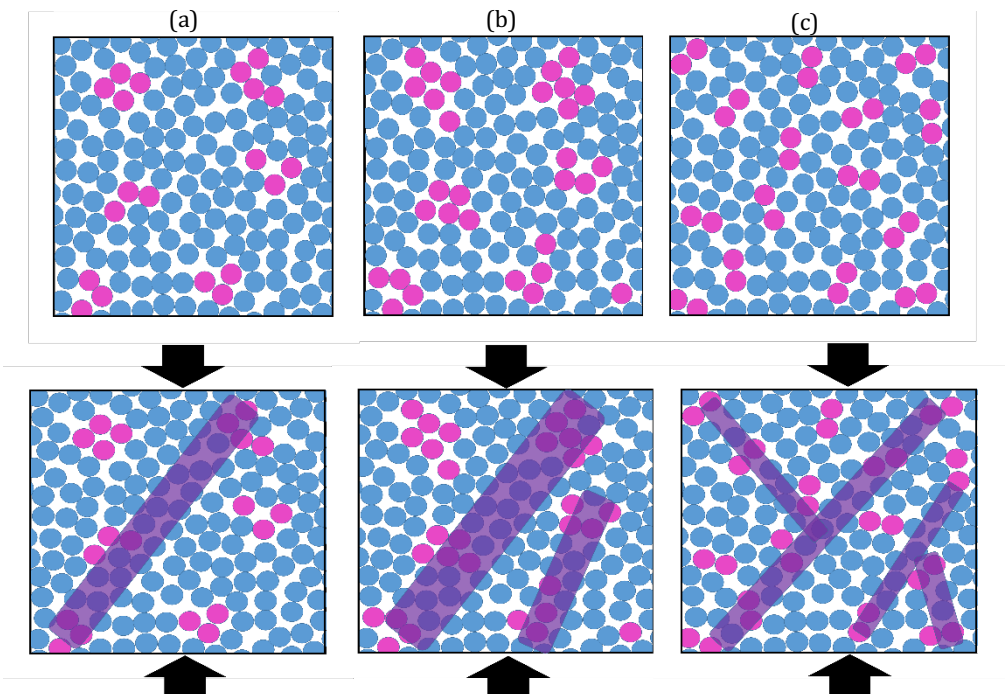

*Figure III-35: The upper part is a schematic illustration of different repartition and density of heterogeneities (pink regions). (a) has small heterogeneities but same repartition as (b). (c) has the same quantity of heterogeneities as (b) but they are more scattered. This intends to illustrate the difference between repartition and quantity. Shear band nucleation, illustrated in the lower part, is affected by the overall volume fraction **and** the repartition of heterogeneities.*

scenarios proposed. Figure III-35 (a) and Figure III-35 (b) exhibit two different quantities of heterogeneities with comparable reparations. Figure III-35 (b) and Figure III-35 (c) exhibit the same quantity of heterogeneities but with different repartitions. In Figure III-35 (b), heterogeneities are more concentrated in large clusters while on (c) heterogeneities repartition is more homogeneous, inducing smaller zones of low densities. Increasing the heterogeneities overall volume fraction will make their percolation easier. Big heterogeneities will involve a larger volume unit, so more energy to be activated, requiring more stress. By spreading out heterogeneities and reducing their size, one could achieve STZs activation with less energy, as a smaller amount of volume units will be involved.

In other words, increasing heterogeneities content without changing distribution could ease shear band formation. A finer spread of the same volume fraction of heterogeneities could promote smaller, more numerous shears bands, increasing shear bands interactions.

We have seen from the literature that the reported mechanical resistance of the $Zr_{56}Co_{28}Al_{16}$ is highly variable from one publication to another. These variations are never commented on in the literature. The $Zr_{56}Co_{28}Al_{16}$ alloy processed at SIMaP was tested in compression and exhibited important variability in its deformability. It should be stressed out that the obvious sources of variations like the casting diameter, the used set-up, different casting parameters (water cooling, temperature of the melt, heating method…) and the operator were accounted for and suppressed in our protocol. So even though these sources of variability may explain the differences in mechanical properties observed in the literature, they do not apply here.

Except for one sample (sample E), they all exhibited comparable yield strength, which does not match with the observation made from the gathering of the data from the literature (yield stress/plastic deformation correlation). Even though the correlation between yield stress and deformability is unclear, the study of the literature shows that deformability variations are usually correlated with yield stress variations. Shear bands development is much more pronounced for the sample which exhibited higher plasticity. This difference is confirmed by the analysis of the serrated flow during plastic deformation. Free-volume is considered as a type of heterogeneity and the presence of approximately 2 vol% of free-volume in the as-cast glass was demonstrated. We could assume, based on our discussion, that for higher deformability, the quantity of heterogeneities is larger, and that its spatial distribution is homogeneous.

We can summarize this first part of the discussion as follows:

What we observe:

- There is a **variability** in plastic strain of our alloy.
- Variability does not come from a change in the processing method.
- Developement on **shear bands** greatly varies between samples.
- Structural state of our glass is **heterogeneous** and a **free-volume** up to 2% is embedded as-cast.

What is known:

- Shear bands **control deformation**. Easier shear band formation favours ductility. Opposignly, delaying shear band formation favour fatigue endurance.
- Shear bands are nucleated from the **percolation of STZ**.
- STZ nucleate in regions of **lower density**, where atomic rearangement is easier.

What we do not know:

- How does the STZ nucleation correlate with the **glass structure?**
- Does the **STZ size** impact **shear band size** or development ?
- What is the link between the regions of low density and regions of high density (probably ISRO).

From these statements, one question arises: how do the presence and the repartition of the heterogeneities correlate with the glass structure of our specific $Zr_{56}Co_{28}Al_{16}$? Based on the observations made, both on the thermal properties and the mechanical properties and helped by the comparison with the Zr-Cu-Al ternary base, we can discuss our glass structure more specifically.

III.2.5. Question on the $Zr_{56}Co_{28}Al_{16}$ glass structure

Even though glasses are very disordered condensed matter, some degree of structural order exists. This subject has focused research for a long time and we do not intend to bring definitive answers. However, we think that it is interesting that we bring our perception of the matter. Metallic glasses can be described at several scales (Figure III-36):

- Considering **long-range order**, no periodic repetition of a specific motif can be observed. This is what defines the amorphous state. It corresponds to the investigations performed with XRD measurements or micro-hardness. XRD measurements do reveal interatomic distances but the measurement is an average over the long-range order.
- At the **intermediate range** between long-range order (LRO) and medium-range order (MRO), we define the intermediate range. It corresponds to the range of the STZ percolation, which forms the shear bands nucleus. This range was characterized by compressive testing, from which is extracted the shear bands dynamic.
- **Medium range order** is often described as soft and hard regions. It extends beyond the first neighbours. During nanoindentation mapping, we probe the soft and hard region repartition. Soft

regions and hard regions differ in their degree of short-range order [85]. The higher the degree of short-range order, the harder the region.

- A high degree of **short-range order** is observed in metallic glasses which is correlated to their high density [91]. It is based on the close-packing of atoms, with the basic unit being tetrahedral clusters of four atoms. This range was not experimentally investigated in this work. We use the literature to apprehend it.

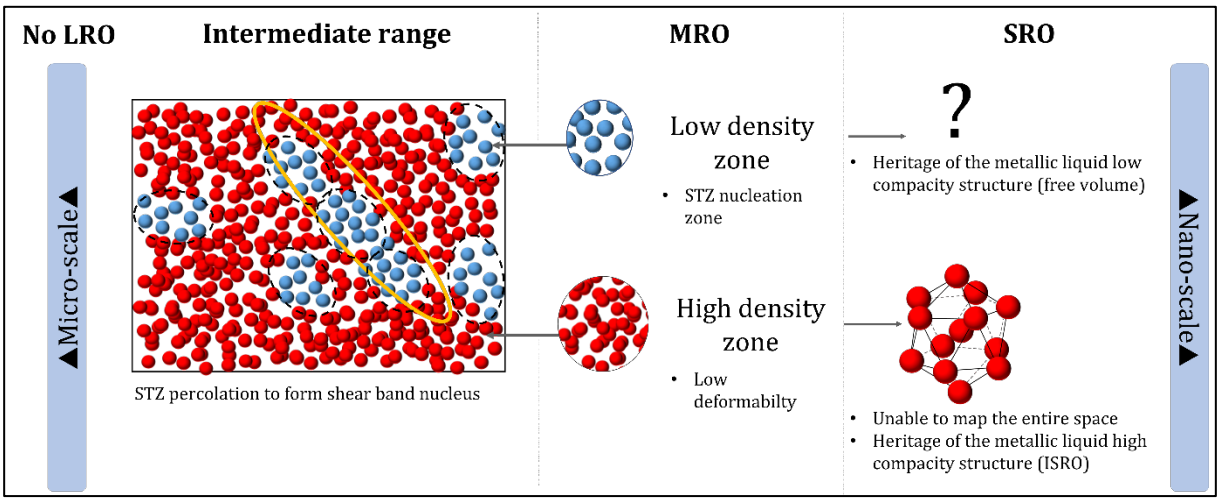

Figure III-36: Schematic representation of the several scales in the description of metallic glasses structures. Adapted from the work of Nomoto et al.. [85]

Tetrahedral clusters, such as icosahedral clusters, are structures of high density. Depending on the composition (constitutive elements and atomic fractions), the glasses will exhibit different structural patterns. One of the most discussed poly-tetrahedra is the icosahedral cluster, often referred to as icosahedral short-range order (ISRO). It is composed of 13 atoms: 12 atoms arranged as an icosahedron around a central atom [151] which results in a coordination number (number of nearest atoms, CN) of 12. But, as fully paving the space is impossible with the tetrahedron, the coordination number for such polyhedron can vary from 10 to more than 15. A. Inoue *et al.* proposed that SRO clusters with CN superior or equal to 12 have no free volume, while SRO clusters with CN numbers inferior to 12 have a certain amount of free volume [147]. Because it is impossible to fully pave the space with icosahedral clusters, there exist in the glass structure some degree of frustration between clusters.

To oversimplify, volumes units containing a high degree of tetrahedral clusters are considered as the denser regions, while volume units containing a low degree of tetrahedral clusters and the connexion between clusters (frustration = higher energy state) are regarded as the less dense regions. As mentioned previously, one of the major questions remaining is the link between the regions of high density and low density, in terms of volume fraction and repartition.

A sign of the short-range order structure can be found in the diffraction patterns acquired from $Zr_{56}Co_{28}Al_{16}$. A so-called "pre-peak" (as it is positioned at lower angles than the main scattering peak) is observed on the diffraction pattern of the as-cast 5-mm diameter $Zr_{56}Co_{28}Al_{16}$, as highlighted in Figure III-37. It was demonstrated [238–242] that the pre-peak is a signature of a specific arrangement of 3d-transition metal atoms in dense-packed polytetrahedral clusters with fivefold symmetry (like ISRO) extending over medium-range order (MRO). Table III-11 gives the electronic configuration of the metals considered throughout this chapter. Co, Fe and Ni are 3d transition metals, Zr is 4d transition metal and Al is a 3p post-transition metal. The d-band for Ni, Fe and Co is partially filled and close to the Fermi level (E_F). This promotes strong interaction with the *sp* electron of the Al atoms. The d-band from the Cu atoms in comparison has much lower energy (further from the Fermi level) and the d-band is (almost) filled. As a consequence, Cu-3d bands will have lower bonding energy resulting in higher interatomic distances [208, 243]. Hen *et al.* showed that substituting Co by Cu in a $Zr_{56.25}$-$(Co_{1-x}$-$Cu_x)_{25}$-$Al_{18.75}$ decreases T_g, T_x and T_l, increases ΔT, increases ε_p and decreases σ_y and E.

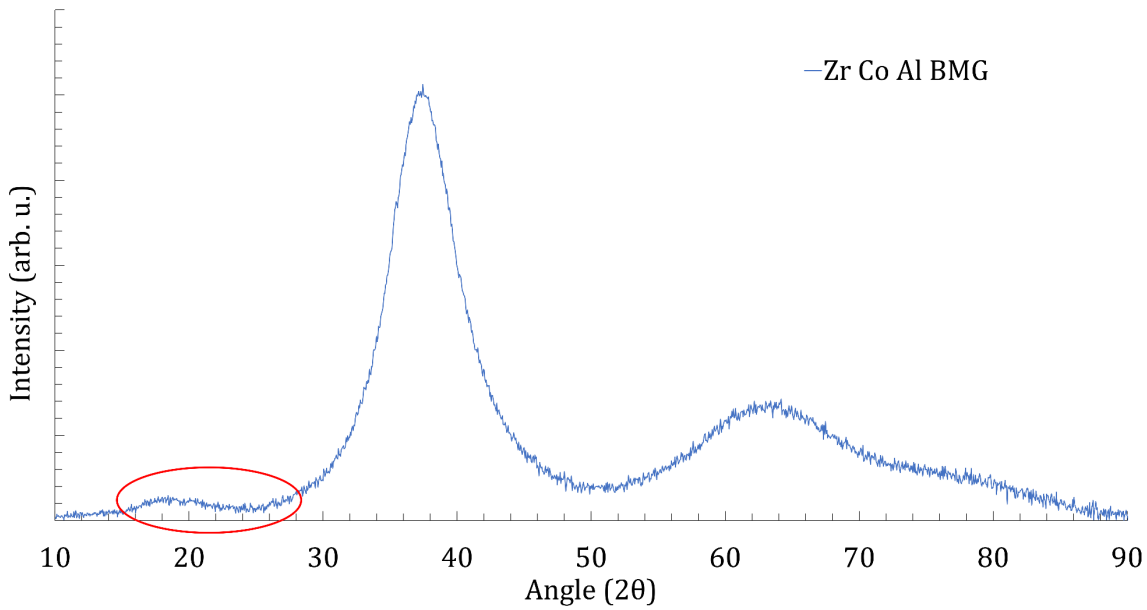

Figure III-37: XRD of the as-cast 5-mm diameter rod of a $Zr_{56}Co_{28}Al_{16}$ BMG. Red circle highlights the pre-peak, at around 18° for 2θ.

D. Yu *et al.* proposed a method in a series of papers to derivate potential cluster compositions from competing crystalline phases as it is reported that "microstructure in a glass former is similar to the local structure of competing phase" [151, 244, 245]. It is hard to compare Zr-TM-Al BMGs as it was demonstrated that simple substitution between Cu and Co (for instance) does not produce equivalent glass-forming ability. Yet some directions have been drawn in terms of the influence of alloy composition on the atomic packing structure [243]: higher Zr concentration leads to lower icosahedral fraction and lower TM and Al fractions also lead to a lower icosahedral fraction. Higher icosahedral fraction has been demonstrated to be potentially related to higher T_g [147, 246] as icosahedral clusters are found to be the

structural unit with the higher shear resistance and thermal stability. Aluminium addition has a dual action, by both favouring TM-centered and Al-centered icosahedron. Zr-Cu-Al BMGs reported in the literature have lower Al content compared to Zr-Co-Al BMGs (as discussed previously). This is another argument for a lower ISRO volume fraction in Zr-Cu-Al BMGs compared to Zr-Co-Al BMGs. The best glass formers in the Zr-Cu-Al system have lower T_g than the best glass former in the Zr-Co-Al system. The stability of our alloy could therefore be attributed to a high-volume fraction of very stable cluster configurations, such as icosahedral clusters which could also explain the high activation energies measured.

From this discussion, we do not want to draw any conclusions, but we are trying to highlight two questions:

- ***What are the structural differences between Zr-Cu-Al and Zr-Co-Al?*** We propose the hypothesis that Co favours a more structured configuration. This higher ordering could be the result of a higher fraction of icosahedral or icosahedral-like clusters.
- Also, ***we raise the question of the connection between these very ordered structures***. Because the $Zr_{56}Co_{28}Al_{16}$ processed at SIMaP does not exhibit similar properties to other $Zr_{56}Co_{28}Al_{16}$ reported in the literature, we suspect that it could have a specific structure. A better understanding of these differences should help get better control of the final properties of the glass.

We have seen through this chapter that the $Zr_{56}Co_{28}Al_{16}$ processed at SIMaP does share most of the properties reported for this specific alloy in the literature. However, we were surprised by its very high activation energies and the absence of crystallization signs after the first exothermic peak. One of the reasons for explaining such differences could be the processing method used at SIMaP. More specifically, we investigated the oxygen content. It was measured around 300 ppm for the as-cast glass, which is usually considered rather high. Unfortunately, the $Zr_{56}Co_{28}Al_{16}$ literature does not mention oxygen content, so we lack a comparison on this point. However, it becomes more and more clear that the oxygen content can strongly influence the glass structure, which would ultimately affect thermal stability [247].

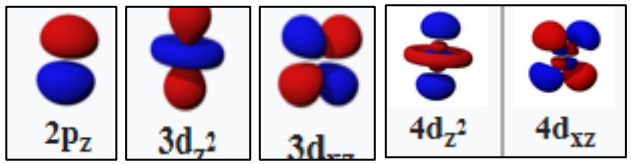

Element	Z	Period	Bloc	Kind	Group	Electronic structure		Pauling electronegativity	Density (g/cm³)	Fusion (K)
Al	13	3	p	post - TM	III B	[Ne] $3s^2\ 3p^1$		1,61	2,699	933
Fe	26	4	d	TM - late	VIII	[Ar] $3d^6\ 4s^2$		1,83	7,874	1811
Co	27	4	d	TM - late	VIII	[Ar] $3d^7\ 4s^2$		1,91	8,900	1768
Ni	28	4	d	TM - late	VIII	[Ar] $3d^8\ 4s^2$		1,88	8,902	1728
Cu	29	4	d	TM - late	IB	[Ar] $3d^{10}\ 4s^1$		1,9	8,960	1358
Zr	40	5	d	TM - early	IV A	[Kr] $4d^2\ 5s^2$		1,33	6,520	2128

Table III-11: Elements of interest electronic properties, density and fusion temperatures

III.3. Conclusions and optimisation axes

In this thesis work, results chapters are concluded in two parts: first a more "classic" general conclusion (along with some perspective) and next some "Take-Home messages", which are highlighting only the key messages of the chapter.

In this chapter, the $Zr_{56}Co_{28}Al_{16}$ has been characterized with potential applications to the biomedical sector in mind. The Zr-Co-Al ternary BMG base is compared to other Zr-based ternary BMG systems, such as Zr-Ni-Al, Zr-Cu-Al and Zr-Fe-Al, as they all belong to the Zr-TM-Al group proposed by A. Takeuchi and A. Inoue. We saw that simple transition metal substitution from the best glass formers of one ternary system to another does not procure a similar glass forming ability. By exploring the differences between the glass formers based on a chemical parameter (ΔH) and topological parameters (S_σ), we saw that Zr-Ni-Al and Zr-Co-Al have lower mixing enthalpy (lower in the negative values) and higher mismatch entropy, explaining their larger GFA compared to Zr-Cu-Al and Zr-Fe-Al. We did not choose the Zr-Fe-Al ternary base because of the too limited D_c achievable. The Zr-Cu-Al ternary base was ruled out because of its poor corrosion resistance.

Between the two remaining ternary bases, Zr-Co-Al was preferred to Zr-Ni-Al as Ni is prohibited in medical devices. Among the compositions reported for the Zr-Co-Al ternary base, $Zr_{56}Co_{28}Al_{16}$ was chosen for its combination of high GFA and promising mechanical properties. It is interesting to note that a new Zr-Co-Al BMG with high glass-forming ability and remarkable specific strength have been proposed recently (2019) with the composition $Zr_{52}Co_{25}Al_{23}$. [212] As an introduction to the glass characterisation, the importance of the casting parameters was highlighted. Injection casting is demonstrated to suppress surface crystallization. More details are available in the article in the supplementary material E.

The $Zr_{56}Co_{28}Al_{16}$ thermal properties were thoroughly characterized and compared to data extracted from the literature. Characteristic temperatures such as T_g and T_x are comparable to data previously published. One striking difference is the apparent lack of correlation between the glass transition and the heating rate. The glass transition temperature appears to be remarkably insensitive to the heating rate, which is against what was previously reported for $Zr_{56}Co_{28}Al_{16}$. This could be induced by a high oxygen content measured in this alloy as-cast.

Corrosion resistance was evaluated to be very satisfying, based on polarisation testing and static immersion. Static immersion revealed low releasing rates, far below the ISO standard requirement. Compared to Cu-bearing (pseudo-)ternary Zr-based BMG, our Zr-Co-Al exhibit better corrosion resistance. Even though the nature of passive films seems to be similar in Zr-Co-Al and Zr-Cu-Al (Zr- and Al-oxides), the resistance to stable pit growth in the Zr-Co-Al has enhanced thanks to the absence of Cu.

We carried out compressive testing which revealed average yield stress around 1926 MPa and an average ultimate strain of around 7%. These values are in the range of the literature. However, we demonstrated a strong variability in plastic strain between samples and studied the associated shear band development in each case. We also characterized the fatigue resistance following ISO standards. We demonstrated that the $Zr_{56}Co_{28}Al_{16}$ has a fitting fatigue endurance limit. More interestingly, we showed that by gradually increasing stress, we were able to reach fatigue endurance limits at least 10% higher.

The extensive characterisation performed on the $Zr_{56}Co_{28}Al_{16}$, which is presented in this chapter, validate the potential of this alloy for medical application. We followed, when it was relevant, the very specific standard of the biomedical industry and always achieved or overcame the key values defined by these standards. This opens the door for more characterisations, for instance on biocompatibility. This alloy could very well be employed for the processing of high precision surgical tools.

Mechanical testing raised the question of shear band development in our glass. Plastic deformation is favoured by the development of numerous shear bands while fatigue resistance is favoured by low shear band nucleation rates. We tried to link characterized properties at several length scales: the LRO, the intermediate range, the MRO and the SRO. We discussed in this chapter our understanding of the heterogeneous nature of the metallic glass structure and highlighted this heterogeneity by nano-indentation mapping. We argued that free-volume quantity should influence shear band development, but we propose that the repartition of the free-volume could have a strong influence.

Finally, we questioned the structure of the $Zr_{56}Co_{28}Al_{16}$ at the SRO and MRO. We showed that this alloy could have a strong proportion of very ordered structures (such as icosahedral clusters). We also tried to link the differences observed between the Zr-Cu-Al and the Zr-Co-Al using the SRO. Namely, we think that the presence of Co promotes very ordered structures, which for instance could correlate with the increase in T_g or Young's modulus. We do not bring answers but we asked questions. We propose the $Zr_{56}Co_{28}Al_{16}$ is more structures than its Zr-Cu-Al counterparts. We will in the following chapter investigate this supposed stability. We will try to alter the structure, either toward a lower energy state (relaxation) or a higher energy state (rejuvenation). By comparing our results to the Zr-Cu-Al, we will try to discern the impact of structural ordering state on the ability one has to alter the structure.

III.4. Take-Home Messages

In this chapter, we exposed the study of the **$Zr_{56}Co_{28}Al_{16}$** bulk metallic glass in its as-cast state:

- This glass belongs to the "**early transition metal + late transition metal + aluminium**" ternary glass formers. In the same group are for instance Zr-Ni-Al, Zr-Fe-Al and **Zr-Cu-Al**.
- We exposed that Zr-Co-Al and Zr-Cu-Al exhibit several differences: Zr-Co-Al has lower mixing enthalpy and higher mismatch entropy. Also, binary Zr-Cu glass formers exist while Zr-Co do not.

We **characterized the $Zr_{56}Co_{28}Al_{16}$** processed at SIMaP Lab. and compared the results to available data in the literature, on the same alloy as well as other Zr-Co-Al and Zr-Cu-Al glass formers:

- The **critical diameter** of the $Zr_{56}Co_{28}Al_{16}$ is at least 5 mm. **T_g** is coherent with the data reported in the literature. The $Zr_{56}Co_{28}Al_{16}$ exhibits a rather unusual thermal stability, characterized by **high activations energies** and no signs of crystallization after thermal treatments above the first transformation peak of the DSC scan. This may be related to **its important oxygen content** (around 300 ppm).
- **Corrosion resistance** is very satisfying for biomedical applications. The glass exhibits spontaneous passivation in NaCl (9 $g.L^{-1}$) at body temperature. Corrosion resistance is **greatly superior compared to Zr-Cu-Al** ternary alloys which confirm the detrimental role of Cu. Immersion resistance is also satisfying as the amount of released compound is well below the medical standard.
- **Yield stress** under **compressive loading** is constant and the **plastic strain** reached by the glass exhibits **variability** which is usual for Zr-based BMG. This variability is rarely mentioned in the literature. In our work, a **specific analysis** regarding **shear banding** is proposed, where the shear band activity is quantified by the analysis of the **serrated flow** revealing a **two-stage** process: **stable** propagation and **catastrophic** propagation. The transition occurs when stress drops reach approximately 25 MPa in our case and this marks the beginning of the **localization of the deformation** in a single shear band.
- **Fatigue resistance** is characterized following a specific test developed for the dental industry and the $Zr_{56}Co_{28}Al_{16}$ overcome the medical standard-imposed threshold. We showed that our glass can be "**educated**" to fatigue resistance. Gradually increasing the stress might increase the ultimate fatigue resistance.
- We experimentally verified that the $Zr_{56}Co_{28}Al_{16}$ has a **heterogeneous structure** by nano-hardness mapping and statistical analysis. As suggested by the literature, we also noticed that our glass may possess very **dense local structures** (icosahedral-like), based on the presence of a "**pre-peak**" (before 30°) in XRD measurements. We discussed that compared to copper, cobalt in Zr-based alloys may promote these icosahedral-like clusters.

Chapter IV:

Evaluation of the structural state modification induced by thermal and mechanical treatments

IV. Evaluation of the structural state modification induced by thermal and mechanical treatments

In Chapter III, we have thoroughly characterized the as-cast $Zr_{56}Co_{28}Al_{16}$. We have highlighted the superior stability of our alloy, characterized by its high activation energies for glass transition and crystallisation. We have also shown, thanks to mechanical testing, that the compressive yield stress is very reproducible but significant variations are observed concerning plastic strain. We have also tried to establish links between the observed properties of our alloy and its supposed structure. We have also concluded that the heterogeneity volume fraction in our alloy plays a crucial role in the properties, but we also proposed that the heterogeneities repartition could be at play. We have seen from Chapter I.3.4.1 that mechanical properties can be tuned by appropriate mechanical or thermal solicitation. More specifically, we reported two main mechanisms: relaxation and rejuvenation. Here we consider relaxation and rejuvenation in terms of energy. The glass is relaxed when it is brought to a lower energy state and is rejuvenated when brought to a higher energy state. This is usually related to respectively a decrease or an increase of the heterogeneity volume fraction.

In this chapter, we will first investigate the behaviour of our alloy when subjected to thermal-induced relaxation. We will see the influence of relaxation on mechanical properties, through compression, dynamical mechanical analysis, and nano-indentation. In the second part, we will investigate mechanical rejuvenation. The main mechanical rejuvenation technics involve permanent geometry alteration of the metallic glass part. This must be avoided as it diminishes the attractiveness of metallic glasses for the casting of near net shape parts. Here we will pursue experimental investigations on rejuvenation via elastic cycling started by O. Baulin. Simulation works have been published on such rejuvenation technics, but to the best of our knowledge, no experimental works have been published other than O. Baulin PhD manuscript (MATEIS Lab. in collaboration with SIMaP)[96].

To sum up, this chapter intends are twofold: first to see how we can alter the mechanical properties of our very specific $Zr_{56}Co_{28}Al_{16}$ BMG, either by bringing it to a lower energy state or a higher energy state. Second, by doing so, we intend to gain knowledge on our alloy structure, to better understand its specificities.

IV.1. Thermal-induced structural relaxation of the $Zr_{56}Co_{28}Al_{16}$

We have seen from Chapter III that our alloy appears to be very stable upon heating. This was characterized by a very stable glass transition T_g, almost independent of the heating rate. It is of high interest to study the impact of fast or prolonged relaxation procedures on mechanical properties. It will help us further understand the structure of our alloy. It will also assess the potential of this alloy for applications in hot environments or thermoforming (which is the subject of a second PhD project at SIMaP Laboratory).

IV.1.1. Influence on mechanical properties

From the review of the literature, we have seen in Chapter I.3.4.1 that relaxation is a natural process for metallic glasses, as the amorphous configuration is metastable. We also reported that relaxation (shifting of the glass state towards a more stable configuration) is usually related to the reduction of the free-volume fraction. In a first approach, we will compare our alloy mechanical behaviour between the as-cast state and after short, near T_g-annealing. This could further confirm our alloy remarkable stability at sub-T_g temperatures.

IV.1.1.1. Short time thermal relaxation

We performed 3 different treatments on our alloy at the same temperature but at different times. The temperature was set at T_g – 30 K, namely 720 K. Three durations were chosen: 20, 40 and 60 minutes. The hardness was measured after the annealing treatments. The as-cast Vickers hardness is measured to be 527 ± 5 HV. Hardnesses are 534 ± 4 HV, 530 ± 7 HV and 525 ± 3 HV for 20, 40 and 60 min of annealing,

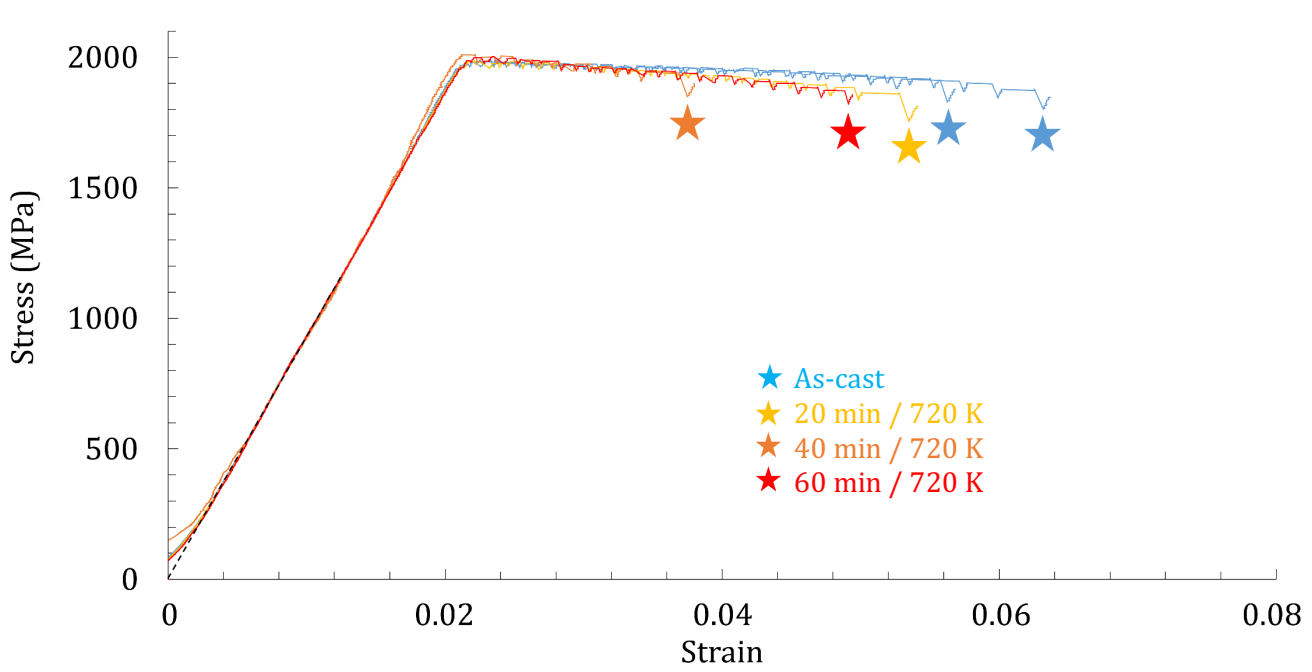

Figure IV-1: Strain-stress curves for as-cast $Zr_{56}Co_{28}Al_{16}$ (blue) and annealed at 720 K for several times: 20 (yellow), 40 (orange) and 60 min (red).

respectively. It suggests that hardness is not affected by such short-time annealing treatments. The corresponding strain-stress curves are reported in Figure IV-1.

All the samples presented in Figure IV-1 are machined from the same BMG rod, produced by injection casting. For the compression testing, we used the same set-up as the one from which we obtained the results presented in Chapter III.2.3.1. From Figure IV-1, we observe that the two as-cast samples have reached ultimate strains of 6.4% and 5.7%. The annealed samples have reached respectively 5.4%, 3.8% and 4.9% for annealing times of 20, 40 and 60 min. Figure IV-2 shows yield stress (a) and plastic strain (b) against the annealing time. First, we note that the as-cast samples behaved similarly that the as-cast samples presented in Chapter III.2.3.1, even though they were machined from a different rod. Second, the deformability variation has to be taken with caution. We have exhibited in Chapter III.2.3.1. that our alloy seems to exhibit a non-negligible variability in its deformability. Having this in mind, we can report that the three samples that were subjected to thermal treatment, have lower deformability than the two as-cast samples. However, there is no clear correlation between the annealing time and the deformability. The yield and ultimate stresses are also very similar. A slight increase with annealing time could be seen but the variations are of small magnitude: less than 20 MPa between the as-cast yield stress and the highest measured yield stress (sample treated for 40 min). These variations are of lower magnitude than the variations among the as-cast samples tested in Chapter III.2.3.1.

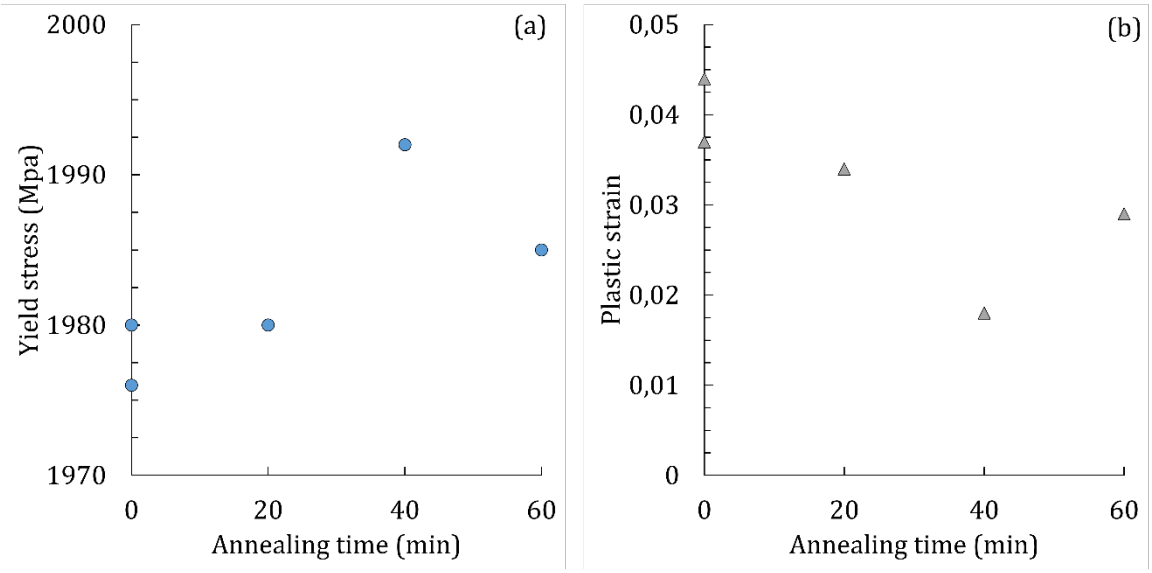

Figure IV-2: (a) yield stress values against the annealing time and (b) plastic strains obtained from the stress-strain curves in Figure IV-1.

The basic study of the strain-stress compression curves, therefore, does not give us enough information to picture any clear impact of this relaxation treatment on the compression behaviour of our alloy. The serration pattern analysis, observed during the plastic strain of our alloy could be in this case very valuable (see Chapter III.2.3.1). Figure IV-3 represents the stress drop analysis for one as-cast sample and the three heat-treated samples. The analysis is based on the same method as previously.

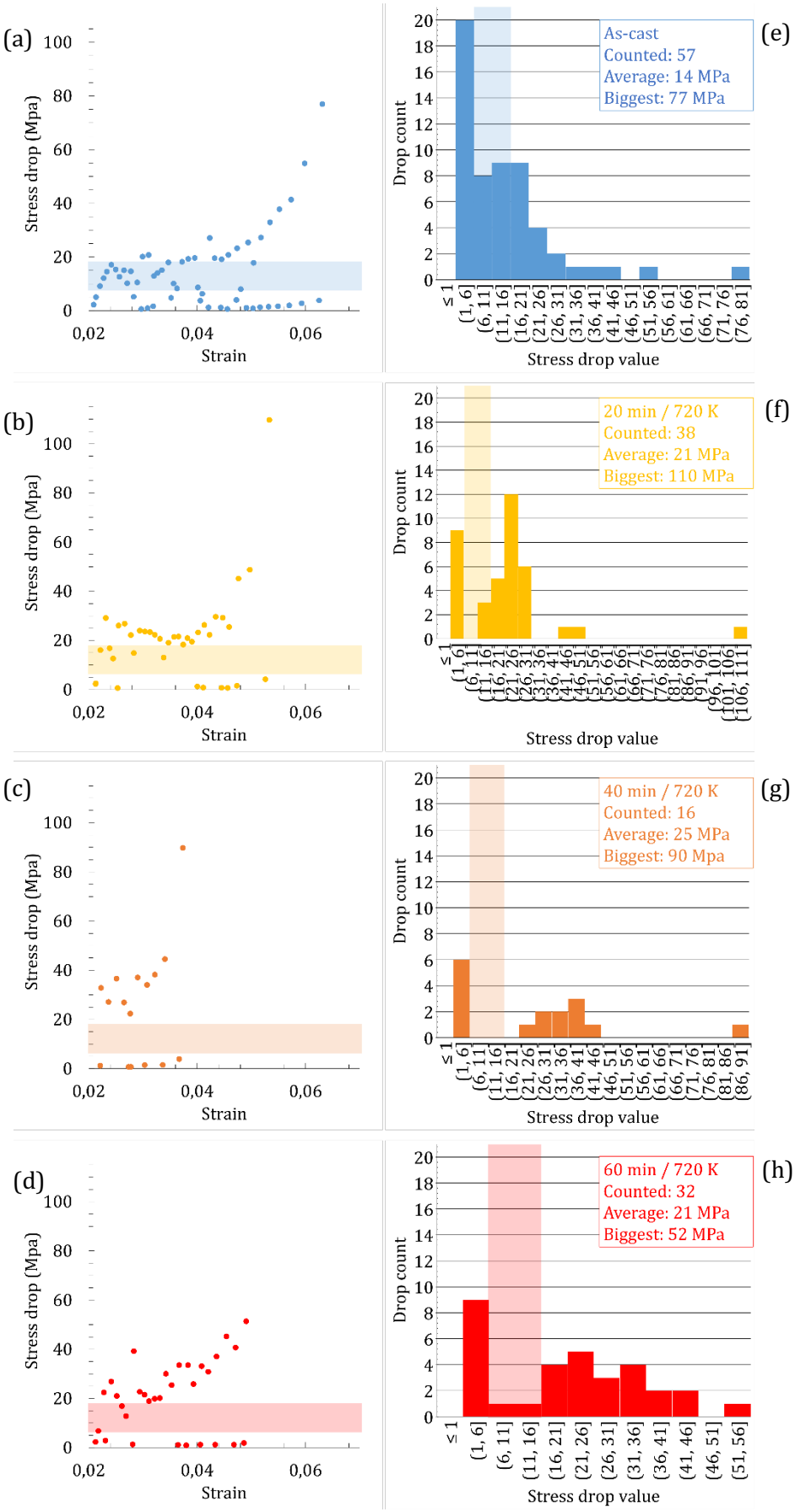

Figure IV-3: (a), (b), (c), (d) are respectively the stress drop repartition as a fucntion of strain for a $Zr_{56}Co_{28}Al_{16}$ as-cast and annealed at 720 K for 20, 40 and 60 min; (e), (f), (g), (h) are respectively the repartition of the stress drops based on their magnitude for each sample.

In Figure IV-3 (a), (b), (c) and (d) are reported the serrations (stress drop), where the magnitude of each stress drop is plotted against the strain level at which it happened. The as-cast sample (a) has a similar stress drop pattern to what was reported in the previous chapter for samples exhibiting "medium" ductility. We first observe the steady propagation regime followed by a more catastrophic propagation regime, leading to failure. The continuous presence of stress drops of small magnitude (less than 20 MPa) carry the plastic deformation and translates in the serration statistical repartition (Figure IV-3 (e)) which can be fitted by a power-law with a square exponential decay function. Interestingly, if we observe the stress drops magnitude repartition of annealed samples (Figure IV-3 (b), (c), (d)), we see that compared to the as-cast sample, there is a lower number of small serrations (namely between 7 and 17 MPa). This results in a gap in the statistical repartition of the serrations between the few very small serrations detected (1 MPa to 6 MPa) and the larger serrations (17 MPa and more). We made the statement in Chapter III that the variety in the stress drop magnitude in the first serration regime is what allows the deformed material to remain in this regime longer, hence reaching higher ultimate strains. Moreover, none of the heat-treated samples exhibits the Self Ordered Criticality (SoC) serration repartition while the as-cast sample does (Figure IV-3 (e), (f), (g),(h)).

Therefore, it appears that even if the macro-scale compression behaviour among the annealed and as-cast samples looks similar, the serration dynamic during the plastic deformation is different. This result highlights the significance of the serration analysis when investigating the deformation behaviour of a sample in a specific state. The absence of "medium" serrations results in a higher average stress drop value: 150%, 179% and 150% of the average stress drop value of the as-cast sample for respectively the samples treated for 20-, 40- and 60-min. This is higher than for any of the three as-cast samples studied in Chapter III. Based on the understanding of the serrated flow mechanic and what was exposed in Chapter III, we believe that: the absence of medium-range serration is the result of a less homogeneous spatial distribution of the local strain in our sample. The strain is concentrated in a small number of shear bands, moving through "big" steps, instead of being spread out via multiple shears bands, resulting in smaller band movements. The reduction of the number of shear band nucleated can be caused by a smaller amount of free volume (flow units), at the origin of the nucleation of the STZ (the precursors of shear bands). Although one might detect changes that may affect the plastic strain dynamic, no changes are observed in the alloy yield stress with annealing up to 60 min at T_g – 30 K. The relation between the yield stress of the alloy, i.e. the initiation of plasticity and the plastic strain of the alloy is still unclear.

For comparison, we performed a similar relaxation treatment on a $Zr_{57}Cu_{20}Al_{10}Ni_8Ti_5$ mastered at SIMaP. Figure IV-4 shows the stress strains curves obtained on two samples of the Zr-Cu-Al-Ti-Ni, one as cast (yellow curve) and one relaxed (blue). After thermal treatment (60 min at T_g -30 K), the sample reaches an ultimate strain of 4.5% before failing. This is approximately half the strain of the as-cast sample. Serration analysis was not performed as unfortunately compression tests on Zr-Cu-Al-Ni-Ti

BMGs were not performed on the same equipment (the original machine was unavailable at the time). This second machine has too much noise on both load and displacement to allow for reliable serration quantification. We observe that the relaxation process induces a reduction of the plastic strain and an increase in the yield stress. It appears that the Zr-Cu-Al-based processed at SIMaP alloy is more sensitive to relaxation than the $Zr_{56}Co_{28}Al_{16}$ processed at SIMaP.

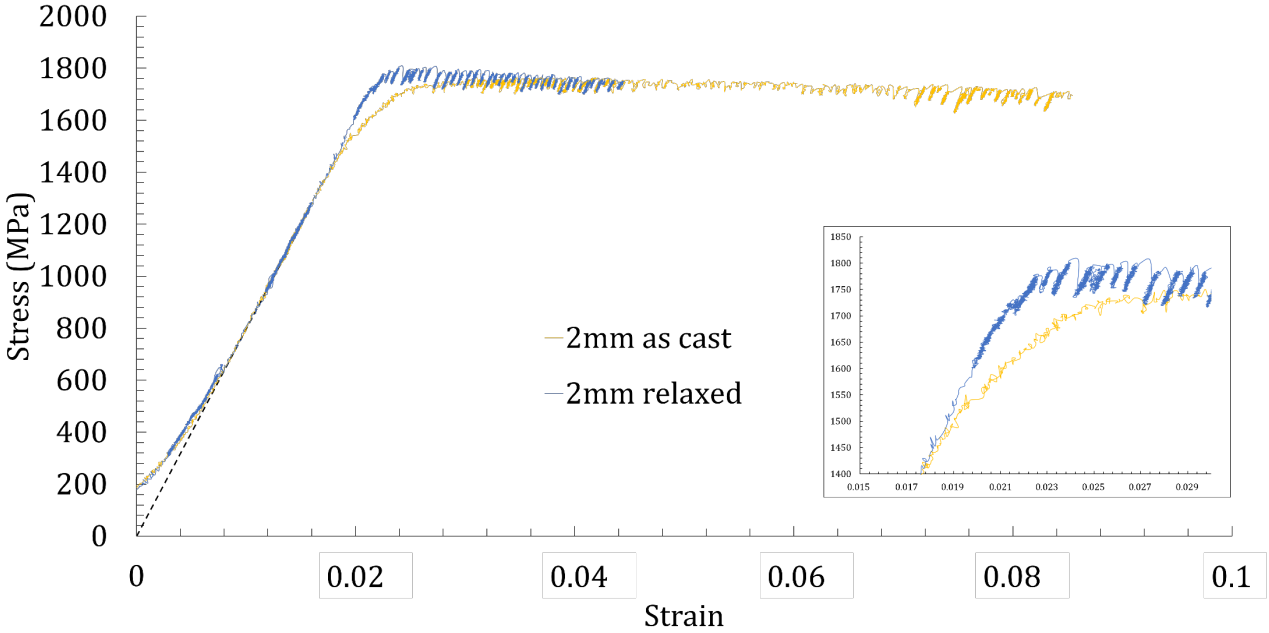

Figure IV-4: Stress-strain curve of the as cast $Zr_{57}Cu_{20}Al_{10}Ni_8Ti_5$ and after relaxation (T_g – 30 K for 1h). The inset highlights the yield stress of the two samples.

Once again, we highlight the apparent stability of our alloy in its as-cast state. This could be better understood by having a better view of the local rearrangement happening during the relaxation of our glass. To study the nature of local motion in our amorphous material and atomic rearrangements during heating, mechanical spectroscopy experiments were performed.

IV.1.1.2. Relaxation and structural transformation measured during DMA and XRD measurements.

This kind of experiment is referred to as dynamical mechanical analysis (DMA). The details of the experimental setup are described in Chapter II.3.3.7 and ref [248]. As a cyclic load is applied, a cyclic deformation is measured, and the time lag is expressed as a phase lag δ. When deformation is applied to a sample of metallic glass, it is not perfectly elastic and some energy is ultimately lost in a viscoelastic response. Therefore, a storage shear modulus (G') related to the elastic response and a loss shear modulus (G"), related to the viscoelastic response can be calculated. The loss factor is expressed as:

$$\tan\delta = \frac{G''}{G'}$$

IV-1

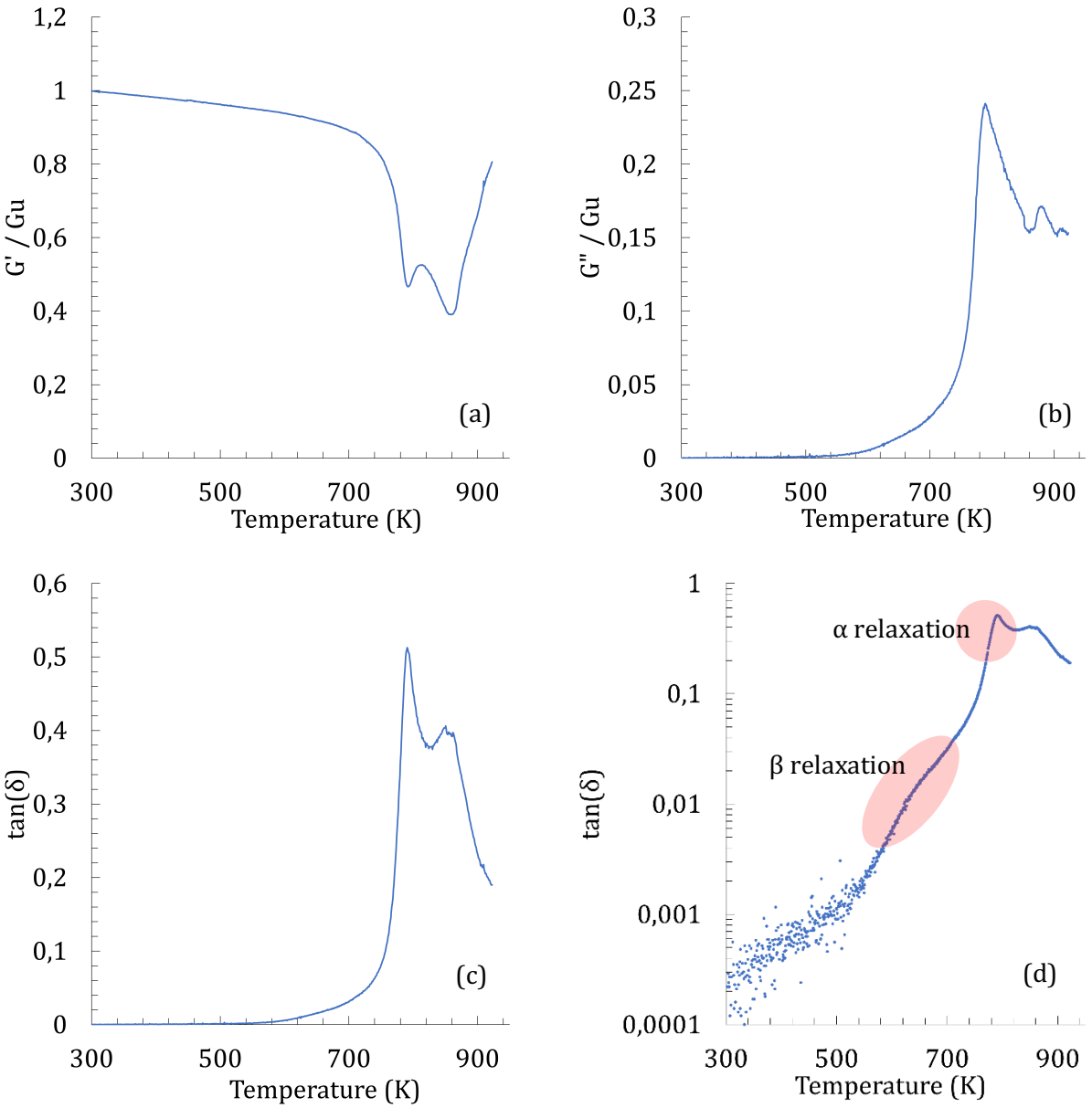

Figure IV-5: DMA results from a $Zr_{56}Co_{28}Al_{16}$ as cast injection 1 mm-thick casted plate. (a) and (b) respectively G', storage modulus and G", loss modulus as a function of the temperature. (c) loss factor tan(δ) as a function of the temperature. (d) same data on a logarithmic scale to highlight variations at low temperatures.

The higher tan(δ), the higher the energy loss during a loading cycle, meaning the higher the atomic mobility. Values of G' and G" are normalized by the value of the module at 300 K (G_u). Figure IV-5 shows G', G" and tan(δ) for the as-cast $Zr_{56}Co_{28}Al_{16}$. With increasing temperature, the storage modulus linearly decreases from 1 at 300 K to 0.92 at 600 K. With further increase of the temperature, the storage modulus dramatically decreases down to 0.33. This corresponds to the α relaxation of the glass and the entrance into the supercooled liquid region (SLR). A minimum value is reached at 793 K, which is very close to the temperature of 795 K measured via DSC at 20 K/min for T_{p1}. DMA measurements are performed at a heating rate of 3 K/min. With lower cooling rates, characteristic temperatures usually shift toward lower

temperatures. T_{p1} measured at 5 K/min using DSC was 783 K, which is still quite close to the value measured by DMA. A second minimum is reached at 860 K and a value of 0.34 for G'. This is very close to the temperature of 862 K measured for T_{p2} via DSC at 5 K/min.

With increasing temperature, loss modulus is almost null from 300K to 650 K. With further increase of the temperature, the loss modulus starts to increase. The increase accelerates dramatically after 700 K to reach a maximum value of 0.19 at 798 K. This value is very close to the temperature corresponding to the minimum value of G'. This corresponds to the glass relaxation and the start of the first transformation event (T_x). After 798 K, the value of G" decrease down to 0.13 at 867 K, where it starts to increase again. A second peak is reached at 885 K where G" equals 0.15. Unlike for G', where the maximum values for the two peaks were close, here the value of the second peak is 22% lower (3% differences for the two peaks if G'). The peak value for the second peak is reached 25 K later for G" than G'.

On the graph illustrating tan(δ) (see Figure IV-5 (d)), it can be observed that there is a small bump in the curve from 560 K to 793 K. This can probably be related to β relaxation which, to the best of our knowledge, was not reported for $Zr_{56}Co_{28}Al_{16}$ in the literature before. This is also observable while plotting the loss modulus G" on a logarithmic scale (not shown here). The peak observed on tan(δ) is characteristic of the α relaxation. α relaxation is related to the glass transition, implying that it involves large-scale atomic movements. β relaxation on the other hand is related to the local movements of atoms, activated at lower energies [17, 249]. β relaxation is usually linked to the short-range order and observing this β relaxation further confirms what was observed in Chapter III. This is another sign supporting the idea of a strong short-range order in the studied glass.

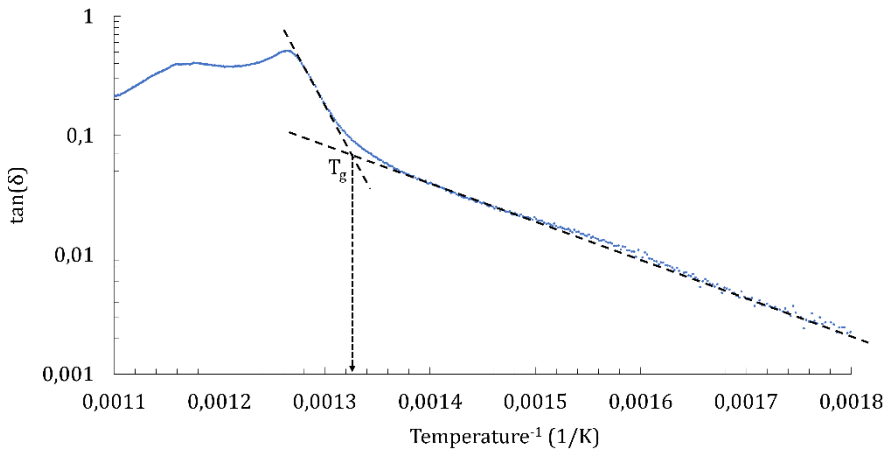

Figure IV-6: Identification of the T_g position during DMA experiment, at heating rate of 3 K/min

Interestingly, we exhibit another sign of the apparent stability of the glass when it comes to T_g. Even at 3 K/min, T_g is located very close to the value obtained thanks to DSC at 20 K/min. Using DMA, we experimentally measure a T_g at 754 K. Figure IV-6 shows the T_g position based on the representation of tan(δ) as the inverse of the temperature (1/K).

Samples used for DMA measurements were cast as 1 mm-thick plates. We can compare with data reported by Qiao *et al.* on the same alloy, using the same set-up, but using plates of 2 mm in thickness [129]. According to their data, G' peaks at 784 K and 849 K with G' values of 0.32 and 0.36 respectively. This is of rather good agreement with the data we obtained, on peaks temperature as well as on G' values. However, G" peaks at 0.29 for the first peak in the work of Qiao *et al.* while our first peak reaches 0.19. A higher loss modulus is related to higher atomic mobility. Interestingly, their second peak reaches 0.15 which is more in the range of our data (0.13). This could be explained by a more pronounced first transformation, leading to the apparition of more crystals, or a more pronounced α relaxation, as their material could contain a larger fraction of free volume in the as-cast state.

We compared DMA results for Zr-Co-Al and Zr-Cu-Al to try to understand the influence of the late transition metal on atomic mobility. We looked at $Zr_{50}Cu_{40}Al_{10}$ [250] and $Zr_{46}Cu_{46}Al_8$ [101] (see Figure IV-7 with diagrams extracted from [101, 250]). For Zr-Cu-Al, the storage modulus reaches almost 0 after the α relaxation and before the initiation of crystallization, while it remains superior to 0.3 in the case of the $Zr_{56}Co_{28}Al_{16}$ (both in our case and in [129]). This could be related to a more stable and wider SLR region for the Zr-Cu-Al alloy which is ultimately related to higher ΔT. With a higher SLR region, the gap between the glass transition and the crystallization is more pronounced, hence G' "has more time" to further decrease before increasing due to crystallization processes.

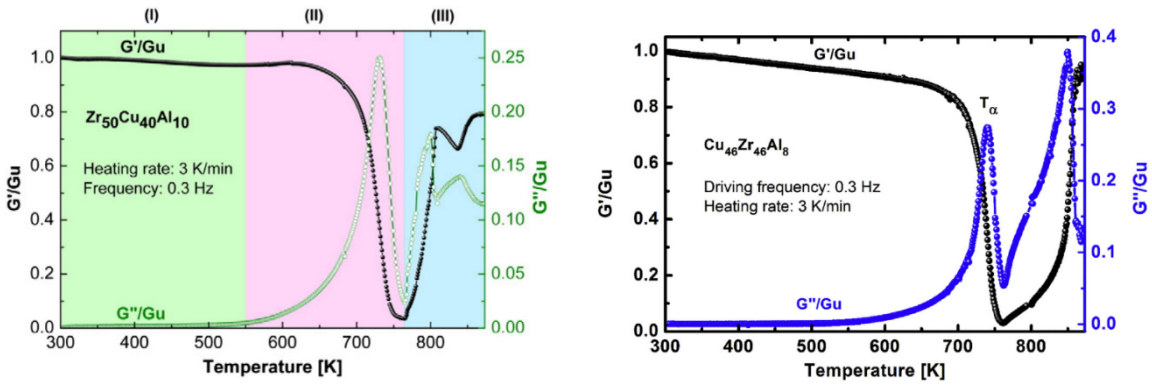

Figure IV-7: Normalized storage (G') and loss modulus (G") for $Zr_{50}Cu_{40}Al_{10}$ and $Zr_{46}Cu_{46}Al_8$ bulk metallic glasses as a function of temperature. Heating rate is 3 K/min and frequency is 0.3 Hz in both cases [101, 250].

Thanks to DMA measurements on as-cast samples, we can conclude that:

- The stability of the glass transition of our alloy is confirmed. The T_g measured during the DMA experiment is very similar to the one measured through the DSC measurements presented in Chapter III.2.1, despite very different heating rates between the two procedures.
- The glass transition is directly followed by the transformation process. As a result, the elastic modulus G' does not reach 0, as it can be observed in some Zr-Cu-Al alloys.

- Before the main relaxation (α), a secondary transition β is observed. This was not reported before for $Zr_{56}Co_{28}Al_{16}$. It is the sign of atomic rearrangement at a short.

From the DMA measurements, we have a better view of the relaxation events happening during annealing. We performed *in situ* XRD measurements. This allows us to have access to two pieces of information: the evolution of the average interatomic distance (based on the position of the amorphous broad peak of the XRD pattern) and the dispersion of the first neighbour distance in the probed volume. The lower the dispersion is, the more organised the glass is. Figure IV-8 shows the XRD measurements from room temperature to 985 K. The effective heating rate is a little lower than 3 K/min.

From Figure IV-8 we see that no crystallization signs (intense sharp peaks) appear before 847 K. This is almost 80 K above the measured T_x through DSC measurements at 5 K/min. It confirms that in the case of our $Zr_{56}Co_{28}Al_{16}$, no crystalline peak is detected by XRD after the first exothermic peak, usually associated with crystallisation. We believe that the first peaks observed from 847 K are related to the second exothermic event observed through DSC.

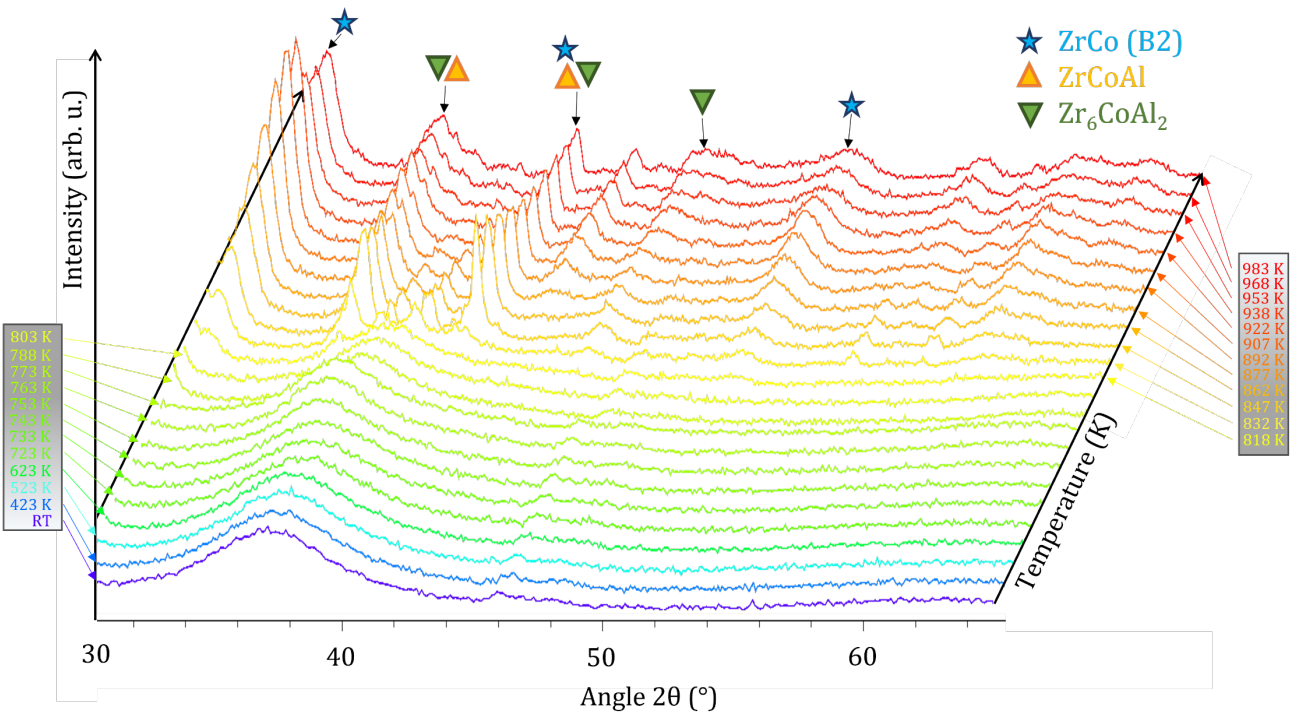

Figure IV-8: In-situ XRD measurements, from room temperature (300K) to 985 K. The heating rate between two consecutive measurements is 5 K/min, and each scan requires 4 min and 40 sec at a constant temperature. The resulting average heating rate is approximately 2.84 K/min.

By fitting the XRD measurements, we can track the shift of the amorphous bump and the variation of the dispersion. Both the position of the bump and the full width at half maximum (FWHM) are represented in Figure IV-9. We observe that the bump shifts toward higher angular values (corresponding to shorter interatomic distances) with increasing temperature. This means that the excess free volume annihilation is of greater magnitude than the thermal expansion of the glass. This phenomenon has already been reported on other metallic glasses [251]. Between 723 K and 733 K, the densification increases, which is probably related to the initiation of the glass transition T_g. From 743 K, we see that the FWHM starts to rapidly decrease. It suggests that from this point, the order degree in our glass increases. This is related to the inflexion point of the glass transition (from which it starts to slow down) or the start of the first transformation (T_x), which is measured at 770 K in a DSC measurement at 5 K/min. This confirms that our glass gets denser, mostly throughout the α relaxation (close to T_g) and supports the idea that there is a particular temperature from which the glass starts to be more structured and homogeneous. However, it is unclear if this happens as early as the glass transition or if this happens later on. Even though we have exhibited that our glass T_g is very stable, it is hard to compare temperatures

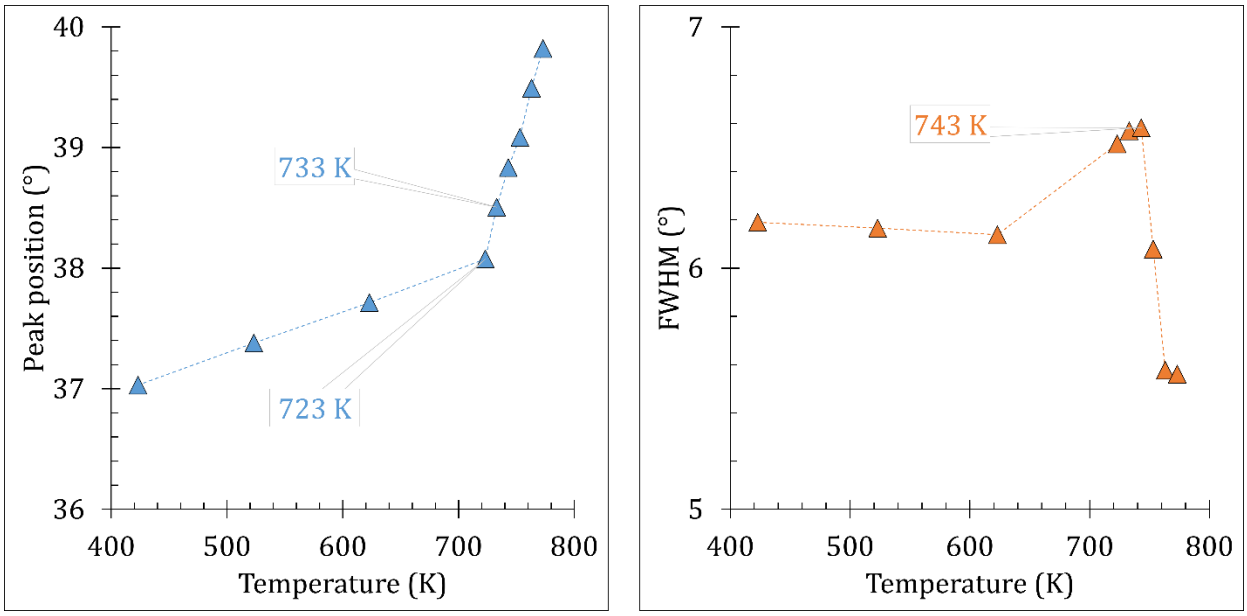

Figure IV-9: peak position (left) and FWHM (right) from the fit of the amorphous hump in Figure IV-8.

extracted from several measurements for which the heating rate greatly varies.

The DMA experiment along with in-situ XRD measurements and the compression tests after a short time of annealing gave us some insight into what happens during the relaxation of our alloy. It appears that short time annealing has a limited impact on compression behaviour. However, longer thermal treatments (DMA and XRD) confirms that the structure evolves. It is interesting to push this further by performing a longer thermal treatment at a lower temperature and observing the influence on its structure. By doing so, we are trying to maximise differences between the as-cast and the relaxed samples.

IV.1.2. Influence of long-term relaxation on $Zr_{56}Co_{28}Al_{16}$'s structure

In chapter III, we have used micro and nanoindentation to probe local heterogeneities that can be revealed by local variation of the hardness. Compared to Vickers's hardness, nano-indentation probes a much lower volume which is a key to revel such local variations. These variations are assumed to result from density variations in the glass with zones of lower density containing a larger volume fraction of flow units (e.g., free volume).

To fully relax our alloy, we performed thermal annealing on $Zr_{56}Co_{28}Al_{16}$ samples at 0.9 x T_g (675 K) for 48 hours. This treatment is similar to the annealing treatment performed by Liu *et al.* [105] to measure free-volume content (on a $Zr_{55}Cu_{30}Ni_5Al_{10}$ BMG). It results in a volume reduction of 2% as presented in Chapter III. Figure IV-10 illustrates the Vickers' hardness measured on our alloy in the as-cast state and after relaxation. We observe that the average hardness increases from 527 HV to 571 HV. The average hardness increase is associated with the reduction of the free-volume volume fraction. The absolute standard deviation between the two measurements is roughly the same (5.4 HV and 5.0 HV for the as-cast and annealed samples, respectively). If we normalize this value by the average hardness measurement, it is also rather similar (about 0.1%). An increase of the hardness of our $Zr_{56}Co_{28}Al_{16}$ is accompanied by an increase of Young's modulus, measured by vibrational technique (see Chapter II), from 93.4 GPa to 98.6 GPa. Table IV-1 gathers all the results from the Vickers hardness measurements, for the as-cast and relaxed sample. From the micro-hardness measurements, we can conclude that our alloy is on average harder after the annealing procedure. On a micro-level, we have reduced the free volume volume fraction. Although to get a finer appreciation of the local variation, we need to use nanoindentation.

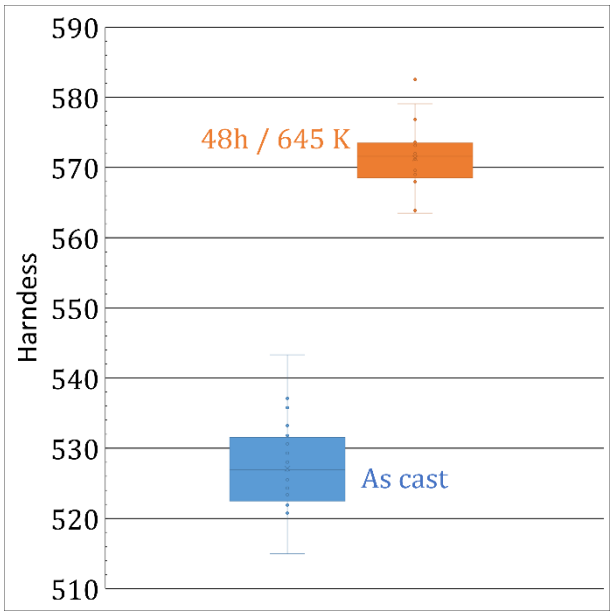

Figure IV-10: Vickers Hardness as-cast (blue, left) and after thermal annealing for 48h at 675 K (orange, right)

Microhardness	Mean	Min.	Deviation of min.	Max.	Deviation of max.
As-cast (HV)	527 ± 5.4	515	2.3%	543	3.1%
Relaxed (HV)	571 ± 5.0	564	1.4%	583	2.0%

Table IV-1: Mean, standard deviation, minimum and maximum from the Vickers-hardness measurements performed on the $Zr_{56}Co_{28}Al_{16}$ BMG, as cast and relaxed for 48h at 675 K.

Figure IV-11 shows the probability density function (PDF) for the raw (a) and normalized (b) nano-hardness measurements of a $Zr_{56}Co_{28}Al_{16}$ 5 mm-diameter rod in the as-cast state and after

relaxation at 0.9 x T_g (675 K) for 48 hours. The more scattered the data are, the higher the heterogeneity level is assumed. The average hardness gives a qualitative indication of the free volume volume fraction. For instance, having the same average value but a lower standard deviation would mean that there is the same amount of free volume in the glass but that the spatial distribution is more homogeneous (smaller, more numerous domains). Table IV-2 gather the statistical data extracted from the analysis of 100 nano-indentation measurements for each sample.

Nano-hardness	Mean	Min.	Deviation of min	Max.	Deviation of max
As-cast (HV)	696 ± 32	623	10%	787	13%
As-cast normalized	1 ± 0.05	0.90		1.1	
Relaxed	796 ± 23	741	6.9%	885	11%
Relaxed normalized	1 ± 0.03	0.93		1.1	

Table IV-2: Mean, standard deviation, minimum and maximum from the 100 nano-hardness measurements performed on the $Zr_{56}Co_{28}Al_{16}$ BMG, as cast and relaxed for 48h at 675 K.

Figure IV-11 (a) shows the probability density function versus the nano-hardness, calculated from the 100 indentations performed on both the as-cast and the annealed samples. We see that hardness increases by approximately 14%, from 696 HV to 796 HV from the as-cast to the annealed samples. One could question the absolute values of hardness, as they are much higher than the ones measured by microhardness. We mentioned in Chapter II.3.3.3. than nano-hardness measurements can be distorted by pile-up effects. The pile-up effect leads to an underestimation of the contact area. Supplementary material G regroups more details and some Atomic Force Microscopy (AFM) measurements exhibiting that we do have pile-up in our case. However, correcting the pile-up effect would require realising AFM measurements on each indentation imprint which would be very time-consuming. We chose not to

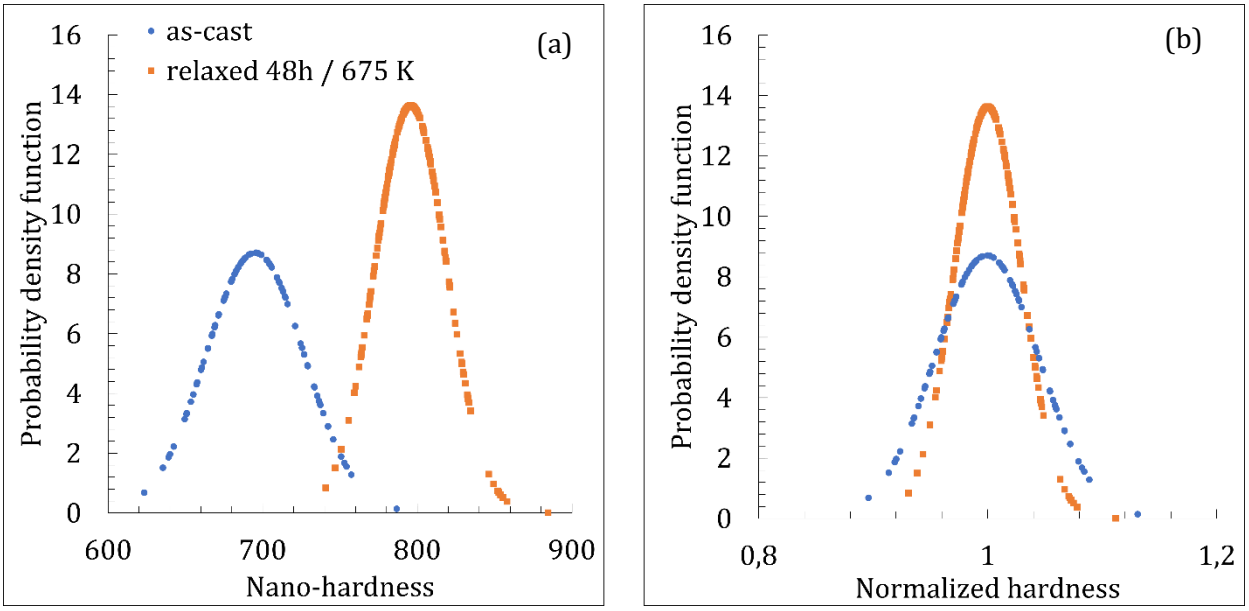

Figure IV-11: Probability density function for the 100 nano-hardness tests performed on a $Zr_{56}Co_{28}Al_{16}$ 5 mm-diameter rod. Hardness is presented as calculated on the left (a) and normalized by the mean value on the right (b).

correct the pile-up effect and instead to work with normalized hardness (using the average hardness of each set of measurements). We can mention that a rough estimate of the pile-up effect does bring the nano-hardness measurement value very close to the value of the micro-hardness measurement.

In addition to the increase of the average value of the hardness, we observe that annealing induces a reduction of the deviation between the measured values (Figure IV-11 (b)). The standard deviation is reduced from 32 HV (4.6%) for the as-cast sample to 23 HV (2.9%) for the annealed sample. The diminution of the standard deviation (hardness distribution is narrower) indicates that the degree of heterogeneity is decreased. By annealing our glass, we reduce the average amount of flow unit under each indentation, and there is a lower variability in the degree of flow unit under each indent. This points out that our glass is more homogeneous after relaxation. Such behaviour has been widely confirmed for other compositions in the literature.

It is rather well established that the relaxation of a metallic glass induces a diminution of the free volume volume fraction through the glass. A novel remarkable parameter here is the reduction of the standard deviation calculated after relaxation. We believe that the heterogeneity distribution and the overall free volume volume fraction both have an independent influence on the deformability of the glass, as exposed in Chapter III.2.3.1. Among all the samples tested (as-cast, in Chapter III.2.3.1. and after a short time of relaxation in this chapter), we have observed variations of the deformability mechanism but the stability of the yield stress. Therefore, we question the link between the initiation of plastic strain (yield) and the development of plastic strain. We believe that the yield stress is correlated to the localization of the strain in a first shear band system whereas the propagation of the deformation is linked to the ability to nucleate active multiple shear bands systems. In other words, because we observe different plastic strains but no changes in yield stress values, we believe that the strain needed to activate the first shear band system is similar among every sample. Also, we conclude that in the sample exhibiting lower plastic strain, the heterogeneities distribution and volume fraction is less favourable to nucleate many shear bands. This needs to be further investigated, for instance by performing nano-indentation tests coupled with more macro-scale testing such as compression tests.

Structural relaxation is interesting to maximize fatigue endurance limit as exposed in Chapter I.3.3.2. Biomaterial needs to have a good balance between mechanical and corrosion-related properties. Relaxation could have an influence on the corrosion resistance of our alloy and this effect needs to be assessed.

IV.2. Mechanical rejuvenation of $Zr_{56}Co_{28}Al_{16}$

The first part of this chapter was dedicated to the study of the relaxation process of our alloy. Relaxation is a natural process for metallic glasses, because of the metastable nature of the amorphous state for metallic alloys. The inverse transformation is however against the natural evolution of bulk

metallic glasses. In Chapter I.34.1., we reviewed the major rejuvenation techniques. We highlighted two main rejuvenation ways: thermal and mechanical. Thermal rejuvenation is mainly obtained by thermal cycling of the BMG across an important temperature gap. The most common technique is to quench the alloy in liquid nitrogen repeatedly (cryogenic cycling [120]). Mechanical techniques are also widely explored for rejuvenation. Unfortunately, these mechanical techniques usually induce permanent geometry changes of the rejuvenated part. This is not ideal as one of the main qualities of BMG is its ability for thermoplastic forming. In this work, we will be focusing on the mechanical rejuvenation of the $Zr_{56}Co_{28}Al_{16}$ using mechanical cycling under yield stress.

IV.2.1. Rejuvenation by mechanical solicitation under the yield stress

As already mentioned in Chapters I, III and this chapter, metallic glasses, despite being amorphous, are heterogeneous. Applying a strain, within the elastic regime on a BMG sample will result in a heterogeneous strain field at the MRO scale, as regions of lesser density will be more easily deformed than the regions of high density. This means that applying an elastic strain on a BMG can result locally in irreversible strain. Such irreversible strain will be accommodated by the surrounding matrix but should result in a higher energy state of the glass.

Rejuvenation by mechanical loading under yield stress has been briefly presented in Chapter I.3.4.1. For approximately two decades, the static compression of BMG under yield stress (elastostatic compression) has been studied for its impact on glass structure [119, 123, 252, 253]. Figure IV-12 illustrate the stress-strain compression curve for a sample subjected to elastostatic loading and compressive loading.

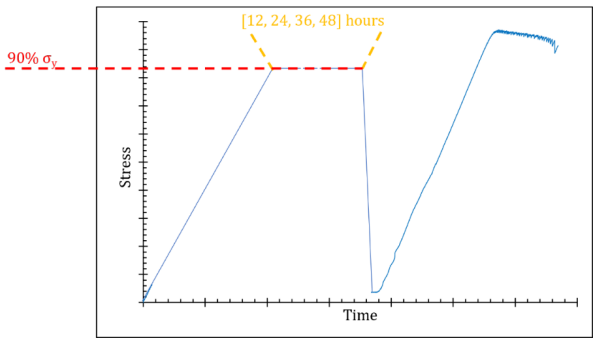

Figure IV-12: Illustration of the stress-strain curve in the case where the sample is subjected to elastostatic loading before compressive loading up to failure.

It has been reported that a prolonged loading close but below the yield stress resulted in residual strain after unloading. Lee *et al.* and Park *et al.* [128, 252] studied a Cu-Zr binary glass on this topic. Both authors found a correlation between the residual strain and the variation of exothermic heat associated with the annihilation of excess free volume: the higher the residual strain was, the higher the increase in exothermic heat was. This is explained by the creation of free volume during the elastostatic solicitation (because of structural disordering). Interestingly, Park *et al.* studied several Cu-Zr binary compositions, ranging from $Cu_{50}Zr_{50}$ to $Cu_{65}Zr_{35}$ [128]. Tested in the as-cast state, the exposed compositions have

different mechanical responses to compression testing: the higher the Cu content is (the lower the Zr content), the higher the yield stress and the lower the plastic strain are. This is correlated to the packing density of each composition: the highest plastic strain corresponds to the sample with the lowest packing density ($Cu_{50}Zr_{50}$ has the lowest, $Cu_{65}Zr_{35}$ has the highest). Investigating the elastostatic compression effect, they drew three conclusions:

- Binary Cu-Zr, close to the equimolar composition, are exhibiting less residual strain than Cu-Zr glass-formers with a more unbalanced Zr/Cu ratio.
- Free-volume creation, monitored by the exothermic heat associated with free-volume annihilation upon heating, reaches a plateau after some time under elastostatic compression. Interestingly, the value at the plateau is similar for both $Cu_{50}Zr_{50}$ and $Cu_{65}Zr_{35}$.
- Elastostatic pre-loading has a stronger effect on the enhancement of the plastic strain and the reduction of yield stress and Young's modulus when applied to glasses of high atomic density. Hence, it seems to be more efficient when the glass contains a low embedded free volume fraction in the as-cast condition.

For this early study, it appears that elastostatic compression is an effective way to induce structural rejuvenation, but its efficiency is strongly related to the as-cast structure of the glass. If the glass is already in a very heterogeneous state, the impact of elastostatic compression can be minimized. Since then, many studies have applied elastostatic loading for the rejuvenation of glass formers. As mentioned in Chapter I.3.4.1., Zhang *et al.* recently applied this technique to a $Zr_{35}Ti_{30}Be_{27.5}Cu_{7.5}$ BMG [119]. They concluded that there was a stress threshold under which the glass was not rejuvenated but relaxed.

This static pre-loading process is interesting as it is efficient even at reduced residual strains (< 0.5% [119]) but it requires quite long treatments (several hours, up to 48h) and its effect strongly depends on the initial packing density of the amorphous alloy. The cyclic loading under the yield stress is another mechanical rejuvenation technique, which has been, up to now, less studied.

IV.2.2. Rejuvenation through cyclic compression

IV.2.2.1. Recent achievements on rejuvenation through cyclic loading

We reported in Chapter I.3.4.1. that Packard *et al.* studied the influence of cyclic loading on the nano-hardness of a Pd-based BMG [135]. They concluded that their glass was hardened (and therefore relaxed) by a low number of cycles. They also exhibited that it exists a stress threshold under which no clear change is observed. This is quite surprising since based on the elastostatic rejuvenation technique, the stress threshold corresponds to the stress limit above which the glass is rejuvenated, not relaxed.

Interestingly, the same group compared elastostatic loading and cyclic loading. They showed that at similar stress, cycled samples (5 cycles) exhibit hardening while elastostatic samples exhibit no changes.

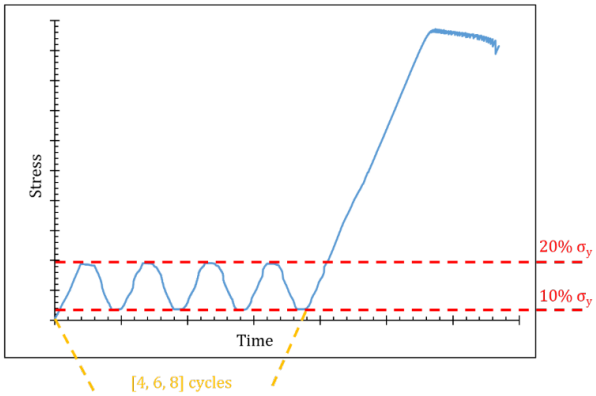

Figure IV-13: Illustration of the stress-strain curve in the case where the sample is subjected to cyclic loading (between 10% and 20 % of yield stress) before compressive loading up to failure

Based on this study, O. Baulin studied the influence of cyclic loading by compressive loading on a Vitreloy 105 alloy ($Zr_{52.5}Cu_{17.9}Ni_{14.6}Al_{10}Ti_5$) [96]. This is, still today and to the best of our knowledge, the most advanced study on the cyclic compression rejuvenation of BMG. She investigated the influence of the number of cycles by performing 0, 2, 4 or 6 pre-loading cycles. She also investigated the influence of the loading stress by performing pre-loading up to 22% (400 MPa), 39% (700 MPa) and 66% (1200 MPa) of the yield stress of the alloy (1843 MPa). Figure IV-13 illustrates the stress-strain curve for a sample subjected to four pre-loading cycles at 20% of the yield stress. Samples are unloaded to 10% and not less to ensure good contact with the compression platen. Depending on the experimental setup, a rather short holding time can be observed between cycles. This corresponds to the time that the machine needs to reverse the moving direction of the crossbeam. Figure IV-14 reports the stress-strain curves, published by O. Baulin, obtained after different pre-loading conditions. For easier reading, Table IV-3 gathers yield stress and plastic strain from all tested samples along with their pre-loading protocols.

Number of cycles	Stress (MPa)	Stress (% yield stress)	Yield stress (MPa)	Plastic strain ε_p (%)
-	-	-	1843	3
2	400	22	1802	5,9
4	400	22	1700	14,8
6	400	22	1851	13,7
2	700	39	1863	6.5
4	700	39	1830	4,6
6	700	39	1796	1,7
2	1200	66	1795	3,1
4	1200	66	1837	3,6
6	1200	66	1797	4,1

Table IV-3: Yield stress and plastic strain for Vitreloy 105 alloys subjected to several pre-loading protocols before compression testing up to failure.

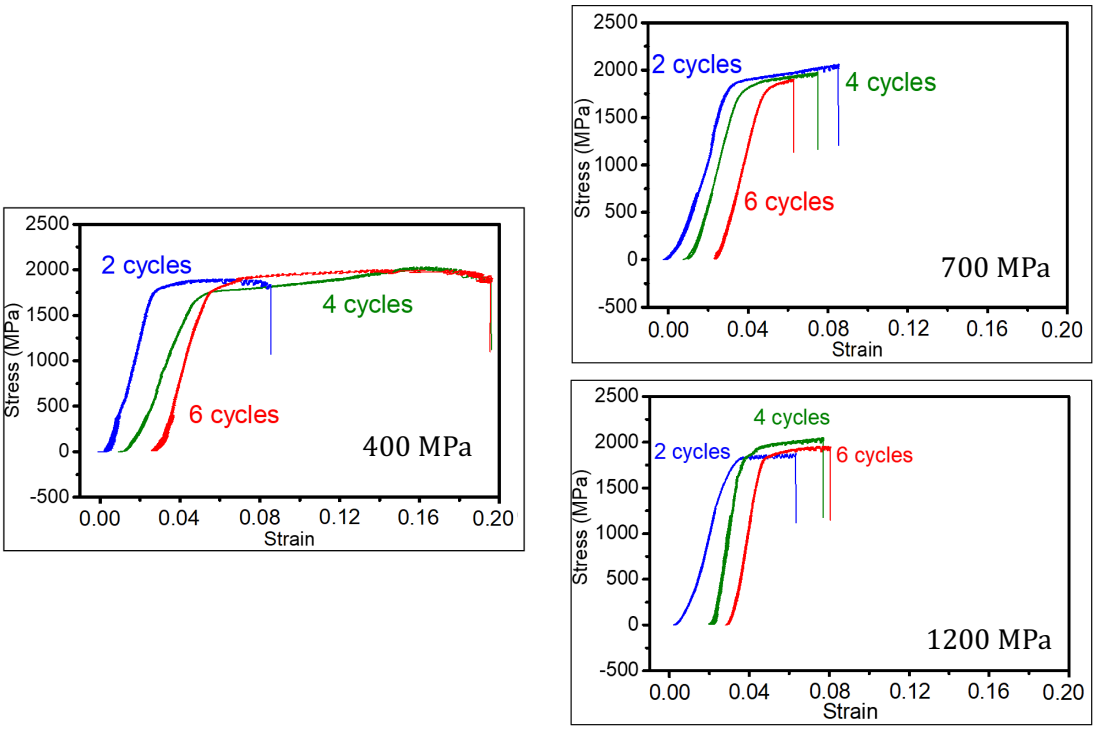

Figure IV-14: Stress-strain curves for pre-cycled samples, at 400 MPa, 700 MPa and 1200 MPa for 2, 4 and 6 cycles.

The as-cast $Zr_{52.5}Cu_{17.9}Ni_{14.6}Al_{10}Ti_5$ sample exhibits yield stress of about 1840 MPa and a plastic strain of about 3%. First, we look at samples pre-deformed at 22% of the yield stress (400 MPa). A beneficial effect is observed on the plastic strain for all three pre-cycled samples. The strongest beneficial effect is observed for 4 and 6 cycles. The yield stress of the sample cycled 4 times before final compression is well below the yield stress of the other samples (as cast and pre-cycled 2 and 6 times). This is the only sample, among all the tested samples that exhibit a change in its yield stress. Second, pre-cycling at 700 MPa, a strong increase of the plastic strain is observed for 2 cycles. For more cycles, the sample deformability appears to decrease. Finally, pre-cycling at 1200 MPa does not seem to have a beneficial or detrimental effect on the plastic strain.

In the next section, we show and discuss the results concerning the application of comparable loading pre-cycling procedure on our glass ($Zr_{56}Co_{28}Al_{16}$) and compare them with those obtained with a Zr-Cu-Al based alloy (a $Zr_{57}Cu_{20}Al_{10}Ni_8Ti_5$, close to the alloy used by O. Baulin).

IV.2.2.2. Rejuvenation through cyclic loading under yield stress on $Zr_{56}Co_{28}Al_{16}$ and $Zr_{57}Cu_{20}Al_{10}Ni_8Ti_5$

O. Baulin work on mechanical rejuvenation revealed that cyclic mechanical solicitation at approximately 20% of the yield stress for 4 cycles had the highest beneficial effect on the ductility of a Zr-Cu-Al-Ti-Ni BMG. We performed such tests on the same sample geometry as the one used in the as-cast compression tests (see Chapter III.2.3.1) and the relaxation tests (see Chapter IV.1.1.1). Figure IV-15

shows five stress-strain curves: two from as-cast samples (blue lines, A_1 and A_2) while three are from samples that were pre-cycled 4 times at 20% of the elastic limit of our as-cast $Zr_{56}Co_{28}Al_{16}$ (samples R_1, R_2 and R_3).

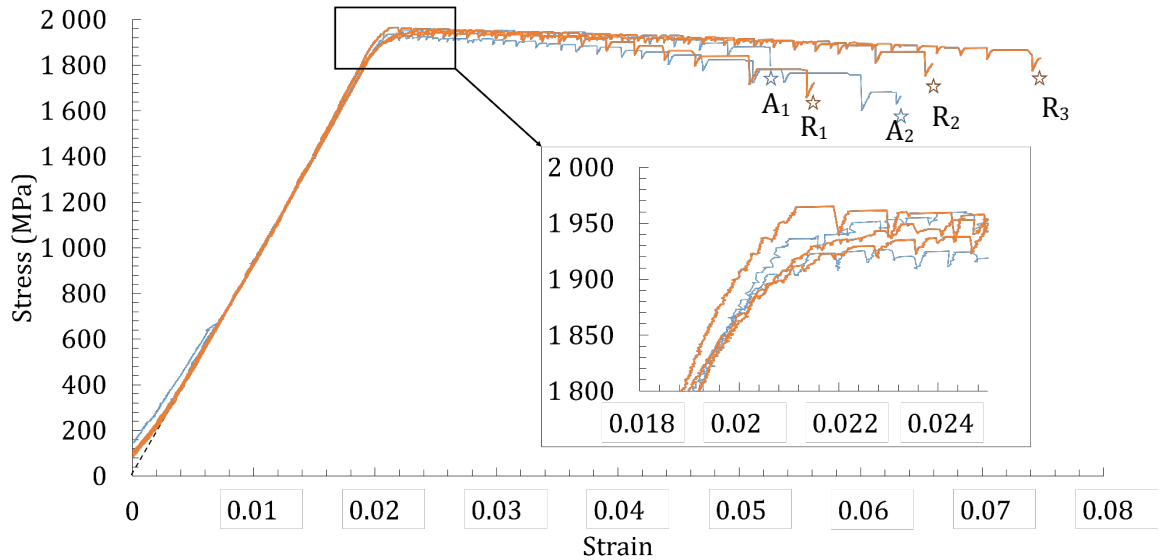

Figure IV-15: stress-strain curves from uniaxial compression tests at 2.5 x 10^{-4} s^{-1}. Blue curves are from as-cast samples (A_1 and A_2), orange curves are from samples pre-cycled four times at 20% of yield stress (R_1, R_2 and R_3). The inset highlights the similarity in the elastic to plastic transitions among the samples.

From Figure IV-15, we can see that among the three samples that were pre-cycled (orange curves), only one sample (named R_1 on the graph) exhibited a lower plastic strain than the two as-cast samples (A_1 and A_2). A_1 and A_2 samples reached ultimate strains of respectively 5.3% and 6.3%. Pre-cycled samples R_1, R_2 and R_3 reached ultimate strains of 5.6%, 6.6% and 7.5%, respectively. Studying the as-cast state of our material, we used serration pattern analysis to go more in-depth into the deformation mechanism at play. Figure IV-16 shows the serration position and magnitude for each sample and the statistical distribution of the serrations based on their magnitude. The two as-cast samples A_1 and A_2 have rather similar behaviours. They do not exhibit the stable serration progression regime observe in Chapter III.2.3.1 but instead, the serration magnitude directly evolves following the catastrophic propagation regime. It is important to note that the serration magnitude statistical distribution seems to follow the SoC pattern for both as-cast samples. Yet we believe that this is misleading. Indeed, this pattern is described as an alternation of small and big serration, which is not the case here. Instead, here we observe an exponential increase of the serration magnitude with the deformation, with almost no small serration and no medium serrations.

The same serration distribution as samples A_1 and A_2 is observed for sample R_1. Samples R_2 and R_3 are quite different: they both exhibit the two serration regimes (steady-state propagation and catastrophic propagation), with an alternation between serration of several sizes in the steady-state propagation regime and a rapid increase of the stress drops magnitude in the catastrophic regime.

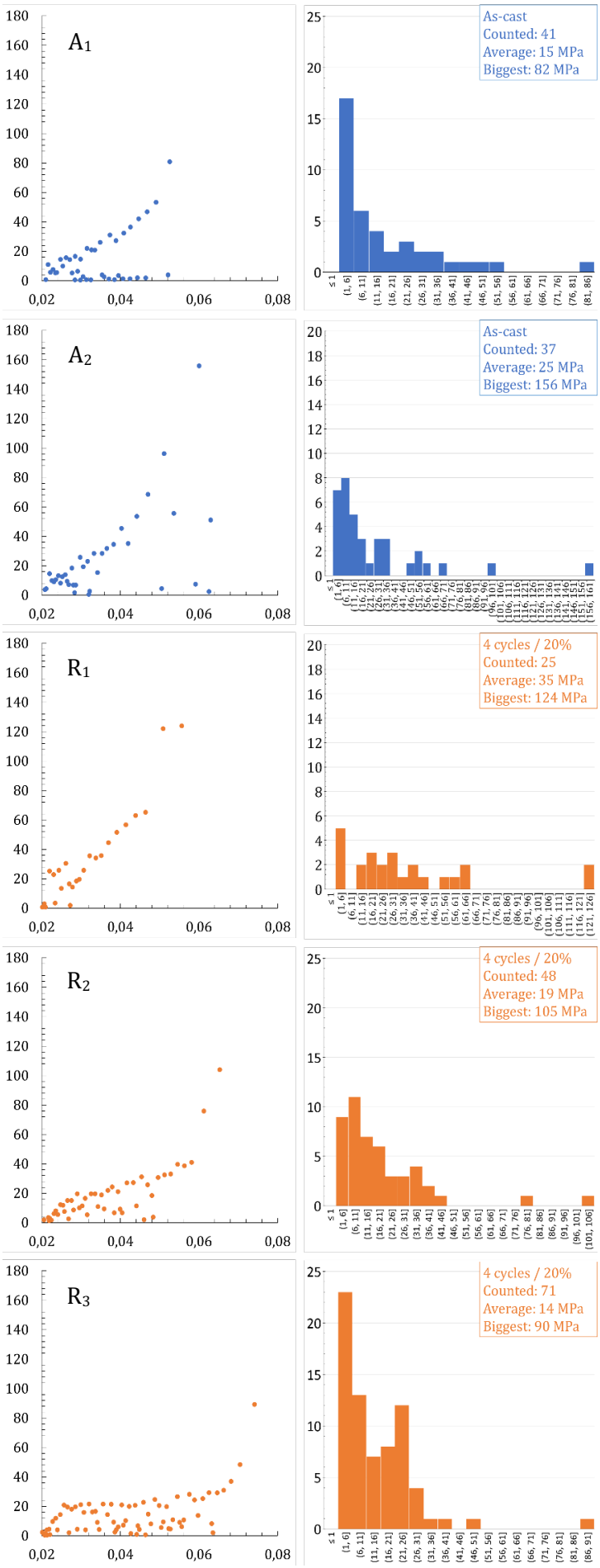

Figure IV-16: The stress drop magnitude as a function of the associated strain (on the right) and the stress drop statistical repartition based on their magnitude (on the left) for samples A_1, A_2, R_1, R_2 and R_3.

The strain-softening is the lowest, for samples R_2 and R_3 among all samples tested in this batch. We believe that strain-softening is correlated to deformation localisation: the higher the localisation, the higher the temperature inside the shear band, the lower the viscosity inside the shear band and ultimately the higher the strain softening. We also note that strain softening is correlated with the apparition of serrations of higher magnitude. This supports the idea that the second serration regime (catastrophic propagation) is associated with the localization of the strain is a limited number of shear bands, probably a single shear band.

At first glance, by reading those results, one could think that the rejuvenation process was efficient for two samples out of the three tested. However, before making any conclusions, one should take a step back and recall the variability observed on the plastic strain of the as-cast samples tested in Chapter III.2.3.1. From the detailed analysis of numerous compression tests on samples produced in the same conditions, we observed important variations in the plastic strain obtained for each sample. The standard deviation measured in plastic strain only was measured to be as high as 3%. We made the hypothesis that these variations were linked to fine structural differences in our as-cast alloy (volume fraction and repartition of heterogeneities).

We do not believe that rejuvenation was triggered using this protocol of 4 cycles at 20% of the yield stress on our samples. If rejuvenation took place (for instance on samples R_2 and R_3), it is hidden by the variability observed on the plastic strain. This is supported by both the stress/strain curves and the serration analysis which both exhibits the same disparities as the as-cast $Zr_{56}Co_{28}Al_{16}$ studied in Chapter III.

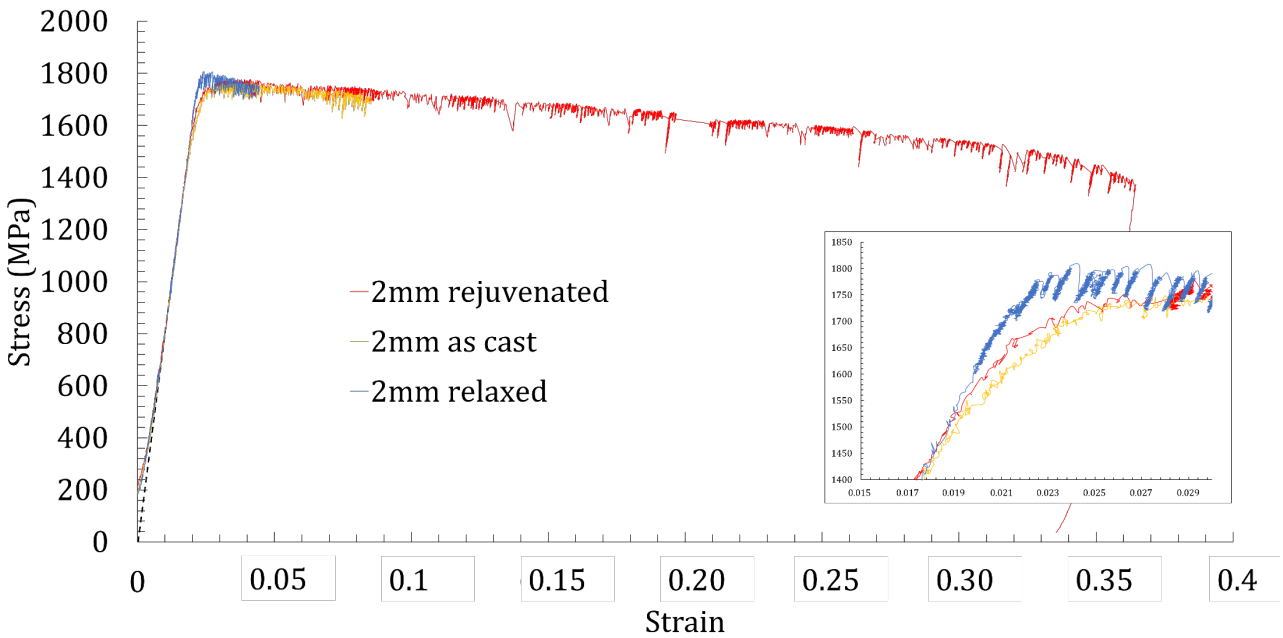

Figure IV-17: Strain-stress curves acquired during the compression testing of 2 mm-diameter samples of a $Zr_{57}Cu_{20}Al_{10}Ni_8Ti_5$ BMG. Three states are represented: as-cast, relaxed (1h at T_g – 30 K) and rejuvenated (4 pre-loading cycles at 20% of the yield stress of the as-cast sample).

Even though rejuvenation could have been triggered on these samples, it is of far lower magnitude than what was achieved by O. Baulin, when the plastic strain of the $Zr_{52.5}Cu_{17.9}Ni_{14.6}Al_{10}Ti_5$ was increased from 3% in the as-cast state to almost 15%. The potential reasons for the lack of results to rejuvenate our glass using the same protocol as O. Baulin are discussed hereafter.

For comparison, we apply the same rejuvenation protocol to another Zr-based BMG. We used a $Zr_{57}Cu_{20}Al_{10}Ni_8Ti_5$ glass (named ZrC), as it is a mastered Zr-Cu-Al based at SIMaP and close to the composition used by O. Baulin. Pre-cycling on $Zr_{57}Cu_{20}Al_{10}Ni_8Ti_5$ was performed on samples produced by suction casting instead of the samples produced via the injection process used for the $Zr_{56}Co_{28}Al_{16}$. This choice was made because the suction casting process allow us to cast 2 mm diameter rods and 3 mm diameter rods in the same conditions, which was not yet possible with the injection casting set-up. Figure IV-17 plots the stress-strain curves of three 2-mm diameter ZrC samples in three different states: as-cast, relaxed (T_g – 30 K for 1h) and pre-loaded (4 cycles at 20% of the yield stress of the as-cast sample). From Figure IV-17 we observe that ductility is drastically increased with the rejuvenation procedure. On the one hand, the as-cast sample exhibits an ultimate strain of 8.5%. On the other hand, the rejuvenated sample was deformed up to an astonishing absolute strain of 36% without failing (we stopped to test at this point due to set-up limitations). This is more than four times the ultimate strain of the as-cast sample. The inset in Figure IV-17 shows a close-up of the yield stress of the three samples. It appears that the yield stress of the relaxed sample is higher (by approximately 100 MPa) while it is approximately equivalent for the as-cast and the rejuvenated sample.

As for the relaxation process tested in section IV.1.1.1, the Zr-Cu-Al-based alloy ($Zr_{57}Cu_{20}Al_{10}Ni_8Ti_5$) tested in the same conditions as the $Zr_{56}Co_{28}Al_{16}$ appears to be much more sensitive to rejuvenation. Applying the same procedure on our Zr-Co-Al BMG does not lead to the enhancement of plasticity. Overall, the Zr-Cu-Al-based alloy seems to be more prone to structural changes than the Zr-Co-Al alloy. In the same way, it influences the mechanical or thermal properties of the glass as cast, its composition appears to also influence the malleability of its structure. Such difference can be related to the as-cast glass structure. We will now discuss, based on our observations and the literature, the influence of the glass structure on its ability to be rejuvenated.

O. Baulin concluded that the rejuvenation process by pre-cycling in the elastic domain is a three-step mechanism, which was illustrated in Figure IV-18 from [96]. This three-step process is detailed as followed: first, in the as-cast state and the case of the Vitreloy 105, the strain is mainly localized in a single shear band, which precipitate failure, as discussed in Chapter III.2.3.1. Then, pre-cycling exhibits a beneficial effect, as it induces the delocalization of the deformation over numerous shear bands, by creating new structural heterogeneities, from which nucleate shear bands. This participates in the homogenization of the deformation, which ultimately increases deformability. Finally, once a critical

stress amplitude or a number of cycles is reached, the created heterogeneities may coalesce and once again promote a single shear band.

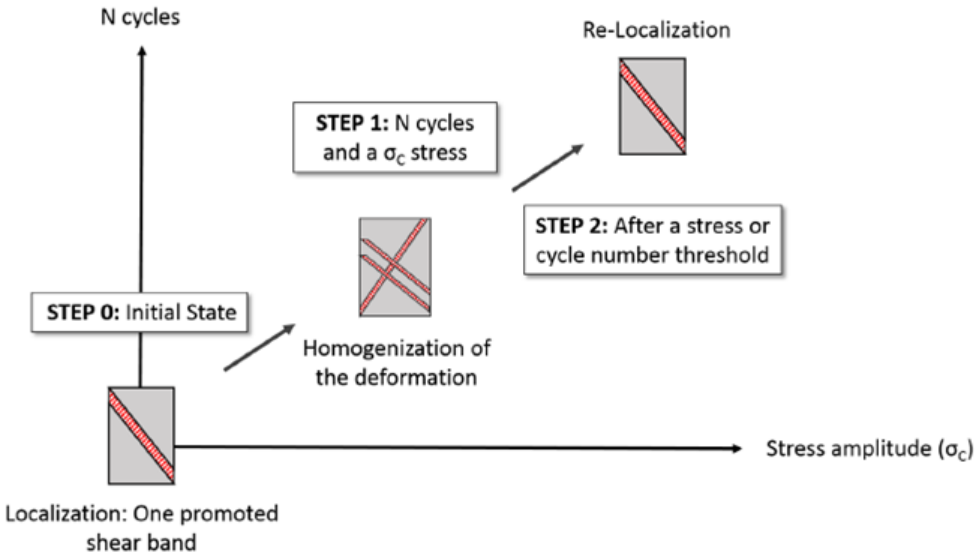

Figure IV-18: Schematic representation of the three steps mechanism observed during experimental rejuvenation test (and atomistic simulation). [96]

O. Baulin proposed some simulation work that confirmed that strain was more homogeneous after pre-cycling. More recently (in 2019 and 2020), simulation work was proposed on the rejuvenation under cyclic loading of a BMG [138, 139]. Simulation works are often (and this is the case here) based on the study of ZrCu binary glass. Shuo Li *et al.* studied the $Zr_{50}Cu_{50}$ binary glass for rejuvenation using molecular dynamics [139]. They simulated the cyclic loading under the elastic limit and showed that local atomic structure rearrangement took place within the elastic regime. They showed that with the increasing number of cycles (N), the change of potential energy per atom was positive and so was the change of the bulk volume (see Figure IV-19 (a)). This confirms that more free volume is created upon cyclic loading. They also noted that the increase in sample volume and potential energy reach a plateau after a critical number of cycles. Moreover, for samples generated at higher cooling rates, this critical cycle number decreases (Figure IV-19 (a) and (b)). In addition, the increase in potential energy and sample volume before the plateau is of lower magnitude with the increasing cooling rate. Using atomic computational tomography (ACT), they showed that a sample after 100 cycles had a higher fraction of looser bonds than an as-cast sample. S. Li *et al.* also performed uniaxial loading tests on samples pre-cycled for 0, 10 and 50 cycles. They showed that deformation was more homogeneous after 50 cycles of pre-loading. They also showed that with the increase of the number of cycles, yield stress was reduced and deformability was enhanced. This numerical study confirms the experimental work proposed by O. Baulin. S. Li *et al.* stressed out that the rejuvenation process induced by cyclic elastic loading is linked to the heterogeneity of the metallic glass and that the rejuvenation magnitude depends on the initial state of the glass. A glass with a higher level of initial heterogeneity will reach saturation faster than a glass containing a low amount of heterogeneities. This is illustrated by the evolution of the potential energy

per atom: the potential energy accumulation rates are calculated to be 7.8 eV/cycle and 16 eV/cycle for samples generated respectively at 10^{11} K.s^{-1} and 10^{13} K.s^{-1}.

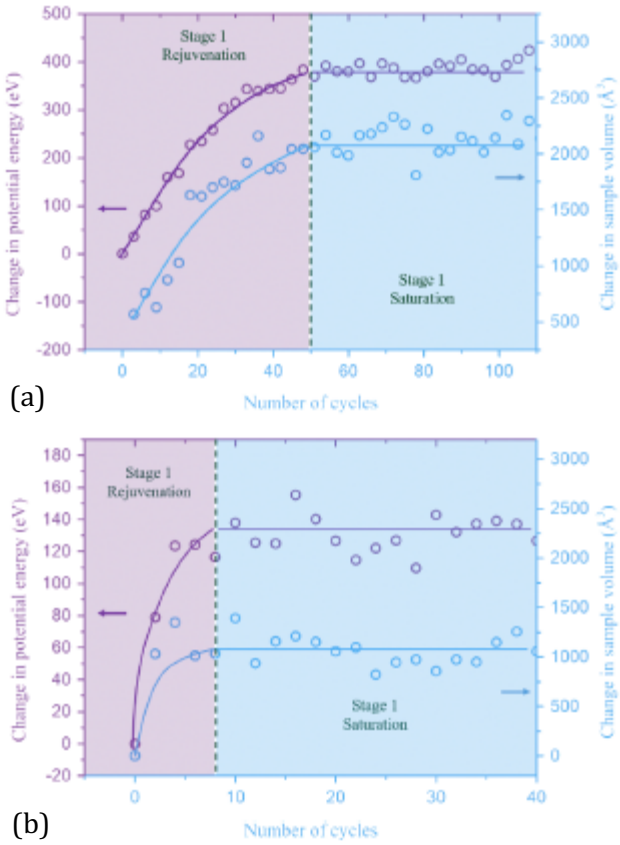

Figure IV-19: the change in potential energy and volume as function of the number of cycles for sample generated at 10^{11} K.s^{-1} (a) and 10^{13} K.s^{-1} (b) [139].

As the ability to be rejuvenated by cyclic loading appears to be strongly correlated to the initial glass structure, P. Wang *et al.* studied the influence of the glass structure and the composition of Zr-Cu binary glass [138]. They exposed several key points while considering the mechanical rejuvenation of Zr-Cu binary glass formers by cyclic solicitation:

- There exists a strain threshold under which the glass is relaxed. Under this threshold, the higher the strain, the higher the magnitude of the relaxation. Above this threshold, the potential energy per atom is increased: the glass is rejuvenated.
- The rejuvenation is faster for the first cycles (up to 5 cycles approximately). After the first cycles, the rejuvenation rate decreases until the potential energy per atom reaches a plateau. Figure IV-21 illustrates both the ageing/rejuvenation transition and the plateau, based on the potential energy evolution per atom as a function of the number of cycles.
- Looking at ageing through cyclic loading (solicitation under the strain threshold), P. Wang *et al.* exposed that the potential energy decrease was more pronounced for glass generated at higher cooling rates which have a lower fraction of ordered structures.

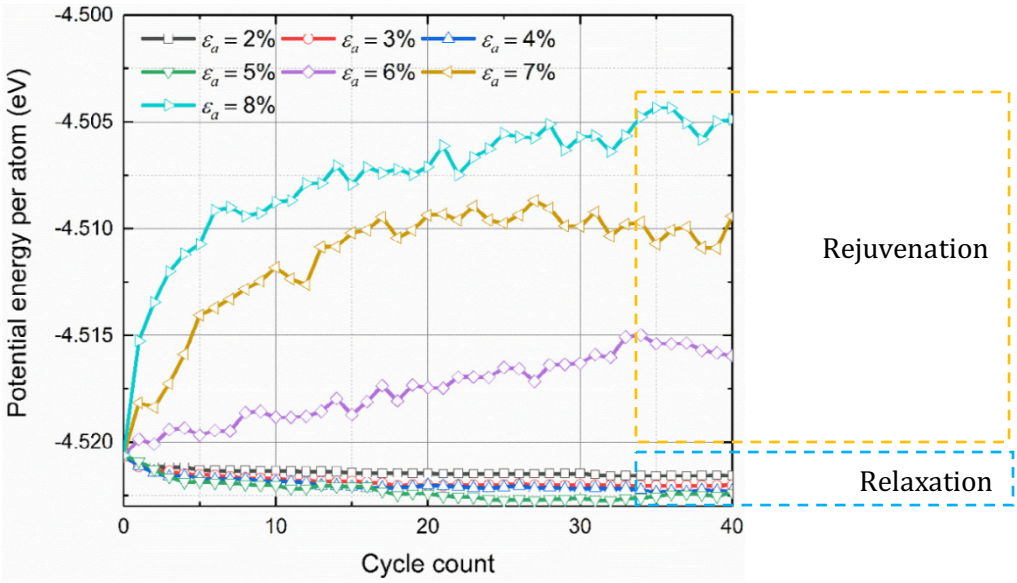

Figure IV-21: Potential energy per atom versus cycle number for cyclic loadings with different cyclic strain amplitudes on a $Cu_{64}Zr_{36}$ generated with a cooling rate of 10^{11} K.s^{-1} [138].

- Finally, they considered that increasing the Cu/Zr ratio increases the atomic ordering of the as-cast structure which contains a high fraction of icosahedral structures. This could imply that they have also less embedded free volume in the as-cast state as Park *et al.* showed that a $Cu_{65}Zr_{35}$ MG had less free volume than a $Cu_{50}Zr_{50}$ [128]. In addition, P. Wang *et al.* exhibited that a $Cu_{64}Zr_{36}$ MG was much more sensible to rejuvenation than a $Cu_{40}Zr_{60}$ MG, with a lower strain threshold to induce rejuvenation (see Figure IV-20). Interestingly, P. Wang *et al.* showed that all compositions had the same "rejuvenation plateau".

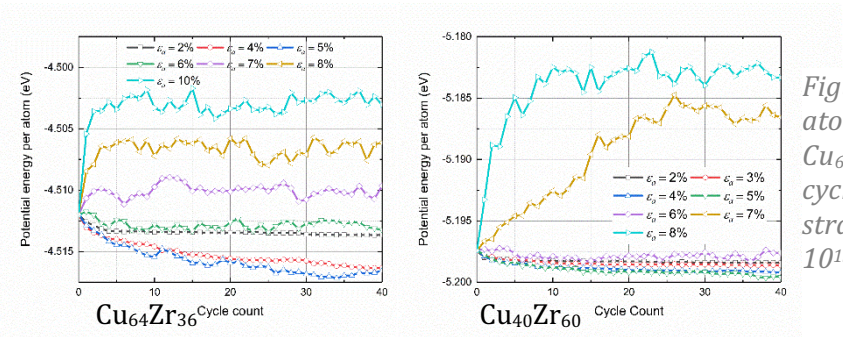

Figure IV-20: Potential energy per atom versus cycle count curves of $Cu_{64}Zr_{36}$ and $Cu_{40}Zr_{60}$ models for cyclic loading at different cyclic strain amplitudes. Quenching rate is 10^{13} K.s^{-1} [138].

P. Wang *et al.* found no linear correlation between the degree of ageing, the rejuvenation kinetic and the degree of icosahedral structure in the simulated glasses. The short-range order plays a key role in the mechanical properties of glass, yet the medium-range order is also to be considered [85]. A stronger comprehension of how the medium-range order influences the rejuvenation process would provide very valuable insights and should be investigated in future studies.

We have seen that a potential stress threshold under which the stress is not sufficient to induce new structural heterogeneities may exist. P. Wang *et al.* proposed that under this threshold, the structure is relaxed. Moreover, according to O. Baulin's work, there is also an upper threshold, above which the stress is too high and is not beneficial to the homogenization of the deformation. These several thresholds are illustrated in Figure IV-22. We also propose that the position of these thresholds based on the pre-cycling intensity level will be different. For instance, the Zr-Co-Al BMG may have a threshold for rejuvenation at a higher pre-cycling intensity than the Zr-Cu-Al. This could explain why we do not observe plasticity increase to the same extent on Zr-Cu-Al and Zr-Co-Al.

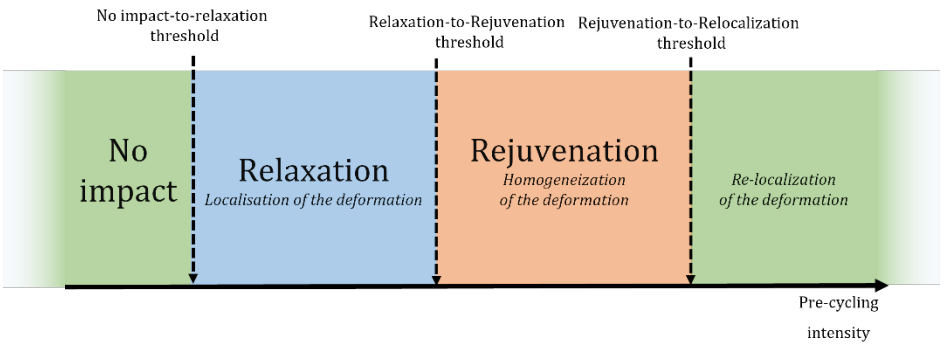

Figure IV-22: Schematic illustration of the relaxation to rejuvenation threshold position based on the pre-cycling intensity

S. Li *et al.* computational work also revealed that there is a plateau to the rejuvenation process, at which the potential energy of the system saturates. However, this plateau does not illustrate the re-localization of the deformation described by O. Baulin. The energy gap between the as-cast state and the saturation state is reduced when increasing the cooling rate used to produce the sample. In other words, samples produced at higher cooling rates are in a higher energy state than samples produced at lower cooling rates. This means that the further from a relaxed state the samples are upon quenching, the more limited the rejuvenation impact will be. This was later confirmed by P. Wang *et al.* This is also confirmed using a different loading mode (elastostatic loading) by K. W. Park *et al.*.

From this summary of the conclusions found in the literature, we can make the following hypothesis concerning the rejuvenation of the $Zr_{56}Co_{28}Al_{16}$:

- The as-cast state of the $Zr_{56}Co_{28}Al_{16}$ is too far from the relaxed state to be rejuvenated (too close to the rejuvenation plateau). In order words, it contains an excessive volume fraction of heterogeneities (such as free volume) to be rejuvenated. This could be coherent with the fact that the $Zr_{56}Co_{28}Al_{16}$ already exhibits a certain amount of deformability after casting.
- The $Zr_{56}Co_{28}Al_{16}$ possesses a different rejuvenation stress threshold (combination of applied stress and number of cycles) than the Vitreloy 105 tested by O. Baulin. This is not contradictory to the preceding statement. As discussed in Chapter III, we do believe that the

presence of Co instead of Cu as the late transition metals favours more ordered configurations such as polyhedrons like icosahedral structures.

The relation between the presence of very ordered structures (such as ISRO) and free volume remains unclear. Roughly speaking, one could say that free volume is favoured by high cooling rates while ordered structures are favoured by low cooling rates. As one cannot pave the space with icosahedral structures, one would need structures of lower density among the dense structures. The length over which the ISRO extends to MRO could be at play. The bigger these domains are, the lower is the need for interface domains. One could also propose that zones of high coordination, like ISRO, are associated with zones of lower coordination and that therefore, the higher the organisation is in zones of high coordination, the lower it is in zones of lower coordination.

We have seen studying the literature, and mainly the computational work, that the initial state of the as-cast BMG strongly dictates its ability to be rejuvenated. It was mentioned that glasses with more free volume are more easily rejuvenated but tend to saturate quicker (in terms of potential energy per atom and volume variation). Each glass composition seems to exhibit an energy plateau, at which the maximum energy potential of the system is reached. The further the as-cast glass is from the lower energy state, the quicker this plateau is reached. Following this logic, any glass, if it is not in a state of maximum energy, can be rejuvenated. From our understanding of glass deformation, rejuvenation upon cyclic loading comes from the creation of a heterogeneous strain field. We have seen that glasses are by nature heterogeneous and will deform homogeneously only at the macro scale, even below the yield stress. We believe that the inclination of a structural state for rejuvenation is related to the resulting heterogeneity of the strain field created upon deformation. This explains why an as-cast glass with a great amount of free volume is very sensible to rejuvenation. This tentative explanation is illustrated by Figure IV-23, which shows the evolution of the potential energy per atom, in a hypothetic glass, in several scenarios. In the three scenarios, the glass is solicited with the same intensity. The more heterogeneous the glass

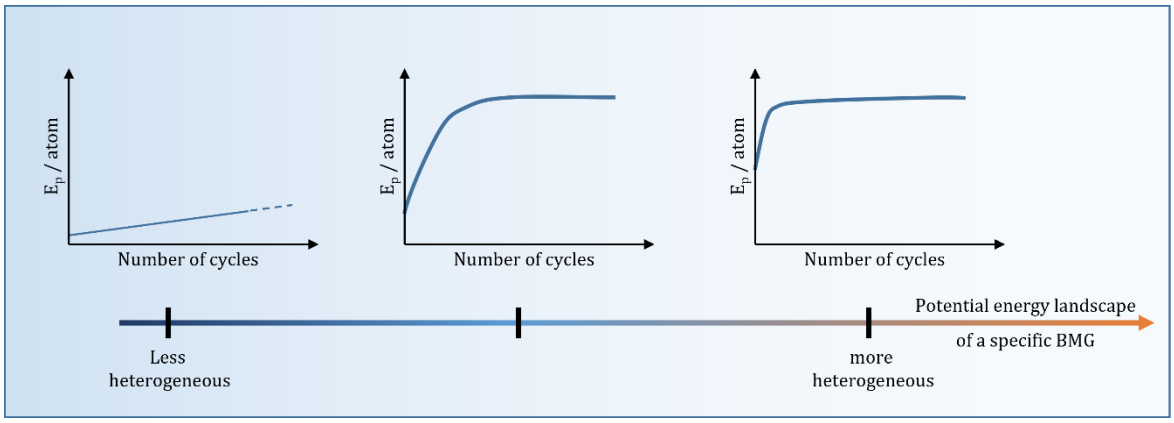

Figure IV-23: Schematic illustration of the influence of cyclic loading at a specific stress on the potential energy per atom, based on the initial position of the alloy on its specific energy landscape.

structure is, the faster the rejuvenation is, but also, the faster saturation in the potential energy per atom is reached.

To put this hypothesis to the test, we performed pre-cycling on two Zr-Cu-Al-Ti-Ni casts with two different diameters (2mm and 3mm). We assume that the increase in the casting diameter will result in a glass with lower free volume content. Based on this assumption, the sample cast with a 3 mm diameter should be less sensitive to rejuvenation than the 2 mm diameter sample.

Figure IV-24 represent the stress-strain curves of two 3-mm samples from the same alloy, as-cast and after pre-loading (also 4 cycles at 20% of yield stress). From Figure IV-24, we observe that the pre-loading process induces an increase in the ultimate strain achievable by the sample. The as-cast 3-mm diameter sample fails at 5.2% of strain which is lower than the 2-mm diameter counterpart. This is coherent as it is usually true that for the same alloy, a larger casting diameter (a lower cooling rate), leads to less embedded heterogeneities (free volume) and hence less deformability [105]. The pre-loaded sample fails at an ultimate strain of 7% which is almost 50% higher than the as-cast sample. Yet the plasticity improvement is of lower magnitude than with the 2-mm diameter sample shown in Figure IV-17. This confirms that the same pre-cycling protocol has more effect on glass with higher free-volume content. Also, based on the simulation work presented earlier, we could think that this 3 mm diameter sample could be further rejuvenated. Theoretically, it should have the same rejuvenation plateau as the 2 mm sample presented earlier. The ability of two glasses, produced with different cooling rates and heterogeneity contents to reach the same rejuvenation plateau should be further studied. Reaching the same rejuvenation plateau could mean that both glasses end up with the same structural configuration.

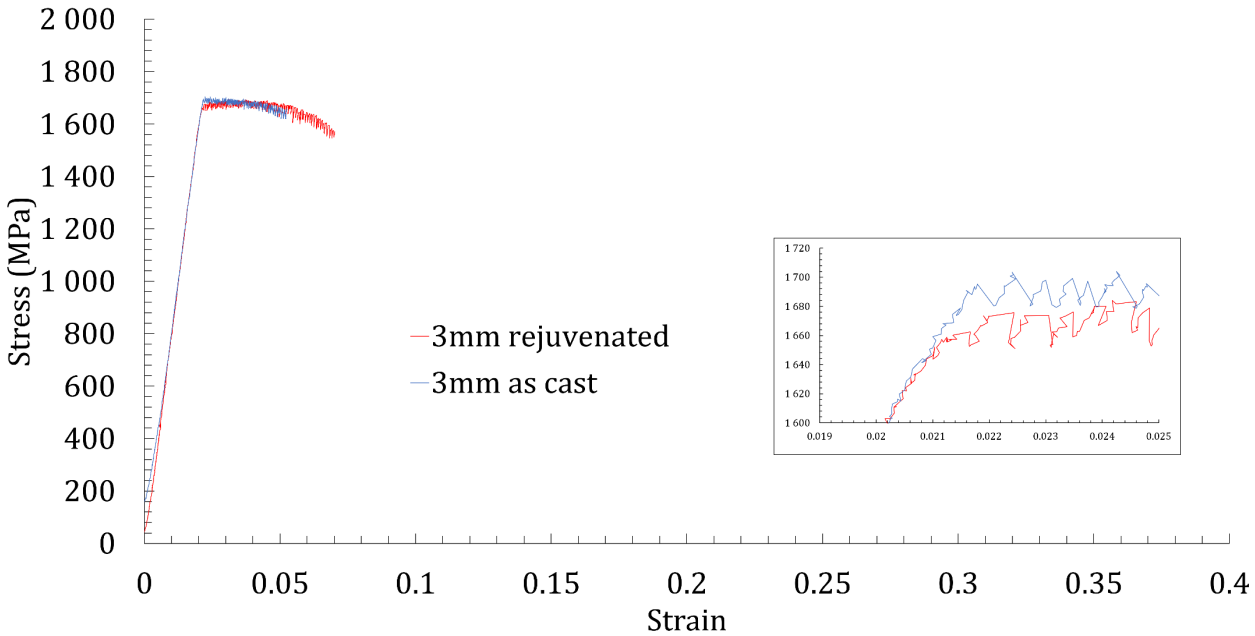

Figure IV-24: Strain-stress curves acquired during the compression testing of 3-mm diameter samples of a $Zr_{57}Cu_{20}Al_{10}Ni_8Ti_5$ BMG. Two states are represented: as-cast and rejuvenated (4 pre-loading cycles at 20% of the yield stress of the as-cast sample).

Also, simulation works did not consider the re-localization of the deformation observed by O. Baulin past a specific cycling intensity. This could prevent the 3 mm diameter glass to reach the same energetic state as the 2 mm diameter glass.

We understand that the more relaxed the glass is (i.e., the closer it is to its minimum energy potential), the more homogeneous it is. This is what was shown with the nano-indentation of the as-cast and relaxed alloy in sub-Chapter IV.1.2 where the standard deviation of the hardness measurement was reduced after relaxation. This brings a first question: ***can a fully relaxed glass be rejuvenated?*** Such glass is very far from its potential maximum energy, therefore far from the plateau, which limits rejuvenation. However, with a reduced heterogeneity content, the resulting strain field created by cyclic loading could be more or as homogeneous and hence disfavouring rejuvenation. This is one of the questions that still need to be answered. In addition, our glass does exhibit a fair amount of free volume, as shown in section IV.1.2. Yet it seems not sensitive to the rejuvenation protocol that worked on the Zr-Cu-Al-based alloys. One could therefore also question if the free-volume spatial distribution is at play here. ***Could the same volume fraction of free volume be more homogeneously distributed through the glass matrix, hence reducing the span of the strain field during loading and ultimately disfavouring rejuvenation?*** The spatial distribution of the zones of lower density than the average density of the glass, containing more free volumes should be strongly correlated to the spatial distribution and the size of the very ordered domains (such as icosahedral-like domains). We believe that the distribution could be as determinant as the overall volume fraction of free volume in all deformation-related phenomenon (yielding, plastic strain, softening…). This question would require further investigation. This could push forward the understanding of the deformation mechanisms of glass formers.

IV.3. Conclusions

In this chapter, we have studied how the $Zr_{56}Co_{26}Al_{16}$ in the as-cast condition is positioned in its potential energy spectrum. We can define the potential energy spectrum of an alloy as the energy range accessible for a specific alloy. It ranges from the lower energy state, where the alloy is not crystallized but fully relaxed, to the higher energy state, which is achievable either directly, by casting at a very high cooling rate, or rejuvenation.

We started by studying the relaxation of our alloy, namely its sensibility to be brought to a state of lower energy. We have seen that exposed to thermal treatments close to the glass transition temperature (T_g -30 K), the macro-scale compression behaviour of our alloy does not change. At least, the change is contained within the standard deviation of the ultimate strain measured on our as-cast alloy. Results are much more conclusive with the Zr-Cu-Al-Ti-Ni alloy, for which plastic strain is reduced. Hence, our alloy seems to be less sensitive to relaxation. Yet we demonstrated that our alloy can be relaxed by

performing DMA measurements and prolonged annealing. We even exposed that both β and α relaxation take place upon heating. Prolonged relaxation (48h at 0.9 times T_g) showed that our as-cast alloy contained a fair amount of free volume (of about 2 % of its original volume). This means that our alloy combines both thermal stability and non-negligible free volume content. This stability is coherent with the high activation energies measured in chapter III.2.1.

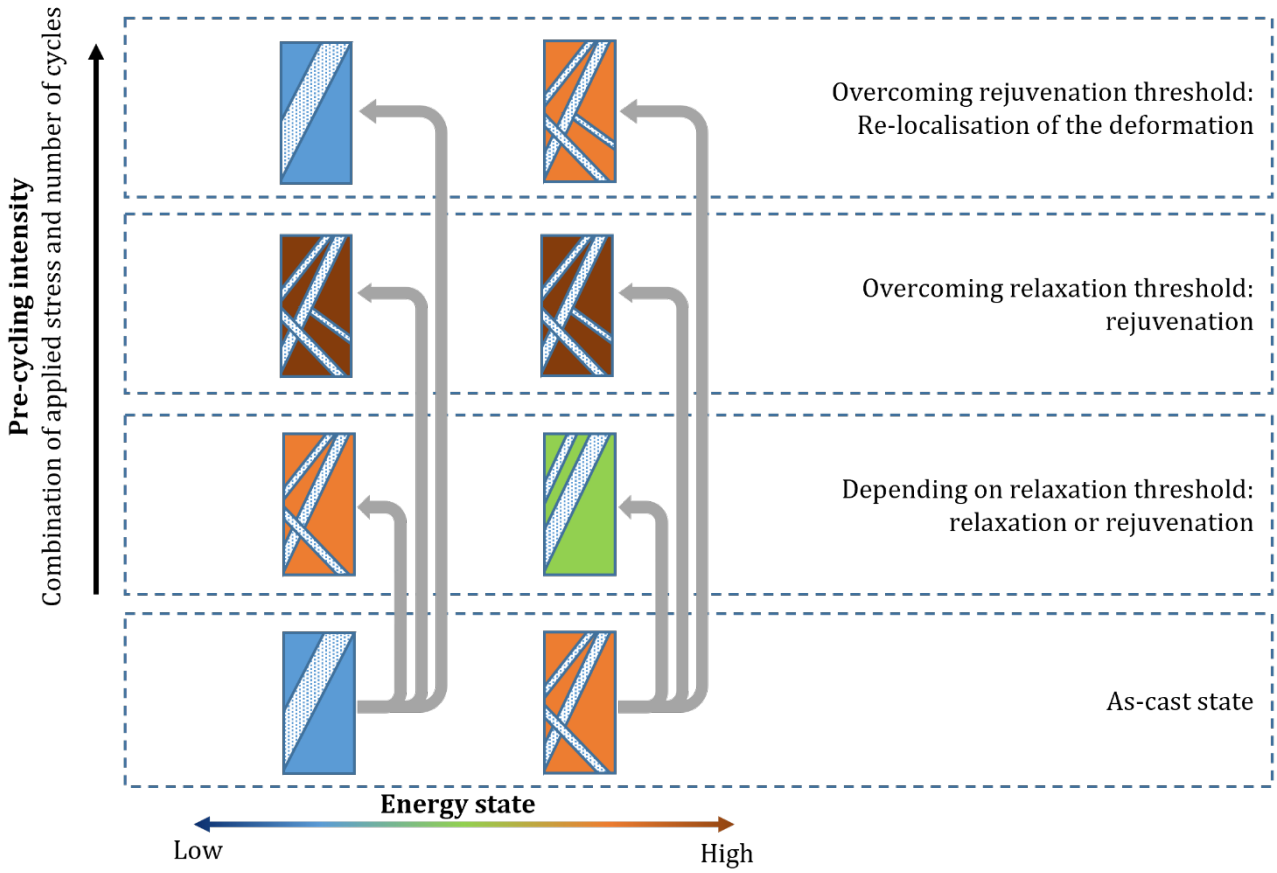

Figure IV-25: Schematical explanation of the "rejuvenation" sensibility of bulk metallic glasses as we conceptualize it. Rejuvenation mode is "cyclic loading under yield stress".

After investigating the sensitivity to relaxation, we investigated the ability towards rejuvenation throughout pre-loading compression cycling. Rejuvenation in this work is defined as the process of bringing the alloy to a higher energy state (opposite to the relaxation process). We first performed a review about mechanical rejuvenation. From this work, we considered that the ability of an alloy to be efficiently rejuvenated depends on the initial energy state of the alloy. Figure IV-25 illustrates how the intensity of the pre-cycling loading will affect the homogenisation of the deformation depending on the energy state of the as-cast alloy:

- Low initial energy state: a low intensity of the pre-cycling process induces deformation homogenisation but above a certain threshold, the effect induces re-localisation of the deformation.

- High initial energy state: a low intensity of the pre-cycling process induces relaxation (localisation of the deformation). Above a certain threshold, homogenisation of the deformation can be induced but gains are low compared to the as-cast state.

We demonstrated that our alloy does not exhibit an enhancement of plasticity with the selected rejuvenation protocol, which however induced an increase in the ductility of the Zr-Cu-Al-Ti-Ni BMG. We considered that this could be because we did not apply the suitable pre-cycling intensity (combination of stress and number of cycles) for the Zr-Co-Al glass. The $Zr_{56}Co_{28}Al_{16}$ processed at SIMaP contains free volume and is very stable. From this, the question arises: ***can glass stability and large free-volume amount co-exist***? Can a glass in a low energy state, with a rather homogeneous strain field be rejuvenated? Even though this chapter did not reveal tremendous plasticity increases for Zr-Co-Al (it did for the Zr-Cu-Al-based BMG), it revealed questions, that should inspire further investigations. Figure IV-26 illustrates in very simple terms the differences that may exist between the two glasses. We illustrate this difference in the case of a Zr-Cu-Al glass and the $Zr_{56}Co_{28}Al_{16}$ processed at SIMaP. Each glass can navigate inside a defined potential energy landscape, knowing that the potential energy of a glass is directly related to its atomic structure. The malleability of the glass structure can be expressed as the ease for a glass to navigate through its potential energy landscape. We have seen that the $Zr_{56}Co_{28}Al_{16}$ requires great effort (greater than for Zr-Cu-Al-based glass) to be either rejuvenated or relaxed.

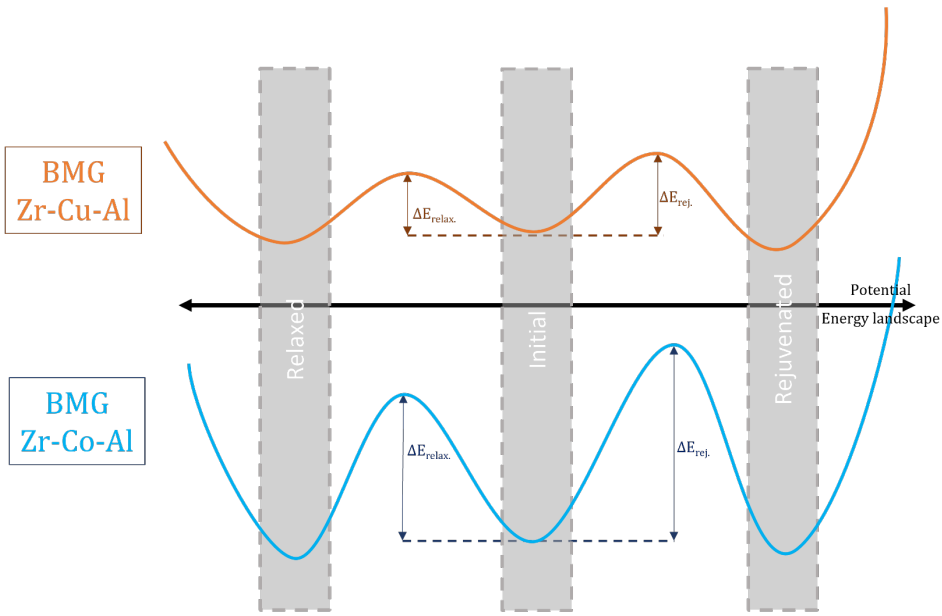

Figure IV-26: Schematical illustration of the potential energy landscape for a Zr-Cu-Al and a Zr-Co-Al glass, based on our comprehension of the differences between the two compositions.

IV.4. Take-Home Messages

We consider that a glass, depending on its composition, is bound to a **potential energy landscape**. We questioned in this chapter the ability of this glass to be moved in its potential energy landscape. To alter the $Zr_{56}Co_{28}Al_{16}$ glass structure toward relaxation, we chose **thermal annealing**. The results are as follow:

- **Short-time thermal treatment** (up to 1h at T_g -30 K) does not affect the compressive behaviour of $Zr_{56}Co_{28}Al_{16}$. It does reduce greatly the plastic strain of a Zr-Cu-Al-based BMG and increase its yield stress.
- DMA measurements show the presence of a **β relaxation** in the $Zr_{56}Co_{28}Al_{16}$, which was not reported in the literature to the best of our knowledge. This observation confirms the presence of zones of **important atomic mobility**. The glass, therefore, combines zones of important mobility and very dense zones (identified in Chapt. III). Moreover, DMA measurements confirm the **stability of the T_g**.
- **Long-time thermal treatment** (48h at 0.9 T_g) does affect $Zr_{56}Co_{28}Al_{16}$ mechanical properties, which indicates that the glass was brought to a different energy state. In the case of nano-indentation, we observe a rise in the average hardness and a **reduction in the dispersion of the measurements**. Additionally in situ XRD measurements show a decrease in the average interatomic distance. We believe that this is due to the reduction of the free volume content and an increase in the density of softer zones, which tends toward **homogenization of the structure** as we preserve mostly zones of higher density.

To alter the $Zr_{56}Co_{28}Al_{16}$ glass structure toward rejuvenation, we chose **cyclic mechanical solicitation under yield stress.** Mechanical rejuvenation under yield stress is linked to the ability to induce a **heterogeneous strain field** in the glass matrix. The results are as follow:

- We demonstrated that a specific **pre-cycling** treatment **improved the ductility of a Zr-Cu-Al-based BMG**. However, this mechanical treatment **does not induce changes in the mechanical behaviour of the $Zr_{56}Co_{28}Al_{16}$**. The structure of the Zr-Co-Al glass may not have been irreversibly affected by the pre-cycling treatment.
- We believe that the **energy barrier** to overcome to bring the $Zr_{56}Co_{28}Al_{16}$ structure to a higher energy state is higher compared to the tested Zr-Cu-Al-based BMG.

Based on the sensibility to relaxation and rejuvenation treatments, we suggest that the **Zr-Co-Al BMG structure can be less easily irreversibly affected than the Zr-Cu-Al-based BMG structure**. However, we highlighted that the Zr-Co-Al possess strong heterogeneities which are mandatory to create the heterogeneous strain field required for rejuvenation. Therefore, the understanding of the **relationships between soft and hard zones in the** Zr-Co-Al **glass remains an open question in order to find the adapted thermo-mechanical treatments influencing its energetic level**.

Chapter V:

Evaluation of the structural state modification induced by Nb minor alloying

V. Evaluation of the structural state modification induced by Nb minor alloying

Chapter III was dedicated to the study of the $Zr_{56}Co_{28}Al_{16}$ alloy that is produced at the SIMaP Laboratory, in the as-cast state. Chapter IV was dedicated to assessing the malleability of our glass structure and its sensitivity to thermal-induced relaxation and mechanical-induced rejuvenation.

As presented earlier, several ways are explored to tune BMGs structure and related properties. They can be classified into three main categories. The first one is composed of post-treatment of the amorphous alloys after elaboration: heat treatment (relaxation), work hardening, rejuvenation. They intend to alter the amorphous alloy structure through thermal (cooling or heating) [133, 138, 254] or mechanical solicitation (below or above yield stress) [123, 131, 132, 138, 254]. This was discussed in Chapter IV. The second one is based on the development of amorphous/crystalline composites, to combine both amorphous and crystalline alloys properties [161–164]. Several tries were made to induce partial crystallization but were inconclusive and are not presented here. Finally, a third way for altering mechanical properties is based on the addition of a small fraction of alloying elements [146, 149, 152–155].

This chapter is dedicated to the study of the influence on key properties (mechanical and related to biocompatibility) of "micro-alloying". Here, micro-alloying refers to the addition of alloying elements to our ternary base in small quantities, namely less than 10% of the atomic composition. More specifically, this chapter is dedicated to the study of niobium (Nb) addition to our alloy. In the first part, we will see how Nb addition affects the glass forming ability and modify the glass structure. In a second part, we will experiment how Nb addition to our ternary alloy affects the alloy properties. We will focus on the properties previously studied in this work: mechanical properties (hardness, compression testing) and corrosion resistance.

A specific micro-alloying path was chosen in this work. The addition of Nb to the $Zr_{56}Co_{28}Al_{16}$ alloy has already been reported in the literature. In this work, we perform Nb addition by substitution of Zr, which was not reported for our alloy to the best of our knowledge. Therefore, a discussion is proposed at the end of this chapter on the influence of the substitution model chosen on glass structure and resulting thermal stability and mechanical properties.

V.1. Nb minor alloying in bulk metallic glasses

Particular attention is put on the influence of Nb addition to BMGs and in particular to Zr-Cu-Al alloys [151, 244]. It was reported that Nb addition to $Zr_{47}Cu_{44}Al_9$ up to 2% (substitution to the entire ternary base) can increase plastic strain and decrease yield strength [149]. With the increase in plastic strain, an increase in shear bands density is observed in the Nb-bearing sample's surface. It is considered Nb addition increases the heterogeneity level in the glass structure, therefore promoting shear bands nucleation and maximising plastic strain before failure. Nb modification of the glass structure is impeded by the author to Nb PHM with Cu and also with Zr. Plasticity enhancement was also reported when adding Nb to $Zr_{60}Ni_{25}Al_{15}$ [152].

Some data are also available for Nb substitution in Zr-Co-Al BGMs. One can already note that enthalpies of mixing are quite different in the Zr-Cu-Al-Nb system compared to the Zr-Co-Al-Nb system. We already mentioned the difference in heat of mixing between the two ternary systems Zr-Cu-Al and Zr-Co-Al in chapter III. Figure V-1 shows the enthalpy of mixing for Zr, Co, Cu, Al and Nb.

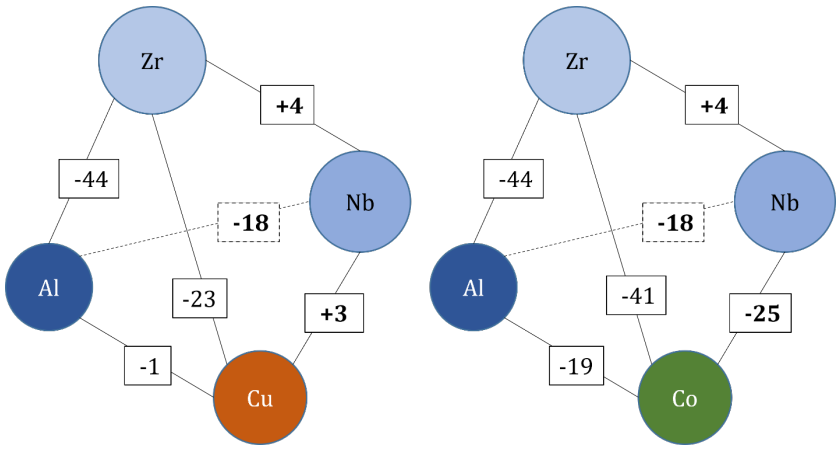

Figure V-1: Mixing enthalpy for each binary couple in the Zr-Cu-Al-Nb and Zr-Co-Al-Nb systems. Values are given in kJ/mol.

The enthalpy of mixing between Zr and Nb is slightly positive (4 kJ/mol) and the enthalpy of mixing between Al and Nb is negative (-18 kJ/mol). Interestingly, the enthalpy of mixing between Cu and Nb is positive (3 kJ/mol) and negative between Co and Nb (-25 kJ/mol). This means that the miscibility between Cu and Nb is much lower than between Co and Nb. Therefore, the results found by studying the Nb addition into Zr-Cu-Al might not apply to Zr-Co-Al. Several Nb substitution modes have been proposed in the past in Zr-Co-Al BMGs: substitution to aluminium $Zr_{55}Co_{25}Al_{20-x}Nb_x$ [150], substitution to cobalt $Zr_{55}Co_{25-x}Al_{20}Nb_x$ [159], $Zr_{56}Co_{28-x}Al_{16}Nb_x$ [157] or "substitution to the ternary base" $(Zr_{56}Co_{28}Al_{16})_{100-x}Nb_x$ [172, 173] but the reason behind the specific substitution route is rarely given in published works. Some choose to replace Al because it may be the least corrosion resistance metal [150], some chose Co because it has possible harmful effects [159] (which is arguable compared to Al) and in most cases, it is not detailed [157, 172, 173].

In these studies, Nb is mostly used to increase corrosion resistance. To this end, Nb addition appears to be a very valuable element, as corrosion resistance was increased for Nb addition to Zr-Co-Al in saline solution [150, 157], Hank's solution [157, 159, 173], sulfuric acid [150] and phosphate-buffered saline solution [159].

Only a pair of those studies looked at mechanical properties. An increase of plastic strain is reported for $Zr_{56}Co_{28-x}Al_{16}Nb_x$ with Nb content up to 5 at%, as illustrated by Figure V-2 [157]. Almost no plastic deformation is observed for 1 at% of Nb. Plastic strains of 1% and 3.5% are measured respectively for 3 at% of Nb and 5 at% of Nb. This demonstrates that substituting Co with Nb can result in a moderate increase of plastic strain. We also observe that yield stress is reduced with Nb addition. When Nb is substituted to Al ($Zr_{55}Co_{25}Al_{20-x}Nb_x$) no clear changes were observed on mechanical properties [150].

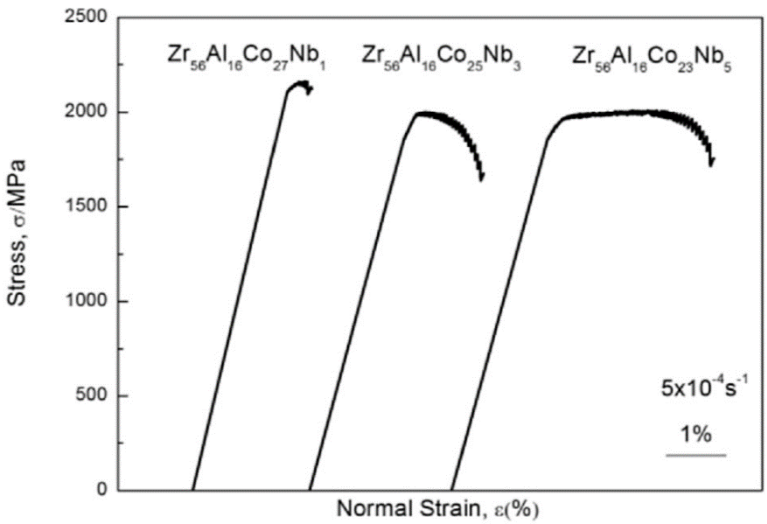

Figure V-2: Compressive stress-strain curves of as-cast $Zr_{56}Co_{28-x}Al_{16}Nb_x$ with x being 1, 3 and 5 at% [157].

It is therefore believed that Nb addition to the Zr-Co-Al ternary base can be beneficial for both the mechanical properties (namely an increase of the ductility) and the corrosion resistance. However, even with a growing comprehension of the glassy structure/property relationships, it is still hard to predict the influence of alloying addition on those properties, depending on the element but also on the substitution path. This study focuses on the substitution of Zr by Nb ($Zr_{56-x}Co_{28}Al_{16}Nb_x$) which has not been reported in the literature for this specific ternary base. Nb has a higher heat of mixing with Co (-25 kJ/mol instead of -41 kJ/mol) and Al (-18 kJ/mol instead of -44 kJ/mol) than Zr and a positive heat of mixing with Zr (4 kJ/mol). Increasing the repulsion between atoms can lead to heterogeneities [146]. In addition, Nb has a smaller atomic radius than Zr (1,45 for 1,55 Å) which could increase compacity and ultimately increase GFA.

Characterisations will cover mechanical properties (Young's modulus, hardness and compression) and will be linked to the structural evolution (DSC, Density, XRD, Grindosonic). Because we are

developing the alloy for biomedical application, we will also test the influence of this specific Nb substitution model on corrosion resistance.

V.2. Influence of Zr substitution with Nb on the $Zr_{56}Co_{28}Al_{16}$ alloy

This part is divided into three sections. First, we will look at the influence of the substitution on the glass forming ability of the alloy and its thermal stability. Second, we will look at the surface properties and more specifically corrosion resistance. Finally, we will investigate the influence of the substitution path on the mechanical properties.

V.2.1. Impact on GFA and thermal stability

Rod-shapes samples with a diameter of 5 mm were used to evaluate the GFA. This diameter allows for sufficient material to machine structural parts that could be used in high technology devices (medical field, sport, high precision engineering…). The glassy structure was characterized through XRD and samples were considered amorphous while no intense and sharp peaks were detectable in the XRD measurements. Samples with Nb content up to 3 at% ($Zr_{56}Co_{28}Al_{16}$, $Zr_{55}Co_{28}Al_{16}Nb_1$ $Zr_{54}Co_{28}Al_{16}Nb_2$ and $Zr_{53}Co_{28}Al_{16}Nb_3$) showed no peak in their XRD measurements. They will respectively be called Nb0, Nb1, Nb2 and Nb3 in the suite of this chapter. Sample with 4 at% of Nb was partially crystallized with positions of the peaks corresponding to previously identified phases: ZrCo, ZrCoAl and Zr_6CoAl_2. Samples with 6 at% and 8 at% Nb were fully crystallized. XRD spectrums for compositions Nb0 to Nb4 are shown in Figure V-3.

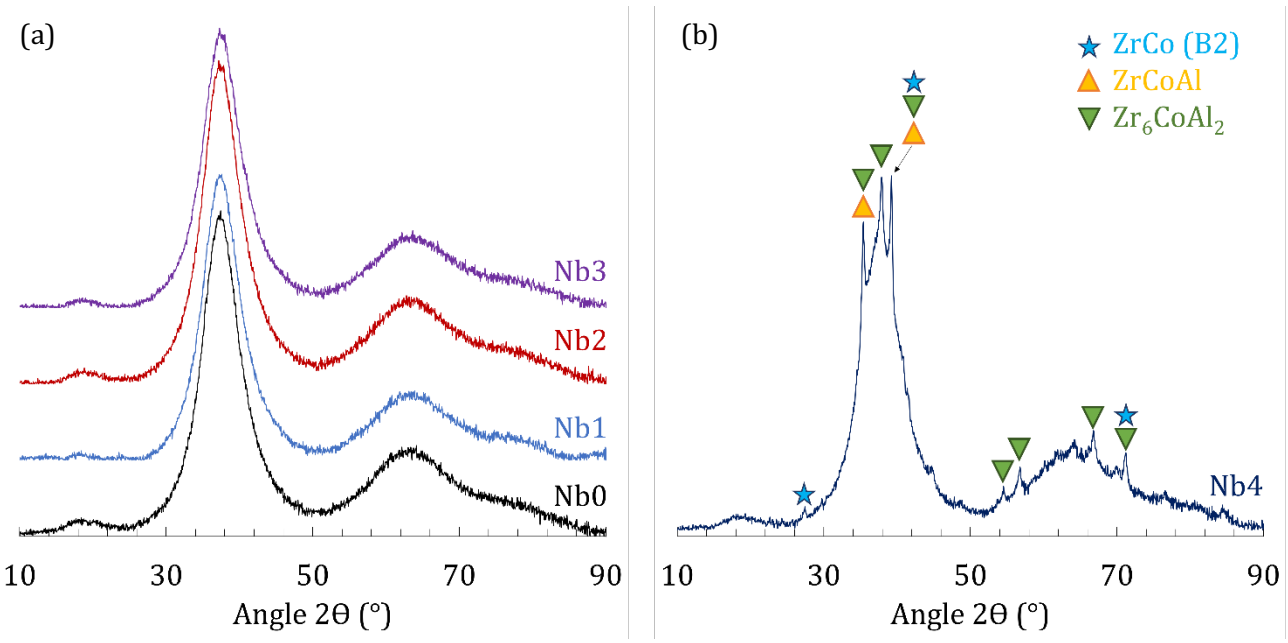

Figure V-3: X-ray diffraction patterns acquired on 5mm-diameter rods cross sections. (a) shows the diffraction patterns for the alloys $Zr_{56}Co_{28}Al_{16}$, $Zr_{55}Co_{28}Al_{16}Nb_1$ $Zr_{54}Co_{28}Al_{16}Nb_2$ and $Zr_{53}Co_{28}Al_{16}Nb_3$. (b) shows the XRD pattern from the $Zr_{52}Co_{28}Al_{16}Nb_4$ samples.

The four XRD patterns from Nb0 to Nb3 present a broad peak typically associated with an amorphous structure. The amorphous bump characteristic of the amorphous state can be fitted using Lorentz's equation. From this fit is extracted the bump position (position of the maximum of the intensity of the amorphous bump). These values indicate the average interatomic distance. The fits were realised on an angular range from 30° to 45° and each fit function exhibited a correlation factor (R^2) over 0.99. Figure V-4 plots the position of the maximum intensity as a function of the Nb content. With increasing Nb content, we observe that the angular value of the bump position increases, meaning that the average first neighbour distance decreases (it is inversely proportional, based on Bragg's law). This suggests the overall densification of the glass structure.

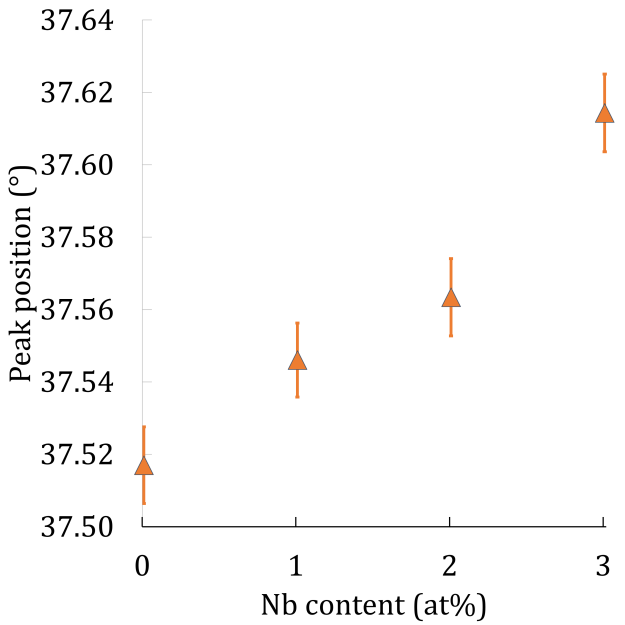

Figure V-4: Plot of the position of the maximum of intensity of the amorphous bump from each XRD pattern (one for each composition).

A reduction of the average interatomic distance can be also connected with a reduction of free volume in the glass with Nb addition. Free volume content was measured through density measurement, as-cast and after thermal treatment. The same annealing treatment, as the one reported in Chapter III and as the long-time relaxation process in Chapter IV, was used. We performed annealing at about 675 for 48 hours. Figure V-5 (a) plots the densities measured in the as-cast state and after relaxation. An increase in the densities with the addition of Nb is measured both in the as-cast (as expected with a substitution of Zr by Nb) and the relaxed state. As-cast density is measured at 6.38 g/cm^3 for Nb0 and increases up to 6.43 g/cm^3 for Nb3. After annealing for 48h at 675 K, one can consider the material fully relaxed, even though we can think that relaxation kinetics may be different with Nb addition. Density variations correspond to the atomic reorganisation with free volume annihilation. The free-volume annihilation induces a volume reduction, which is reported in Figure V-5 (b). This volume variation is observed to be slightly lower for higher Nb content, suggesting that less free volume is annihilated. This could imply that less free volume was embedded in the as-cast glass with Nb addition.

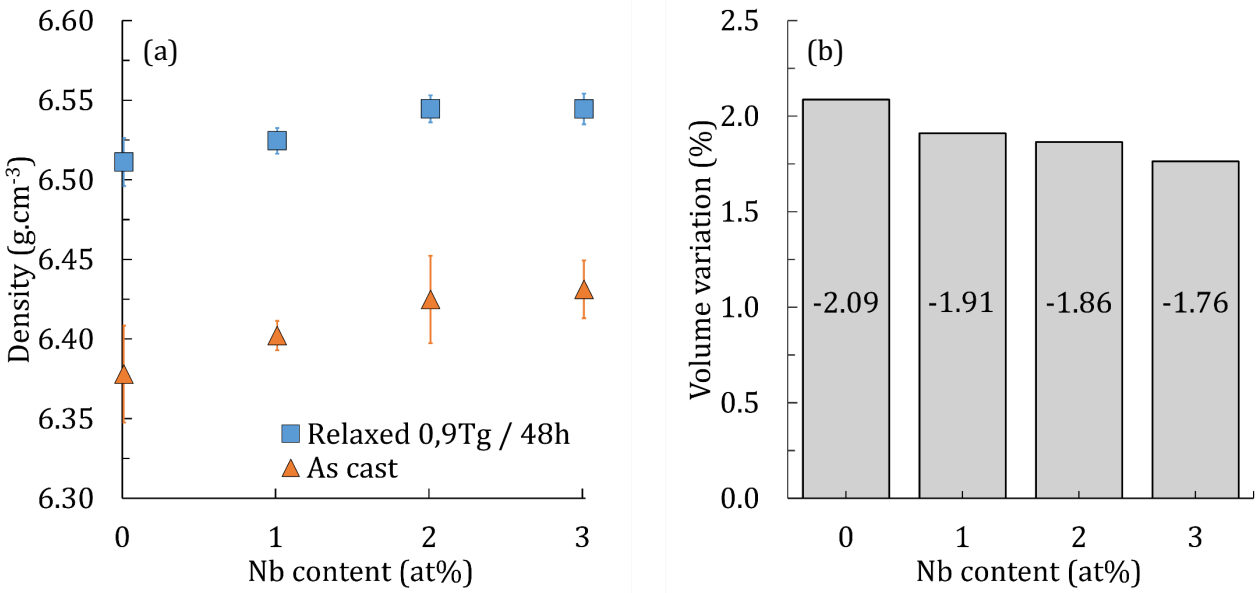

Figure V-5: (a) plots the densities as-cast and after relaxation for the several Nb content studied. (b) plots of the volume variation resulting from the relaxation process.

We have seen in this first section that Zr by Nb substitution reduces critical diameter when Nb reaches 3 at%. However, we can not make a statement on the evolution of the critical diameter for Nb1 and Nb2. Based on the literature study and Inoue's criterion for the design of glass formers, this is coherent since Nb has a PMH with Zr and a NMH of lower absolute value with Co and Al than Zr. So, the total mixing enthalpy of our alloy (as described in chapter III) rises from -44.9 kJ/mol (for Nb0) to -43.6 kJ/mol (for Nb3). From the study of the glass structure through XRD, we have seen that Nb addition by Zr substitution appears to increase the atomic density. This is supported by the performed density measurements, which show that Nb addition both increases the glass density and reduces the volume fraction of free volume embedded in the glass matrix.

V.2.2. Impact of Zr by Nb substitution on the thermal stability of the glass

Figure V-6 shows the DSC measurements for the four amorphous alloys: Nb0, Nb1, Nb2 and Nb3. DSC curves are acquired using samples from 5-mm diameter rods. All characteristic temperatures are reported in Table V-1. Values reported in Table V-1 are averages between two sets of measurements (standard deviations remain under half a kelvin).

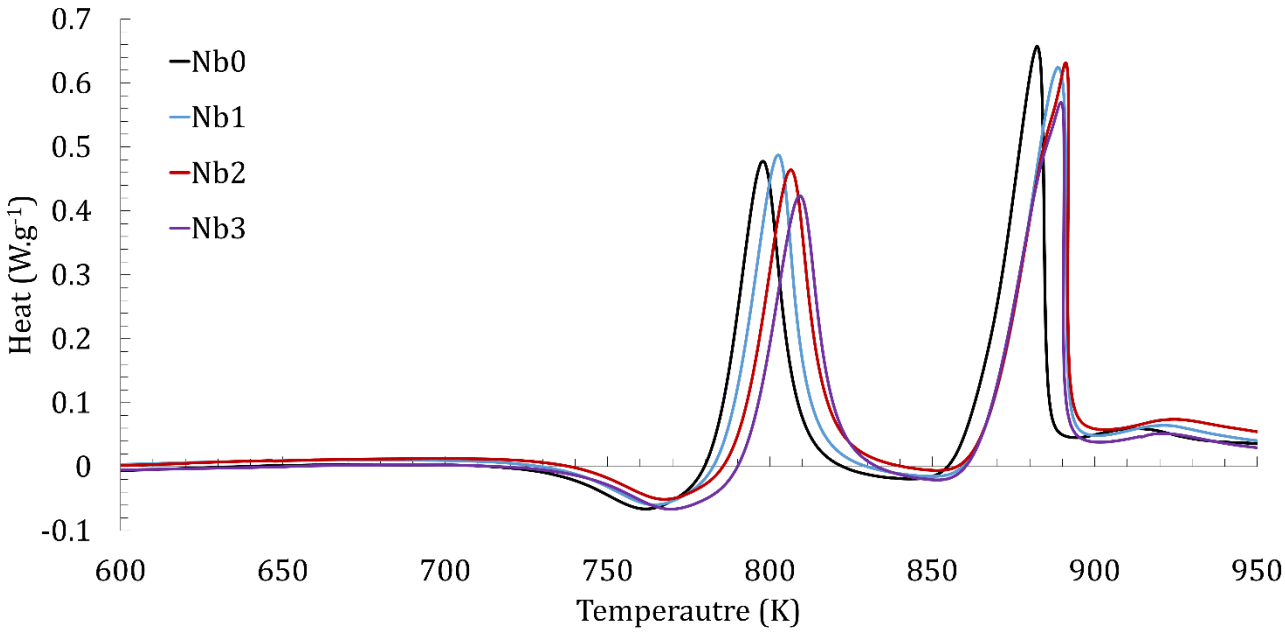

Figure V-6: DSC measurements at 20 K.min^{-1} for Nb0, Nb1, Nb2 and Nb3.

Alloy	Composition (at%)	T_g (K)	T_x (K)	T_{p1} (K)	T_{p2} (K)	ΔT (K)
Nb0	$Zr_{56}Co_{28}Al_{16}$	752	784	797	880	33
Nb1	$Zr_{55}Co_{28}Al_{16}Nb_1$	753	787	800	884	34
Nb2	$Zr_{54}Co_{28}Al_{16}Nb_2$	755	791	804	887	35
Nb3	$Zr_{53}Co_{28}Al_{16}Nb_3$	759	794	807	886	35

Table V-1: Characteristic temperatures (in K) taken as the average of two sets of DSC measurements for Zr-Co-Al-Nb alloys with Nb content from 0 to 3 at%. The standard deviation between the several temperatures measured in the two sets of measurements was below 0.5 K.

T_g rises from 752 K to 759 K when adding 3 at% of Nb. T_x also shifts toward higher temperatures, as it is measured at 784 K for Nb0 and 794 K for Nb3. Because T_g and T_x shift of the same amount, ΔT is relatively constant around 33K, with a negligible increase for Nb2 and Nb3.

We can note the two characteristic transformation peaks are conserved with Nb addition. This could imply that the transformation kinetic upon heating is not drastically changed with minor Nb addition. It appears that Zr by Nb substitution induces a rise in T_g, T_x and T_{p1}. The rise is of the same magnitude for all three measurements (about 10 K). This correlates with the increase in density observed through XRD and density measurement. Zr by Nb substitution induces densification and a rise in T_g and T_x.

V.2.3. Impact on corrosion resistance properties

Nb addition to the Zr-Co-Al ternary glass former is mostly reported in the literature to increase corrosion resistance. Finally, as we are studying glass formers for biomedical application, we must check that Nb addition does not alter corrosion properties. Therefore, this section is dedicated to the study of the influence of this specific alloying method on the corrosion resistance of our alloy. We performed corrosion testing following the same procedure as introduced in Chapter III for the study of our base alloy. Figure V-7 regroups the polarization curves in NaCl electrolyte for Nb0, Nb1, Nb2 and Nb3.

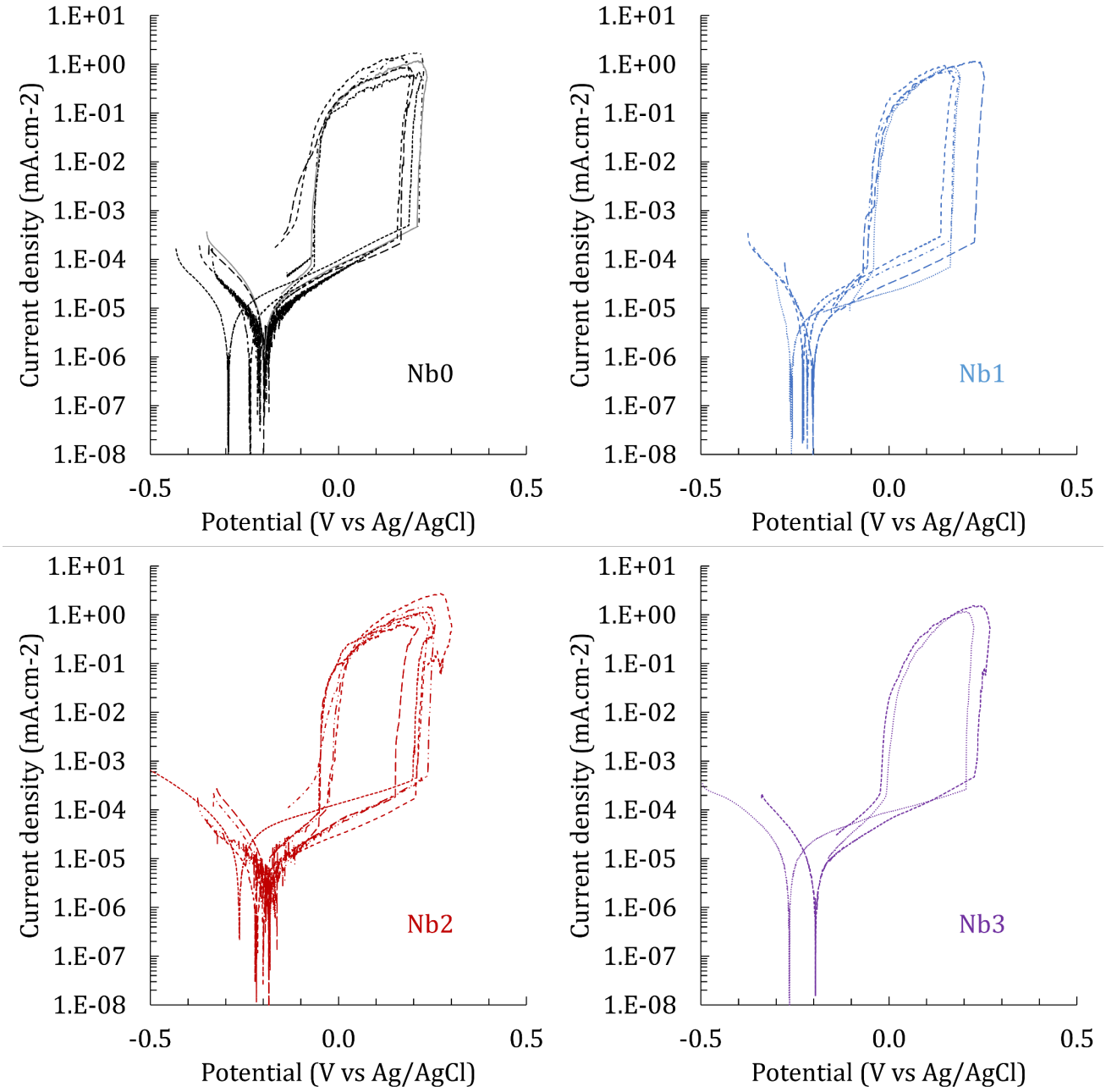

Figure V-7: Polarisation curves of $Zr_{56-x}Co_{28}Al_{16}Nb_x$ with x ranging from 0 to 3 at%. Electrolyte is NaCl 9g.L^{-1} at 310 K.

Before polarisation testing, all samples were subjected to 24 hours immersion at open circuit potential (OCP). All compositions exhibited spontaneous passivation when immersed in saline solution. After 24 hours of immersion, the potential is still slowly rising for all the grades, indicating that the passive film is still growing or getting denser.

For each grade, we performed multiple measurements on the same sample. Polishing was performed between each test to suppress the volume of material affected by the previous test. We observe that Nb addition does not affect the general response of the alloy to polarisation. We still observe a passivation plateau after the corrosion potential, up to pitting breakdown. Also, after pitting potential, lowering the potential induces re-passivation before the corrosion potential. All the characteristic potentials extracted from the polarisation curves reported in Figure V-7 are regrouped in Table V-2. All values are given as the average of the values measured on each curve.

Alloy	**Composition (at%)**	**E_{ocp} (V vs ref)**	**E_{pit} (V vs ref)**	**E_{pp} (V vs ref)**
Nb0	$Zr_{56}Co_{28}Al_{16}$	-0,195 ± 0,051	0,186 ± 0,030	-0,075 ± 0,031
Nb1	$Zr_{55}Co_{28}Al_{16}Nb_{1}$	-0,171 ± 0,051	0,191 ± 0,027	-0,054 ± 0,022
Nb2	$Zr_{54}Co_{28}Al_{16}Nb_{2}$	-0,150 ± 0,024	0,203 ± 0,033	-0,080 ± 0,042
Nb3	$Zr_{53}Co_{28}Al_{16}Nb_{3}$	-0,097 ± 0,140	0,206 ± 0,227	0 ± 0,03

Table V-2: average values of characteristic potentials extracted from the polarisation tests in NaCl 9 g.L^{-1} at 310 K performed on Nb0, Nb1, Nb2 and Nb3. Values are given in V versus the reference electrode (Ag/AgCl)

The average value of E_{ocp} and E_{pit} appears to be slightly increasing. However, if we consider the variability associated with corrosion resistance measurement, the magnitude of the variation is not significantly larger. Additionally, the morphology of the pitting site is globally unchanged as illustrated by Figure V-8 showing typical pit sites in both $Zr_{56}Co_{28}Al_{16}$ and $Zr_{54}Co_{28}Al_{16}Nb_{2}$ alloys. The pit morphologies are still characteristic of a homogeneous dissolution, based on a delamination process. Interestingly, the re-passivation potential E_{pp} does not exhibit similar shifting and is still close to the oxidation/reduction potential of Co^{2+} / Co (which is reported around -0.058 V vs Ag/AgCl).

From those results, we can conclude that the substitution of Zr by Nb in our alloy maintains the excellent corrosion resistance of the $Zr_{56}Co_{28}Al_{16}$. Nevertheless, the corrosion resistance is not enhanced in NaCl 9 g/L at 310 K. This result may suggest that as for Cu-bearing BMG, the TM content controls the pitting corrosion susceptibility of the BMG. This result differs from what was reported in the literature [150, 157, 159, 173].

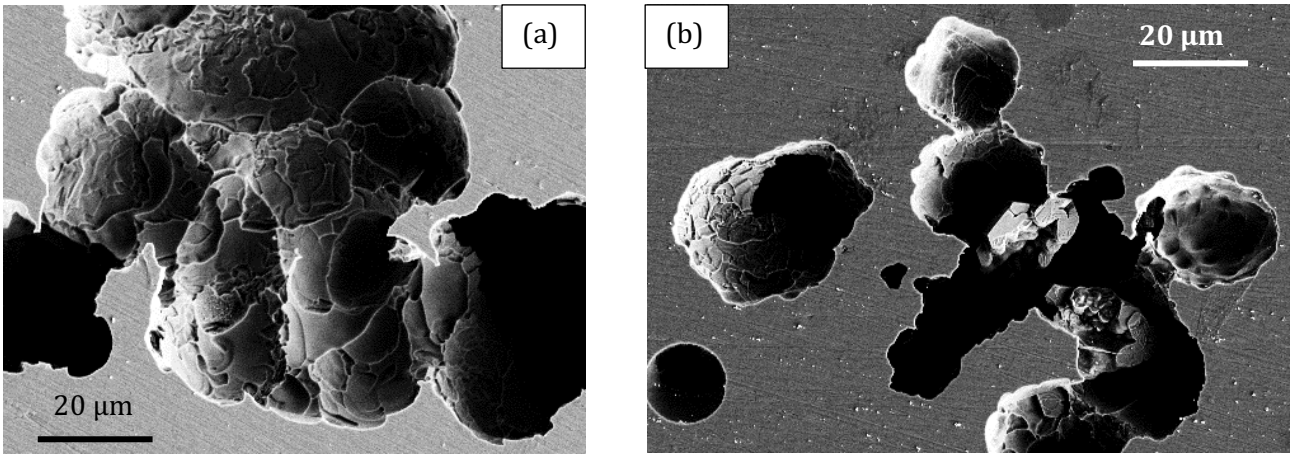

Figure V-8: SEM image of the multiple pit sites on a $Zr_{56}Co_{28}Al_{16}$ sample (a) and a $Zr_{54}Co_{28}Al_{16}Nb_2$ sample (b). The pit morphology of the Nb2 sample is very similar to what was observed on Chapter III on the $Zr_{56}Co_{28}Al_{16}$.

Two hypotheses can be proposed to explain such differences:

1. First, we were able to add Nb only up to 3 at%, as the choice was made to keep a critical diameter of 5 mm minimum. Literature reports Nb addition up to 5 at%. Higher Nb atomic fraction may have a more noticeable influence on corrosion behaviour.
2. Because this work is performed to explore the potential of this ternary base for biomedical applications, we decided to follow ISO standards to design some of our testing procedures, including the polarization tests. Therefore, we study here our alloy corrosion resistance in a saline solution and the results are very likely to differ in other electrolytes. For instance, it was demonstrated by B. Guan *et al.* that PO_4^{3-} cations, found in Hank solution, slow down the absorption of Cl^- cations which are very aggressive [157].

V.2.4. Impact on mechanical properties

V.2.4.1. Young's modulus and Vickers's hardness

Young's modulus was measured through a vibrational technique to be able to compensate for machine deformation during compression testing. The effect of Nb content on Young's modulus was estimated. Note that to calculate Young's modulus using the equation reported in chapter II.3.3.1, we used a Poisson's ratio to 0.36 but considering a Poisson's ratio of 0.35 or 0.37 would not change the result here. With Nb addition, Young's modulus increases from 93 GPa for Nb0 to about 98 GPa for Nb3 as reported in Figure V-9. The value for Nb0 is coherent with data available in the literature (see chapter I) but as this substitution mode is not reported in the literature, no data are available for the Nb1, Nb2 and Nb3 alloys. Measurements were also performed after the relaxation treatment (*i.e.* 675 K for 48h). During relaxation, as excepted Young's modulus increased by approximately 5% for all compositions.

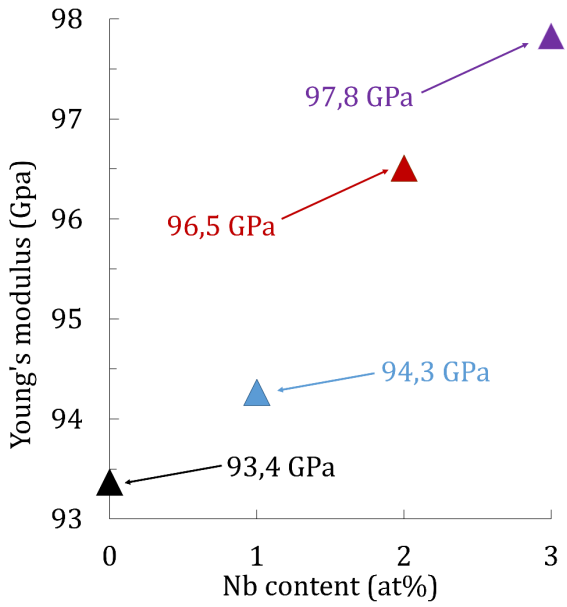

Figure V-9: Young's modulus measurements for compositions from Nb0 to Nb3

Consequently, T_g and E both variate toward higher values with the increase of the Nb content. This correlation between E and T_g has already been reported in the literature, for instance for Zr-Ti-Cu-Al glass formers [97]. Moreover, the increase in Young's modulus supports the idea that Nb addition in this specific mode brings the glass to a denser or more cohesive state.

Vickers hardness measurement also supports such a view. Figure V-10 shows box plots drawn from 40 Vickers hardness measurements performed on each composition.

Figure V-10: Box plots of the Vickers's hardness measurement on Nb0, Nb1, Nb2 and Nb3.

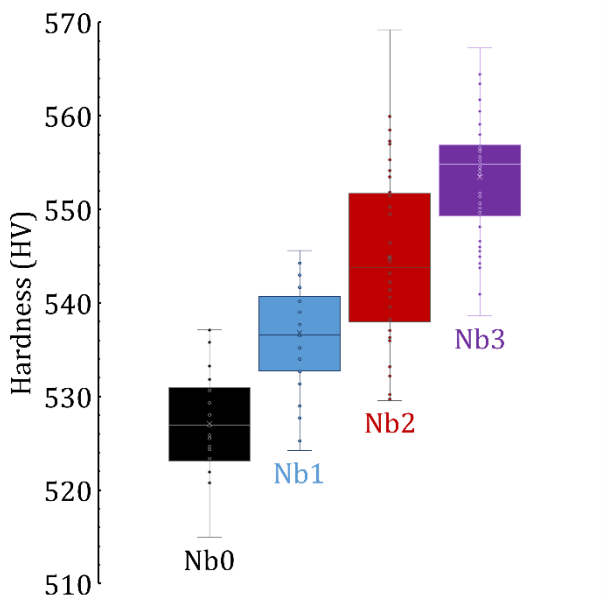

The average hardness values of 527 HV, 537 HV, 545 HV and 553 HV are measured respectively for Nb0, Nb1, Nb2 and Nb3. Standard deviations are respectively of ±5 HV, ±6 HV, ±9 HV, and ±7 HV. Considering the precision of the equipment, and even though we tried to improve the procedure by adding microscopy to measure indent sizes, we can not conclude that this variation in standard deviations

is significant. Once again, these new results are coherent with the other characterisations. Glass transition temperature, Young's modulus, density and hardness are all increasing. An equation originally developed for crystalline alloy (Tabor's equation) gives a relationship between hardness (H) and yield strength (σ_y):

$$H = K.\sigma_y$$

V-1

where K is a constraint factor depending on the indenter shape and mechanical properties of the indented alloy [37]. This relationship has since been applied to metallic glasses and is often reported as $H \approx 3\sigma_y$ [255, 256]. This relation is far from being completely off from our experience as the average yield stress measured in chapter III.2.3.1 is 1.926 ± 44 GPa which is 2.68 ± 0.06 times less than our average Vickers hardness of 5.168 GPa. Anyhow, the increasing hardness with increasing Nb atomic fraction could mean that the compressive yield stress of the alloy is also increasing. Taking 2.68 as the K value in Tabor's equation, we could expect roughly 100 MPa of increase between the yield stress of Nb0 and Nb3.

V.2.4.2. Compression tests

As mentioned earlier, literature reports a strong influence of Nb addition on the compressive behaviour of several bulk metallic glasses, such as Zr-Cu-Al [149], Zr-Ni-Al [152] and Zr-Co-Al [157] ternary bases. To assess the influence of Nb addition in this specific substitution mode, we performed compression testing following the procedure used earlier in this manuscript. A series of tests were carried out for each composition (Nb0 to Nb3) in the as-cast state. Figure V-11 shows compression stress-strain curves obtained for compositions Nb0 to Nb3.

Table V-3 shows two parameters: firstly, the position of the first stress drop (serration) detected for each composition (Nb0 to Nb2, Nb3 does not exhibit plasticity). It also gives the extent of the plastic strain.

	Nb0		**Nb1**		**Nb2**		**Nb3**	
	Stress (MPa)	**Strain (%)**	**Stress (MPa)**	**Strain (%)**	**Stress (MPa)**	**Strain (%)**	**Stress (MPa)**	**Strain (%)**
Position of first serration	1899 ± 55	2.1 ± 0.1	1981 ± 12	2.2 ± 0.1	1901 ± 58	2.1 ± 0.1	-	-
Plastic strain	-	3.9 ± 0.9	-	2.2 ± 0.6	-	2.7 ± 1.2	-	0

Table V-3: Position of the average first stress drop (stress and strain) with standard deviations for Nb0, Nb1, Nb2 and Nb3 and average ultimate stress and plastic strain for the same compositions.

From Figure V-11 and Table V-3, we see that Nb addition slightly decreases plastic strain. The Nb0 series has an average plastic strain of around 3.94% and this value drops to 2.15% and 2.66% for Nb1 and Nb2, respectively. The reduction of the alloy ductility is coherent with the results previously exposed in this chapter. Indeed, we have seen that with Nb addition in this specific substitution mode, we

are inducing densification of the alloy, along with a decrease of the free-volume volume fraction and an increase in the hardness.

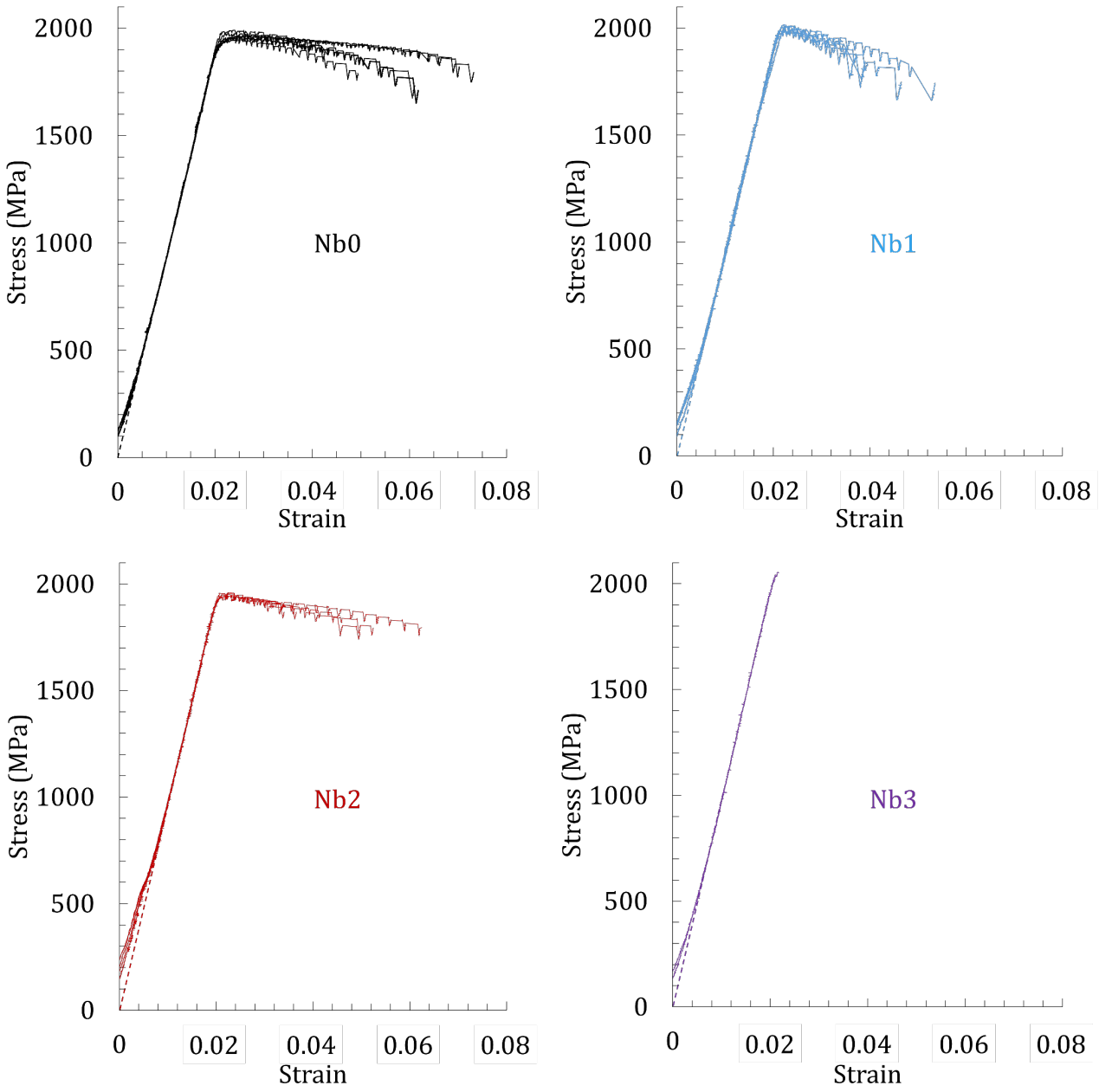

Figure V-11: Strain-stress curves from compressive testing acquired at room temperature, with a strain rate of 2.5 .10^{-4} s^{-1}, for Nb0, Nb1, Nb2 and Nb3.

As previously mentioned, the hardness increases along with Nb addition suggested an increase of the yield stress. This increase is not obvious in the present results. Because of the standard deviation on the yield stress, which prevents the observation of small changes in the absolute value of this

parameter, we got interested in the first serration. This first serration is associated with the apparition of a detectable shear event inside the glass matrix, which happens shortly after the yield stress is reached. Here, we do not observe major differences in the position of the first stress drop among the studied compositions.

We have seen in the previous chapters that the analysis of the serration pattern over the plastic deformation can give valuable information on the shear band propagation behaviour. Each stress-strain curve was analysed following the same process as in previous chapters. The detailed results for each curve are available in supplementary material H for Nb0, Nb1 and Nb2. Nb3 is voluntarily left out of this specific analysis as no plastic deformation was observed for any of the samples tested with this specific composition.

We can note that almost none of the Nb-bearing samples tested exhibited the two shear band propagation regimes described in Chapter III. Samples Nb1 and Nb2 directly presented the catastrophic propagation regime, with a fast increase in stress drops magnitude. Table V-4 regroups the number of counted drops and the average magnitude (in MPa) of the drops for each sample.

Nb0			Nb1			Nb2		
Sample	**Drops counted**	**Average magnitude**	**Sample**	**Drops counted**	**Average magnitude**	**Sample**	**Drops counted**	**Average magnitude**
Nb0 - A	46	19	Nb1 - A	26	36	Nb2 - A	40	18
Nb0 - C	50	19	Nb1 - B	18	31	Nb2 - C	30	18
Nb0 - D	35	19	Nb1 - C	22	35	Nb2 - D	12	23
Nb0 - E	71	13	Nb1 - D	15	32	Nb2 - E	20	25
Nb0 - F	24	19	Nb1 - E	19	29	Nb2 - F	13	19
Nb0 - G	67	15						
Average	*49 ± 18*	*17 ± 2.7*	***Average***	*20 ± 4.2*	*33 ± 2.9*	***Average***	*23 ± 12*	*21 ± 3.2*

Table V-4: Number of counted serrations (over 1 MPa) and the average magnitude of the serrations in MPa, for Nb0, Nb1 and Nb2 samples subjected to compressive testing.

From Table V-4, we observe that the average number of counted drops during plastic deformation decreases with Nb addition. The plastic deformation decreases with Nb addition does not appear to increase linearly with Nb content. If we normalize the number of counted drops by the average reach of the plastic deformation, the difference is greatly reduced. We obtain 12.4 drops/strain unit, 7.5 drops/strain unit and 8.6 drops/strain unit for $Zr_{56}Co_{28}Al_{16}$ (Nb0), $Zr_{55}Co_{28}Al_{16}Nb_1$ (Nb1) and $Zr_{54}Co_{28}Al_{16}Nb_2$ (Nb2), respectively. This means that per unit of strain, there is a lower amount of shear band movement detected for Nb1 and Nb2 compared to Nb0. This correlates with the fact that the average stress drop magnitude is increased with Nb addition and to the fact that there is no steady-state propagation regime in Nb1 and Nb2 samples. In other words, the serrations are bigger in Nb1 and Nb2 than in Nb0. Finally, we can mention that none of the samples tested with Nb addition exhibited the **S**elf **O**rdered **C**riticality (SoC) serration statistical repartition. The serration pattern analysis performed on

the plastic deformation during compressive testing showed that Nb addition to our $Zr_{56}Co_{28}Al_{16}$ BMG by substitution of Zr induced more erratic shear band propagation behaviour. From this analysis, we can hypothesis that a lower number of shear bands are nucleated and share the stress under uniaxial loading. Compared to the alloy without Nb, the load is less spread, leading to an increase in the stress drop magnitude, precipitating failure. This is coherent with the lower ductility observed when comparing ultimate strains between samples. However, it should be acknowledged that the difference is tenuous between the alloys with and without Nb (up to 2 at%). We can even conclude that no major differences are observed between Nb1 and Nb2 samples. Also, the variability in the strain to fracture is rather comparable between compositions. Additionally, like for the alloy without Nb, while dispersion is observed in the plastic strain, the yield stress appears to remain remarkably stable.

The bullet points below summarize the influence of the Nb addition to our alloy on its compressive loading behaviour:

- Up to 2 at% of Nb, the samples maintain plastic strain.
- At 3 at% of Nb, a total absence of plasticity is observed. However, even though Nb3 samples appears to be very brittle, they did not fracture following the "fragmentation mode" presented in Chapter I.3.2.3 which is usual for very brittle glasses. They failed following the "shear fracture mode", typical of ductile samples. Nb3 do exhibit a vein pattern which is typical of ductile failure (see Figure V-12), even though they did not show plasticity under compressive loading. However, the vein pattern observed on Nb3 samples is less smooth and less regular than the pattern on Nb0 samples. The absence of plastic strain of Nb3 samples could be attributed to nano-crystallisation, not detectable through XRD measurements.

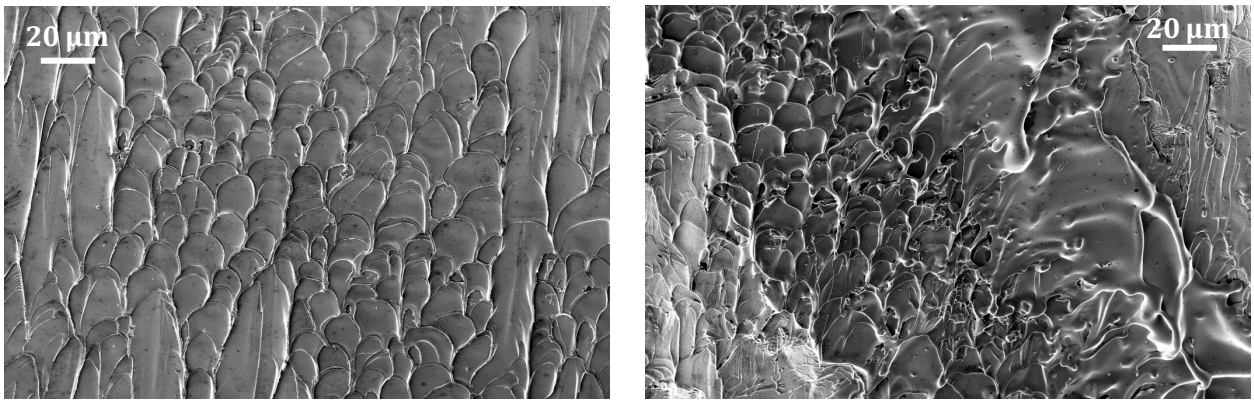

Figure V-12: SEM images of the typical vein pattern at the surface of samples Nb0 and Nb3. Sample Nb3 does exhibit a vein pattern but this latter is not as smooth as the pattern observed on Nb0 sample.

- Samples with 1 at% and 2 at% of Nb exhibited on average less plasticity than the samples without Nb. It is however difficult to differentiate behaviours between samples containing 1 at% and 2 at% of Nb.

- The dispersion in the ultimate strain of Nb-free samples discussed in chapter III.2.3.1 is also observed for samples containing 1 at% and 2 at% of Nb.

The reduction of the overall ductility of the alloy with Nb addition is coherent with the other characterisation exposed earlier in this chapter. We have seen that Nb addition may induce a rise in the glass transition, coupled with a reduction of the free-volume volume fraction embedded in the glass as-cast and an increase of the hardness. Surprisingly, the hardness increase is hardly correlated to an increase in the yield stress. The relation between hardness and yield stress is directly related to the glass structure. Undeniably, Zr for Nb substitution has an impact on our glass structure and chemical stability, which ultimately results in changes in characterized properties.

We identified variations in the characterized properties with Nb addition. These properties, as mentioned earlier and detailed in the previous chapters, are correlated to the glass structure. In the following sub-chapter (V.2.5), we discuss the influence of this specific substitution of Zr by Nb on the $Zr_{56}Co_{28}Al_{16}$. Subsequently, the last sub-chapter (V.3) will put this discussion in perspective by comparing the influence of other Nb alloying methods on the Zr-Co-Al ternary BMG.

V.2.5. Impact on glass structure

The influence of Nb addition on the studied properties is regrouped in Table V-5 together with the possible influence deduced from each characterisation.

Property	Characterisation procedure	Influence of Nb addition	Possible relation with the structure
Glass forming ability	Processing of 5mm diameter rods	Reduced above 3 at% of Nb	Unknown
Average first neighbour distance	XRD measurement	Reduced with increasing Nb content	Shorter bond length (atomic densification)
Density	Archimedes procedure	Increased with Nb addition	Volume densification
Free-volume fraction	Density measurements before and after relaxation	Reduced with Nb addition	Densification
Thermal stability	DSC measurements	T_g and T_x both shift towards higher temperatures	Stabilization
Corrosion resistance	Polarisation testing	No noticeable change	Unknown
Young's modulus	Vibrational measurements	Increased with Nb addition	Stronger atomic interaction
Hardness	Vickers' hardness tests	Increased with Nb addition	Densification
Compression resistance	Compression testing	No plasticity above 2 at% of Nb	Fewer shear bands

Table V-5: Evolution of the characterized properties with Zr substitution by Nb, and a possible link to structural changes.

From this summary, we observe that the average atomic bond length, the density, the embedded free-volume volume fraction, the Young's modulus and the hardness all point towards densification of the glass with Nb addition.

The analysis of the compression resistance should be more nuanced. A slight reduction of the plasticity is observed with Nb addition up to 2 at%. No change is observed on the magnitude of the variability of the plastic deformation, or the yield stress, compared to the Nb-free alloy. With 3 at% of Nb addition, however, the influence is clear as no plasticity is detected.

The analysis of the thermal stability points towards the stabilization of the glass with Nb addition. This is somehow coherent with the densification of the glass. Based on our understanding, a dense glass is composed of closely packed structures, such as icosahedral and icosahedral-like structures. Because of their high compacity, these structures tend to be more stable. As mentioned earlier, the glass transition evolution has already been used as an indicator of mechanical properties evolutions [97]. Similar to the conclusion exposed by Q. He *et al.*, we observe that both Young's modulus and the glass transition temperature increase with Nb addition. Figure V-13 exposes the correlation between T_g and Young's modulus for several Zr-Ti-Cu-Al alloys presented in [97], Zr-Co-Al alloys and the $Zr_{56-x}Co_{28}Al_{16}Nb_x$ alloy studied in this chapter. All indicators converge toward the hypothesis that Zr substitution by Nb induces densification of the glass.

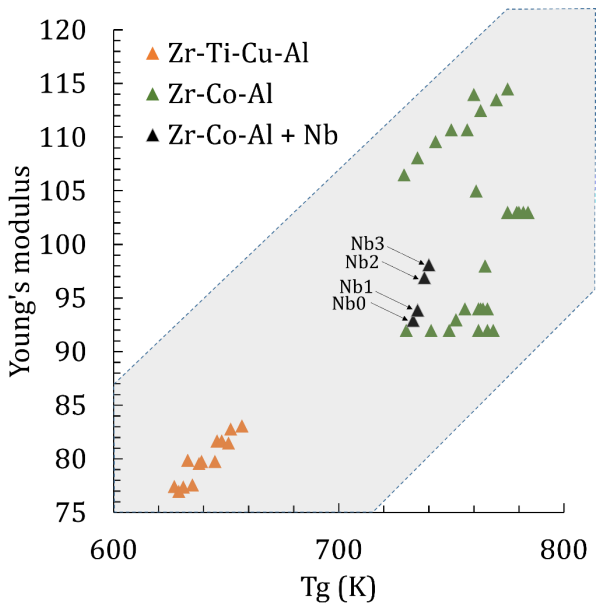

Figure V-13: Young's modulus as a function of T_g for the $Zr_{56-x}Co_{28}Al_{16}Nb_x$ (x = [0:3]) and for Zr-Co-Al and Zr-Ti-Cu-Al alloys for comparison.

The mixing enthalpy of a system illustrates the chemical affinity between the components among a specific system. Q. He *et al.* demonstrated that in the Zr-Cu-Al-Ti system, the value of T_g decrease when the heat of mixing of the system increases (diminution of its absolute value in the negative range). Figure V-14 shows the evolution of T_g measured on several Zr-Cu-Al and Zr-Co-Al ternary glasses as a function of the calculated enthalpy of mixing of each system. The same trends as reported by Q. He *et al.* appears to exist for Zr-Co-Al ternary glasses. We observe that while T_g decreases, ΔH_{mix} increases.

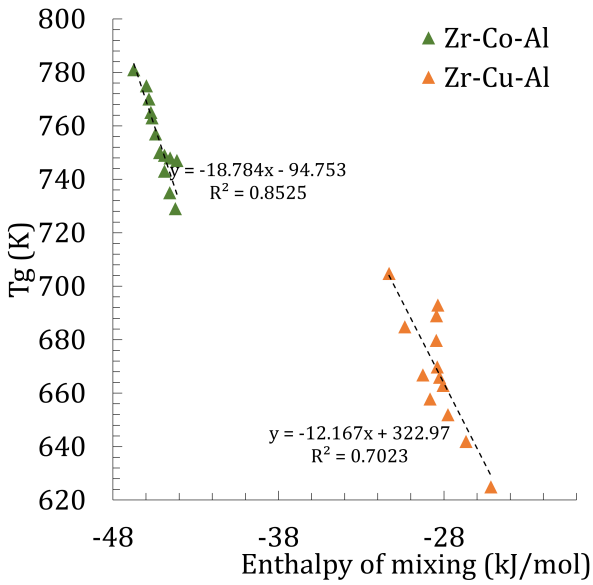

Figure V-14 : Plot of calculated heat of mixing against glass transition temperature (T_g) for ternary Zr-Cu-Al BMGs and Zr-Co-Al BMGs. The lines represent linear fitting.

V.2.5.1. Influence of Nb addition on mixing enthalpy and mismatch entropy

From the analysis of our experimental results, the Zr substitution by Nb appears to induce densification of the glass. This is coherent with our measurement concerning the increase of T_g. Figure V-15 plots the calculated heat of mixing against the measured glass transition temperature for the four compositions studied in this chapter. Interestingly, glass transition temperature rises along with the increase in the total enthalpy of mixing of the system, which is the opposite of what is reported in Figure V-14.

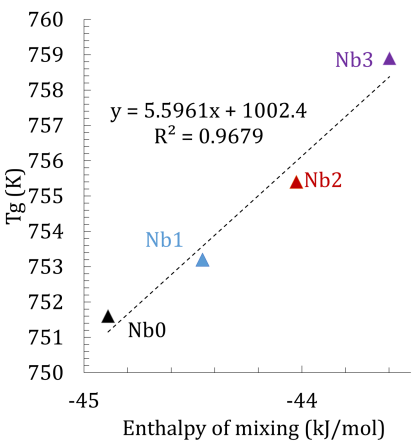

Figure V-15: Plot of calculated heat of mixing against measured T_g for $Zr_{56-x}Co_{28}Al_{16}Nb_x$ alloys (x = [0:3]). The line represents linear fitting.

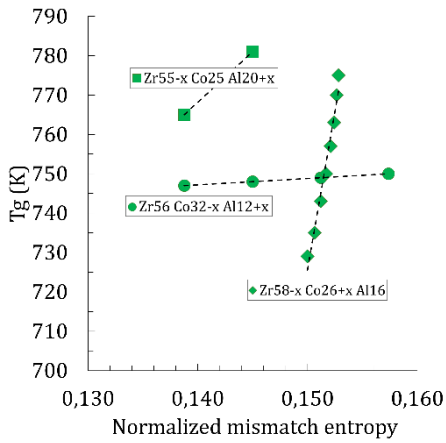

Figure V-16: Glass transition temperature in several Zr-Co-Al BMG as a function of the normalized mismatch entropy [150, 157, 159].

One explanation could be that the chemical affinity between elements is not the only parameter that can influence all properties and structure. As presented in Chapter III.1, a topological criterion also exists. The mismatch entropy is based on the atomic radii ratio among elements. Figure V-16 plots the glass transition temperature of several Zr-Co-Al glass formers as a function of the calculated mismatch entropy depending on their variation of composition. From this figure, we observe that the correlation between the two parameters is weaker compared to the one between the enthalpy of mixing and the glass transition temperature (T_g) in Figure V-14. In Figure V-16 we see that for each composition, an increase in the normalized mismatch entropy is accompanied by an increase in the glass transition temperature. However, we observe that depending on the composition and the atomic ratios, the correlation factor between normalized mismatch entropy and T_g greatly varies. For instance, for the $Zr_{58-x}Co_{26+x}Al_{16}$ alloys series, small variations of mismatch entropy are correlated with a great increase of glass transition temperature. On contrary, great variations in the mismatch entropy in the Zr_{56} Co_{32-x} Al_{16+x} are correlated with a moderate increase of T_g.

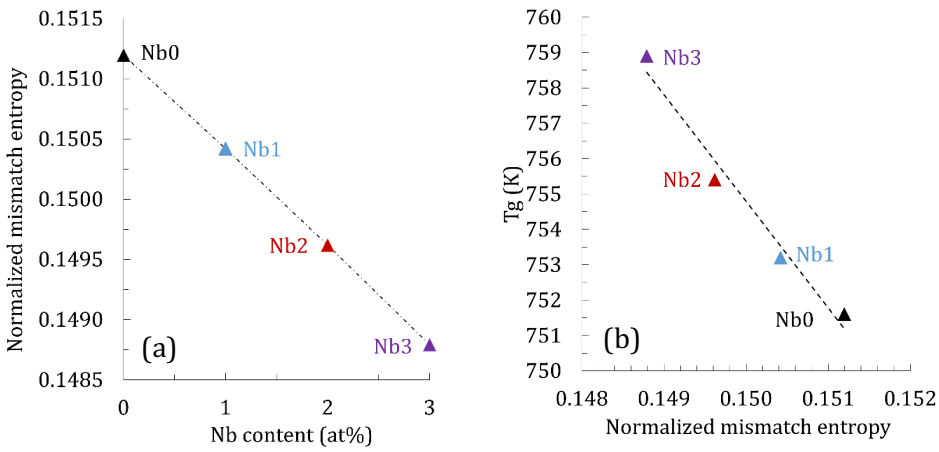

Figure V-17: (a) calculated normalized mismatch entropy as a function of the Nb content and (b) glass transition temperature (T_g) as a function of the normalized mismatch entropy.

In our case, with Zr substitution by Nb, the mismatch entropy decreases as shown in Figure V-17 (a). A decrease of the atomic mismatch usually results in a decrease of the GFA, which we observe over

3at% of Nb. A reduction of the mismatch entropy would lower the liquid "confusion" during cooling and favour atomic rearrangements. This, therefore, explains the reduction of the free volume content and the creation of a denser glass with increasing of the Nb content. Figure V-17 (b) plots the T_g measured for each alloy as a function of the mismatch entropy. We observe that in our case, contrary to what could be expected from Figure V-16 a decrease in the mismatch entropy is associated with a decrease of T_g.

We see from this analysis that calculated parameters such as the enthalpy of mixing and the mismatch entropy do not correlate to what can be extracted from the literature with the evolution of T_g. Both the mixing enthalpy and the mismatch entropy are parameters used to apprehend a glass former as a global system. This does not consider the SRO configuration nor the inhomogeneity of the structure of the glass. There may be other factors at play, such as the local order, that are neglected by these two parameters. We now discuss the influence of Nb addition with a finer approach to the glass structure.

V.2.5.2. Influence of Nb addition on Zr-Co-Al short-range order

W. K. Le *et al.* got interested in the way Nb was integrated into the glass structure while added to the Zr-Co-Al ternary base [172]. Nb shares similar features with Zr, as summarized in Table V-6. They belong to the same period and bloc of the periodic table. They also present dissimilarities: Nb has a smaller atomic radius, a higher electronegativity, a higher density, and a higher melting point.

W. K Le *et al.* assumed that the local structure was somehow like the phases obtained after crystallization. For the Zr-Co-Al ternary system, three main phases are identified: ZrCo (B2), Zr_6CoAl_2 and ZrCoAl (see Chapter III). Like Y. Dechuan *et al.* [151], W. K. Le *et al.* defined the local structures (icosahedral or else) based on the stoichiometry of these phases. These three phases are used to define quasi-equivalent clusters, namely α, β and γ clusters in Le *et al.* work. W. K. Le *et al.* also assumed that Nb should not be integrated as interstitial atoms, as this would be highly unfavourable from an energetical point of view: Nb is too big and would cause a large distortion of the local structure. W. K. Le *et al.* assumed that Nb would be integrated by being substituted to another atom in the local structure.

For both α and β quasi-equivalent clusters, the total energy of the cluster was calculated. W. K. Le *et al.* showed that compared to a cluster without Nb, the more favourable configuration was to substitute the Zr atom. The substitution of Co (in α and β quasi-equivalent clusters) or Al (in β quasi-equivalent cluster) atoms induces higher total energy. Based on some calculations, it could be suggested that Nb-bearing icosahedral clusters have a greater compacity than Nb-free clusters [172].

Following this reasoning, we can emit the hypothesis that substituting Co or Al by Nb is somehow equivalent to an increase of the Zr content in the alloy. This is considering our ternary alloy as the combination of an early transition metal (Zr, Nb), a late transition metal (Co) and Al. This once again stresses the importance of the substitution route when performing minor alloying.

Element	Z	Period	Bloc	Kind	Group	Electronic structure		Pauling electronegativity	Density (g/cm³)	Fusion (K)
Al	13	3	p	Poor metal	III B	[Ne] $3s^2\ 3p^1$	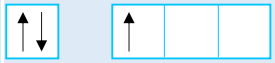	1,61	2,699	933
Co	27	4	d	TM - late	VIII	[Ar] $3d^7\ 4s^2$	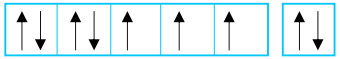	1,91	8,900	1768
Zr	40	5	d	TM - early	IV A	[Kr] $4d^2\ 5s^2$		1,33	6,520	2128
Nb	41	5	d	TM - early	V A	[Kr] $4d^4\ 5s^1$	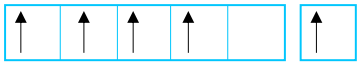	1,6	8,570	2750

Table V-6: Elements of interest electronic properties, density, and fusion temperatures

V.3. The importance of the substitution route…

We have seen from the analysis of the results reported in the literature (see chapter V.1.2) that minor Nb addition in Zr-based bulk metallic glasses **usually**:

- decreases glass transition temperature and/or supercooled liquid region [148–150, 154, 157, 159]
- increases plasticity and decreases yield stress [149, 152, 157]
- increases corrosion resistance in various solutions [148, 150, 154, 155, 157, 159, 172]

However, it appears that **in our case**, Zr substitution by Nb in the $Z_{56}Co_{28}Al_{16}$ ternary alloy induces:

- a reduction of the average interatomic distance
- a rise of the glass transition temperature
- a loss of ductility (mostly over 2 at% of Nb)
- no major evolution of the yield stress
- no major changes in the corrosion resistance in NaCl 0.9 g/L at 310 K.

This specific behaviour could be attributed to the way the Nb addition was performed. Indeed, we did not add Nb by substitution of Co or Al, or the entire base, as it is reported in the literature. Therefore, the way the substitution is performed seems as important as the element of choice for minor alloying. This section is dedicated to the study of the influence on this specific alloying method based on three main fields of interest: thermal stability, mechanical properties, and corrosion resistance.

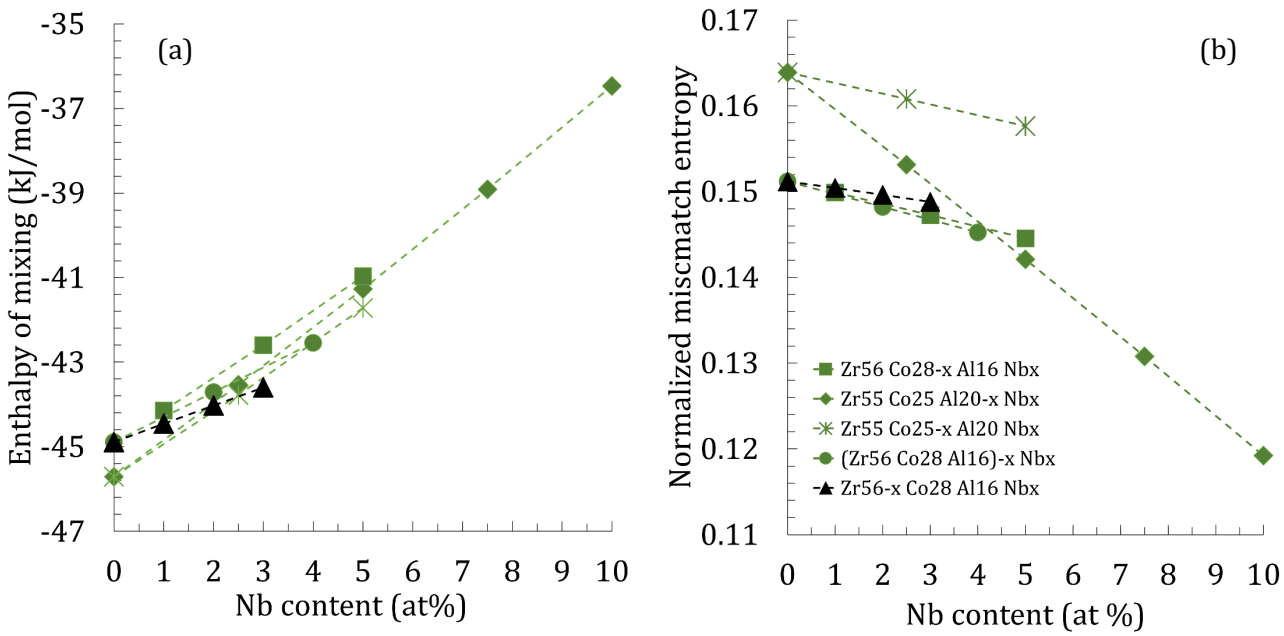

Figure V-18: (a) Enthalpy of mixing and (b) mismatch entropy for several Zr-Co-Al-Nb alloys (including present work) as a function of the Nb atomic fraction. Data are extracted from the literature and compared to our work. [150, 157, 159, 173]

By first looking at the two parameters studied previously (mixing enthalpy and mismatch entropy), we observe that Nb addition, no matter which substitution route is chosen, appears to both increase the mixing enthalpy and decrease the mismatch entropy. Figure V-18 (a) plots the mixing enthalpy as a function of the Nb content and Figure V-18 (b) plots that mismatch entropy as a function of the Nb content [150, 157, 159, 173]. We observe that the substitution mode chosen in this work has the lowest effect on both parameters.

V.3.1. ... on thermal stability

Figure V-19 plots the glass transition temperature of several Zr-Co-Al ternary glasses with Nb additions. Data are extracted from the literature: $Zr_{55}Co_{25}Al_{20-x}Nb_x$ [150], $Zr_{55}Co_{25-x}Al_{20}Nb_x$ [159] and $Zr_{56}Co_{28-x}Al_{16}Nb_x$ [157]. This figure clearly illustrates the two trends observed while performing minor additions of Nb to the Zr-Co-Al ternary system. We observe from those data that for two different initial compositions ($Zr_{55}Co_{25}Al_{20}$ and $Zr_{56}Co_{28}Al_{16}$) Co substitution by Nb induces a lowering of T_g. To our knowledge, a T_g increase with Nb addition has never been reported in the Zr-Co-Al system and we can therefore assume that this is due to our substitution method.

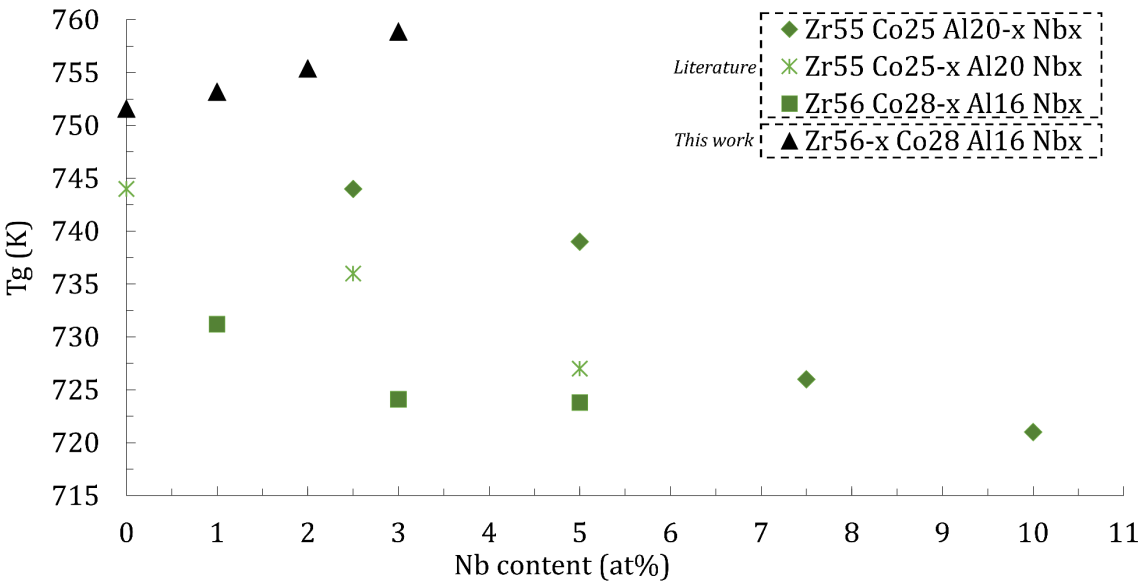

Figure V-19: Plot of the T_g for several Zr-Co-Al alloys with Nb addition against the Nb content. Data are extracted from the literature and compared to our work.

We made the hypothesis in chapter V.2.5.2 that substituting Co or Al by Nb in the Zr-Co-Al ternary glass was more or less equivalent to increasing the Zr/Co or Zr/Al ratio in the ternary glass. Several publications are dedicated to the study of the influence of the Zr/Co or Zr/Al ratio in the Zr-Co-Al ternary base. The influence of the variation of these specific ratios on the thermal stability of the alloy (T_g and ΔT_x) is reported in Table V-7.

Alloy	x	Ratio	T_g evolution	ΔT_x evolution	Ref.
$Zr_xCo_{84-x}Al_{16}$	x = [51:58]	Zr/Co ↗	↘	→	[205]
$Zr_{80-x}Co_xAl_{20}$	x = [10:30]	Zr/Co ↗	↘	↗	[202]
$Zr_{55}Co_{25-x}Al_{20}Nb_x$	x = [0:5]	(Zr+Nb)/Co ↗	↘	unspecified	[159]
$Zr_{56}Co_{28-x}Al_{16}Nb_x$	x = [1:5]	(Zr+Nb)/Co ↗	↘	↘	[157]
$Zr_{55-x}Co_{25}Al_{20+x}$	x = [0,3]	Zr/Al ↗	↘	↘	[212]
$Zr_{55}Co_{25}Al_{20-x}Nb_x$	x = [2.5:10]	(Zr+Nb)/Al ↗	↘	↘	[150]
$Z_{56-x}Co_{28}Al_{16}Nb_x$	**x = [0:3]**	**(Zr+Nb)/Co → (Zr+Nb)/Al →**	↗	→	**This work**
$Zr_{56}Co_{44-x}Al_x$	x = [12:18]	Co/Al ↗	↘	↘	[222]
$Zr_{55}Co_{33-x}Al_{12+x}$	x = [0:16]	Co/Al ↗	↘	unspecified	[187]

Table V-7: Evolution of T_g and ΔT_x with the evolution of several atomic ratios, in both Zr-Co-Al and Zr-Co-Al-Nb alloys.

From this analysis, we can observe that the increase of the Zr/Co and Zr/Al decreases the glass transition temperature (T_g). The influence on the width of the supercooled liquid region (characterized by ΔT_x) is less clear: for a reduction of the Zr/Co ratio, no general trend can be extracted. However, by increasing the Zr/Al ratio, it appears that the width of the supercooled liquid region is reduced. Now, if we compare these tendencies to the influence of the (Zr+Nb)/Co and (Zr+Nb)/Al ratios in the thermal stability we observe, based on data reported in the literature, that:

- Zr/Co and (Zr+Nb)/Co ratio have the same influence on the thermal stability, i.e. an increase of these ratios induces a lowering of the glass transition temperature
- Zr/Al and (Zr+Nb)/Al ratio have the same influence on the thermal stability, i.e. an increase of these ratios induces a lowering of the glass transition temperature and a decrease of the width of the supercooled liquid temperature range.

It also clearly showed that substitution of Zr by Nb, which does not affect the (Zr+Nb)/Co and (Zr+Nb/Al) ratio, does not have the same effect on the thermal stability of the alloy as the other substitution routes. By adding Nb to the alloy and maintaining both (Zr+Nb)/Co and (Zr+Nb)/Al ratio constants, we observe a rise in the glass transition temperature and no change in the width of the supercooled liquid region (ΔT_x).

This finding helps us understand why we do not observe the same trends as previously reported for Nb addition on Zr-Co-Al ternary glasses in the literature. An increase of the glass transition temperature has already been observed in the literature for a Zr-based BMG subjected to Nb addition but in the Zr-Cu-Al system [147]. Zhu *et al.* studied the influence of Zr substitution by Nb in the $Zr_{70}Cu_{13.5}Ni_{8.5}Al_8$. They added up to 10 at% of Nb and showed that the alloy remained amorphous (based on XRD measurements) up to 7 at% of Nb. They also measured that the glass transition temperature

increased with Nb addition, from 621 K for 0 at% Nb, to 630 K for 2 at% Nb to 660 for 7 at% Nb. The width of the supercooled region is reduced between 0 at 2 at% of Nb but is stable between 2 at 7 at% of Nb. Zhu. *et al.* concluded that the ISRO content increased with Nb addition. The ISRO structures are very dense and stable, hence explaining the increase of the glass transition temperature. However, we can argue that even if the SRO (represented by ISRO here) is very important, the MRO should be as important and should be taken into account.

Zhu *et al.* also performed compression testing. They exposed that plasticity was similar for all samples bearing 0 to 7 at% of Nb. However, they measured that yield stress increased with Nb addition. This brings us back to the question of the relation between the structure and the mechanical properties of metallic glasses. It now clearly appears that Nb addition in our case induces densification of the glass and stabilization against thermal solicitation. This is rather opposed to what was presented previously for Nb addition in the Zr-Co-Al ternary system. We demonstrated that this was linked to the alloying route we chose in this work. The influence of Nb alloying on the mechanical properties of the Zr-Co-Al ternary base is not much discussed in the literature. This is the subject of the following section.

V.3.2. ... on mechanical properties

We have concluded in section V.3.1 that Zr by Nb substitution in the $Zr_{56}Co_{28}Al_{16}$ ternary glass former induces densification of the glass. We have seen that the embedded free volume content is reduced with Nb addition. Looking at mechanical properties, we observe no changes in the yield stress, however, plasticity is slightly decreased for Nb1 and Nb2 samples compared to Nb0 samples. Also, a strong transition from ductile to brittle is observed between Nb2 and Nb3 samples. Nb3 exhibit absolutely no plastic deformation. Fracture stress of Nb3 samples is of the same order as for the other Nb content (Nb0, Nb1 and Nb2). Also, the fracture mode is the same between all samples, including Nb3. They all failed according to the shear mode, characteristic of ductile behaviour, and not the fragmentation behaviour, characteristic of brittle behaviour. It is surprising that even though Nb3 samples are brittle, they failed in the shear mode.

Guan *et al.* reported a plasticity increase while substituting Co by Nb in the $Zr_{56}Co_{28}Al_{16}$ ternary alloy [157]. They proposed that the plasticity increase was induced by a greater proportion of soft zones (free-volume zones) from which shear bands can nucleate. It is admitted that a greater number of shears helps the homogenization of the deformation and results in greater ductility. Yet this lacks a clear explanation of the influence of the Nb addition. Along with the addition of Nb, the Co content is reduced as it is substituted by Nb. Co-based metallic glasses are known to have high yield stresses and be very brittle [92]. Therefore, the increase in plasticity, while substituting Co by Nb, could be either caused by the addition of Nb, the reduction of the Co content, or more likely a combination of both.

Here we see that, at constant Co and Al content, our alloy shows embrittlement. This is coherent with the apparent lower free volume with Nb addition. We could suppose that the change in the glass structure associated with Nb addition disfavours shear band nucleation. The densification may be accompanied by lower dispersion of densities in the glass, reducing the level of heterogeneity of the strain/stress field during loading. This is supported by the serration analysis performed on the compression testing of samples Nb0, Nb1 and Nb3, which showed a more erratic shear band propagation. The reduction of the shear band nucleation rate disfavours plastic deformation and leads to earlier failure. Moreover, this same behaviour could enhance fatigue resistance as we have seen that the fatigue endurance limit in bulk metallic glasses was controlled by shear band nucleation rather than shear band propagation. A lower shear band nucleation rate could promote higher fatigue resistance. We performed preliminary fatigue testing on Nb-bearing alloys, but because of technical issues (influence of the surface roughness), we were not able to analyse the results. This should be further investigated.

V.3.3. … on corrosion resistance

Based on our measurements, Nb addition appears to maintain the excellent corrosion resistance of the alloy in saline solution. This shows us that the passive film ultimate resistance against pitting is rather similar between all compositions. We also performed impedance spectroscopy analysis on the 3 compositions after 24 hours of immersion. The analysis, carried out by Benoit Ter-Ovanessian from the MATEIS laboratory, revealed that film thickness and density was similar for all samples. Ultimately, the corrosion testing allows us to conclude that the Nb addition, with this specific alloying method, does not deteriorate our alloy corrosion resistance in saline solution. From these results, it seems that Nb contributes neither to the passive film nor the pitting corrosion resistance. The latter is probably governed by the content of the TM within the BMG. XPS measurements should be performed to examine the composition of the passive film for each grade to evaluate the contribution of Nb within the passive film.

However, we believe that our testing protocol is not dedicated to studying the first stage of passivation or the passivation ability. The saline solution, which promotes pitting, might not be suitable to detect differences induced by Nb addition on film formation. We propose that new corrosion tests in acid solutions (pH = 0) are realised to identify differences (if there is any), in passive film formation with Nb addition.

V.4. Conclusions and perspectives

In this chapter, we have studied Nb minor-alloying on the $Zr_{56}Co_{28}Al_{16}$ glass former studied in the present work. Based on its low positive mixing enthalpy with Zr, its similarities with Zr and the reported enhancement of properties in the literature, we chose Nb as the alloying element. Because we consider the $Zr_{56}Co_{28}Al_{16}$ as a combination of an early transition metal (Zr), a late transition metal (Co) and Al, and because this specific substitution route was not reported in the literature, we chose to add Nb by Zr substitution. This way, this study is twofold:

- We evaluate the influence of Nb alloying on numerous properties of the $Zr_{56}Co_{28}Al_{16}$: thermal stability, corrosion resistance, hardness and mechanical compressive resistance.
- We also evaluate the influence of the substitution route. By comparing our results to results reported in the literature, we can highlight differences and discuss possible causes.

We started by characterizing the impact of GFA and thermal stability of Zr by Nb substitution in the $Zr_{56}Co_{28}Al_{16}$ alloy. We cast 5-mm diameter rod samples and observed that above 3 at% of Nb, the GFA was reduced as Nb4 samples were partially crystallized and Nb6 and Nb8 samples were fully crystallized. We can not affirm that GFA was progressively reduced with Nb addition. Based on the XRD spectrum, we measured that the average inter-atomic distance was reduced with Nb addition. This could indicate the densification of the glass. Density measurement performed via Archimedes technique also revealed density increase of the as-cast state with Nb addition. This could be related to the fact that Nb has a greater density than Zr, but also by the fact that the embedded free-volume fraction is reduced via Nb addition. By performing full relaxation (48h at 0.9 T_g), we noted that the resulting gap in density (linked to free volumes annihilation) was of lower magnitude with increasing the Nb content. The Nb0 alloy showed a volume reduction of roughly 2.09 vol% while the Nb3 samples showed a volume reduction of 1.76 vol%. This proves that less free volume was annealed during the relaxation of the Nb-bearing alloys.

DSC measurements revealed that the glass transition temperature, along with the temperature of the first exothermic transformation (T_x) were increased by Nb addition. However, the width of the supercooled liquid region remained stable (around 30 K) and the DSC spectrum still exhibited the rather characteristic two-phases transformation (two exothermic peaks observed on DSC spectrums). Hardness measurements revealed an increase of the hardness of the as-cast alloys, by approximately 30 HV between Nb0 and Nb3. Young's modulus is also increased, from 93.4 to 97.8 GPa for Nb0 and Nb3 respectively. Young's modulus increase is coherent with the increase of the glass transition. This, simply put, translate to a more cohesive state of the matter, with Nb addition. This could be coherent with the densification discussed above.

The excellent corrosion resistance of our alloy is preserved with Nb addition. However, we present the hypothesis that the solution used is not challenging enough to be discriminant. More tests should be

performed to assess the influence of Nb addition on the passive film formation for instance. We recommend using a solution of higher acidity, without chloride ions.

Compressive resistance is characterized in the same conditions as in chapters III and IV. We show that Nb addition up to 2 at% appears to slightly reduce plastic deformation. Accordingly, the monitored shear band activity (via the serration analysis) appears to be more erratic. Namely, the two-stage shear band propagation process (steady propagation and catastrophic propagation), defined in Chapter III is not observed for Nb1 and Nb2 samples. Serrations detected in Nb1 and Nb2 samples are of greater magnitude than for Nb0 samples, indicating larger shear band movements. From our understanding, this indicates that a lower number of shear band systems are activated with Nb addition. Nb3 samples do not exhibit any signs of plastic deformation. However, Nb3 samples fail in the shear mode, which is usually observed for ductile samples (such as Nb0, Nb1 and Nb2). Accordingly, the characteristic vein pattern is observed on Nb3 fracture surfaces. Nb3 samples' lack of ductility could be related to nano-crystallization, which could not be detected with XRD measurements.

Every characterization performed on the $Zr_{56-x}Co_{28}Al_{16}Nb_x$ points toward the idea that Nb addition induces embrittlement of our glass, possibly a density and overall higher order at the SRO/MRO. Interestingly, this was not reported for other Nb alloying works on Zr-Co-Al alloys. We present the hypothesis that the substitution route plays a role as important as the chosen alloying element in the alteration of a glass structure and properties. In our specific case, we observe that reported alteration of properties (such as T_g) with Nb addition is also correlated with changes in Zr/Co or Zr/Al ratios in the glass. Considering that the $Zr_{56}Co_{28}Al_{16}$ is a combination of an early transition metal (Zr), a late transition metal (Co) and Al, the Nb falls in the early transition metal category. Therefore, substituting Co or Al by Nb increases the (Zr+Nb)/Co or (Zr+Nb)/Al ratios. In our case, these ratios are unchanged. This explains why we do not observe similar properties variations as in other published work.

This work brings forward our comprehension of minor-alloying mechanisms and structure-properties relationships. The way the minor-alloying is performed should be more investigated and argued in future studies. The embrittlement of the alloy with Nb addition should favour fatigue resistance but this is still to be tested. Nb addition appears to directly affect glass structure. It could be interesting to investigate its influence on the ability of the glass to be rejuvenated.

V.5. Take-Home Messages

In this chapter, we performed **minor alloying** to evaluate a potential impact on the $Zr_{56}Co_{28}Al_{16}$ glass structure. In this work, we chose **Nb as the alloying element**. We observe that:

- Casting 5-mm diameter rods, Zr can be substituted by Nb up to **3 at%** to obtain amorphous samples. From 4 at% and above, XRD patterns show signs of crystallization.
- It induces **shorter inter-atomic distances**. The structure of the as-cast glass is more compact, and the embedded as-cast free-volume content is reduced.

We chose to perform **Nb alloying by substituting Zr** while the literature is based on other substitution routes (Co by Nb substitution, Al by Nb substitution, Nb addition to the entire base). Several properties as characterized and results are compared to data from the literature:

Property	**Zr by Nb substitution**	**Other substitution routes**
T_g, T_x, T_p	**Increased**, from 750 to 757 K for T_g.	Reduced
Corrosion resistance	**Unchanged** in NaCl 9 $g.L^{-1}$ 310 K	Enhanced in various electrolytes
Young's modulus	**Increased**, from 93 to 98 Gpa, in agreement with T_g increase	*Not enough data*
Ductility	**Decreased**, no plasticity at 3 at% of Nb	Increased

- We observed that for all properties characterized, results are coherent and indicate a **denser structure**. This is supported by XRD measurements which revealed shorter interatomic distances and density measurements which revealed lower free volume content with Nb addition. Zr substituted by Nb in an **icosahedral-like structure** could give denser structures, as Nb is smaller. Interestingly, results do not match with previously reported results for Nb minor alloying.
- We expose that not only the alloying element impact properties but also **the way the substitution is performed**.
- Zr-Co-Al and Zr-Cu-Al glasses are both based on the *Zr+Transition metal+Al* structure. Zr and Nb are considered equivalent in this sense. Substituting Zr by Nb does not change the **(Zr+Nb)/Co** or (Zr+Nb)/Al ratios. Publications reporting Co or Al by Nb substitutions described the same trends as in work studying the increase of **Zr/Co** or **Zr/Al** ratios (lowering T_g, increasing ductility…).

Conclusion and outlooks

Conclusions and perspectives

Conclusions

This thesis work was dedicated to the study of the $Zr_{56}Co_{28}Al_{16}$ metallic glass for biomedical applications. This study was realized as the biomedical industry is currently facing a challenge regarding the miniaturization of medical devices. There is a need for biocompatible materials with superior mechanical resistance, outperforming currently used conventional alloys, such as TA6V, 316L Stainless steel or Co-Cr-W alloys. In this regard, bulk metallic glasses are very promising. This project involved two laboratories, SIMaP and MATEIS, and two industrial actors, Anthogyr SAS and Vulkam Inc.

The $Zr_{56}Co_{28}Al_{16}$ composition was chosen after a comparative study of several Zr-based ternary systems: Zr-Ni-Al, Zr-Fe-Al, Zr-Cu-Al and Zr-Co-Al. Targeting biomedical applications, we defined some required specifications to reach. We demonstrated that the studied $Zr_{56}Co_{28}Al_{16}$ satisfies these specifications:

- It can be processed in the amorphous state with diameters above 5 mm, which is the threshold that we defined for the production of small implantable devices and surgical tooling.
- Its mechanical resistance is also satisfying. In compression, it shows yield stress approximately twice as high as the one of TA6V. It also shows compressive plasticity to some extent (roughly between 4 and 10 %).
- Using a specific set-up designed to assess the fatigue endurance limit of materials for biomedical applications, indicates that the $Zr_{56}Co_{28}Al_{16}$ BMG meets the industrial standard.
- We also characterized biocompatibility-related properties, such as corrosion resistance during polarisation testing and immersion resistance. Once again following biomedical testing standards, we showed that the studied $Zr_{56}Co_{28}Al_{16}$ has very satisfying corrosion resistance in saline solution at body temperature. Releasing rates of metallic elements were also demonstrated to be far below the standard limits.

Such results open a wide range of applications in the biomedical sector for the $Zr_{56}Co_{28}Al_{16}$. A series of quaternary alloys Zr-Co-Al-Nb were also tested for similar applications. Up to 3 at% of Nb, the alloy retains its amorphous character when cast as 5-mm diameter rods. The corrosion resistance remained very satisfying as well as the compressive resistance. Fatigue and immersion resistance was not tested at this stage, but there is every reason to believe that they will not be deteriorated compared to the base ternary alloy.

The Zr-Co-Al ternary base is not new for bulk metallic glass processing as it was firstly reported almost 20 years ago. $Zr_{56}Co_{28}Al_{16}$ is one of the most studied compositions in the ternary base, because of

its very attractive properties and consequently, we did not study a new ternary base in this thesis work. Apart from the new characterisations proposed (such as nano-indentation mapping, immersion resistance and fatigue resistance), we confirmed some properties gathered from the scattered literature available (hardness, compressive resistance). By performing an extensive literature review, we were also able to compare our results with results from the Zr-Cu-Al base, as along this work is discussed the influence of the late transition metal, LTM (in this example Co and Cu) on the Zr-LTM-Al ternary bases.

Even though we confirmed some properties reported in the literature, the $Zr_{56}Co_{28}Al_{16}$ studied in this work exhibited peculiarities. The glass transition temperature measured via DSC has a particularly low sensibility to the heating rate resulting in higher activation energies than those reported in the literature for this composition. Also, the $Zr_{56}Co_{28}Al_{16}$ exhibits two exothermic transformations events (which is not so frequent among Zr-based ternary alloys) but exhibits no clear signs of crystallization after the first exothermic event. This led us to think that the alloy could possess specific stability, probably linked to a specific atomic arrangement, which could be related to its relatively high oxygen content. Interestingly, a "pre-peak" was detected on XRD measurements (below 30°), which is the sign of a strong polytetrahedral order. Additionally, to these zones of strong order, we detected the presence of a β relaxation in DMA measurements, which is the marker of zones of high atomic mobility. In consequence, even if it is now well accepted that glass structure presents density variations, we have in mind that the $Zr_{56}Co_{28}Al_{16}$ processed at SIMaP could have a relatively strong contrast between these zones of high order (high density) and low order (low density). One of the questions emerging from this concerns the interconnection between these zones, which is still unclear.

We also questioned the ability of the specific structure of our alloy to be tuned, or more specifically, to be shifted toward lower or higher energy states (respectively referred to as relaxation and rejuvenation). We saw that the $Zr_{56}Co_{28}Al_{16}$ was far less sensitive to relaxation or rejuvenation than a Zr-Cu-Al-based BMG. From the dual study of the relaxation and the rejuvenation, we concluded that the $Zr_{56}Co_{28}Al_{16}$ was hard to move in its potential energy landscape, typically harder than a Zr-Cu-Al-based BMG. In addition to the oxygen content, we therefore proposed, based on both our observations and the literature, that the "stability" of the structure of the $Zr_{56}Co_{28}Al_{16}$ compared to Zr-Cu-Al ternary alloys could also be promoted by the presence of Co.

We performed Zr substitution by Nb in the ternary base, which was not previously reported in the literature for the $Zr_{56}Co_{28}Al_{16}$. We showed that Zr by Nb substitution in the $Zr_{56}Co_{28}Al_{16}$ resulted in slight embrittlement of the alloy, higher glass transition and crystallisation temperatures, a higher density and a lower free volume content. All these results contrast with previously reported results for Nb addition to the Zr-Co-Al ternary base. We consequently proposed that the alloying element is not the only factor to consider while performing minor alloying by highlighting that the substitution route also plays a key role. We suggested that Nb alloying appears to have the same influence as modifying the ratios

of the elements in the ternary BMG. For instance, replacing Al by Nb appears to have the same influence on the glass structure as increasing the Zr/Al ratio. The same trend is observed for Co. In the present work, by replacing Zr with Nb, we do not change the (Zr+Nb)/Co and (Zr+Nb)/Al ratios, which could explain why we do not observe the same behaviour as previously reported.

We also gave specific attention to the variability of the mechanical response in compression testing. It is known that bulk metallic glasses exhibit intrinsic variability in their mechanical response, because of the stochastic distribution of the heterogeneities. Serration analysis based on the statistical distribution of the magnitude of the stress drops during plastic deformation has been already reported for BMGs. In this thesis work, we propose an approach where stress drop magnitude is considered based on the associated deformation of the glass. By doing so, we concluded that there are two serration regimes: a steady propagation of the shear bands followed by a catastrophic propagation.

In this thesis work, we have proposed a vision of the Zr56Co28Al16 glass structure based on the different characterizations performed. Our understanding of the glass structure, as specialists of mechanics of materials, essentially emanates from the analysis of the mechanical properties and the deformation mechanisms. It would be interesting in future collaborations to be able to confront this vision with that of experts in the physical characterisation of glass structures or numerical simulations, at the atomic scale.

Short-term outlooks

- In this thesis work, we tried to put in perspective the results acquired on the $Zr_{56}Co_{28}Al_{16}$ with results acquired on Zr-Cu-Al ternary BMG or Zr-Cu-Al-based BMGs. This comparative study was performed to better understand the influence of cobalt in the ternary base. However, atomic ratios between the studied Zr-Co-Al and Zr-Cu-Al composition are significantly different and this can strongly influence the results. As a short-term outlook, it would be interesting to perform such a comparison using a Zr-Cu-Al composition closer to the $Z_{56}Co_{28}Al_{16}$. This work was already started with the elaboration of the $Zr_{60}Cu_{30}Al_{10}$ BMG. This Zr-Cu-Al composition is rich in Zr and is close to the $Zr_{56}Co_{28}Al_{16}$ regarding atomic ratios.
- In this manuscript, the spotlight was more concentrated on mechanical properties than corrosion resistance. We initiated a collaboration between SIMaP Lab. and Mateis Lab. which is also supported by Benoit Ter-Ovanessian (Mateis) and Remi Daudin (SIMaP), to study the corrosion resistance of BMGs. The free-volume content (controlled through annealing treatments) and the Nb content, are currently being investigated regarding their influence on the formation of the passive film (rather than its breaking during pitting).

- The study of minor alloying on the $Zr_{56}Co_{28}Al_{16}$ by Nb addition underlines the importance of the alloying route chosen. This should be further investigated, for instance by calculating activation energies for each composition (Kissinger's Method) or performing DMA on Nb-bearing samples. Preliminary work was already carried out in this direction and Figure 0-1 compares the loss factor tan(δ) as a function of temperature for Nb0 ($Zr_{56}Co_{28}Al_{16}$) and Nb1 ($Zr_{55}Co_{28}Al_{16}Nb_1$) alloys. It seems that the Nb bearing alloy has a lower loss factor compared to the Nb-free alloy, up to approximately 750 K, suggesting lower atomic mobility in the Nb-bearing alloy. This may even be related to a less pronounced β relaxation. This correlates with the observation made in Chapter V and should be reproduced for Nb2 and Nb3. It could also be interesting to perform the same analysis on Nb4 which is partially crystallized.

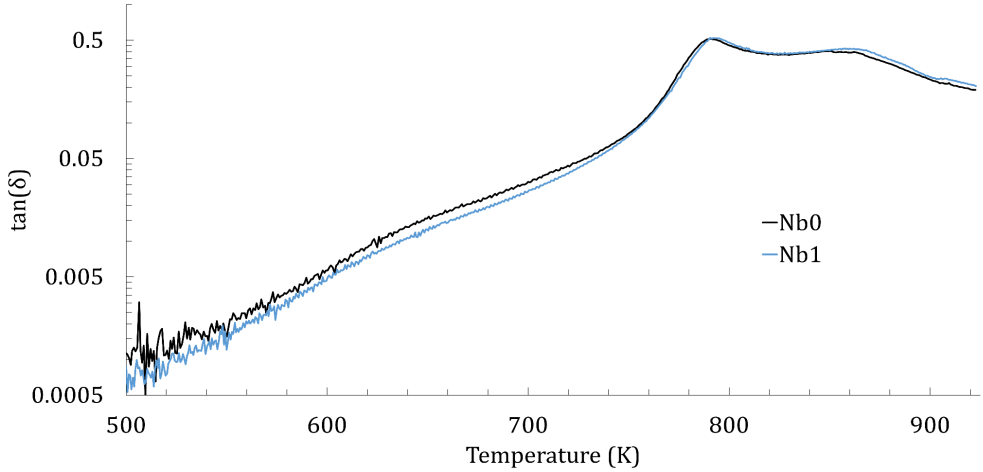

Figure 0-1: Loss factor tan(δ) as a function of temperature measured by DMA.

- Conversely, to what is sometimes reported in the literature, no significant signs of crystallization were detected after a thermal treatment above the first exothermic peak. In consequence, we think that it would be interesting to study in more detail the crystallization sequence of the alloy at least for two reasons:
    - First, the phases appearing upon crystallization may be a marker of the SRO or MRO structures in the amorphous state. To our opinion, the presence of two peaks, which is limited to a few ternary glass formers, is maybe too often ignored. A better understanding of the crystallization process, with the phase apparition order, could be very interesting.
    - Second, the study of the crystallization sequence could be the gateway toward the processing of metallic glass/crystalline alloys composites. The Zr-Co-Al ternary base is being studied for such applications as it bears the potential to form the B2 phase which could considerably increase the alloy ductility. Since 2019, Chen *et al*. published several papers regarding the formation of the B2 phase in the Zr-Co-Al amorphous matrix [122, 156, 161, 162]. We saw in Chapter III that three main phases appear during conventional annealing of the $Zr_{56}Co_{28}Al_{16}$: Zr_6CoAl_2, ZrCoAl and ZrCo (B2). Increasing the heating rate

should favour the B2 phase according to Chen *et* al. We also performed flash annealing using a Gleeble device at MATEIS on the $Zr_{56}Co_{28}Al_{16}$.

Figure 0-2 (a) shows the XRD measurements acquired after several annealing treatments, where the $Zr_{56}Co_{28}Al_{16}$ was heated up to 950 K using varying heating rates. The blue zone highlights the position of some peak characteristics of the B2 ZrCo phase. We did not observe a strong proportion of B2 phase with heating rates from 5 K/s to 45 K/s, as we lack the two characteristic peaks around 30°. The difference is visible when compared with Chen *et al*. XRD measurements shown in Figure 0-2 (b). The difference might again be attributed to the specific stability of the alloy processed at SIMaP. This should be further investigated and extended to Nb-bearing alloys as suggested by Chen *et al* [156].

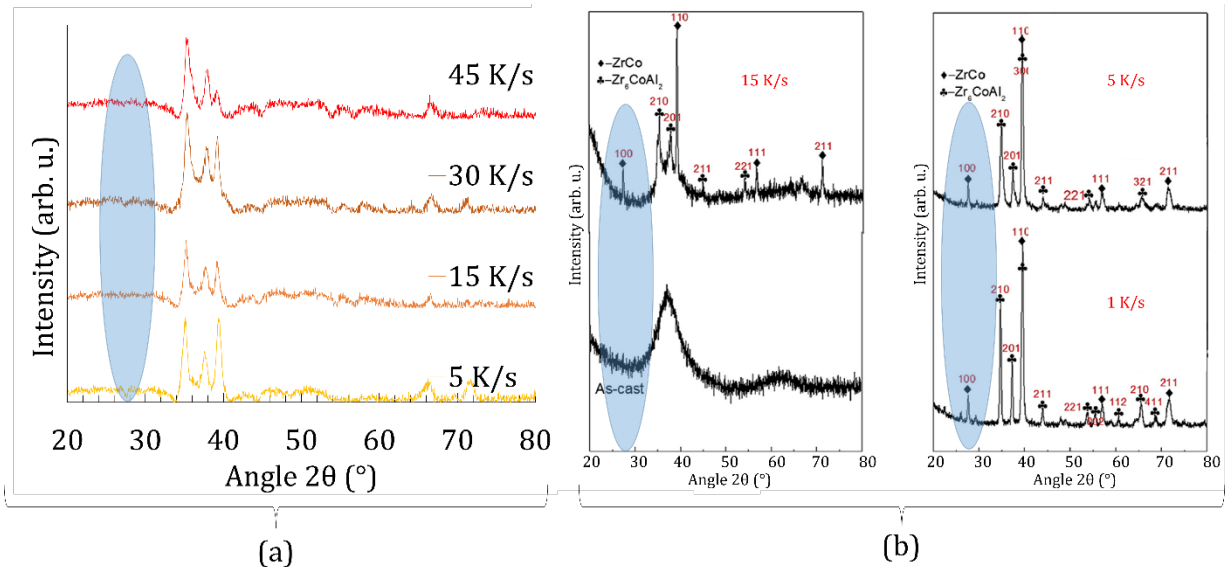

Figure 0-2: XRD measurements after heat treatments around 950 K. (a) This work on $Zr_{56}Co_{28}Al_{16}$ with several heating rates being used: flash (5 to 45 K/s). (b) Work of Chen et al. on $Zr_{55}Co_{31}Al_{14}$ with heating rates of 1, 5 and 15 K/s. *The blue zones show the position of diffraction peaks characteristic of the B2 phase on Chen et al [156].*

Long-term outlooks

- The rejuvenation process during mechanical solicitation under the yield stress should be investigated in more detail. The ability to tune the shear band nucleation rate should be very useful, for instance, to find the right balance between ultimate mechanical resistance and fatigue endurance limit. Based on the example of the Zr-Co-Al and the Zr-Cu-Al, we have seen that every glass is different and has a different sensibility to relaxation/rejuvenation. It should be stressed out here that rejuvenation is often presented as a creation of free volume. However here, we presented it simply as an increase of the potential energy of the system. The nuance may be important as it considers that rejuvenation could be obtained without free volume creation, only by changing the distribution of the heterogeneities. This could be supported by the observation that free volume creation often induce an increase in plastic strain but also a decrease of yield

stress [132]. In our work and O. Baulin work [96], we do not observe yield stress changes when increasing plastic strain. To better understand rejuvenation by cyclic loading, it would be particularly interesting to perform characterization, before compression testing. Nanoindentation could for instance be used to probe heterogeneity distribution. Also, structural changes or "education" during staircase fatigue testing should be further investigated. A simpler fatigue testing set-up, like three or four points bending, should also be used. This will allow better control of the stress applied to the sample. Additionally, characterization such as DSC measurements, nano-indentation or vibrational measurements should be performed to assess structural changes.

- At last, an incompletely solved question from this work concerns the remarkable stability of the glass transition temperature and the absence of any signs of crystallization after the first exothermic peak recorded in DSC measurements. We suspect that the relatively high oxygen content detected in the studied alloy (≈ 300 ppm) may strongly influence the structure. Oxygen is often depicted as unfavourable for GFA as it can trigger crystallization. However, recent studies proposed that the effect of oxygen, if incorporated homogeneously in the amorphous structure, could be more complex than that and that oxygen could for instance increase ductility, as shown in Figure 0-3 from [247, 257]. The composition studied in this work is the $Zr_{20}Cu_{20}Hf_{20}Ti_{20}Ni_{20}$.

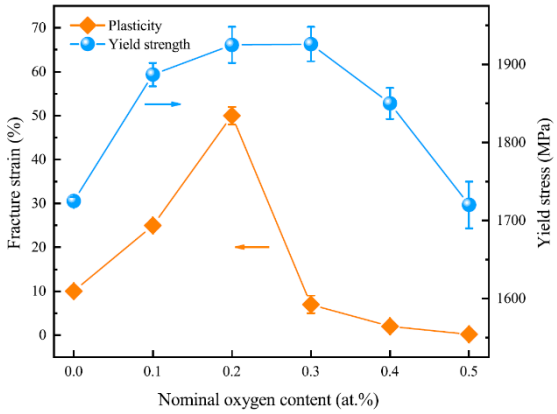

Figure 0-3: Variation of fracture strength and plasticity with addition of oxygen [247]

A second very recent publication studied the addition of oxygen in a Zr-Cu-Al ternary BMG and showed that the addition of 0.25 at% of oxygen increases plasticity as it increases heterogeneity level [258]. Unfortunately, only a few studies report the oxygen content when it is not the subject of this study. The oxygen content in the $Zr_{56}Co_{28}Al_{16}$ processed at SIMaP, and its impact on the properties should be further investigated. There should be a maximum value at which properties are enhanced (as in Figure 0-3). This maximum should variate depending on the glass composition. We could for instance try to recycle the alloy multiple times (several melting and casting steps), which should increase oxygen content. We could also try to use raw metals of lower purity. This study is even more relevant as more and more processes are used to synthesise BMG, with for instance powder-based processes, such as additive manufacturing. In this regard, the oxygen content could be a real challenge.

References

References

1. Morrison ML, Buchanan RA, Leon R V., et al (2005) The electrochemical evaluation of a Zr-based bulk metallic glass in a phosphate-buffered saline electrolyte. J Biomed Mater Res - Part A 74:430–438. https://doi.org/10.1002/jbm.a.30361

2. Zhang S, Holy CE, Eichenbaum G, et al (2021) Carcinogenic assessment of cobalt-containing alloys in medical devices or cobalt in occupational settings: A systematic review and meta-analysis of overall cancer risk from published epidemiologic studies. Regul Toxicol Pharmacol 125:. https://doi.org/10.1016/j.yrtph.2021.104987

3. Peker A, Johnson WL (1993) A highly processable metallic glass: Zr41.2Ti 13.8Cu12.5Ni10.0Be22.5. Appl Phys Lett 63:2342–2344. https://doi.org/10.1063/1.110520

4. Axinte E (2011) Glasses as engineering materials: A review. Mater Des 32:1717–1732. https://doi.org/10.1016/j.matdes.2010.11.057

5. Dussubieux L, Gratuze B, Blet-Lemarquand M (2010) Mineral soda alumina glass: Occurence and meaning. J Archaeol Sci. https://doi.org/10.1016/j.jas.2010.01.025

6. Inoue A (2011) Metallic Glasses. In: Bulk Metallic Glasses. pp 11–48

7. Shechtman D, Blech I (1984) Metallic Phase with Long-Range Orientational Translational Symmetry. 53:1951–1954

8. Klement W, WILLENS RH, DUWEZ POL, et al (1960) Non-crystalline Structure in Solidified Gold–Silicon Alloys. Nature 187:869. https://doi.org/10.1038/187869b0

9. Duwez P, Willens RH, Klement W (1960) Continuous series of metastable solid solutions in silver-copper alloys. J Appl Phys 31:1136–1137. https://doi.org/10.1063/1.1735777

10. Inoue A (2010) Glass-forming ability of alloys. In: Bulk Metallic Glasses. pp 473–480

11. Weinberg MC, Uhlmann DR, Zanotto ED (1989) "Nose Method" of Calculating Critical Cooling Rates for Glass Formation. J Am Ceram Soc 72:2054–2058. https://doi.org/10.1111/j.1151-2916.1989.tb06030.x

12. Weinberg MC (1996) Glass-formation and crystallization kinetics. Thermochim Acta 280/281:63–71

13. Onorato PIK, Uhlmann DR (1976) Nucleating heterogeneities and glass formation. J Non Cryst Solids 22:367–378

14. Barandiaran J., Colmenro J (1981) Continuous cooling approximation for the formation of a glass. J Non Cryst Solids 46:277–287. https://doi.org/10.1016/0160-7987(81)90042-9

15. Lin XH, Johnson WL (1995) Formation of Ti-Zr-Cu-Ni bulk metallic glasses. J Appl Phys 78:6514–6519. https://doi.org/10.1063/1.360537

16. Greer AL (2001) Metallic glasses. Encycl. Mater. Sci. Technol. 5529–5537

17. Qiao JC, Wang Q, Pelletier JM, et al (2019) Structural heterogeneities and mechanical behavior of amorphous alloys. Prog Mater Sci 104:250–329. https://doi.org/10.1016/j.pmatsci.2019.04.005

18. Tan J, Zhang Y, Stoica M, et al (2011) Study of mechanical property and crystallization of a ZrCoAl bulk metallic glass. Intermetallics 19:567–571. https://doi.org/10.1016/j.intermet.2010.12.006

19. Šimon P, Illeková E, Mojumdar SC (2006) Kinetics of crystallization of metallic glasses studied by non-isothermal and isothermal DSC. J Therm Anal Calorim. https://doi.org/10.1007/s10973-005-7067-z

20. Turnbull D (1969) Under What Conditions Can A Glass Be Formed? Contemp Phys 10:473–488. https://doi.org/10.1080/00107516908204405

21. Lu ZP, Li Y, Ng SC (2000) Reduced glass transition temperature and glass forming ability of bulk glass forming alloys. J Non Cryst Solids. https://doi.org/10.1016/S0022-3093(00)00064-8

22. Inoue A (2000) Stabilization of metallic supercooled liquid and bulk amorphous alloys. Acta Mater 48:279–306. https://doi.org/10.1016/S1359-6454(99)00300-6

23. Lu ZP, Liu CT (2002) A new glass-forming ability criterion for bulk metallic glasses. Acta Mater. https://doi.org/10.1016/S1359-6454(02)00166-0

24. Du XH, Huang JC, Liu CT, Lu ZP (2007) New criterion of glass forming ability for bulk metallic glasses. J Appl Phys. https://doi.org/10.1063/1.2718286

25. Mondal K, Murty BS (2005) On the parameters to assess the glass forming ability of liquids. J Non Cryst Solids. https://doi.org/10.1016/j.jnoncrysol.2005.03.006

26. Chen Q, Shen J, Zhang D, et al (2006) A new criterion for evaluating the glass-forming ability of bulk metallic glasses. Mater Sci Eng A. https://doi.org/10.1016/j.msea.2006.06.053

27. Suryanarayana C, Seki I, Inoue A (2009) A critical analysis of the glass-forming ability of alloys. J Non Cryst Solids. https://doi.org/10.1016/j.jnoncrysol.2008.12.009

28. Inoue A (2000) Stabilization of Metallic Supercooled Liquid. Acta Mater. https://doi.org/10.1016/S1359-6454(99)00300-6

29. Inoue A (1996) Recent progress of Zr-based bulk amorphous alloys. Sci Reports Rerearch Institutes Tohoku Univ Ser A-Physics

30. Inoue A (1997) Stabilization of supercooled liquid and opening-up of bulk glassy alloys. Proc Japan Acad Ser B Phys Biol Sci. https://doi.org/10.2183/pjab.73.19

31. Inoue A, Kong FL, Zhu SL, et al (2015) Production methods and properties of engineering glassy alloys and composites. Intermetallics 58:20–30. https://doi.org/10.1016/j.intermet.2014.11.001

32. Inoue A, Zhang T, Masumoto T (1990) Production of Amorphous Cylinder and Sheet of La55Al25Ni20 Alloy by a Metallic Mold Casting Method. Mater Trans JIM

33. Chatterjee Ritam (2017) Manufacturing of Metallic Glasses. Adv Mater Manuf Charact 7:24–29

34. Inoue A (2011) Synthesis of Bulk Metallic Glasses. In: Bulk Metallic Glasses. pp 145–186

35. Inoue A (2015) Bulk Glassy Alloys: Historical Development and Current Research. Engineering 1:185–191. https://doi.org/10.15302/J-ENG-2015038

36. Qiao J, Jia H, Liaw PK (2016) Metallic glass matrix composites. Mater Sci Eng R Reports 100:1–69. https://doi.org/10.1016/j.mser.2015.12.001

37. Aqida SN, Shah LH, Naher S, Brabazon D (2014) Rapid Solidification Processing and Bulk Metallic Glass Casting. Elsevier

38. Greer AL (2009) Metallic glasses...on the threshold. Mater Today 12:14–22. https://doi.org/10.1016/S1369-7021(09)70037-9

39. Kui HW, Greer AL, Turnbull D (1984) Formation of bulk metallic glass by fluxing. Appl Phys Lett. https://doi.org/10.1063/1.95330

40. Nishiyama N, Takenaka K, Miura H, et al (2012) The world's biggest glassy alloy ever made. Intermetallics. https://doi.org/10.1016/j.intermet.2012.03.020

41. Inoue A, Zhang T, Nishiyama N, et al (1993) Preparation of 16 mm diameter rod of amorphous Zr65Al7.5Ni10Cu17.5 alloy. Mater Trans JIM. https://doi.org/10.2320/matertrans1989.34.1234

42. Lou HB, Wang XD, Xu F, et al (2011) 73 mm-diameter bulk metallic glass rod by copper mould casting. Appl Phys Lett. https://doi.org/10.1063/1.3621862

43. Guo F, Wang HJ, Poon SJ, Shiflet GJ (2005) Ductile titanium-based glassy alloy ingots. Appl Phys Lett. https://doi.org/10.1063/1.1872214

44. Tang MQ, Zhang HF, Zhu ZW, et al (2010) TiZr-base Bulk Metallic Glass with over 50 mm in Diameter. J Mater Sci Technol. https://doi.org/10.1016/S1005-0302(10)60077-1

45. Park ES, Kim DH (2005) Formation of Mg-Cu-Ni-Ag-Zn-Y-Gd bulk glassy alloy by casting into cone-shaped copper mold in air atmosphere. J Mater Res. https://doi.org/10.1557/JMR.2005.0181

46. Zheng Q, Xu J, Ma E (2007) High glass-forming ability correlated with fragility of Mg-Cu(Ag)-Gd alloys. J Appl Phys. https://doi.org/10.1063/1.2821755

47. Schroers J, Johnson WL (2004) Highly processable bulk metallic glass-forming alloys in the Pt-Co-Ni-Cu-P system. Appl Phys Lett. https://doi.org/10.1063/1.1738945

48. Zeng Y, Nishiyama N, Yamamoto T, Inoue A (2009) Ni-rich bulk metallic glasses with high glass-forming ability and good metallic properties. Mater Trans. https://doi.org/10.2320/matertrans.MRA2008453

49. Ponnambalam V, Poon JS, Shiflet GJ (2004) Fe-based bulk metallic glasses with diameter thickness larger than one centimeter. J Mater Res. https://doi.org/10.1557/JMR.2004.0176

50. Shen J, Chen Q, Sun J, et al (2005) Exceptionally high glass-forming ability of an FeCoCrMoCBY alloy. Appl Phys Lett. https://doi.org/10.1063/1.1897426

51. Senkov ON, Miracle DB, Scott JM (2006) Development and characterization of Ca-Mg-Zn-Cu bulk metallic glasses. Intermetallics. https://doi.org/10.1016/j.intermet.2006.01.024

52. Park ES, Kim DH (2004) Formation of Ca-Mg-Zn bulk glassy alloy by casting into cone-shaped copper mold. J Mater Res. https://doi.org/10.1557/jmr.2004.19.3.685

53. Xu D, Duan G, Johnson WL (2004) Unusual glass-forming ability of bulk amorphous alloys based on ordinary metal copper. Phys Rev Lett. https://doi.org/10.1103/PhysRevLett.92.245504

54. Jia P, Guo H, Li Y, et al (2006) A new Cu-Hf-Al ternary bulk metallic glass with high glass forming ability and ductility. Scr Mater. https://doi.org/10.1016/j.scriptamat.2006.02.042

55. Men H, Pang SJ, Zhang T (2006) Effect of Er doping on glass-forming ability of Co50 Cr15 Mo14 C15B6 alloy. J Mater Res. https://doi.org/10.1557/jmr.2006.0109

56. Guo F, Poon SJ, Shiflet GJ (2003) Metallic glass ingots based on yttrium. Appl Phys Lett. https://doi.org/10.1063/1.1614420

57. Inoue A, Zhang T (1997) Thermal stability and glass-forming ability of amorphous Nd-Al-TM (TM = Fe, Co, Ni or Cu) alloys. Mater Sci Eng A. https://doi.org/10.1016/s0921-5093(97)80050-0

58. Jiang QK, Zhang GQ, Yang L, et al (2007) La-based bulk metallic glasses with critical diameter up to 30 mm. Acta Mater. https://doi.org/10.1016/j.actamat.2007.04.021

59. Yue X, Inoue A, Liu CT, Fan C (2017) The development of structure model in metallic glasses. Mater Res 20:326–338. https://doi.org/10.1590/1980-5373-MR-2016-0318

60. Georgarakis K, Hennet L, Evangelakis GA, et al (2015) Probing the structure of a liquid metal during vitrification. Acta Mater 87:174–186. https://doi.org/10.1016/j.actamat.2015.01.005

61. Kresse G (1995) Ab initio molecular dynamics for liquid metals. J Non Cryst Solids. https://doi.org/10.1016/0022-3093(95)00355-X

62. Luo SY, Li JH, Cui YY, Liu BX (2013) Glass-formation and atomic structures of Cux(Zr 0.22Hf0.78)1-x and (Cu0.61Hf 0.39)1-xZrx alloys investigated by Monte Carlo simulation. Mater Lett. https://doi.org/10.1016/j.matlet.2013.02.092

63. Bernal JD (1959) A geometrical approach to the structure Of liquids. Nature. https://doi.org/10.1038/183141a0

64. Bernal JD (1960) Geometry of the Structure of Monatomic Liquids. Nature. https://doi.org/10.1038/185068a0

65. Bernal JD, Mason J (1960) Packing of spheres: Co-ordination of randomly packed spheres. Nature. https://doi.org/10.1038/188910a0

66. Wang Wei-Hua (2013) The nature and properties of amorphous matter. Prog Phys

67. Turnbull D, Cohen MH (1970) On the free-volume model of the liquid-glass transition. J Chem Phys. https://doi.org/10.1063/1.1673434

68. Turnbull D, Cohen MH (1961) Free-volume model of the amorphous phase: Glass transition. J Chem Phys. https://doi.org/10.1063/1.1731549

69. Spaepen F (1976) Mechanism for Steady State Inhomogeneous Flow in. Acta Metall 25:407–415

70. Spaepen F (1977) A microscopic mechanism for steady state inhomogeneous flow in metallic glasses. Acta Metall 25:407–415. https://doi.org/10.1016/0001-6160(77)90232-2

71. Zheng Q, Zhang Y, Montazerian M, et al (2019) Understanding Glass through Differential Scanning Calorimetry. Chem Rev 119:7848–7939. https://doi.org/10.1021/acs.chemrev.8b00510

72. Trexler MM, Thadhani NN (2010) Mechanical properties of bulk metallic glasses. Prog Mater Sci 55:759–839. https://doi.org/10.1016/j.pmatsci.2010.04.002

73. Argon AS (1979) Plastic deformation in metallic glasses. Acta Metall. https://doi.org/10.1016/0001-6160(79)90055-5

74. Falk ML, Langer JS (1998) Dynamics of viscoplastic deformation in amorphous solids. Phys Rev E - Stat Physics, Plasmas, Fluids, Relat Interdiscip Top. https://doi.org/10.1103/PhysRevE.57.7192

75. Langer JS (2006) Shear-transformation-zone theory of deformation in metallic glasses. Scr Mater. https://doi.org/10.1016/j.scriptamat.2005.10.005

76. Gaskell PH (1978) A new structural model for transition metal-metalloid glasses. Nature

77. Laws KJ, Miracle DB, Ferry M (2015) A predictive structural model for bulk metallic glasses:Supplementary Materials. Nat Commun 6:8123. https://doi.org/10.1038/ncomms9123

78. Wang R (1979) Short-Range structure for amorphous intertransition metal alloys. Nature. https://doi.org/10.1038/278700a0

79. Miracle DB (2004) A structural model for metallic glasses. Nat Mater 3:697–702. https://doi.org/10.1038/nmat1219

80. Miracle DB, Egami T, Flores KM, Kelton KF (2007) Structural aspects of metallic glasses. MRS Bull 32:629–634. https://doi.org/10.1557/mrs2007.124

81. Cheng YQ, Ma E, Sheng HW (2009) Atomic level structure in multicomponent bulk metallic glass. Phys Rev Lett. https://doi.org/10.1103/PhysRevLett.102.245501

82. Cheng YQ, Ma E (2011) Atomic-level structure and structure-property relationship in metallic glasses. Prog. Mater. Sci.

83. Cohen MH, Grest GS (1979) Liquid-glass transition, a free-volume approach. Phys Rev B. https://doi.org/10.1103/PhysRevB.20.1077

84. Dmowski W, Iwashita T, Chuang CP, et al (2010) Elastic heterogeneity in metallic glasses. Phys Rev Lett. https://doi.org/10.1103/PhysRevLett.105.205502

85. Nomoto K, Ceguerra A V., Gammer C, et al (2021) Medium-range order dictates local hardness in bulk metallic glasses. Mater Today xxx: https://doi.org/10.1016/j.mattod.2020.10.032

86. Dong C, Wang ZJ, Zhang S, Wang YM (2020) Review of structural models for the compositional interpretation of metallic glasses. Int Mater Rev 65:286–296. https://doi.org/10.1080/09506608.2019.1638581

87. Nagel SR, Tauc J (1975) Nearly-Free-Electron Approach to the Theory of Metallic Glass Alloys. Phys Rev Lett 35:380–383. https://doi.org/10.1103/PhysRevLett.35.380

88. Ashby MF, Greer AL (2006) Metallic glasses as structural materials. Scr Mater 54:321–326. https://doi.org/10.1016/j.scriptamat.2005.09.051

89. Egami T, Iwashita T, Dmowski W (2013) Mechanical Properties of Metallic Glasses. Metals (Basel) 3:77–113. https://doi.org/10.3390/met3010077

90. Greer AL, Cheng YQ, Ma E (2013) Shear bands in metallic glasses. Mater Sci Eng R Reports 74:71–132. https://doi.org/10.1016/j.mser.2013.04.001

91. Hufnagel TC, Schuh CA, Falk ML (2016) Deformation of metallic glasses: Recent developments in theory, simulations, and experiments. Acta Mater 109:375–393. https://doi.org/10.1016/j.actamat.2016.01.049

92. Sun BA, Wang WH (2015) The fracture of bulk metallic glasses. Prog Mater Sci 74:211–307. https://doi.org/10.1016/j.pmatsci.2015.05.002

93. Schuh CA, Hufnagel TC, Ramamurty U (2007) Mechanical behavior of amorphous alloys. Acta Mater 55:4067–4109. https://doi.org/10.1016/j.actamat.2007.01.052

94. Wang WH (2012) The elastic properties, elastic models and elastic perspectives of metallic glasses. Prog Mater Sci 57:487–656. https://doi.org/10.1016/j.pmatsci.2011.07.001

95. Xi XK, Zhao DQ, Pan MX, et al (2005) Fracture of brittle metallic glasses: Brittleness or plasticity. Phys Rev Lett 94:25–28. https://doi.org/10.1103/PhysRevLett.94.125510

96. Baulin O (2018) Development of amoprhous metallic alloys for biomedical applications and understanding of the plasticity phenomena. Université de Lyon

97. He Q, Xu J (2012) Locating Malleable Bulk Metallic Glasses in Zr-Ti-Cu-Al Alloys with Calorimetric Glass Transition Temperature as an Indicator. J Mater Sci Technol 28:1109–1122. https://doi.org/10.1016/S1005-0302(12)60180-7

98. Zhang ZF, Eckert J, Schultz L (2003) Difference in compressive and tensile fracture mechanisms of Zr59Cu20Al10Ni8Ti3 bulk metallic glass. Acta Mater 51:1167–1179. https://doi.org/10.1016/S1359-6454(02)00521-9

99. Chen HM, Huang JC, Song SX, et al (2009) Flow serration and shear-band propagation in bulk metallic glasses. Appl Phys Lett 94:. https://doi.org/10.1063/1.3117508

100. Du Y, Zhou Q, Jia Q, et al (2020) Imparities of shear avalanches dynamic evolution in a metallic glass. Mater Res Lett 8:357–363. https://doi.org/10.1080/21663831.2020.1771450

101. Qiao JC, Feng SD, Pelletier JM, et al (2017) Physical aging effects on the dynamic relaxation behavior and mechanical properties of Cu46Zr46Al8 metallic glass. J Alloys Compd 726:195–200. https://doi.org/10.1016/j.jallcom.2017.07.291

102. Zhou J, Sun B, Wang Q, et al (2019) Effects of Ni and Si additions on mechanical properties and serrated flow behavior in FeMoPCB bulk metallic glasses. J Alloys Compd 783:555–564. https://doi.org/10.1016/j.jallcom.2018.12.331

103. Sun BA, Pauly S, Tan J, et al (2012) Serrated flow and stick-slip deformation dynamics in the presence of shear-band interactions for a Zr-based metallic glass. Acta Mater 60:4160–4171. https://doi.org/10.1016/j.actamat.2012.04.013

104. Asadi Khanouki MT, Tavakoli R, Aashuri H (2019) Serrated flow during inhomogeneous bending deformation of bulk metallic glasses: From self-organized critical to chaotic dynamics. J Non Cryst Solids 505:62–71. https://doi.org/10.1016/j.jnoncrysol.2018.10.038

105. Liu LH, Liu ZY, Huan Y, et al (2018) Effect of structural heterogeneity on serrated flow behavior of Zr-based metallic glass. J Alloys Compd 766:908–917. https://doi.org/10.1016/j.jallcom.2018.07.026

106. Samavatian M, Gholamipour R, Amadeh AA, Mirdamadi S (2019) Correlation Between Plasticity and Atomic Structure Evolution of a Rejuvenated Bulk Metallic Glass. Metall Mater Trans A Phys Metall Mater Sci 50:4743–4749. https://doi.org/10.1007/s11661-019-05391-x

107. Sarmah R, Ananthakrishna G, Sun BA, Wang WH (2011) Hidden order in serrated flow of metallic glasses. Acta Mater 59:4482–4493. https://doi.org/10.1016/j.actamat.2011.03.071

108. Sun BA, Yu HB, Jiao W, et al (2010) Plasticity of ductile metallic glasses: A self-organized critical state. Phys Rev Lett 105:1–4. https://doi.org/10.1103/PhysRevLett.105.035501

109. Sun BA, Hu YC, Wang DP, et al (2016) Correlation between local elastic heterogeneities and overall elastic properties in metallic glasses. Acta Mater 121:266–276. https://doi.org/10.1016/j.actamat.2016.09.014

110. Tong Y, Qiao JC, Pelletier JM, Yao Y (2020) Aspect ratio effects on the serrated flow dynamic of TiZrHfCuNiBe high entropy metallic glass. Intermetallics 119:. https://doi.org/10.1016/j.intermet.2020.106726

111. Wang Z, Li JJ, Ren LW, et al (2016) Serration Behavior in Zr-Cu-Al Glass-forming Systems. J Iron Steel Res Int 23:42–47. https://doi.org/10.1016/S1006-706X(16)30009-7

112. Jia H, Wang G, Chen S, et al (2018) Fatigue and fracture behavior of bulk metallic glasses and their composites. Prog Mater Sci 98:168–248. https://doi.org/10.1016/j.pmatsci.2018.07.002

113. Wang GY, Liaw PK, Morrison ML (2009) Progress in studying the fatigue behavior of Zr-based bulk-metallic glasses and their composites. Intermetallics 17:579–590. https://doi.org/10.1016/j.intermet.2009.01.017

114. Sha Z, Lin W, Poh LH, et al (2020) Fatigue of Metallic Glasses. Appl Mech Rev 72:. https://doi.org/10.1115/1.4048056

115. Wang XD, Ren XC, Qu RT, Zhang ZF (2019) Compression-compression fatigue behavior of a Zr-based metallic glass with different free volume contents. J Alloys Compd 810:. https://doi.org/10.1016/j.jallcom.2019.151924

116. Slipenyuk A, Eckert J (2004) Correlation between enthalpy change and free volume reduction during structural relaxation of Zr55Cu30Al10Ni 5 metallic glass. Scr Mater 50:39–44. https://doi.org/10.1016/j.scriptamat.2003.09.038

117. Wang XD, Song SL, Zhu ZW, et al (2021) Fatigue behavior of a Ti-based metallic glass: Effect of sampling location in association with free volume. J Alloys Compd 861:. https://doi.org/10.1016/j.jallcom.2020.158432

118. Wang XD, Qu RT, Wu SJ, et al (2019) Improving fatigue property of metallic glass by tailoring the microstructure to suppress shear band formation. Materialia 7:. https://doi.org/10.1016/j.mtla.2019.100407

119. Zhang M, Wang YM, Li FX, et al (2017) Mechanical Relaxation-to-Rejuvenation Transition in a Zr-based Bulk Metallic Glass. Sci Rep 7:1–12. https://doi.org/10.1038/s41598-017-00768-7

120. Ketov S V., Sun YH, Nachum S, et al (2015) Rejuvenation of metallic glasses by non-affine thermal strain. Nature. https://doi.org/10.1038/nature14674

121. Hua N, Liao Z, Chen W, et al (2017) Effects of noble elements on the glass-forming ability, mechanical property, electrochemical behavior and tribocorrosion resistance of Ni- and Cu-free Zr-Al-Co bulk metallic glass. J Alloys Compd 725:403–414. https://doi.org/10.1016/j.jallcom.2017.07.167

122. Chen Y, Jiang J (2020) A novel strategy to design Zr – Co – Al BMG composites containing only B2 – ZrCo phase. Intermetallics 123:2–12. https://doi.org/https://doi.org/10.1016/j.intermet.2020.106821

123. Zhang S, Shi B, Wang J, et al (2021) Rejuvenation of a naturally aged bulk metallic glass by elastostatic loading. Mater Sci Eng A 806:1–5. https://doi.org/10.1016/j.msea.2021.140843

124. Shi B, Xu Y, Ma W, et al (2015) Effect of Ti addition on the glass forming ability, crystallization, and plasticity of Zr-Cu-Ni-Al bulk metallic glasses. Mater Sci Eng A 639:345–349

125. Lewandowski JJ, Wang WH, Greer AL (2005) Intrinsic plasticity or brittleness of metallic glasses. Philos Mag Lett 85:77–87. https://doi.org/10.1080/09500830500080474

126. Bian XL, Wang G, Chen HC, et al (2016) Manipulation of free volumes in a metallic glass through Xe-ion irradiation. Acta Mater 106:66–77. https://doi.org/10.1016/j.actamat.2016.01.002

127. Zhang M, Wang YM, Li FX, et al (2017) Mechanical Relaxation-to-Rejuvenation Transition in a Zr-based Bulk Metallic Glass. Sci Rep 7:1–12. https://doi.org/10.1038/s41598-017-00768-7

128. Park KW, Lee CM, Wakeda M, et al (2008) Elastostatically induced structural disordering in amorphous alloys. Acta Mater 56:5440–5450. https://doi.org/10.1016/j.actamat.2008.07.033

129. Qiao JC, Pelletier JM, Esnouf C, et al (2014) Impact of the structural state on the mechanical properties in a Zr-Co-Al bulk metallic glass. J Alloys Compd 607:139–149. https://doi.org/10.1016/j.jallcom.2014.04.008

130. Huang H, Zhang J, Shek CH, Yan J (2016) Effects of pre-compression deformation on nanoindentation response of Zr65Cu15Al10Ni10 bulk metallic glass. J Alloys Compd 674:223–228. https://doi.org/10.1016/j.jallcom.2016.03.057

131. Pan J, Wang YX, Guo Q, et al (2018) Extreme rejuvenation and softening in a bulk metallic glass. Nat Commun 9:. https://doi.org/10.1038/s41467-018-02943-4

132. Pan J, Ivanov YP, Zhou WH, et al (2020) Strain-hardening and suppression of shear-banding in rejuvenated bulk metallic glass. Nature 578:559–562. https://doi.org/10.1038/s41586-020-2016-3

133. Li BS, Xie S, Kruzic JJ (2019) Toughness enhancement and heterogeneous softening of a cryogenically cycled Zr–Cu–Ni–Al–Nb bulk metallic glass. Acta Mater 176:278–288. https://doi.org/10.1016/j.actamat.2019.07.012

134. Packard CE, Homer ER, Al-Aqeeli N, Schuh CA (2010) Cyclic hardening of metallic glasses under hertzian contacts: Experiments and STZ dynamics simulations. Philos Mag 90:1373–1390. https://doi.org/10.1080/14786430903352664

135. Packard CE, Witmer LM, Schuh CA (2008) Hardening of a metallic glass during cyclic loading in the elastic range. Appl Phys Lett 92:8–11. https://doi.org/10.1063/1.2919722

136. Ross P, Küchemann S, Derlet PM, et al (2017) Linking macroscopic rejuvenation to nano-elastic fluctuations in a metallic glass. Acta Mater 138:111–118. https://doi.org/10.1016/j.actamat.2017.07.043

137. Meylan CM, Greer AL (2020) The effects of elastic cycling in nanoindentation of a metallic glass. Philos Mag 100:3141–3154. https://doi.org/10.1080/14786435.2020.1814494

138. Wang P, Yang X (2020) Atomistic investigation of aging and rejuvenation in CuZr metallic glass under cyclic loading. Comput Mater Sci 185:109965. https://doi.org/10.1016/j.commatsci.2020.109965

139. Li S, Huang P, Wang F (2019) Rejuvenation saturation upon cyclic elastic loading in metallic glass. Comput Mater Sci 166:318–325. https://doi.org/10.1016/j.commatsci.2019.05.007

140. Gwon H, Kim JK, Shin S, et al (2017) The effect of vanadium micro-alloying on the microstructure and the tensile behavior of TWIP steel. Mater Sci Eng A 696:416–428. https://doi.org/10.1016/j.msea.2017.04.083

141. Liao Z, Li S, Zheng Z, et al (2012) The effect of Ge addition on Al-3.5Cu-0.4Mg (wt.%) alloy. Scr Mater 66:447–450. https://doi.org/10.1016/j.scriptamat.2011.12.011

142. Rana RS, Purohit R, Das S (2012) Reviews on the influence of alloying elements on the microstructure and mechanical properties of aluminum alloys and aluminun alloy composites. Int J Sci Res Publ 2:275–279

143. Zheng Q, Ye Z, Jiang H, et al (2020) Effect mechanisms of Micro-Alloying Element La on Solidification Microstructure and Mechanical Properties of Hypoeutectic Al-Si Alloys. Jinshu Xuebao/Acta Metall Sin 57:103–110. https://doi.org/10.11900/0412.1961.2020.00158

144. Wang WH (2007) Roles of minor additions in formation and properties of bulk metallic glasses. Prog Mater Sci 52:540–596. https://doi.org/10.1016/j.pmatsci.2006.07.003

145. Calin M, Gebert A, Ghinea AC, et al (2013) Designing biocompatible Ti-based metallic glasses for implant applications. Mater Sci Eng C 33:875–883. https://doi.org/10.1016/j.msec.2012.11.015

146. Cao D, Wu Y, Liu XJ, et al (2019) Enhancement of glass-forming ability and plasticity via alloying the elements having positive heat of mixing with Cu in Cu48Zr48Al4 bulk metallic glass. J Alloys Compd 777:382–391. https://doi.org/10.1016/j.jallcom.2018.10.396

147. Zhu ZW, Gu L, Xie GQ, et al (2011) Relation between icosahedral short-range ordering and plastic deformation in Zr-Nb-Cu-Ni-Al bulk metallic glasses. Acta Mater 59:2814–2822. https://doi.org/10.1016/j.actamat.2011.01.020

148. Cao QP, Peng S, Zhao XN, et al (2016) Effect of Nb substitution for Cu on glass formation and corrosion behavior of Zr-Cu-Ag-Al-Be bulk metallic glass. J Alloys Compd 683:22–31. https://doi.org/10.1016/j.jallcom.2016.05.077

149. Cao G, Liu K, Liu G, et al (2019) Improving the glass-forming ability and the plasticity of Zr-Cu-Al bulk metallic glass by addition of Nb. J Non Cryst Solids 513:105–110. https://doi.org/10.1016/j.jnoncrysol.2019.03.009

150. Pang S, Zhang T, Asami K, Inoue A (2003) Formation, corrosion behavior, and mechanical properties of bulk glassy Zr-Al-Co-Nb alloys. J Mater Res 18:1652–1658. https://doi.org/10.1557/JMR.2003.0227

151. Yu D, Li X, Wu X, Li S (2019) Understanding and designing good glass formers in Zr-Al-Co-(Nb) system combining clusters and mixing entropy. Mater Lett 234:291–293. https://doi.org/10.1016/j.matlet.2018.09.124

152. Li Y, Zhang W, Dong C, et al (2011) Enhancement of glass-forming ability and corrosion resistance of Zr-based Zr-Ni-Al bulk metallic glasses with minor addition of Nb. J Appl Phys 110:24–29. https://doi.org/10.1063/1.3606642

153. Campos Neto ND de, Paula WM de, Pereira FS, et al (2018) Influence of Small Content Elements Additions on the Glass Forming Ability of Zr-based Bulk Metallic Glasses Alloys. Mater Res 21:. https://doi.org/10.1590/1980-5373-mr-2017-1088

154. Qin C, Asami K, Zhang T, et al (2003) Corrosion behavior of Cu-Zr-Ti-Nb bulk glassy alloys. Mater Trans 44:749–753. https://doi.org/10.2320/matertrans.44.749

155. Qin C, Zhang W, Kimura H, et al (2004) New Cu-Zr-Al-Nb bulk glassy alloys with high corrosion resistance. Mater Trans 45:1958–1961. https://doi.org/10.2320/matertrans.45.1958

156. Chen Y, Jiang JZ (2021) The plasticity, crystallization and micro-hardness of Zr–Co–Al-(Nb) BMGs upon rapid quenching and conventional annealing. J Alloys Compd 856:157130. https://doi.org/10.1016/j.jallcom.2020.157130

157. Guan B, Shi X, Dan Z, et al (2016) Corrosion behavior, mechanical properties and cell cytotoxity of Zr-based bulk metallic glasses. Intermetallics 72:69–75. https://doi.org/10.1016/j.intermet.2016.02.001

158. Yuan ZZ, Le WK, Zhang XY (2016) Effect of alloying on the corrosion resistance of Zr–Co–Al metallic glasses. Mater Res Innov 22:51–57. https://doi.org/10.1080/14328917.2016.1265230

159. Lu XY, Huang L, Pang SJ, Zhang T (2012) Formation and biocorrosion behavior of Zr-Al-Co-Nb bulk metallic glasses. Chinese Sci Bull 57:1723–1727. https://doi.org/10.1007/s11434-012-5027-0

160. Wang S, Wang Y, Wu Y, et al (2015) High plastic Zr – Cu – Fe – Al – Nb bulk metallic glasses for biomedical applications. 22:648–653. https://doi.org/10.1007/s12613-015-1118-7

161. Chen Y, Jiang JZ (2020) Formation of the B2–ZrCo phase and micro-hardness evolution in Zr–Co–Al BMGs via conventional and flash annealing. J Alloys Compd 834:1–16. https://doi.org/10.1016/j.jallcom.2020.154230

162. Chen Y, Tang C, Laws K, et al (2020) Zr-Co-Al bulk metallic glass composites containing B2 ZrCo via rapid quenching and annealing. J Alloys Compd 820:153079. https://doi.org/10.1016/j.jallcom.2019.153079

163. Kim WC, Kim KC, Na MY, et al (2017) Formation of crystalline phase in the glass matrix of Zr-Co-Al glass-matrix composites and its effect on their mechanical properties. Met Mater Int 23:1216–1222. https://doi.org/10.1007/s12540-017-6851-1

164. Ning Z, Liang W, Zhang M, et al (2016) High tensile plasticity and strength of a CuZr-based bulk metallic glass composite. Mater Des 90:145–150. https://doi.org/10.1016/j.matdes.2015.10.117

165. Wu Y, Wang H, Wu HH, et al (2011) Formation of Cu-Zr-Al bulk metallic glass composites with improved tensile properties. Acta Mater 59:2928–2936. https://doi.org/10.1016/j.actamat.2011.01.029

166. Li C, Lu W, Tan J, et al (2017) Microstructure and mechanical properties of Zr-Co-Al alloys prepared by rapid solidification. J Mater Res 32:2570–2577. https://doi.org/10.1557/jmr.2017.118

167. Li CJ, Tan J, Wang G, et al (2013) Enhanced strength and transformation-induced plasticity in rapidly solidified Zr-Co-(Al) alloys. Scr Mater 68:897–900. https://doi.org/10.1016/j.scriptamat.2013.02.029

168. Calin M, Gebert A, Ghinea AC, et al (2013) Designing biocompatible Ti-based metallic glasses for implant applications. Mater Sci Eng C 33:875–883. https://doi.org/10.1016/j.msec.2012.11.015

169. Jiang WH, Jiang F, Green BA, et al (2007) Electrochemical corrosion behavior of a Zr-based bulk-metallic glass. Appl Phys Lett 91:2–5. https://doi.org/10.1063/1.2762282

170. Zhang Y, Yan L, Zhao X, Ma L (2018) Enhanced chloride ion corrosion resistance of Zr-based bulk metallic glasses with cobalt substitution. J Non Cryst Solids 496:18–23. https://doi.org/10.1016/j.jnoncrysol.2018.05.005

171. Liens A, Ter-Ovanessian B, Courtois N, et al (2020) Effect of alloying elements on the microstructure and corrosion behavior of TiZr-based bulk metallic glasses. Corros Sci 177:. https://doi.org/10.1016/j.corsci.2020.108854

172. Le WK, Yuan ZZ, Zhang XY (2017) Experimental and theoretical study on the corrosion resistance of Zr–Co–Al–Nb metallic glasses. J Theor Appl Phys 11:37–43. https://doi.org/10.1007/s40094-016-0234-8

173. Yuan ZZ, Le WK, Zhang XY (2018) Effect of alloying on the corrosion resistance of Zr–Co–Al metallic glasses. Mater Res Innov 22:51–57. https://doi.org/10.1080/14328917.2016.1265230

174. Hua N, Huang L, Wang J, et al (2012) Corrosion behavior and in vitro biocompatibility of Zr-Al-Co-Ag bulk metallic glasses: An experimental case study. J Non Cryst Solids 358:1599–1604. https://doi.org/10.1016/j.jnoncrysol.2012.04.022

175. Gong P, Deng L, Jin J, et al (2016) Review on the research and development of Ti-based bulk metallic glasses. Metals (Basel) 6:. https://doi.org/10.3390/met6110264

176. Wada T, Qin F, Wang X, et al (2009) Formation and bioactivation of Zr-Al-Co bulk metallic glasses. J Mater Res 24:2941–2948. https://doi.org/10.1557/jmr.2009.0348

177. Xie G, Qin F, Zhu S (2013) Recent progress in Ti-based metallic glasses for application as biomaterials. Mater Trans 54:1314–1323. https://doi.org/10.2320/matertrans.MF201315

178. Han K, Wang Y, Qiang J, et al (2019) Low-cost Zr-based bulk metallic glasses for biomedical devices applications. J Non Cryst Solids 520:119442. https://doi.org/10.1016/j.jnoncrysol.2019.05.018

179. Buzzi S, Jin K, Uggowitzer PJ, et al (2006) Cytotoxicity of Zr-based bulk metallic glasses. Intermetallics 14:729–734. https://doi.org/10.1016/j.intermet.2005.11.003

180. Baulin O, Fabrègue D, Kato H, et al (2018) A new, toxic element-free Mg-based metallic glass for biomedical applications. J Non Cryst Solids 481:397–402. https://doi.org/10.1016/j.jnoncrysol.2017.11.024

181. Li HF, Zheng YF (2016) Recent advances in bulk metallic glasses for biomedical applications. Acta Biomater 36:1–20. https://doi.org/10.1016/j.actbio.2016.03.047

182. Niinomi Mitsuo (2019) Metals for Biomedical Devices 2nd Edition, 2nd Edition. Elsevier, Tohoku

183. Liens A, Etiemble A, Rivory P, et al (2018) On the potential of Bulk Metallic Glasses for dental implantology: Case study on Ti40Zr10Cu36Pd14. Materials (Basel) 11:. https://doi.org/10.3390/ma11020249

184. European Union European Chemicals Agency. https://echa.europa.eu/fr/. Accessed 7 Oct 2021

185. Chen Q, Liu L, Zhang SM (2010) The potential of Zr-based bulk metallic glasses as biomaterials. Front Mater Sci China 4:34–44. https://doi.org/10.1007/s11706-010-0004-5

186. Baulin O, Fabrègue D, Kato H, et al (2018) A Ni-, Al-, Be-free Zr-based metallic glass for biomedical applications. J Non Cryst Solids 500:78–83. https://doi.org/10.1016/j.jnoncrysol.2018.06.026

187. Wada T, Zhang T, Inoue A (2002) Formation, Thermal Stability and Mechanical Properties in Zr-Al-Co Bulk Glassy Alloys. Mater Trans 43:2843–2846. https://doi.org/10.2320/matertrans.43.2843

188. Xie G, Qin F, Zhu S, Inoue A (2012) Ni-free Ti-based bulk metallic glass with potential for biomedical applications produced by spark plasma sintering. Intermetallics. https://doi.org/10.1016/j.intermet.2012.05.006

189. Zhu SL, Wang XM, Inoue A (2008) Glass-forming ability and mechanical properties of Ti-based bulk glassy alloys with large diameters of up to 1 cm. Intermetallics. https://doi.org/10.1016/j.intermet.2008.05.006

190. Kim YC, Bae DH, Kim WT, Kim DH (2003) Glass forming ability and crystallization behavior of Ti-based amorphous alloys with high specific strength. J Non Cryst Solids. https://doi.org/10.1016/S0022-3093(03)00327-2

191. Xie KF, Yao KF, Huang TY (2010) A Ti-based bulk glassy alloy with high strength and good glass forming ability. In: Intermetallics

192. Abdi S, Oswald S, Gostin PF, et al (2016) Designing new biocompatible glass-forming Ti75-xZr10NbxSi15 (x = 0, 15) alloys: Corrosion, passivity, and apatite formation. J Biomed Mater Res - Part B Appl Biomater. https://doi.org/10.1002/jbm.b.33332

193. Takeuchi A, Inoue A (2005) Classification of Bulk Metallic Glasses by atomic Size Difference, Heat of Mixing and Period of Consituent Elements and Its Application to Characterisation of the Main Alloying Element. Mater Trans 46:2817–2829

194. Limbach R, Kosiba K, Pauly S, et al (2017) Serrated flow of CuZr-based bulk metallic glasses probed by nanoindentation: Role of the activation barrier, size and distribution of shear transformation zones. J Non Cryst Solids 459:130–141. https://doi.org/10.1016/j.jnoncrysol.2017.01.015

195. Wang D, Tan H, Li Y (2005) Multiple maxima of GFA in three adjacent eutectics in Zr – Cu – Al alloy system – A metallographic way to pinpoint the best glass forming alloys. 53:2969–2979. https://doi.org/10.1016/j.actamat.2005.03.012

196. Fan C, Liaw PK, Haas V, et al (2006) Structures and mechanical behaviors of Zr55 Cu35 Al10 bulk amorphous alloys at ambient and cryogenic temperatures. Phys Rev B - Condens Matter Mater Phys 74:1–6. https://doi.org/10.1103/PhysRevB.74.014205

197. Zhang T, Inoue A, Masumoto T (1991) Amorphous Zr-Al-TM (TM=Co,Ni,Cu) Alloys with Significant Supercooled Liquid Region of Over 100 K

198. Yokoyama Y, Yamasaki T, Liaw PK, et al (2007) Glass-structure changes in tilt-cast Zr – Cu – Al glassy alloys. 451:621–626. https://doi.org/10.1016/j.msea.2006.02.422

199. Yu P, Bai HY (2008) Poisson's ratio and plasticity in CuZrAl bulk metallic glasses. Mater Sci Eng A 485:1–4. https://doi.org/10.1016/j.msea.2007.07.062

200. Zhang GQ, Jiang QK, Chen LY, et al (2006) Synthesis of centimeter-size Ag-doped Zr-Cu-Al metallic glasses with large plasticity. J Alloys Compd 424:176–178. https://doi.org/10.1016/j.jallcom.2006.06.088

201. Wang T, Ma X, Chen Y, et al (2020) Structural heterogeneity originated plasticity in Zr–Cu–Al bulk metallic glasses. Intermetallics 121:. https://doi.org/10.1016/j.intermet.2020.106790

202. Zhang T, Inoue A (2002) New Glassy Zr-Al-Fe and Zr-Al-Co Alloys with a Large Supercooled Liquid Region. Mater Trans 43:267–270. https://doi.org/10.2320/matertrans.43.267

203. Tabeshian A, Mao H, Arnberg L, Aune RE (2019) Investigation of glass forming ability in the Zr-rich part of the Zr-Fe-Al ternary system. J Appl Phys 125:8–15. https://doi.org/10.1063/1.5066554

204. Li YH, Zhang W, Dong C, et al (2012) Glass-forming ability and corrosion resistance of Zr-based Zr-Ni-Al bulk metallic glasses. J Alloys Compd 536:117–121. https://doi.org/10.1016/j.jallcom.2011.11.073

205. Yu KM, Cao QP, Yu Q, et al (2018) Glass forming ability and bending plasticity evolutions in Zr-Co-Al bulk metallic glasses and their structural origin. J Non Cryst Solids 488:52–62. https://doi.org/10.1016/j.jnoncrysol.2018.02.030

206. Hu Y, Cao W, Shek C (2014) The corrosion and oxidation behavior of Zr-based metallic glasses. J Mater Res 29:1248–1255. https://doi.org/10.1557/jmr.2014.107

207. Tan J, Pan FS, Zhang Y, et al (2012) Effect of Fe addition on glass forming ability and mechanical properties in Zr-Co-Al-(Fe) bulk metallic glasses. Mater Sci Eng A 539:124–127. https://doi.org/10.1016/j.msea.2012.01.068

208. Han K, Qiang J, Wang Y, Häussler P (2017) Zr-Al-Co-Cu bulk metallic glasses for biomedical devices applications. J Alloys Compd 729:144–149. https://doi.org/10.1016/j.jallcom.2017.09.144

209. Liu Z, Chan KC, Liu L (2013) Effect of Alloying Elements with Positive Heat of Mixing on the Free Volume and Compressive Plasticity in ZrCoCuAl Bulk Metallic Glasses. Mater Trans 54:2209–2214. https://doi.org/10.2320/matertrans.M2013241

210. Hasegawa M, Taketomi T, Kato H, et al (2005) Comparative Study on Glassy Phase Stabilities of Zr-Co-Al and Zr-Ni-Al Metallic Glasses. Mater Trans 46:2785–2790. https://doi.org/10.2320/matertrans.46.2785

211. Hua N, Pang S, Li Y, et al (2011) Ni- and Cu-free Zr-Al-Co-Ag bulk metallic glasses with superior glass-forming ability. J Mater Res 26:539–546. https://doi.org/10.1557/jmr.2010.65

212. Dong Q, Pan YJ, Tan J, et al (2019) A comparative study of glass-forming ability, crystallization kinetics and mechanical properties of Zr55Co25Al20 and Zr52Co25Al23 bulk metallic glasses. J Alloys Compd 785:422–428. https://doi.org/10.1016/j.jallcom.2019.01.180

213. Zhang XF, Wang YM, Qiang JB, et al (2004) Optimum Zr-Al-Co bulk metallic glass composition Zr53Al 23.5Co23.5. Intermetallics 12:1275–1278. https://doi.org/10.1016/j.intermet.2004.07.004

214. Cao WH, Zhang JL, Shek CH (2012) Oxidation behavior of Zr56Co28Al16 bulk metallic glasses. Corros Sci 65:528–534. https://doi.org/10.1016/j.corsci.2012.08.057

215. Qin XM, Tan J, Li CJ, et al (2015) On the formation, mechanical properties and crystallization behaviors of a Zr56Co24Al20 bulk metallic glass. J Alloys Compd 647:204–208. https://doi.org/10.1016/j.jallcom.2015.04.241

216. Zhang QS, Zhang W, Inoue A (2010) High Glass-Forming Ability and Unusual Deformation Behavior of New Zr-Cu-Fe-Al Bulk Metallic Glasses. 1042–1045. https://doi.org/10.4028/www.scientific.net/MSF.654-656.1042

217. Chen C, Pang S, Cheng Y, Zhang T (2015) A centimeter-size Zr 40 Hf 10 Ti 4 Y 1 Al 10 Cu 25 Ni 7 Co 2 Fe 1 bulk metallic glass with high mixing entropy designed by multi-substitution. J Non Cryst Solids 410:39–42. https://doi.org/10.1016/j.jnoncrysol.2014.11.032

218. Kwon OJ, Kim YC, Kim KB, et al (2006) Formation of amorphous phase in the binary Cu-Zr alloy system. Met Mater Int 12:207–212. https://doi.org/10.1007/BF03027532

219. Takeuchi A, Inoue A (2000) Calculations of mixing enthalpy and mismatch entropy for ternary amorphous alloys. Mater Trans JIM. https://doi.org/10.2320/matertrans1989.41.1372

220. Li Y, Xu J (2017) Role of late transition metals on pitting resistance of Zr-Ti-(Cu, Ni, Co)-Al bulk metallic glasses in 0.6 M NaCl aqueous solution. J Mater Sci Technol 33:1278–1288. https://doi.org/10.1016/j.jmst.2017.04.010

221. Yuan CC, Yang F, Xi XK, et al (2020) Impact of hybridization on metallic-glass formation and design. Mater Today 32:26–34. https://doi.org/10.1016/j.mattod.2019.06.001

222. Tan J, Pan FS, Zhang Y, et al (2012) Formation of Zr-Co-Al bulk metallic glasses with high strength and large plasticity. Intermetallics 31:282–286. https://doi.org/10.1016/j.intermet.2012.08.003

223. Zhang T, Inoue A (2004) Formation, thermal and mechanical properties of bulk glassy alloys in Zr-Al-Co and Zr-Al-Co-Cu systems. Mater Sci Eng A 375–377:432–435. https://doi.org/10.1016/j.msea.2003.10.233

224. Koster UWE (1988) Surface Crystallization of Metallic Glasses. 97:233–239

225. Sun Y, Zhu L, Kearns KL, et al (2011) Glasses crystallize rapidly at free surfaces by growing crystals upward. Proc Natl Acad Sci 108:5990–5995. https://doi.org/10.1073/pnas.1017995108

226. Guérin E, Daudin R, Lenain A, et al (2020) Effect of the alloy/mould contact on surface crystallisation of a biocompatible ZrCoAl bulk metallic glass. J Phys Condens Matter 32:. https://doi.org/10.1088/1361-648X/ab7132

227. MOHAMMADI RAHVARD M, TAMIZIFAR M, Ali BOUTORABI SM (2018) Zr-Co(Cu)-Al bulk metallic glasses with optimal glass-forming ability and their compressive properties. Trans Nonferrous Met Soc China (English Ed 28:1543–1552. https://doi.org/10.1016/S1003-6326(18)64796-X

228. Mohammadi Rahvard M, Tamizifar M, Boutorabi SMA (2018) The effect of Ag addition on the non-isothermal crystallization kinetics and fragility of Zr56Co28Al16 bulk metallic glass. J Non Cryst Solids 481:74–84. https://doi.org/10.1016/j.jnoncrysol.2017.10.026

229. Hua N, Huang L, Chen W, et al (2014) Biocompatible Ni-free Zr-based bulk metallic glasses with high-Zr-content: Compositional optimization for potential biomedical applications. Mater Sci Eng C 44:400–410. https://doi.org/10.1016/j.msec.2014.08.049

230. Kissinger HE (1957) Reaction Kinetics in Differential Thermal Analysis. Anal Chem 29:1702–1706. https://doi.org/10.1021/ac60131a045

231. Yang K, Bing L, Yanhong L, et al (2021) Crystallization kinetics of Cu–Zr–Al bulk metallic glass with Nd addition. Int J Chem Kinet 1–11. https://doi.org/10.1002/kin.21521

232. Bing L, Yanhong L, Ke Y, et al (2016) Effect of yttrium addition on the non-isothermal crystallization kinetics and fragility of Cu-Zr-Al bulk metallic glass. Thermochim Acta 642:105–110. https://doi.org/10.1016/j.tca.2016.08.001

233. Nkou Bouala GI, Etiemble A, Der Loughian C, et al (2018) Silver influence on the antibacterial activity of multi-functional Zr-Cu based thin film metallic glasses. Surf Coatings Technol 343:108–114. https://doi.org/10.1016/j.surfcoat.2017.10.057

234. Tan J, Zhang Y, Sun BA, et al (2011) Correlation between internal states and plasticity in bulk metallic glass. Appl Phys Lett 98:15–17. https://doi.org/10.1063/1.3580774

235. Louzguine-Luzgin D V., Jiang J, Bazlov AI, et al (2019) Phase separation process preventing thermal embrittlement of a Zr-Cu-Fe-Al bulk metallic glass. Scr Mater 167:31–36. https://doi.org/10.1016/j.scriptamat.2019.03.030

236. Wang GY, Liaw PK, Yokoyama Y, Inoue A (2011) Size effects on the fatigue behavior of bulk metallic glasses. J Appl Phys 110:. https://doi.org/10.1063/1.3664846

237. Wang XD, Qu RT, Liu ZQ, Zhang ZF (2015) Shear band-mediated fatigue cracking mechanism of metallic glass at high stress level. Mater Sci Eng A 627:336–339. https://doi.org/10.1016/j.msea.2015.01.008

238. Holland-Moritz D, Schenk T, Simonet V, Bellissent R (2006) Short-range order in undercooled and stable melts forming

quasicrystals and approximants and its influence on nucleation. Philos Mag 86:255–262. https://doi.org/10.1080/14786430500253992

239. Schenk T, Simonet V, Holland-Moritz D, et al (2004) Temperature dependence of the chemical short-range order in undercooled and stable Al-Fe-Co liquids. Europhys Lett 65:34–40. https://doi.org/10.1209/epl/i2003-10062-x

240. Brillo J, Bytchkov A, Egry I, et al (2006) Local structure in liquid binary Al-Cu and Al-Ni alloys. J Non Cryst Solids 352:4008–4012. https://doi.org/10.1016/j.jnoncrysol.2006.08.011

241. Pasturel A, Jakse N (2018) Role of five-fold symmetry in undercooled Al-Cu binary alloys. J Appl Phys 123:. https://doi.org/10.1063/1.5027663

242. Roik OS, Samsonnikov O, Kazimirov V, Sokolskii V (2010) Short- and medium-range order in Al-Co-Ni Alloys. Zeitschrift für Naturforsch 65:123–131

243. He Q, Cheng Y, Ma E, Xu J (2011) Locating bulk metallic glasses with high fracture toughness : Chemical effects and composition optimization. Acta Mater 59:202–215. https://doi.org/10.1016/j.actamat.2010.09.025

244. Yu D, Geng Y, Li Z, et al (2015) A new method locating good glass-forming compositions. J Alloys Compd 646:620–625. https://doi.org/10.1016/j.jallcom.2015.05.184

245. Yu D, Shi X, Fu H, et al (2015) Glass formation in Zr – Al – Fe – Cu system. Mater Lett 157:299–302. https://doi.org/10.1016/j.matlet.2015.05.142

246. Cheng YQ, Cao AJ, Ma E (2009) Correlation between the elastic modulus and the intrinsic plastic behavior of metallic glasses: The roles of atomic configuration and alloy composition. Acta Mater 57:3253–3267. https://doi.org/10.1016/j.actamat.2009.03.027

247. Wu Y, Cao D, Yao Y, et al (2021) Substantially enhanced plasticity of bulk metallic glasses by densifying local atomic packing. Nat Commun 12:1–9. https://doi.org/10.1038/s41467-021-26858-9

248. Etienne S, Cavaille JY, Perez J, et al (1982) Automatic system for analysis of micromechanical properties. Rev Sci Instrum 53:1261–1266. https://doi.org/10.1063/1.1137153

249. Yang DS, Wang J, Pelletier JM, et al (2021) Characteristic of dynamic mechanical relaxation processes in Cu46Zr46Al8 and La43.4Ce18.6Ni24Al14 metallic glasses. J Alloys Compd 887:2–7. https://doi.org/10.1016/j.jallcom.2021.161392

250. Qiao JC, Casalini R, Pelletier JM (2015) Main (α) relaxation and excess wing in Zr50Cu40Al10 bulk metallic glass investigated by mechanical spectroscopy. J Non Cryst Solids 407:106–109. https://doi.org/10.1016/j.jnoncrysol.2014.08.009

251. Yavari AR, Moulec A Le, Inoue A, et al (2005) Excess free volume in metallic glasses measured by X-ray diffraction. Acta Mater 53:1611–1619. https://doi.org/10.1016/j.actamat.2004.12.011

252. Lee SC, Lee CM, Lee JC, et al (2008) Structural disordering process of an amorphous alloy driven by the elastostatic compression at room temperature. Appl Phys Lett 92:1–4. https://doi.org/10.1063/1.2908218

253. Ke HB, Wen P, Peng HL, et al (2011) Homogeneous deformation of metallic glass at room temperature reveals large dilatation. Scr Mater 64:966–969. https://doi.org/10.1016/j.scriptamat.2011.01.047

254. Lou H, Zeng Z, Zhang F, et al (2020) Two-way tuning of structural order in metallic glasses. Nat Commun 11:. https://doi.org/10.1038/s41467-019-14129-7

255. Georgarakis K, Li Y, Aljerf M, et al (2010) Glass formation in the Nb-Si binary system. J Alloys Compd 504:14–17. https://doi.org/10.1016/j.jallcom.2010.03.034

256. Zhang HW, Subhash G, Jing XN, et al (2006) Evaluation of hardness-yield strength relationships for bulk metallic glasses. Philos Mag Lett 86:333–345. https://doi.org/10.1080/09500830600788935

257. Cao D, Wu Y, Li HX, et al (2018) Beneficial effects of oxygen addition on glass formation in a high-entropy bulk metallic glass. Intermetallics 99:44–50. https://doi.org/10.1016/j.intermet.2018.05.007

258. Wang T, Hou Q, Zhang L (2022) Enhanced heterogeneity and plasticity in a Zr - Cu – Al bulk metallic glass with micro-addition of oxygen. Mater Sci Eng A 831:142222. https://doi.org/10.1016/j.msea.2021.142222

259. Zhang C, Li N, Pan J, et al (2010) Enhancement of glass-forming ability and bio-corrosion resistance of Zr-Co-Al bulk metallic glasses by the addition of Ag. J Alloys Compd 504:163–167. https://doi.org/10.1016/j.jallcom.2010.02.078

260. Hua N, Li R, Wang H, et al (2011) Formation and mechanical properties of Ni-free Zr-based bulk metallic glasses. J Alloys Compd 509:S175–S178. https://doi.org/10.1016/j.jallcom.2011.01.078

261. Inoue A, Zhang T, Masumoto T (1990) Zr-Al-Ni Amorphous Alloys with High Glas Transition temperature and significant supercooled liquid region. 177–183

262. Pauling L (1947) Atomic Radii and Interatomic Distances in Metals. J Am Chem Soc 69:542–553. https://doi.org/10.1021/ja01195a024

263. Slater JC (1964) Atomic radii in crystals. J Chem Phys 41:3199–3204. https://doi.org/10.1063/1.1725697

264. Brandes EA, Brook GB (1992) Smithells Metals Reference Book, Seventh ed. Butterwoth-Heinemann

265. Cordero B, Gómez V, Platero-Prats AE, et al (2008) Covalent radii revisited. J Chem Soc Dalt Trans 2832–2838. https://doi.org/10.1039/b801115j

266. Marimuthu KP, Lee K, Han J, et al (2020) Nanoindentation of zirconium based bulk metallic glass and its nanomechanical properties. J Mater Res Technol 9:104–114. https://doi.org/10.1016/j.jmrt.2019.10.034

267. Burgess T, Ferry M (2009) Nanoindentation of metallic glasses. Mater Today 12:24–32. https://doi.org/10.1016/S1369-7021(09)70039-2

268. Haag F, Beitelschmidt D, Eckert J, Durst K (2014) Influences of residual stresses on the serrated flow in bulk metallic glass under elastostatic four-point bending - A nanoindentation and atomic force microscopy study. Acta Mater 70:188–197. https://doi.org/10.1016/j.actamat.2014.01.053

Supplementary materials

A. C&L classification of some materials of interest (updated 05/10/2021)

Hazard class	Code	Signification	Be	Co	Ni	Zr	Cu
Acute Tox. 2	H330	Fatal if inhaled	X				
Acute Tox. 3	H301	Toxic if swallowed	X				
Acute Tox. 4	H302	Harmful if swallowed					X
Aquatic Chronic 2	H411	Toxic to aquatic life with long-lasting effects					X
Aquatic Chronic 3	H412	Harmful to aquatic life			X		
Aquatic Chronic 4	H413	May cause long-lasting harmful effects to aquatic life		X			
Carc. 1B	H350(i)	May cause cancer (by inhalation)	X	X			
Car. 2	H351	Suspected of causing cancer			X		X
Eye Irrit. 1	H319	Causes serious eye irritation	X				
Eye Irrit. 2	H319	Causes serious eye irritation					X
Muta. 2	H341	Suspected of causing genetic defects		X			
Repro. 1B	H360F	May damage fertility		X			
Resp. Sens. 1	H334	May cause allergy or asthma symptoms or breathing difficulties in inhaled		X			
Skin Irrit. 2	H315	Causes skin irritation	X				
Skin Sens. 1	H317	May cause an allergic skin reaction	X	X	X		X
STOT RE 1	H372	Causes damage to organs through prolonged or repeated exposure	X		X		
STOT RE 2	H373	May cause damage to organs (central nervous…) through prolonged or repeated exposure (inhalation, oral…)					X
STOT SE 3	H335	May cause respiratory irritation	X				
Pyr. Sol. 1	H250	Catches fire spontaneously if exposed to air				X	
Water-react. 1	H260	In contact with water releases flammable gases which may ignite spontaneously				X	

Table A-1: C&L classification reported on the ECHA website (www.echa.europa.eu/fr/home) for Be, Co, Ni, Zr and Cu. Data updated on 05/10/2021.

B. Extended summary of reported Zr-Co-Al-based compositions

Zr-Co-Al

Comp.	Dc / used (mm)	Density (g/cm3)	Mechanical										Elaboration		Thermal									Ref
			σy (Mpa)	σmax (Mpa)	E	ε e (%)	ε p (%)	Strain rate (s-1)	G (Gpa)	K (Gpa)	Poisson ratio	HV	Fusion	Casting	Tg (K)	Tx (K)	ΔT (K)	Tp1 (K)	Tp2 (K)	Tm (K)	Tl (K)	Tg/Tl	Heating rate (K/s)	
$Zr_{48.5}Co_{48.5}Al_3$	Crist.		683.67	1420		0.2	26.2	5.0E-04																[166]
$Zr_{49.5}Co_{49.5}Al_1$	Crist.		328.26	2570		0.2	54.5	5.0E-04																[166]
$Zr_{49}Co_{49}Al_2$	Crist.		477.28	1610		0.2	29.6	5.0E-04																[166]
$Zr_{50}Co_{25}Al_{25}$													AM	SRS								0.64	40	[210]
$Zr_{50}Co_{30}Al_{20}$													AM	CMC	791						1340	0.59	40	[202]
$Zr_{51}Co_{33}Al_{16}$	2	6.622			115				41.9	142.6	0.366	618	AM	CMC	775	828	53			1171	1258	0.616	20	[205]
$Zr_{52}Co_{25}Al_{23}$	2	6.106	2190	2308	103	2.1	2.5	2.5E-04					AM	CMC	775	827	51	834	852				10	[212]
	2	6.106	2190	2308	103	2.1	2.5	2.5E-04					AM	CMC	779	838	59	843	852		1320		20	[212]
	2	6.106	2190	2308	103	2.1	2.5	2.5E-04					AM	CMC	780	845	65	849					30	[212]
	2	6.106	2190	2308	103	2.1	2.5	2.5E-04					AM	CMC	782	850	68	854					40	[212]
	2	6.106	2190	2308	103	2.1	2.5	2.5E-04					AM	CMC	784	852	68	856					50	[212]
$Zr_{52}Co_{32}Al_{16}$	3	6.6			114				41.5	142.6	0.367	607	AM	CMC	770	824	54			1172	1256	0.613	20	[205]
$Zr_{53}Co_{23.5}Al_{23.5}$	3												AM	CMC	783	849	66			1230	1320	0.59	20	[213]
$Zr_{53}Co_{23.5}Al_{23.5}$	3												AM	CMC	772	841	69			1217	1296	0.596	20	[259]
$Zr_{53}Co_{31}Al_{16}$	3	6.48	1980	2170	93	2	1.8	2.1E-04				550	AM	CMC	752	812	60				1303	0.577	20	[121]
	3		1980	2170	93	2	1.8	2.1E-04	34	116	0.366	550	AM	ICCM	752	812	60				1303	0.577	20	[211]
	3												AM	ICCM										[211]
	5	6.567			113				41.2	140.1	0.366	598	AM	CMC	763	812	49			1175	1257	0.607	20	[205]
$Zr_{54.4}Co_{22.8}Al_{22.8}$	3												AM	CMC	764	824	60			1231	1334	0.573	20	[213]
$Zr_{54}Co_{24}Al_{22}$	3												AM	CMC	768	843	75			1230	1316	0.584	20	[213]
$Zr_{54}Co_{30}Al_{16}$	6	6.547			111				40.5	138.6	0.367	589	AM	CMC	757	806	49			1180	1258	0.602	20	[205]
$Zr_{55.4}Co_{22.3}Al_{22.3}$	3												AM	CMC	767	815	48			1233	1326	0.578	20	[213]
$Zr_{55.8}Co_{19.4}Al_{24.8}$	3												AM	CMC	751	820	69			1232	1302	0.577	20	[213]
$Zr_{55}Co_{17}Al_{28}$													AM	CMC	782						1290	0.606	40	[187]
$Zr_{56}Co_{12}Al_{34}$													AM	CMC	760						1280	0.59	40	[187]
$Zr_{55}Co_{25}Al_{20}$													AM	SRS			80						40	[210]
	5			2100	98	2.9	0.9	3.3E-04				550	AM	CMC	765	840	75						40	[150]
	5			2100	98	2.9	0.9	3.3E-04				550	AM	CMC	765	840	75						40	[150]
	2	6.348	2110	2115	94	2.2	0.5	2.5E-04					AM	CMC	756	801	45	813	876				10	[212]
	2	6.348	2110	2115	94	2.2	0.5	2.5E-04					AM	CMC	762	810	48	823	887		1295		20	[212]
	2	6.348	2110	2115	94	2.2	0.5	2.5E-04					AM	CMC	763	819	56	831	891				30	[212]
	2	6.348	2110	2115	94	2.2	0.5	2.5E-04					AM	CMC	764	824	60	837	896				40	[212]
	2	6.348	2110	2115	94	2.2	0.5	2.5E-04					AM	CMC	766	827	61	839	898				50	[212]
	3												AM	CMC			64						40	[223]
	3												AM	CMC	764	839	75			1231	1310	0.583	20	[213]
	10												AM		759	830	71				1245	0.609	40	[176]
	2.5			1900	114	1.5	0.2	5.0E-04					AM	CMC	760	838	79				1245	0.61	40	[187]
	5												AM	ICCM	746	821	75						20	[159]
	5												AM	ICCM										[159]
	5												AM	ICCM										[159]
	3		2050	2200	92	2.1	0.9	2.4E-04					AM	CMC	769		64				1260	0.61	40	[202]
$Zr_{55}Co_{29}Al_{16}$													AM	CMC	760						1270	0.595	40	[187]
$Zr_{55}Co_{29}Al_{16}$	7	6.514			111				40.5	139.5	0.367	579	AM	CMC	750	799	49			1185	1258	0.596	20	[205]
$Zr_{55}Co_{33}Al_{12}$													AM	CMC	760						1280	0.59	40	[187]
$Zr_{56.25}Co_{25}Al_{18.75}$	3	6.34	2200		105		0.5	5.0E-04					AM	CMC	761	811	50			1215	1361	0.559	40	[208]
$Zr_{56}Co_{24}Al_{20}$	2	6.23	2177	2280		2	8	2.5E-04					AM	CMC	725	785	60						5	[215]
	2	6.23	2177	2280		2	8	2.5E-04					AM	CMC	740	801	61						10	[215]
	2	6.23	2177	2280		2	8	2.5E-04					AM	CMC	755	810	55						20	[215]
	2	6.23	2177	2280		2	8	2.5E-04					AM	CMC	765	830	70						40	[215]
	2	6.23	2177	2280		2	8	2.5E-04					AM	CMC	775	861	86						60	[215]

(Table B- continued)

Comp.	Dc / used (mm)	Density (g/cm3)	Mechanical										Elaboration		Thermal									RRef
			σy (Mpa)	σmax (Mpa)	E	Ɛ e (%)	Ɛ p (%)	Strain rate (s-1)	G (Gpa)	K (Gpa)	Poisson ratio	HV	Fusion	Casting	Tg (K)	Tx (K)	ΔT (K)	Tp1 (K)	Tp2 (K)	Tm (K)	Tl (K)	Tg/Tl	Heating rate (K/s)	
	2		1897	2136	92	2	8.2						AM	CMC	730	775	45	785	870				5	[18]
	2		1897	2136	92	2	8.2						AM	CMC	741	787	46	798	884				10	[18]
	2		1897	2136	92	2	8.2						AM	CMC	730	775	45	785	870				5	[18]
	2		1897	2136	92	2	8.2						AM	CMC	741	787	46	798	884				10	[18]
	2		1897	2136	92	2	8.2						AM	CMC	749	791	42	803	891				20	[18]
	2		1897	2136	92	2	8.2						AM	CMC	762	810	48	820	909				40	[18]
	2		1897	2136	92	2	8.2						AM	CMC	766	812	46	821	912				60	[18]
	3												AM	CMC	738	793	55						20	[206]
	3												AM	CMC	738	793	55						20	[206]
	18								34			520	AM	CMC	741	785	44	800	901				20	[129]
$Zr_{56}Co_{28}Al_{16}$	2		1959	2190		2.1	11.9	2.5E-04					AM	CMC	742	787	45				1252		20	[207]
	2		1880	2078		2	3.8	1.0E-04					AM	CMC										[209]
	2		1880			2	1	1.0E-04					AM	CMC										[209]
	2	6.312	2112	2477		2	11.3	2.5E-04					AM	CMC	750	809	59	820					20	[222]
	2	6.506	1959	2192		2	9.96	2.5E-04					AM	CMC	749	791	42	803					20	[222]
	3												AM	CMC	749	794	45	806	888				20	[214]
	18												AM		753	797	44				1208	0.623	40	[176]
	Ribbon												AM	MS									20	[173]
	2	6.5	1950	2150		2	10	2.5E-04					AM	CMC	740	785	45						20	[215]
	Ribbon												AM	MS					775	920	1220	1240	20	[172]
	7	6.496			110				40.1	136.8	0.367	571	AM	CMC	743	792	49			1191	1258	0.591	20	[205]
$Zr_{56}Co_{30}Al_{14}$	2	6.513	2076	2112		2	5.9	2.5E-04					AM	CMC	748	788	40	802					20	[222]
$Zr_{56}Co_{32}Al_{12}$	2	6.74	1851	2018		2	5.06	2.5E-04					AM	CMC	747	785	38	795					20	[222]
$Zr_{57.5}Co_{16.9}Al_{25.6}$	3												AM	CMC	744	786	42			1236	1300	0.572	20	[213]
$Zr_{57.6}Co_{21.3}Al_{21.1}$	3												AM	CMC	761	794	33			1234	1252	0.608	20	[213]
$Zr_{57}Co_{27}Al_{16}$	5	6.479			108				39.5	136.6	0.367	560	AM	CMC	735	787	52			1167	1260	0.583	20	[205]
$Zr_{57}Co_{28}Al_{15}$	15												AM		745	781	36				1203	0.619	40	[176]
$Zr_{58.6}Co_{26}Al_{15.4}$	3												AM	CMC	724	773	49			1232	1282	0.565	20	[213]
$Zr_{58}Co_{26}Al_{16}$	2	6.45			107				39	133.5	0.367	548	AM	CMC	729	780	51			1199	1282	0.569	20	[205]
$Zr_{58}Co_{28}Al_{14}$	15												AM		732	770	38				1205	0.607	40	[176]
$Zr_{60}Co_{20}Al_{2}$	3												AM	CMC	731	780	49			1231	1247	0.586	20	[213]
													AM	CMC	765						1275	0.6	40	[202]
$Zr_{60}Co_{26.7}Al_{13.3}$	3												AM	CMC	718	757	39			1234	1254	0.573	20	[213]
$Zr_{61.2}Co_{19.4}Al_{19.4}$	3												AM	CMC	720	771	51			1232	1249	0.576	20	[213]
$Zr_{64.6}Co_{17.7}Al_{17.7}$	Crist.												AM	CMC										[213]
$Zr_{67.2}Co_{18.2}Al_{14.4}$	Crist.												AM	CMC										[213]
$Zr_{69.8}Co_{19.1}Al_{11.1}$	Crist.												AM	CMC										[213]
$Zr_{70}Co_{10}Al_{20}$													AM	CMC	718						1380	0.52	40	[202]
$Zr_{72.4}Co_{19.8}Al_{7.8}$	Crist.												AM	CMC										[213]
$Zr_{74.9}Co_{20.5}Al_{20.5}$	Crist.												AM	CMC										[213]

Table B-1: Mechanical and thermal data gathered from literature for Zr-Co-Al ternary BMGs.

Comp.	Dc / used (mm)	Density (g/cm3)	Polarisation					Elaboration		Thermal									Ref
			E corr (V)	E pit (V)	Passive region (V)	Solution	Passivation current (A)	Fusion	Casting	Tg (K)	Tx (K)	ΔT (K)	Tp1 (K)	Tp2 (K)	Tm (K)	Tl (K)	Tg/Tl	Heating rate (K/s)	
$Zr_{53}Co_{23.5}Al_{23.5}$	3		-0.2	0	0.2	PBS 37°C pH 7,4	1.0E-05	AM	CMC	772	841	69			1217	1296	0.596	20	[259]
$Zr_{53}Co_{31}Al_{16}$	3	6.48	-0.53	0.03	0.56	PBS		AM	CMC	752	812	60				1303	0.577	20	[121]
	3		-0.52	0.02		PBS 37°C with 4 vol% N2O2	3.0E-06	AM	ICCM	752	812	60				1303	0.577	20	[211]
	3		-0.5	0.03		PBS 37°C with 4 vol% N2O2	3.0E-06	AM	ICCM										[211]
$Zr_{55}Co_{25}Al_{20}$	5		-0.5	0		3% mass NaCl open to air 25°C	5.0E-05	AM	CMC	765	840	75						40	[150]
	5		-0.35	1.5		1 N H2SO4 open to air 25°C	1.0E-05	AM	CMC	765	840	75						40	[150]
	10					Hanks balanced salt solution open to air		AM		759	830	71				1245	0.610	40	[176]
	5		-0.6	0.23		Hank's balanced salt solution 37°C	8.0E-06	AM	ICCM										[159]
	5		-0.55	0.125		PBS 37°C	8.0E-06	AM	ICCM										[159]
$Zr_{56}Co_{28}Al_{16}$	3		-0.23			0,5 M NaCl open to air pH 7		AM	CMC	738	793	55						20	[206]
	3		-0.1	No pitting		1 M H2SO4 open to air pH <0,5		AM	CMC	738	793	55						20	[206]
	18		-0.6	0.3	0.7	Hanks balanced salt solution open to air	3.0E-02	AM		753	797	44				1208	0.623	40	[176]
	Ribbon		-0.004			Hanks' solution pH 7,4 open to air	1.1E-05	AM	MS									20	[173]
	Ribbon		-0.248			Hanks' solution pH 7,4 open to air	1.2E-05	AM	MS					775	920	1220	1240	20	[172]
$Zr_{57}Co_{28}Al_{15}$	15					Hanks balanced salt solution open to air		AM		745	781	36				1203	0.619	40	[176]
$Zr_{58}Co_{28}Al_{14}$	15					Hanks balanced salt solution open to air		AM		732	770	38				1205	0.607	40	[176]

Table B-2: Polarisation and thermal data gathered from literature for Zr-Co-Al ternary BMGs.

Zr-Co-Al + Cu/Fe

Comp.	Dc / used (mm)	Density (g/cm3)	Mechanical								Elaboration		Thermal									Ref
			σy (Mpa)	σmax (Mpa)	E	Ɛe (%)	Ɛp (%)	Strain rate (s-1)	G (Gpa)	K (Gpa)	Fusion	Casting	Tg (K)	Tx (K)	ΔT (K)	Tp1 (K)	Tp2 (K)	Tm (K)	Tl (K)	Tg/Tl	Heating rate (K/s)	
$Zr_{56}Co_{28}Al_{16}$	2		1959	2190		2.1	11.9	2.5E-04			AM	CMC	742	787	45				1252		20	[207]
$Zr_{56}Co_{27}Fe_1Al_{16}$	2		1940	2160		2.1	11.8	2.5E-04			AM	CMC	740	789	49				1249		20	
$Zr_{56}Co_{26}Fe_2Al_{16}$	2		1868	2080		2	15.1	2.5E-04			AM	CMC	736	787	51				1242		20	
$Zr_{56}Co_{24}Fe_4Al_{16}$	2		1858	2070		1.9	10.8	2.5E-04			AM	CMC	735	784	49				1269		20	
$Zr_{56}Co_{20}Fe_8Al_{16}$	2		1650	1650		1.5	1.5	2.5E-04			AM	CMC	701	754	53				1280		20	
$Zr_{56}Co_{14}Fe_{14}Al_{16}$	2		590	590		0.4	0.4	2.5E-04			AM	CMC										
$Zr_{56.25}Co_{25}Al_{18.75}$	3	6.34	2200		105		0.5	5.0E-04			AM	CMC	761	811	50			1215	1361	0.559	40	[208]
$Zr_{56.25}Co_{18.75}Cu_{6.25}Al_{18.75}$	10	6.32	2050		92.4		3.5	5.0E-04	33.7	119.1	AM	CMC	749	810	61			1211	1277	0.587	40	
$Zr_{56.25}Co_{21.875}Cu_{3.125}Al_{18.75}$	8	6.33	2060		91.7		1.3	5.0E-04	33.4	119.3	AM	CMC	754	811	57			1216	1284	0.587	40	
$Zr_{56.25}Co_{15.625}Cu_{9.375}Al_{18.75}$	8	6.31	2020		92.9		3.2	5.0E-04	34	116.8	AM	CMC	741	807	66			1204	1270	0.583	40	
$Zr_{56.25}Co_{12.5}Cu_{12.5}Al_{18.75}$	5	6.3	2020		90		2	5.0E-04	32.8	115.6	AM	CMC	735	798	63			1190	1242	0.592	40	
$Zr_{56}Co_{28}Al_{16}$	2		1880	2078		2	3.8	1.0E-04			AM	CMC										[209]
$Zr_{56}Co_{13}Cu_{15}Al_{16}$	2		1880			2		1.0E-04			AM	CMC										
$Zr_{56}Co_{16}Cu_{12}Al_{16}$	2		1880			2		1.0E-04			AM	CMC										
$Zr_{56}Co_{22}Cu_6Al_{16}$	2		1880			2		1.0E-04			AM	CMC										
$Zr_{56}Co_{25}Cu_3Al_{16}$	2		1880	2241		2	10.4	1.0E-04			AM	CMC										
$Zr_{56}Co_7Cu_{21}Al_{16}$	2		1880			2		1.0E-04			AM	CMC										
$Zr_{55}Co_{20}Al_{20}Cu_5$	3		1960	2200	92	2.1	0.6	2.5E-03			AM	CMC	750	830	80					> 0,6	40	[223]

Table B-3: Mechanical and thermal data gathered from literature for Zr-Co-(Cu, Fe)-Al BMGs.

Zr-Co-Al + Other alloying elements

Comp.	Dc / used (mm)	Density (g/cm3)	Mechanical										Elaboration									Ref
			σy (Mpa)	σmax (Mpa)	E	ε e (%)	ε p (%)	Strain rate (s-1)	G (Gpa)	K (Gpa)	Poisson ratio	HV	Fusion	Casting	Tg (K)	Tx (K)	ΔT (K)	Tm (K)	Tl (K)	Tg/Tl	Heating rate (K/s)	
$Zr_{56}Co_{28}Al_{16}$	3												AM	CMC	738	793	55				20	[206]
$Zr_{56}Co_{28}Al_{16}$	3												AM	CMC	738	793	55				20	
$Zr_{49.84}Co_{24.92}Al_{14.24}Ag_{11}$	3												AM	CMC	751	796	45				20	
$Zr_{51.52}Co_{25.76}Al_{14.72}Ag_{8}$	3												AM	CMC	743	790	47				20	
$Zr_{54.32}Co_{27.16}Al_{15.52}Ag_{3}$	3												AM	CMC	741	791	50				20	
$Zr_{49.84}Co_{24.92}Al_{14.24}Ag_{11}$	3												AM	CMC	751	796	45				20	
$Zr_{51.52}Co_{25.76}Al_{14.72}Ag_{8}$	3												AM	CMC	743	790	47				20	
$Zr_{54.32}Co_{27.16}Al_{15.52}Ag_{3}$	3												AM	CMC	741	791	50				20	
$Zr_{53}Co_{31}Al_{16}$	3	6.48	1980	2170	93	2	1.8	2.1E-04				550	AM	CMC	752	812	60		1303	0.577	20	[121]
$Zr_{53}Co_{31}Al_{16}Au_{5}$	5	6.85	2170	2310	95	2	4	2.1E-04				570	AM	CMC	777	833	56		1249	0.622	20	
$Zr_{53}Co_{31}Al_{16}Pd_{5}$	5	6.55	2080	2230	93	2	2.1	2.1E-04				570	AM	CMC	769	809	40		1267	0.607	20	
$Zr_{53}Co_{31}Al_{16}Pt_{5}$	5	6.9	2130	2230	97	2	1.6	2.1E-04				565	AM	CMC	773	806	33		1266	0.611	20	
$Zr_{55}Co_{25}Al_{15}Nb_{5}$	2.5			2100	98	2.9	0.9	3.3E-04				550	AM	CMC	740	790	50				40	[150]
$Zr_{55}Co_{25}Al_{15}Nb_{5}$	2.5			2100	98	2.9	0.9	3.3E-04				550	AM	CMC	740	790	50				40	
$Zr_{55}Co_{25}Al_{17.5}Nb_{2.5}$	3.5			2100	98	2.9	0.9	3.3E-04				550	AM	CMC	745	810	65				40	
$Zr_{55}Co_{25}Al_{17.5}Nb_{2.5}$	3.5			2100	98	2.9	0.9	3.3E-04				550	AM	CMC	745	810	65				40	
$Zr_{53}Co_{31}Al_{16}$	3		1980	2170	93	2	1.8	2.1E-04	34	116	0.366	550	AM	ICCM	752	812	60		1303	0.577	20	[211]
$Zr_{53}Co_{23.25}Al_{16}Ag_{7.75}$	20		2000	2165	94	2.1	1.2	2.1E-04	35	114	0.362	560	AM	ICCM	755	791	36		1234	0.612	20	
$Zr_{53}Co_{24.8}Al_{16}Ag_{6.2}$	16		2000	2170	93	2.2	1.4	2.1E-04	34	114	0.364	542	AM	ICCM	754	792	38		1234	0.611	20	
$Zr_{53}Co_{21.7}Al_{16}Ag_{9.3}$	16		1985	2180	93	2.1	1.1	2.1E-04	34	112	0.361	555	AM	ICCM	756	791	35		1234	0.613	20	
$Zr_{53}Co_{18.6}Al_{16}Ag_{12.4}$	14		2000	2160	93	2.1	0.8	2.1E-04	34	111	0.36	557	AM	ICCM	759	790	31		1231	0.617	20	
$Zr_{53}Co_{18.5}Al_{23.5}Ag_{5}$	10												AM	CMC	776	839	63	1185	1245	0.623	20	[259]
$Zr_{53}Co_{20.5}Al_{23.5}Ag_{3}$	5												AM	CMC	773	839	66	1189	1297	0.596	20	
$Zr_{53}Co_{16.5}Al_{23.5}Ag_{7}$	5												AM	CMC	770	830	60	1215	1261	0.61	20	
$Zr_{53}Co_{14.5}Al_{23.5}Ag_{9}$	5												AM	CMC	769	821	52	1195	1265	0.608	20	
$Zr_{53}Co_{23.5}Al_{23.5}$	3												AM	CMC	772	841	69	1217	1296	0.596	20	
$Zr_{53.35}Co_{19.4}Cu_{4.85}Al_{19.4}Ag_{3}$	16		2010	2210	98		1.4	2.1E-04					AM	ICCM	740	805	65	1178	1246	0.59	20	[260]
$Zr_{52.25}Co_{19}Cu_{4.75}Al_{19}Ag_{5}$	16		2000	2170	98		1	2.1E-04					AM	ICCM	747	806	59	1174	1220	0.61	20	
$Zr_{51.15}Co_{18.6}Cu_{4.65}Al_{18.6}Ag_{7}$	14		2100	2280	100		0.6	2.1E-04					AM	ICCM	753	806	53	1169	1220	0.62	20	
$Zr_{54.45}Co_{19.8}Cu_{4.95}Al_{19.8}Ag_{1}$	10		2080	2180	102		2.5	2.1E-04					AM	ICCM	739	813	74	1194	1275	0.58	20	
$Zr_{55}Co_{20}Al_{20}Nb_{5}$	2												AM	ICCM	728	790	62				20	[159]
$Zr_{55}Co_{22.5}Al_{20}Nb_{2.5}$	3												AM	ICCM	735	805	70				20	
$Zr_{55}Co_{25}Al_{20}$	5												AM	ICCM	746	821	75				20	
$Zr_{56}Co_{23}Al_{16}Nb_{5}$	2		1900	2000		1.5	3.5	5.0E-04					AM	ICCM	724	776	51.8	1196	1225		20	[157]
$Zr_{56}Co_{25}Al_{16}Nb_{3}$	2		1850	2000		1.5	1	5.0E-04					AM	ICCM	724	782	57.9	1205.1	1236		20	
$Zr_{56}Co_{27}Al_{16}Nb_{1}$	2		2100	2150		1.5	0.2	5.0E-04					AM	ICCM	731	790	59.2	1218.7	1250		20	
$Zr_{53.76}Co_{26.88}Al_{15.36}Nb_{4}$	Ribbon												AM	MS				920	1220	1240	20	[172]
$Zr_{54.88}Co_{27.44}Al_{15.68}Nb_{2}$	Ribbon												AM	MS				920	1220	1240	20	
$Zr_{56}Co_{28}Al_{16}$	Ribbon												AM	MS				920	1220	1240	20	

Table B-4: Mechanical and thermal data gathered from literature for Zr-Co-Al-(Ag, Au, Pd, Pt, Nb) BMGs.

Comp.	Dc / used (mm)	Density (g/cm3)	Polarisation					Elaboration		Thermal									Ref
			E corr (V)	E pit (V)	Passive region (V)	Solution	Passivation current (A)	Fusion	Casting	Tg (K)	Tx (K)	ΔT (K)	Tp1 (K)	Tp2 (K)	Tm (K)	Tl (K)	Tg/Tl	Heat. rate (K/s)	
$Zr_{56}Co_{28}Al_{16}$	3		-0.23			0,5 M NaCl open to air pH 7		AM	CMC	738	793	55						20	[206]
$Zr_{56}Co_{28}Al_{16}$	3		-0.1	No pitting		1 M H2SO4 open to air pH <0,5		AM	CMC	738	793	55						20	
$Zr_{49.84}Co_{24.92}Al_{14.24}Ag_{11}$	3		-0.05		0.22	0,5 M NaCl open to air pH 7		AM	CMC	751	796	45						20	
$Zr_{51.52}Co_{25.76}Al_{14.72}Ag_{8}$	3		-0.1		0.17	0,5 M NaCl open to air pH 7		AM	CMC	743	790	47						20	
$Zr_{54.32}Co_{27.16}Al_{15.52}Ag_{3}$	3		-0.12			0,5 M NaCl open to air pH 7		AM	CMC	741	791	50						20	
$Zr_{49.84}Co_{24.92}Al_{14.24}Ag_{11}$	3		0.19	No pitting		1 M H2SO4 open to air pH <0,5		AM	CMC	751	796	45						20	
$Zr_{51.52}Co_{25.76}Al_{14.72}Ag_{8}$	3		0.12	No pitting		1 M H2SO4 open to air pH <0,5		AM	CMC	743	790	47						20	
$Zr_{54.32}Co_{27.16}Al_{15.52}Ag_{3}$	3		0.1	No pitting		1 M H2SO4 open to air pH <0,5		AM	CMC	741	791	50						20	
$Zr_{53}Co_{31}Al_{16}$	3	6.48	-0.53	0.03	0.56	PBS		AM	CMC	752	812	60				1303	0.577	20	[121]
$Zr_{53}Co_{31}Al_{16}Au_{5}$	5	6.85	-0.29	0.09	0.38	PBS		AM	CMC	777	833	56				1249	0.622	20	
$Zr_{53}Co_{31}Al_{16}Pd_{5}$	5	6.55	-0.18	0.06	0.24	PBS		AM	CMC	769	809	40				1267	0.607	20	
$Zr_{53}Co_{31}Al_{16}Pt_{5}$	5	6.9	-0.21	0.49	0.7	PBS		AM	CMC	773	806	33				1266	0.611	20	
$Zr_{55}Co_{25}Al_{15}Nb_{5}$	2.5		-0.41	0.42		3% mass NaCl open to air 25°C	5.0E-05	AM	CMC	740	790	50						40	[150]
$Zr_{55}Co_{25}Al_{15}Nb_{5}$	2.5		-0.2	1.5		1 N H2SO4 open to air 25°C	1.0E-05	AM	CMC	740	790	50						40	
$Zr_{55}Co_{25}Al_{17.5}Nb_{2.5}$	3.5		-0.45	0.1		3% mass NaCl open to air 25°C	5.0E-05	AM	CMC	745	810	65						40	
$Zr_{55}Co_{25}Al_{17.5}Nb_{2.5}$	3.5		-0.27	1.5		1 N H2SO4 open to air 25°C	1.0E-05	AM	CMC	745	810	65						40	
$Zr_{53}Co_{31}Al_{16}$	3		-0.52	0.02		PBS 37°C with 4 vol% N2O2	3.0E-06	AM	ICCM	752	812	60				1303	0.577	20	[211]
$Zr_{53}Co_{24.8}Al_{16}Ag_{6.2}$	16		-0.4	0.22		PBS 37°C with 4 vol% N2O2	5.0E-06	AM	ICCM	754	792	38				1234	0.611	20	
$Zr_{53}Co_{27.9}Al_{16}Ag_{3.1}$	3		-0.42	0.11		PBS 37°C with 4 vol% N2O2	4.0E-06	AM	ICCM										
$Zr_{53}Co_{23.25}Al_{16}Ag_{7.75}$	3		-0.39	0.23		PBS 37°C with 4 vol% N2O2	5.0E-06	AM	ICCM										
$Zr_{53}Co_{16.5}Al_{23.5}Ag_{7}$	5		0.18	0.8	0.62	PBS 37°C pH 7,4	2.9E-07	AM	CMC	770	830	60			1215	1261	0.61	20	[259]
$Zr_{53}Co_{14.5}Al_{23.5}Ag_{9}$	5					PBS 37°C pH 7,4		AM	CMC	769	821	52			1195	1265	0.608	20	
$Zr_{53}Co_{23.5}Al_{23.5}$	3		-0.2	0	0.2	PBS 37°C pH 7,4	1.0E-05	AM	CMC	772	841	69			1217	1296	0.596	20	
$Zr_{55}Co_{20}Al_{20}Nb_{5}$	2		-0.42	0.6		Hank's balanced salt solution 37°C	8.0E-06	AM	ICCM										[159]
$Zr_{55}Co_{20}Al_{20}Nb_{5}$	2		-0.47	0.52		PBS 37°C	8.0E-06	AM	ICCM										
$Zr_{55}Co_{22.5}Al_{20}Nb_{2.5}$	3		-0.56	0.51		Hank's balanced salt solution 37°C	8.0E-06	AM	ICCM										
$Zr_{55}Co_{22.5}Al_{20}Nb_{2.5}$	3		-0.5	0.33		PBS 37°C	8.0E-06	AM	ICCM										
$Zr_{55}Co_{25}Al_{20}$	5		-0.6	0.23		Hank's balanced salt solution 37°C	8.0E-06	AM	ICCM										
$Zr_{55}Co_{25}Al_{20}$	5		-0.55	0.125		PBS 37°C	8.0E-06	AM	ICCM										
$Zr_{56}Co_{27}Al_{16}Nb_{1}$	2		-0.6	0	0.6	0,114 M NaCl 37°C open to air	3.0E-06	AM	ICCM										[157]
$Zr_{56}Co_{25}Al_{16}Nb_{3}$	2		-0.6	0.18	0.78	0,114 M NaCl 37°C open to air	3.0E-06	AM	ICCM										
$Zr_{56}Co_{23}Al_{16}Nb_{5}$	2		-0.6	0.4	1	0,114 M NaCl 37°C open to air	3.0E-06	AM	ICCM										
$Zr_{56}Co_{27}Al_{16}Nb_{1}$	2		-0.25	1.25	1.5	0,2 M PBS 37°C open to air	5.0E-06	AM	ICCM										
$Zr_{56}Co_{25}Al_{16}Nb_{3}$	2		-0.25	1.25	1.5	0,2 M PBS 37°C open to air	5.0E-06	AM	ICCM										
$Zr_{56}Co_{23}Al_{16}Nb_{5}$	2		-0.25	1.25	1.5	0,2 M PBS 37°C open to air	5.0E-06	AM	ICCM										
$Zr_{56}Co_{27}Al_{16}Nb_{1}$	2		-0.6	0.2	0.8	Hanks's solution with pH 7,4 and 37°C open to air	5.0E-06	AM	ICCM										
$Zr_{56}Co_{25}Al_{16}Nb_{3}$	2		-0.6	0.55	1.15	Hanks's solution with pH 7,4 and 37°C open to air	5.0E-06	AM	ICCM										
$Zr_{56}Co_{23}Al_{16}Nb_{5}$	2		-0.6	0.7	1.3	Hanks's solution with pH 7,4 and 37°C open to air	5.0E-06	AM	ICCM										
$Zr_{56}Co_{28}Al_{16}$	Ribbon		-0.004			Hanks' solution pH 7,4 open to air	1.1E-05	AM	MS									20	[173]
$Zr_{54.88}Co_{27.44}Al_{15.68}Y_{2}$	Ribbon		-0.037			Hanks' solution pH 7,4 open to air	7.8E-06	AM	MS									20	
$Zr_{53.76}Co_{26.88}Al_{15.36}Y_{4}$	Ribbon		-0.018			Hanks' solution pH 7,4 open to air	7.6E-06	AM	MS									20	
$Zr_{53.76}Co_{26.88}Al_{15.36}Nb_{4}$	Ribbon		-0.167			Hanks' solution pH 7,4 open to air	3.1E-06	AM	MS					775	920	1220	1240	20	[172]
$Zr_{54.88}Co_{27.44}Al_{15.68}Nb_{2}$	Ribbon		-0.189			Hanks' solution pH 7,4 open to air	5.4E-06	AM	MS					775	920	1220	1240	20	
$Zr_{56}Co_{28}Al_{16}$	Ribbon		-0.248			Hanks' solution pH 7,4 open to air	1.2E-05	AM	MS					775	920	1220	1240	20	

Table B-5: Polarisation and thermal data gathered from literature for Zr-Co-Al-(Ag, Au, Pd, Pt, Nb, Y) BMGs.

C. Summary of the composition used in Chapter III.1.1

Zr	Cu	Al	Ref
55	35	10	Chen *et al.* 2015 [217]
55	35	10	Fan *et al.* 2006 [196]
60	30	10	Georgarakis *et al.* 2015 [60]
44	51	5	Wang *et al.* 2005 [195]
45	49	6	Wang *et al.* 2005 [195]
45	50	5	Wang *et al.* 2005 [195]
48	46	6	Wang *et al.* 2005 [195]
49	45	6	Wang *et al.* 2005 [195]
54	38	8	Wang *et al.* 2005 [195]
56	36	8	Wang *et al.* 2005 [195]
47,25	47,25	5,5	Wang *et al.* 2020 [201]
49,25	45,25	5,5	Wang *et al.* 2020 [201]
51,25	43,25	5,5	Wang *et al.* 2020 [201]
53,25	41,25	5,5	Wang *et al.* 2020 [201]
55,25	39,25	5,5	Wang *et al.* 2020 [201]
45	45	10	Wu *et al.* 2011 [165]
45,5	45,5	9	Wu *et al.* 2011 [165]
46	46	8	Wu *et al.* 2011 [165]
46,5	46,5	7	Wu *et al.* 2011 [165]
47	47	6	Wu *et al.* 2011 [165]
47,5	47,5	5	Wu *et al.* 2011 [165]
48	48	4	Wu *et al.* 2011 [165]
48,5	48,5	3	Wu *et al.* 2011 [165]
47,5	42,5	10	Yokoyama *et al.* 2007 [198]
50	37,5	12,5	Yokoyama *et al.* 2007 [198]
50	40	10	Yokoyama *et al.* 2007 [198]
50	42,5	7,5	Yokoyama *et al.* 2007 [198]
50	45	5	Yokoyama *et al.* 2007 [198]
52,5	37,5	10	Yokoyama *et al.* 2007 [198]
55	35	10	Yokoyama *et al.* 2007 [198]
60	30	10	Yokoyama *et al.* 2007 [198]
45	45	10	Yu *et al.* 2008 [199]
46	46	8	Yu *et al.* 2008 [199]
47	47	6	Yu *et al.* 2008 [199]
47,25	47,25	5,5	Yu *et al.* 2008 [199]
47,5	47,5	5	Yu *et al.* 2008 [199]
47,75	47,75	4,5	Yu *et al.* 2008 [199]
48	48	4	Yu *et al.* 2008 [199]
50	50	0	Yu *et al.* 2008 [199]
65	27,5	7,5	Zhang *et al.* 1991 [197]
50	40	10	Zhang *et al.* 2006 [200]

Zr	Ni	Al	Ref
60	20	20	Inoue *et al.* 1991 [261]
60	25	15	Inoue *et al.* 1991 [261]
65	20	15	Inoue *et al.* 1991 [261]
65	25	10	Inoue *et al.* 1991 [261]

Zr	Fe	Al	Ref
67	24	9	Tabeshian *et al.* 2019 [203]
68	22	10	Tabeshian *et al.* 2019 [203]
69	19	12	Tabeshian *et al.* 2019 [203]
69	22	9	Tabeshian *et al.* 2019 [203]
70	20	10	Tabeshian *et al.* 2019 [203]
70	22	8	Tabeshian *et al.* 2019 [203]
71	20	9	Tabeshian *et al.* 2019 [203]
71	21	8	Tabeshian *et al.* 2019 [203]
72	19	9	Tabeshian *et al.* 2019 [203]
73	18	9	Tabeshian *et al.* 2019 [203]
72.5	17.5	10	Tabeshian *et al.* 2019 [203]
65	15	20	Zhang *et al.* 2002 [202]
70	15	15	Zhang *et al.* 2002 [202]
70	17.5	12.5	Zhang *et al.* 2002 [202]
75	15	10	Zhang *et al.* 2002 [202]
75	17.5	7.5	Zhang *et al.* 2002 [202]
72.5	17.5	10	Zhang *et al.* 2002 [202]

Zr	Ni	Al	Ref
70	20	10	Inoue *et al.* 1991 [261]
54	25	21	Li *et al.* 2012 [204]
54	27	19	Li *et al.* 2012 [204]
55	30	15	Li *et al.* 2012 [204]
56	23	21	Li *et al.* 2012 [204]
56	25	19	Li *et al.* 2012 [204]
56	27	17	Li *et al.* 2012 [204]
57	30	13	Li *et al.* 2012 [204]
58	21	21	Li *et al.* 2012 [204]
58	23	19	Li *et al.* 2012 [204]
58	25	17	Li *et al.* 2012 [204]
58	27	15	Li *et al.* 2012 [204]
60	21	19	Li *et al.* 2012 [204]
60	23	17	Li *et al.* 2012 [204]
60	25	15	Li *et al.* 2012 [204]
60	27	13	Li *et al.* 2012 [204]
62	21	17	Li *et al.* 2012 [204]
62	23	15	Li *et al.* 2012 [204]
62	25	13	Li *et al.* 2012 [204]
62	27	11	Li *et al.* 2012 [204]
64	21	15	Li *et al.* 2012 [204]
64	23	13	Li *et al.* 2012 [204]
64	25	11	Li *et al.* 2012 [204]
64	27	9	Li *et al.* 2012 [204]
66	23	11	Li *et al.* 2012 [204]
67	21	12	Li *et al.* 2012 [204]
67	25	8	Li *et al.* 2012 [204]

Zr	Co	Al	Ref	Zr	Co	Al	Ref
50	25	25	Hasegawa *et al.* 2005 [210]	60	26,7	13,3	Zhang *et al.* 2004 [213]
55	25	20	Hasegawa *et al.* 2005 [210]	61,2	19,4	19,4	Zhang *et al.* 2004 [213]
53	31	16	Hua *et al.* 2011 [211]	56	24	20	Qin *et al.* 2015 [215]
52	25	23	Dong *et al.* 2019 [212]	56	28	16	Qin *et al.* 2015 [215]
55	25	20	Dong *et al.* 2019 [212]	56	32	12	Qin *et al.* 2015 [215]
55	25	20	Pang *et al.* 2003 [150]	55	25	20	Lu *et al.* 2012 [159]
50	30	20	Zhang *et al.* 2004 [223]	51	33	16	Yu *et al.* 2018 [205]
55	25	20	Zhang *et al.* 2004 [223]	52	32	16	Yu *et al.* 2018 [205]
60	20	20	Zhang *et al.* 2004 [223]	53	31	16	Yu *et al.* 2018 [205]
70	10	20	Zhang *et al.* 2004 [223]	54	30	16	Yu *et al.* 2018 [205]
56	26	18	Tan *et al.* 2012 [222]	55	29	16	Yu *et al.* 2018 [205]
56	28	16	Tan *et al.* 2012 [222]	56	28	16	Yu *et al.* 2018 [205]
56	30	14	Tan *et al.* 2012 [222]	57	27	16	Yu *et al.* 2018 [205]
56	32	12	Tan *et al.* 2012 [222]	58	26	16	Yu *et al.* 2018 [205]
56	28	16	Tan *et al.* 2011 [18]	53	23,5	23,5	Zhang *et al.* 2010 [259]
56	28	16	Cao *et al.* 2012 [214]	50	30	20	Zhang *et al.* 2002 [202]
55	25	20	Wada *et al.* 2009 [176]	55	25	20	Zhang *et al.* 2002 [202]
55	28	17	Wada *et al.* 2009 [176]	60	20	20	Zhang *et al.* 2002 [202]
56	28	16	Wada *et al.* 2009 [176]	70	10	20	Zhang *et al.* 2002 [202]
57	27	16	Wada *et al.* 2009 [176]	53	23,5	23,5	Zhang *et al.* 2004 [213]
57	28	15	Wada *et al.* 2009 [176]	54	24	22	Zhang *et al.* 2004 [213]
57	29	14	Wada *et al.* 2009 [176]	54,4	22,8	22,8	Zhang *et al.* 2004 [213]
58	28	14	Wada *et al.* 2009 [176]	55	25	20	Zhang *et al.* 2004 [213]
55	17	28	Wada *et al.* 2002 [187]	55,4	22,3	22,3	Zhang *et al.* 2004 [213]
55	21	24	Wada *et al.* 2002 [187]	55,8	19,4	24,8	Zhang *et al.* 2004 [213]
55	25	20	Wada *et al.* 2002 [187]	57,5	16,9	25,6	Zhang *et al.* 2004 [213]
55	29	16	Wada *et al.* 2002 [187]	57,6	21,2	21,2	Zhang *et al.* 2004 [213]
55	33	12	Wada *et al.* 2002 [187]	58,6	26	15,4	Zhang *et al.* 2004 [213]
56	28	16	Qiao *et al.* 2014 [129]	60	20	20	Zhang *et al.* 2004 [213]
56	28	16	Tan *et al.* 2012 [207]	56	28	16	Hu *et al.* 2014 [206]
56,25	25	18,75	Han *et al.* 2017 [208]	56	28	16	Hu *et al.* 2014 [206]
56	28	16	Liu *et al.* 2013 [209]	53	31	16	Hua *et al.* 2017 [121]

Table C-1: summary of the ternary compositions used in Chapter III.1.1.

D. Calculation of the mismatch entropy

Mismatch entropy can be calculated as follows:

$$S_\sigma = k_B\left[\frac{3}{2}(\zeta^2-1)y_1 + \frac{3}{2}(\zeta-1)^{2y_2} - \left\{\frac{1}{2}(\zeta-1)(\zeta-3) + ln\zeta\right\}(1-y_3)\right]$$

$$\zeta = {}^{1}/_{(1-\xi)}$$

$$y_1 = \frac{1}{\sigma^3}\sum_{j>i=1}^{4}(d_i+d_j)(d_i-d_j)^2 c_i c_j$$

$$y_2 = \frac{\sigma^2}{(\sigma^3)^2}\sum_{j>i=1}^{4} d_i d_j (d_i-d_j)^2 c_i c_j$$

$$y_3 = \frac{(\sigma^2)^3}{(\sigma^3)^2}$$

$$\sigma^k = \sum_{i=1}^{4} c_i d_i^k \; ; k = 2,\ 3$$

where c_i is the atomic fraction of the i constituent and d_i is its atomic diameter, k_B is the Boltzmann constant (1.38 x 10^{-23} $m^2.kg.s^{-2}.K^{-1}$) and ξ = 0.64 which is the packing fraction [219]. This last parameter is chosen based on the calculation of the dense random packing of hard perfect same-size spheres, which is 0.64. This is of course an approximation and the packing fraction in glasses should be higher.

An important question raised by this parameter is the choice of the atomic radii. Among the literature, authors have used covalent radii [262, 263], but also Goldschmidt radii [264] and empirical radii proposed by J.C. Slater [263]. It is also important when using this parameter to have in mind that effective atomic radii, for a chosen bonding-type, will change depending on the nature of the elements implied and the coordination number [221]. In other words, this parameter is very interesting but should be used with caution. The biggest difference among the several radii considered is on the aluminium atomic radius, which is in some cases bigger than the late transition metal considered (Ni, Co, Cu and Fe). Here we will consider atomic radius proposed by J.C. Slater such as: r_{Al} = 1.25 Å, r_{Ni} = 1.35 Å, r_{Co} = 1.35 Å, r_{Cu} = 1.35 Å, r_{Fe} = 1.40 Å and r_{Zr} = 1.55 Å [265].

E. Effect of the alloy/mould contact on surface crystallization of a biocompatible Zr-Co-Al bulk metallic glass

IOP Publishing Journal of Physics: Condensed Matter
J. Phys.: Condens. Matter **32** (2020) 214008 (6pp) https://doi.org/10.1088/1361-648X/ab7132

Effect of the alloy/mould contact on surface crystallisation of a biocompatible ZrCoAl bulk metallic glass

E Guérin[1,4], R Daudin[1], A Lenain[2], N Mendil[2], S Gravier[2], B Ter-Ovanessian[3], D Fabregue[3] and J-J Blandin[1]

[1] Univ. Grenoble Alpes, Grenoble INP, CNRS, SIMaP, Saint Martin d'Hères, France
[2] Vulkam Inc. Amorphous metal micro casting, Saint Martin d'Hères, France[5]
[3] INSA Lyon, CNRS, MATEIS, Villeurbanne, France

E-mail: eliott.guerin2@simap.grenoble-inp.fr

Received 31 October 2019, revised 13 January 2020
Accepted for publication 29 January 2020
Published 27 February 2020

Abstract

Casting of metallic glasses (MG) sometimes induces surface crystallisation despite the fact that the surface is expected to be the region where the cooling rate is the highest. This phenomenon has been observed on various MG, even for those with large critical diameters. Such surface crystallisation can be detrimental when the target applications are focused on surface properties, such as corrosion resistance for biomedical applications.

In this paper, a $Zr_{56}Co_{28}Al_{16}$ bulk metallic glass (BMG) with a large critical diameter was used. We reveal that samples processed using common copper-mould suction casting present surface crystallisation up to 20 μm in thickness, greatly deteriorating corrosion resistance. Using in-house highly reproducible suction casting and injection micro-casting processes, the influence of the processing parameters (mould material and temperature, working atmosphere, applied pressure) were investigated. The origin of surface crystallisation was found to arise from the complex thermal history of the alloy depending on the alloy/mould contact quality. By ensuring a tight contact between the solidifying alloy and the mould, BMG samples without crystalline surface defects were obtained.

Keywords: bulk metallic glass, surface crystallisation, casting, processing, net shape, corrosion resistance

(Some figures may appear in colour only in the online journal)

1. Introduction

Since the development of rapid cooling solidification techniques, bulk metallic glasses (BMG) have attracted much attention for industrial applications [1, 2]. Thanks to the amorphous structure and therefore the lack of defects linked to crystalline structures (e.g. dislocations, grains boundaries etc), BMG exhibit peculiar properties. Among them, one can mention high strength [3] and hardness or excellent micro moulding ability [4] (down to a few micrometers) as well as appealing biocompatibility making them of particular interest for medical applications [5]. Nowadays, cystalline metallic materials are commonly used in restoration surgeries, such as load bearing implants. Currently Ti–6Al–4V, CoCrW or 316L are most commonly used, yet they present two major drawbacks [6]:

- A low elastic limit preventing downsizing
- Higher Young's modulus compared to the one of the bone creating a stress-shielding effect and deteriorating the load transfer.

Zr-based BMG present a lower Young's modulus and a higher elastic limit compared to their crystalline counterparts. Moreover, they can reach critical diameters in the range of

[4] Author to whom any correspondence should be addressed.
[5] www.vulkam.com

several milimeters without using harmful elements such as nickel or copper [7]. But, even though properties of the bulk are very appealing, a particular focus has to be made on surface features. Indeed, biocompatibility is strongly linked to the alloy/organism interactions and therefore will be driven by surface properties, such as corrosion and wear resistance [8–11].

For a given alloy, it is known that various amounts of free volumes can be obtained depending on the processing parameters (melt temperature, cooling rates, atmosphere etc). The amount of free volume will have an influence on mechanical properties but is however not believed to play a major role on surface properties and therefore on biocompatibility. Nonetheless, such surface properties can be greatly influenced by surface defects, such as crystals. It is therefore important to investigate the surface crystallisation phenomenon that can arise during the processing of metallic glasses and has been already mentioned quite early in the literature [12, 13]. Köster explained that nucleation and accelerated growth can occur preferentially at the surface. This is justified by a decrease in the total energy, a greater ease in diffusion and stress relaxation and finally local changes in composition. Köster found out that this phenomenon is also strongly influenced by the processing conditions. The number of publications is however very scarse on the subject, and most of the papers available focus on the study of ribbons and not BMG.

Cao *et al* [14] found out that atomic surface diffusion happens 10^5 times faster than bulk diffusion at temperatures below glass transition (T_g) in a $Pd_{40}Cu_{30}Ni_{10}P_{20}$ metallic glass. They linked this behavior to the observation that fast crystallisation below T_g takes place 10^2 times faster at the surface than in the bulk.

In the 80s, Grànàsy [15] already modeled that the thermal history of the melt pool has a strong influence on the localization of quenched-in crystallites formed by homogeneous nucleation in the amorphous matrix. Depending on the quenching rate, crystallites were shown to develop (a) uniformly over the whole cross-section or localized either (b) near the free surface of the ribbon, (c) or in the center part of the ribbon (d) or at the contact surface with the wheel. More recently, Haag *et al* [16] experimentally corroborated such complicated thermal history occuring in the melt during suction casting of an AuCuAgSi BMG. Using high-speed infrared monitoring, they were able to track the temperature of the alloy in several locations during the entire casting process. They showed that the alloy undergo a complex thermal history while filling the mould cavity. They observed what they call a 'thermal rebound', meaning that during cooling, the temperature of the alloy first decreases as expected but subsquently goes up again. This 're-heating' reaches almost 100 °C in the center of the alloy. This behavior was attributed to the continuous flow of hot melt into the mould cavity. Even though this publication does not make a clear link between the thermal rebound and surface cristallization, it underlines the complexity of the cooling processes during BMG casting.

Other papers [17, 18] claim that surface crystallisation can be attributed to either heterogeneous nucleation on the mould surface or compositional changes due to carbon pollution during sample production. The thickness of the surface crystallisation ranges from 0.01 mm to 0.2 mm, depending on the alloy composition. Yet for biomedical applications requiring excellent surface properties, we believe that there is a need to adress the surface crystallisation issue on BMG during casting which is often overlooked in the community because most samples are polished before being studied.

In the present paper we investigate the influence of the processing parameters on the presence of surface crystallisation on a Zr-based BMG. For this study we used a ZrCoAl BMG, as it offers great stability and is a ternary system promising for biomedical applications.

2. Materials and method

$Zr_{56}Co_{28}Al_{16}$ (at%) primary alloys were prepared by arc melting mixtures of ultra-pure (>99.99%) Zr, Co and Al metals in argon atmosphere with a Ti getter for controlling any pollution traces. The same batch of primary material was used through all elaborations. Each primary alloy was melted at least five times to ensure a high quality of the chemical homogeneity. Two processes were then used to cast the alloy:

- Suction casting: the primary alloy is melted using an electric arc under argon atmosphere (Ti-gettered) and then casted using pressure difference between the crucible and the mould cavity. Plate-shaped samples with dimensions of $55 \times 15 \times 2\,mm^3$ and 5 mm-diameter rods were produced.
- Injection casting: the primary alloy is melted via induction under controlled atmosphere (vacuum or any gas) and then pushed inside the mould cavity by a plunger. Plate-shaped samples with dimensions of $15 \times 8 \times 1\,mm^3$ were produced.

Electrochemical measurements were performed using a Gamry 600+ potentiostat. The working electrode is the ZrCoAl BMG alloy, the reference electrode is Ag/AgCl, the counter electrode is graphite and finally the electrolyte is an aqueous solution of NaCl 9 g l^{-1} at 37 °C. This configuration is based on the ISO 10271. Tested samples undergo a 2 h open circuit potential (OCP) before the polarization curve. The scanning rate is 1 mV s^{-1} and the scan is performed from −150 mV below the OCP value up to 1 V versus Ag/AgCl.

The amorphous or crystalline structure of each sample was controlled by x-ray diffraction (XRD) measurements using a PANalytical equipment with Cu-Kα radiation. XRD measurements were performed both on the as-cast surface and on the bulk part of the samples, after polishing. The glass transition temperature ($T_g = 450$ °C) and the crystallisation temperature ($T_x = 520$ °C) were determined using differential scanning calorimetry (DSC) on a Melter set-up, at a heating rate of 20 °C min^{-1}.

The optical observations were carried out on the polished cross sections of samples using an opto-digital Microscope Olympus DSX 500 with a differential interference contrast

J. Phys.: Condens. Matter **32** (2020) 214008 E Guérin *et al*

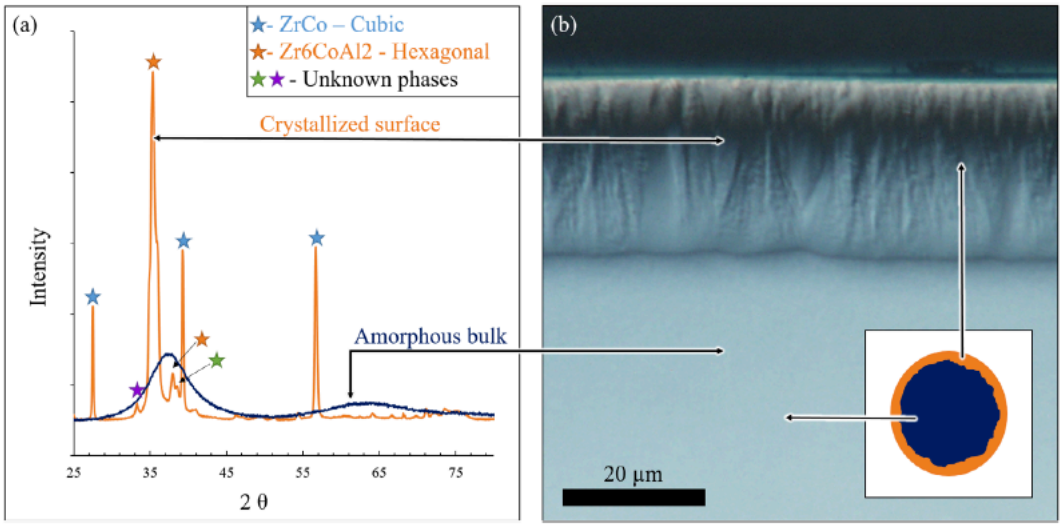

Figure 1. (a) XRD measurements of the as-cast surface and the bulk, (b) optical observation of the cross-section of a 5 mm in diameter rod produced using suction casting. The inset is a schematic representation of the repartition of the crystallised area (orange) on the cross-section of such rods.

mode (DIC). Indeed, DIC utilizes a special type of optical prism to produce a much-improved pseudo-3D shadow image of crystal phases. In that way, crystallisation is better revealed compared to conventional optical observations. Cross-section surfaces were investigated by scanning electron microscopy using a Zeiss ultra 55 SEM-FEG operating at 15 kV for energy dispersive x-ray spectroscopy (EDXS) analyses.

3. Results and discussion

The XRD patterns of the as-cast and polished-to-the-bulk Zr–Co–Al alloys prepared via arc melting/suction casting are shown in figure 1(a). The measurement on the as-cast surface indicates the presence of several crystalline phases (multiple peaks) whereas the measurement on the bulk (more than 0.1 mm removed from the surface via polishing) does not show the presence of any peak. This confirms the presence of a crystallised outer layer on Zr–Co–Al samples prepared via suction casting while the bulk remains amorphous. This layer can be directly observed through optical microscopy as shown in figure 1(b). The homogeneous phase at the bottom of the image corresponds to the amorphous part while the columnar like phase at the top of the image corresponds to the crystallised layer. The crystallised layer has been measured up to 20 μm in thickness.

We compared the peaks' positions from the XRD measurements to previous XRD measurements performed on the same alloy annealed via DSC (DSC,10 K $\cdot$ min^{-1}) and data taken from the literature [19, 20]. The most common crystalline phases associated with this Zr–Co–Al BMG alloy are ZrCo, $ZrCo_2Al$ and Zr_6CoAl_2. Even though we were able to identify some of those phases on samples annealed via DSC, there was no direct match with peaks obtained on the crystallised outer layer. This would imply either a difference on the lattice parameter or the nucleation of new phases.

Figure 2 shows polarisation curves obtained on the ZrCoAl alloy as-cast surface and bulk. This illustrates how crystalline phases at the surface of an amorphous samples deteriorate surface properties. While currents on the passive plateau are the same, corrosion and pitting potentials are different. Testing only the amorphous structure allows the shift of pitting potential to higher potential, improving the corrosion resistance. The pitting phenomenon is catastrophic in the case of the crystallised layer while there is no clear breakdown of the passivation layer on the amorphous bulk.

Compositions of the samples were investigated using EDXS analysis but no composition shift was observed compared to the targeted one (under EDXS uncertainties). Such possible cause for surface crystallisation [18] can therefore be ruled out. Also, because the $Zr_{56}Co_{28}Al_{16}$ is a stable alloy with a large critical diameter, a small composition shift should not lead to crystallisation.

Looking for the process parameters that could prevent/promote crystallisation we kept the same method for the preparation of primary alloys and we used an injection casting set up as our suction casting set up is not fitted for parameter tuning. This set-up is specifically designed to be adaptable which allowed us to control each parameter individually. The tested parameters are the following:

- Mould material: copper and tungsten
- Mould temperature: room temperature mould and heated mould
- Chamber atmosphere: argon and vacuum.

Different configurations have been tested and are summed up in table 1. The corresponding XRD analysis of the samples surfaces are shown in figure 3.

Test one concerns the mould temperature. Copper was kept as mould material but the mould was heated. The copper mould was heated up to 250 °C. With a higher temperature,

J. Phys.: Condens. Matter **32** (2020) 214008 E Guérin *et al*

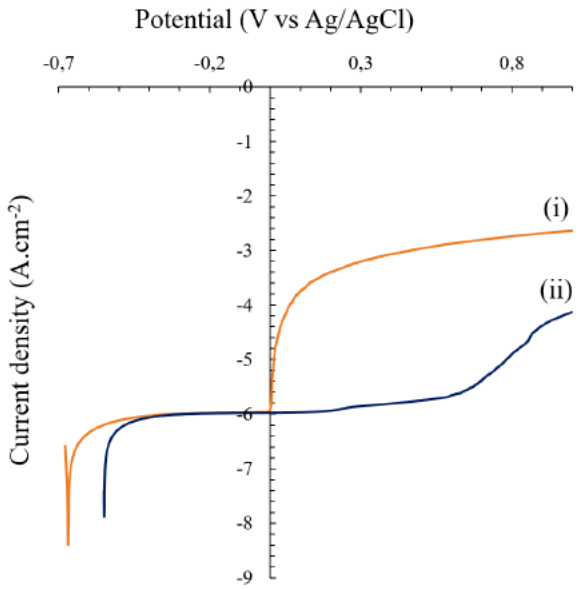

Figure 2. Polarisation curves of the ZrCoAl alloy in a NaCl 9 g l^{-1} aqueous solution at 37 °C: (i) crystallised surface and (ii) amorphous bulk.

Table 1. Parameters used for different injection casting conditions.

	Mould material	Mould temperature	Atmosphere
Test 1	Copper	HT	Argon
Test 2	Copper	RT	Vacuum
Test 3	Copper	HT	Vacuum
Test 4	Tungsten	HT	Vacuum

HT = high temperature, RT = room temperature.

we would have risked damaging the mould at the metal/mould interface (the melting temperature of copper is 1085 °C). This would rise the interface temperature between the alloy and the mould. Test two investigates the influence of the atmosphere. The mould temperature is set back to room temperature, as it was in the suction casting set up. Test three is a combination of tests one and two. Finally, in test four, we used a different material for the mould, to test the hypothesis according which copper is the source for surface crystallisation. We chose tungsten for its high thermal conductivity. Before the injection, the mould is heated to 400 °C, to get closer to the interface temperature in the suction casting process. The entire process takes place under vacuum.

It can be seen from tests one and two that no surface crystallisation is observed either under high vacuum or with a heated copper mould, suggesting that the absence of surface crystallisation does not rise from these parameters. This can be explained by the fact that either vacuum or the mould temperature will not affect drastically the quenching rate in the early stage of cooling, especially for this composition presenting a high glass forming ability. This also ruled out the possibility that crystallisation is caused by a bad argon purity.

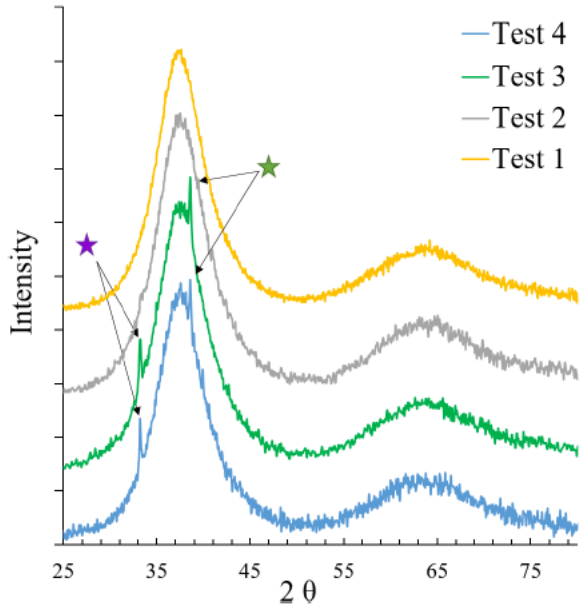

Figure 3. XRD measurements performed on the as-cast surface of the four ZrCoAl samples processed with different configurations of the modified injection set-up (see table 1).

The samples from tests three and four each present two peaks at the same locations on the XRD diagrams obtained from their surfaces. Those peaks are of rather low intensity compared to the intensity of the broad diffusion peak of the amorphous regions. Interestingly they correspond to the two unidentified peaks in figure 1 that are also of very low intensity compared to the others main surface crystallisation peaks. Still it could be a sign of surface crystallisation but of a far smaller extent compared to suction casting (figure 1). The fact that we obtained the same XRD patterns with tests three and four allowed us to rule out the hypothesis that surface crystallisation is due to heterogeneities on copper mould surfaces. Tests three and four both combine high temperature and vacuum, which are two factors promoting a bad heat extraction as heat can only be transferred via conduction.

As a result, the hypothesis of a complex thermal history remains as a valid hypothesis. Based on conclusions made by Grànàsy [15] and Haag *et al* [16] suggesting that the thermal dynamic of the melt plays a key role, we thus believe that each process results in a different thermal history of the melt and therefore of the solidified alloy. To explain this, we can split the casting process in three successive steps: filling, conformation and cooling (see figure 4). In suction casting, the melt is pushed inside the mould cavity by a pressure difference while in the injection casting process, it is pushed by a plunger. While the filling step is known to be challenging to understand [16], we believe that no significant differences arise in the melt at this stage between both processes. However, the second step is thought to be essential for the presence or not of surface crystallisation. Indeed, for the injection process, once the melt is inside the mould cavity, the plunger keeps on

J. Phys.: Condens. Matter **32** (2020) 214008 E Guérin *et al*

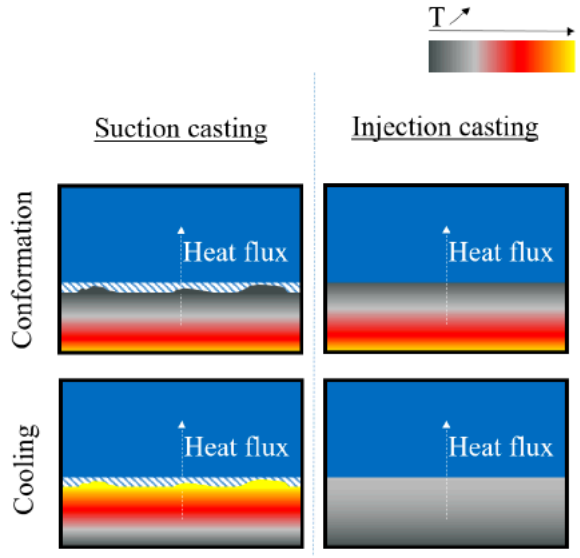

Figure 4. Schematic representation of the proposed thermal history of the melt in the suction casting process (top) and in the injection casting process (bottom) explaining the existence or not of surface crystallisation.

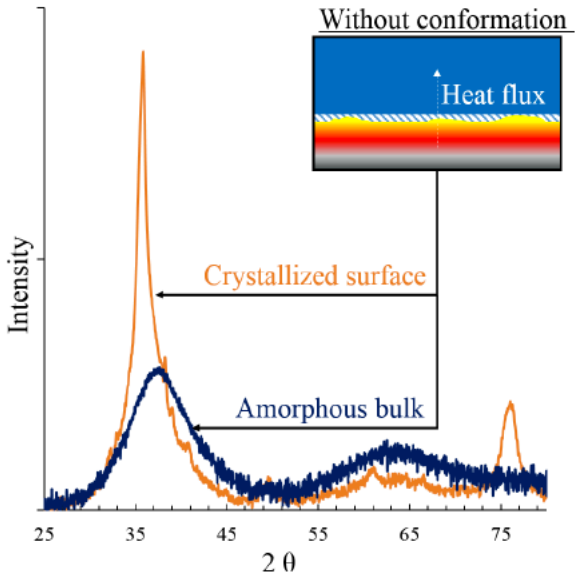

Figure 5. XRD measurements of the as-cast surface and the bulk for a ZrCoAl sample injected without conformation.

applying a pressure to the viscous melt, ensuring conformation, i.e. a complete filling of the whole cavity through a tight contact between the solidifying melt and the mould. This conformation stage does not exist in the suction casting process, because of the open end. The lack of conformation leads to a poor thermal contact between the solidifying melt and the mould (see figure 4). The heat coming from the solidifying melt pool is believed to cause an accumulation of calories near the metal/mould interface. The outer layer of the casted part which was initially quenched will undergo a temperature rise, or the so-called thermal rebound. This thermal rebound will be enough to start crystallisation locally at surface, where is has been shown that thermodynamic stability is lower [14, 21]. Unfortunately, we are not able to measure the extent of the reheating, as Haag *et al* [16], as this would require an instrumented and dedicated set-up. One can however mentioned that Li and Li [21], using atomistic simulations, showed that surface melting can happen at temperature as low as 30% below T_g. Even though such phenomenon should happen at a lower extent over 20 μm, this could imply the re-heating of the surface induced by the bad thermal contact may lead to surface remelting and re-solidification.

Nevertheless, as in the injection casting process the plunger maintains a good contact between the alloy and the mould, the thermal rebound does not take place, or at a smaller extent and therefore surface crystallisation does not occur. In order to validate this hypothesis, an injection casting test was realised without the conformation stage to deliberately deteriorate the contact between the melt and the mould and trigger surface crystallisation.

Figure 5 shows XRD measurements realized on both the surface and in the centre of a sample realized via injection casting without the conformation step. As expected, the surface shows clear signs of crystallisation, with intense and narrow peaks while the centre of the sample is completely amorphous, with no sign of partial crystallisation. It is interesting to mention that in this case, we do not observe as many peaks as with the suction casting process. This could mean that depending on the alloy/mould contact quality, i.e. on the level of re-heating, which is not fully controlled here, various crystalline phases could form. Whether surface crystallisation arises from potential quenched-in crystals [15], amorphous to crystal transformations [14] or local remelting followed by slow solidification [21] is still unclear. In order to go further in the thermodynamic history, phase identification could be necessary. In any case, it confirms that a good melt/mould contact preventing local heterogeneous thermal gradient is crucial to avoid surface crystallisation.

4. Conclusions

The effect of the suction and injection process differences on the formation of surface crystallisation of a BMG (ZrCoAl) has been investigated. Surface crystallisation occurs in the suction casting process on this alloy on a thickness up to 20 μm. The presence of crystals on the surface greatly deteriorates corrosion resistance in saline solution. This layer does not appear with injection casting.

Composition changes, influence of the mould material, mould temperature, and atmosphere have been ruled out as potential causes for surface crystallisation.

The influence of the quality of the melt/mould contact, in the conformation stage has been shown to play a key role on the presence of surface crystallisation. Samples produced without conformation exhibit surface crystallisation while samples produced with conformation are totally amorphous. This is explained by the complex thermal history of the melt.

The outer layer of the casted part, which is shown to be less stable than the bulk, undergoes re-heating after the initial quenching because of a bad metal/mould contact.

This result is important for the further work on the industrialisation of casting and micro-casting of BMG parts. It is of great importance to be able to cast near net shape parts with excellent surface finish. It would be a big step forward on the path to bring BMGs to the market. The importance of conformation also needs to be taken into account when casting complexes shapes, for which the level of conformation may vary depending on the geometry.

Acknowledgments

This work was performed as part of the AMA-MED project and the financial support from Région Auvergne Rhône-Alpes is gratefully acknowledged. The authors would also like to acknowledge the participation of Vulkam engineers in the preparation of the samples.

ORCID iDs

E Guérin https://orcid.org/0000-0002-6386-0580
R Daudin https://orcid.org/0000-0001-8922-2555
A Lenain https://orcid.org/0000-0001-6325-4276
S Gravier https://orcid.org/0000-0001-9679-501X
B Ter-Ovanessian https://orcid.org/0000-0002-1208-3689
D Fabregue https://orcid.org/0000-0002-3048-7281
J-J Blandin https://orcid.org/0000-0002-9898-5711

References

[1] Khan M M *et al* 2018 Recent advancements in bulk metallic glasses and their applications: a review *CRC Crit. Rev. Solid State Mater. Sci.* **43** 233–68
[2] Li H F and Zheng Y F 2016 Recent advances in bulk metallic glasses for biomedical applications *Acta Biomater.* **36** 1–20
[3] Schroers J, Kumar G, Hodges T M, Chan S and Kyriakides T R 2009 Bulk metallic glasses for biomedical applications *JOM* **61** 21–9
[4] Schroers J 2010 Amorphous metal alloys form like plastics *Adv. Mater.* **22** 1566–97
[5] Han K, Wang Y, Qiang J, Jiang H and Gu L 2019 Low-cost Zr-based bulk metallic glasses for biomedical devices applications *J. Non-Cryst. Solids* **520** 119442
[6] Calin M *et al* 2013 Designing biocompatible Ti-based metallic glasses for implant applications *Mater. Sci. Eng.* C **33** 875–83
[7] Hua N *et al* 2011 Ni- and Cu-free Zr–Al–Co–Ag bulk metallic glasses with superior glass-forming ability *J. Mater. Res.* **26** 539–46
[8] Geurtsen W 2002 Biocompatibility of dental casting alloys *Crit. Rev. Oral Biol. Med.* **13** 71–84
[9] Li T H *et al* 2017 Biocompatibility study on Ni-free Ti-based and Zr-based bulk metallic glasses *Mater. Sci. Eng.* C **75** 1–6
[10] Hua N *et al* 2012 Corrosion behavior and *in vitro* biocompatibility of Zr–Al–Co–Ag bulk metallic glasses: an experimental case study *J. Non-Cryst. Solids* **358** 1599–604
[11] Liu L *et al* 2009 Biocompatibility of Ni-free Zr-based bulk metallic glasses *Intermetallics* **17** 235–40
[12] Koster U W E 1988 Surface crystallisation of metallic glasses *Mater. Sci. Eng.* **97** 233–9
[13] Li Z, Shen H and He Y 1994 Surface crystallization of metallic glass $Fe_{71}Ni_3Cr_4Si_8B_{14}$ *Phys. Status Solidi* a **141** 135–44
[14] Cao C R, Lu Y M, Bai H Y and Wang W H 2015 High surface mobility and fast surface enhanced crystallisation of metallic glass *Appl. Phys. Lett.* **107** 8–12
[15] Gránásy L 1989 Models for continuous casting of metallic glass ribbons II: the effect of the melt pool on the cross-sectional homogeneity *Mater. Sci. Eng.* A **111** 129–44
[16] Haag F, Geisel S, Kurtuldu G and Löffler J F 2018 Bulk metallic glass casting investigated using high-speed infrared monitoring and complementary fast scanning calorimetry *Acta Mater.* **151** 416–23
[17] Wang X 2014 Surface crystallisation in Mg-based bulk metallic glass during copper mold casting *Adv. Mater. Sci. Eng.* **2014** 798479
[18] Abrosimova G E *et al* 2001 Crystalline layer on the surface of Zr-based bulk metallic glasses *J. Non-Cryst. Solids* **288** 121–6
[19] Wada T, Zhang T and Inoue A 2002 Formation, thermal stability and mechanical properties in Zr–Al–Co bulk glassy alloys *Mater. Trans.* **43** 2843–6
[20] Tan J *et al* 2011 Study of mechanical property and crystallisation of a ZrCoAl bulk metallic glass *Intermetallics* **19** 567–71
[21] Li Q K and Li M 2008 Surface structure and properties of NiZr model metallic glasses: a molecular dynamics simulation *J. Non-Cryst. Solids* **354** 2060–5

F. Crystalline phase labelling on the Zr-Co-Al ternary base

To identify the specific phases obtained by the crystallization of the $Zr_{56}Co_{28}Al_{16}$, we performed a systematic analysis of the phase identifications from XRD measurements on the Zr-Co-Al ternary system available in the literature. These data are available in Table F-1. The set-up used for XRD measurement at SIMaP laboratory uses the Cu Kα wavelength (0.15406 nm). The same wavelength is used predominantly for the acquisition of the data found in the literature. As the mesh parameter of a specific phase can vary (depending on a variety of factors) and impact the diffraction angle, we calculated the average angle for each contribution of each phase based on the collected data.

Ref.	Alloy	Sourc	Phase	Angle 2θ (°)	Ref.	Alloy	Sour	Phase	Angle 2θ (°)
[161, 162]	$Zr_{52,5}Co_{37,5}Al_{10}$	Cu α	ZrCo B2	27,61	[167	$Zr_{49}Co_{49}Al_2$	?	ZrCo B2	32,47
[161, 162]	$Zr_{55}Co_{31}Al_{14}$	Cu α	ZrCo B2	27,62	[166	$Zr_{48,5}Co_{48,5}Al_3$	Cu α	ZrCo B2	39,82
[161, 162]	$Zr_{55}Co_{31}Al_{14}$	Cu α	ZrCo B2	39,39	[167	$Zr_{49}Co_{49}Al_2$	?	ZrCo B2	46,66
[161, 162]	$Zr_{52,5}Co_{37,5}Al_{10}$	Cu α	ZrCo B2	39,57	[166	$Zr_{48,5}Co_{48,5}Al_3$	Cu α	ZrCo B2	49,35
[161, 162]	$Zr_{52,5}Co_{37,5}Al_{10}$	Cu α	ZrCo B2	57,05	[167	$Zr_{49}Co_{49}Al_2$	?	ZrCo B2	57,96
[161, 162]	$Zr_{55}Co_{31}Al_{14}$	Cu α	ZrCo B2	71,78	[166	$Zr_{48,5}Co_{48,5}Al_3$	Cu α	ZrCo B2	64,73
[161, 162]	$Zr_{52,5}Co_{37,5}Al_{10}$	Cu α	ZrCo B2	71,89	[167	$Zr_{49}Co_{49}Al_2$	?	ZrCo B2	68,21
[161, 162]	$Zr_{55}Co_{31}Al_{14}$	Cu α	ZrCoAl	35,34	[166	$Zr_{48,5}Co_{48,5}Al_3$	Cu α	ZrCo B2	72,2
[161, 162]	$Zr_{55}Co_{31}Al_{14}$	Cu α	ZrCoAl	37,84	[166	$Zr_{48,5}Co_{48,5}Al_3$	Cu α	ZrCo B2	85,83
[161, 162]	$Zr_{54,5}Co_{33,5}Al_{12}$	Cu α	Zr_2Al	38,11	[167	$Zr_{49}Co_{49}Al_2$	?	ZrCo B2	86,61
[161, 162]	$Zr_{54,5}Co_{33,5}Al_{12}$	Cu α	Zr_2Al	40,8	[166	$Zr_{48,5}Co_{48,5}Al_3$	Cu α	ZrCo B2	99,15
[161, 162]	$Zr_{54,5}Co_{33,5}Al_{12}$	Cu α	Zr_2Al	67,43	[167	$Zr_{49}Co_{49}Al_2$	?	ZrCo B2	104,77
[161, 162]	$Zr_{54,5}Co_{33,5}Al_{12}$	Cu α	Zr_2Co	35,39	[167	$Zr_{49}Co_{49}Al_2$	?	ZrCo B33	43,41
[161, 162]	$Zr_{54,5}Co_{33,5}Al_{12}$	Cu α	Zr_2Co	38,11	[167	$Zr_{49}Co_{49}Al_2$	?	ZrCo B33	49,9
[161, 162]	$Zr_{54,5}Co_{33,5}Al_{12}$	Cu α	Zr_2Co	45,11	[166	$Zr_{48,5}Co_{48,5}Al_3$	Cu α	Co_2Zr	44,4
[161, 162]	$Zr_{54,5}Co_{33,5}Al_{12}$	Cu α	Zr_2Co	60,67	[166	$Zr_{48,5}Co_{48,5}Al_3$	Cu α	Co_2Zr	77,81
[161, 162]	$Zr_{54,5}Co_{33,5}Al_{12}$	Cu α	Zr_2Co	66,7	[166	$Zr_{48,5}Co_{48,5}Al_3$	Cu α	Co_2Zr	92,25
[161, 162]	$Zr_{54,5}Co_{33,5}Al_{12}$	Cu α	Zr_2Co	71,5	[166	$Zr_{48,5}Co_{48,5}Al_3$	Cu α	Zr_2Co	38,17
[161, 162]	$Zr_{43}Co_{43}Al_{14}$	Cu α	$Zr_5Co_7Al_3$	35,59	[166	$Zr_{48,5}Co_{48,5}Al_3$	Cu α	Zr_2Co	57,62
[161, 162]	$Zr_{43}Co_{43}Al_{14}$	Cu α	$Zr_5Co_7Al_3$	39,05	[129	$Zr_{56}Co_{28}Al_{16}$	Cu α	?	35
[161, 162]	$Zr_{43}Co_{43}Al_{14}$	Cu α	$Zr_5Co_7Al_3$	42,1	[129	$Zr_{56}Co_{28}Al_{16}$	Cu α	?	37,51
[161, 162]	$Zr_{43}Co_{43}Al_{14}$	Cu α	$Zr_5Co_7Al_3$	42,88	[129	$Zr_{56}Co_{28}Al_{16}$	Cu α	?	39,69
[161, 162]	$Zr_{43}Co_{43}Al_{14}$	Cu α	$Zr_5Co_7Al_3$	66,22	[129	$Zr_{56}Co_{28}Al_{16}$	Cu α	?	57,43
[161, 162]	$Zr_{55}Co_{31}Al_{14}$	Cu α	Zr_6CoAl_2	35,17	[129	$Zr_{56}Co_{28}Al_{16}$	Cu α	Zr_6CoAl_2	27,86
[161, 162]	$Zr_{53,5}Co_{36,5}Al_{10}$	Cu α	Zr_6CoAl_2	35,48	[129	$Zr_{56}Co_{28}Al_{16}$	Cu α	Zr_6CoAl_2	29,38

[161, 162]	$Zr_{55}Co_{31}Al_{14}$	Cu α	Zr_6CoAl_2	37,78
[161, 162]	$Zr_{53,5}Co_{36,5}Al_{10}$	Cu α	Zr_6CoAl_2	37,94
[161, 162]	$Zr_{53,5}Co_{36,5}Al_{10}$	Cu α	Zr_6CoAl_2	39,44
[161, 162]	$Zr_{55}Co_{31}Al_{14}$	Cu α	Zr_6CoAl_2	39,62
[161, 162]	$Zr_{55}Co_{31}Al_{14}$	Cu α	Zr_6CoAl_2	44,2
[161, 162]	$Zr_{53,5}Co_{36,5}Al_{10}$	Cu α	Zr_6CoAl_2	44,88
[161, 162]	$Zr_{53,5}Co_{36,5}Al_{10}$	Cu α	Zr_6CoAl_2	54,4
[161, 162]	$Zr_{55}Co_{31}Al_{14}$	Cu α	Zr_6CoAl_2	54,6
[161, 162]	$Zr_{55}Co_{31}Al_{14}$	Cu α	Zr_6CoAl_2	57,22
[161, 162]	$Zr_{53,5}Co_{36,5}Al_{10}$	Cu α	Zr_6CoAl_2	66,61
[163]	$Zr_{53}Co_{38}Al_{19}$	Cu α	ZrCo B2	27,74
[163]	$Zr_{53}Co_{38}Al_{19}$	Cu α	ZrCo B2	39,62
[163]	$Zr_{53}Co_{38}Al_{19}$	Cu α	ZrCo B2	49,13
[163]	$Zr_{53}Co_{38}Al_{19}$	Cu α	ZrCo B2	65,08
[163]	$Zr_{53}Co_{38}Al_{19}$	Cu α	ZrCo B2	71,34
[163]	$Zr_{53}Co_{38}Al_{19}$	Cu α	Zr_6CoAl_2	35,26
[163]	$Zr_{53}Co_{38}Al_{19}$	Cu α	Zr_6CoAl_2	37,71
[163]	$Zr_{53}Co_{38}Al_{19}$	Cu α	Zr_6CoAl_2	39,5
[163]	$Zr_{53}Co_{38}Al_{19}$	Cu α	Zr_6CoAl_2	44,62
[163]	$Zr_{53}Co_{38}Al_{19}$	Cu α	Zr_6CoAl_2	66,34
[129	$Zr_{56}Co_{28}Al_{16}$	Cu α	Zr_6CoAl_2	35,05
[129	$Zr_{56}Co_{28}Al_{16}$	Cu α	Zr_6CoAl_2	37,53
[129	$Zr_{56}Co_{28}Al_{16}$	Cu α	Zr_6CoAl_2	39,73
[129	$Zr_{56}Co_{28}Al_{16}$	Cu α	Zr_6CoAl_2	44,22
[129	$Zr_{56}Co_{28}Al_{16}$	Cu α	Zr_6CoAl_2	54,64
[129	$Zr_{56}Co_{28}Al_{16}$	Cu α	Zr_6CoAl_2	55,76
[129	$Zr_{56}Co_{28}Al_{16}$	Cu α	Zr_6CoAl_2	65,79
[129	$Zr_{56}Co_{28}Al_{16}$	Cu α	Zr_6CoAl_2	72,16
[223	$Zr_{64,6}Co_{17,7}Al_{17,7}$	Cu α	ZrCo B2	30,02
[223	$Zr_{64,6}Co_{17,7}Al_{17,7}$	Cu α	ZrCo B2	58,09
[223	$Zr_{64,6}Co_{17,7}Al_{17,7}$	Cu α	ZrCo B2	71,71
[223	$Zr_{64,6}Co_{17,7}Al_{17,7}$	Cu α	ZrCoAl	37,25
[223	$Zr_{64,6}Co_{17,7}Al_{17,7}$	Cu α	ZrCoAl	38,92
[223	$Zr_{64,6}Co_{17,7}Al_{17,7}$	Cu α	Zr_6CoAl_2	22,34
[223	$Zr_{64,6}Co_{17,7}Al_{17,7}$	Cu α	Zr_6CoAl_2	25,79
[223	$Zr_{64,6}Co_{17,7}Al_{17,7}$	Cu α	Zr_6CoAl_2	34,31
[223	$Zr_{64,6}Co_{17,7}Al_{17,7}$	Cu α	Zr_6CoAl_2	37,15
[223	$Zr_{64,6}Co_{17,7}Al_{17,7}$	Cu α	Zr_6CoAl_2	38,98
[223	$Zr_{64,6}Co_{17,7}Al_{17,7}$	Cu α	Zr_6CoAl_2	43,99
[223	$Zr_{64,6}Co_{17,7}Al_{17,7}$	Cu α	Zr_6CoAl_2	47,81
[223	$Zr_{64,6}Co_{17,7}Al_{17,7}$	Cu α	Zr_6CoAl_2	53,25
[223	$Zr_{64,6}Co_{17,7}Al_{17,7}$	Cu α	Zr_6CoAl_2	55,39
[223	$Zr_{64,6}Co_{17,7}Al_{17,7}$	Cu α	Zr_6CoAl_2	60,84
[223	$Zr_{64,6}Co_{17,7}Al_{17,7}$	Cu α	Zr_6CoAl_2	65,24
[223	$Zr_{64,6}Co_{17,7}Al_{17,7}$	Cu α	Zr_6CoAl_2	68,24
[223	$Zr_{64,6}Co_{17,7}Al_{17,7}$	Cu α	Zr_6CoAl_2	69,7

Table F-1: Angle/phase correspondence for the Zr-Co-Al ternary system extracted from the literature.

G. Impact of the pile-up on nano-hardness measurement

Raw data from nano-hardness are of very high values, far higher than hardness measured through classical Vickers hardness measurements (see Figure). Microhardness gives an average Vickers hardness of 527 HV while nano-hardness gives an average value of 696 HV. As mentioned in Chapter II, an overestimation of the hardness in nano-hardness measurement could come from a pile-up effect, where the contact area is underestimated [266–268].

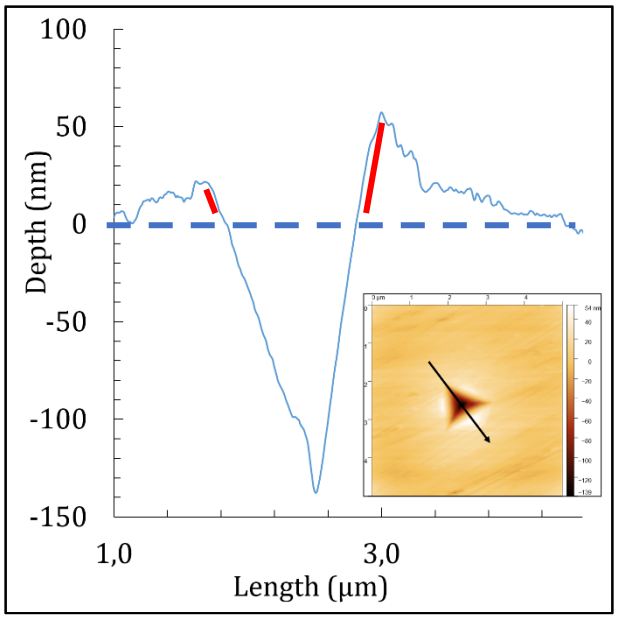

Figure G-1: depth profil over an indent in nano-hardness. Inset shows where the profile is taken (black arrow). Blue dot line shows sample surface and red lines highlight the extra contact surface from the pile-up.

The Pile-up effect was studied by using AFM on a nano-indent. Figure G-1 shows the depth profile measure via AFM while crossing over the indent (see inset). Pile-up is visible on the profile as we measure height clearly above sample surface (set at 0 nm). If we consider Berkovick's indent triangular footprint, pile-up is maximum along the triangle side (peaking at almost 60 nm). Figure G-2 shows a 3D image on the sample surface including a representative indent. From this image, it can be concluded that pile-up arises equally on the three sides of the triangular footprint. Pile-up is maximum at the middle of each side. Pile-up explains hardness over-estimation. Yet it is not of primary importance as we compare nano-hardness values acquired in the same conditions (penetration rate and maximum depth). Acquiring AFM surface plots for each indent would have been very time consuming and it was chosen not to correct the hardness absolute values but to work with normalized values

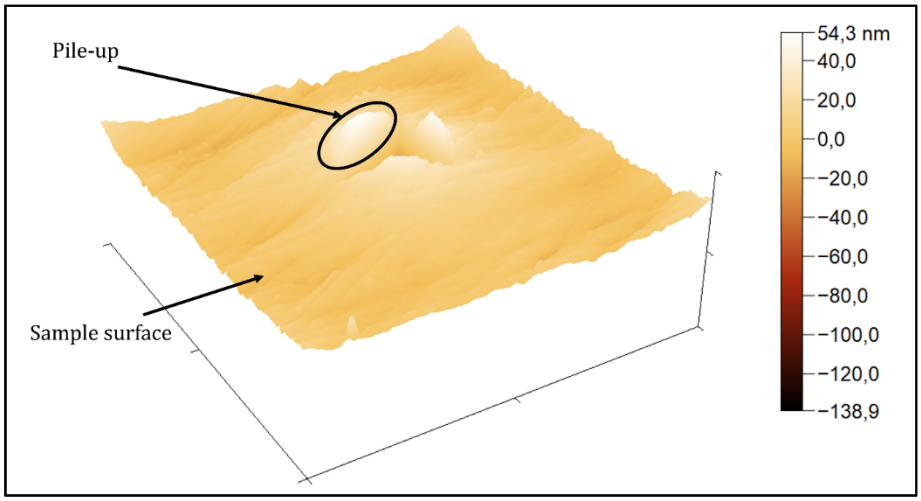

Figure G-2: 3D-image from the sample surface (AFM measurement) showing the pile up around the indent.

H. Serrated behaviour analysis of Nb0, Nb1 and Nb2

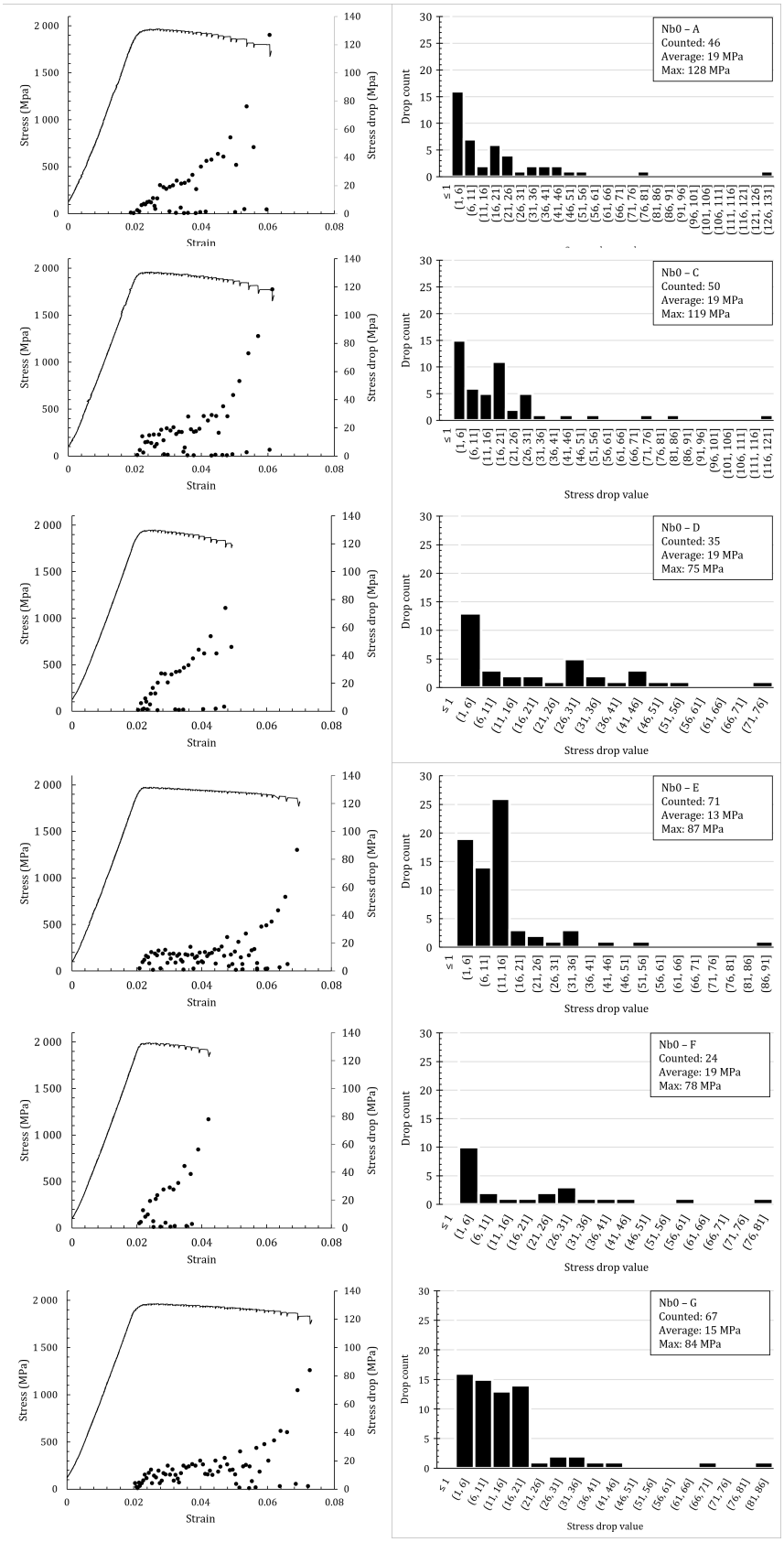

Figure H-1: stress strain curves, stress drop detection and stress drops statistical repartition for each compressive test on $Zr_{56}Co_{28}Al_{16}$ used in this chapter.

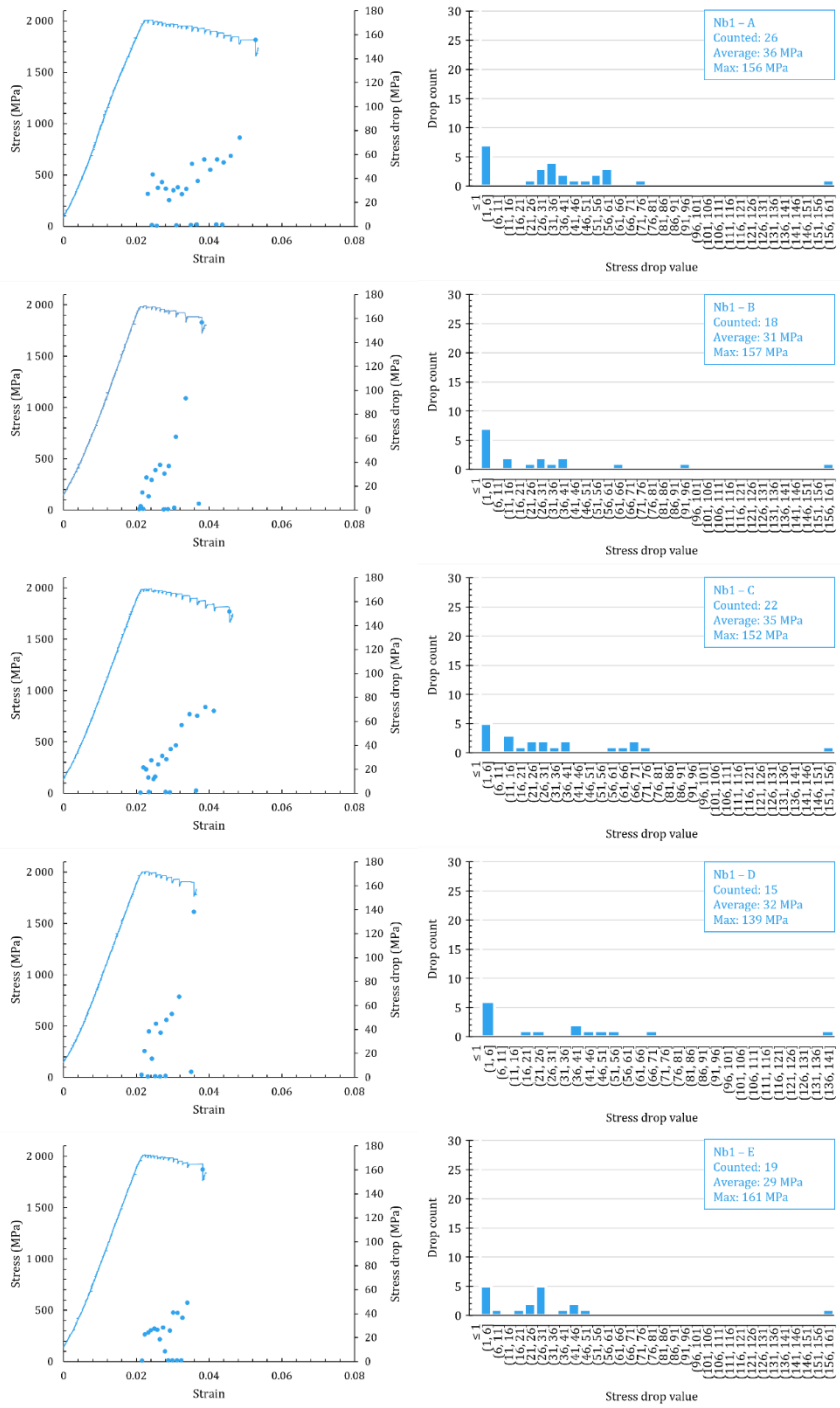

Figure H-2: stress strain curves, stress drop detection and stress drops statistical repartition for each compressive test on $Zr_{55}Co_{28}Al_{16}Nb_1$ used in this chapter.

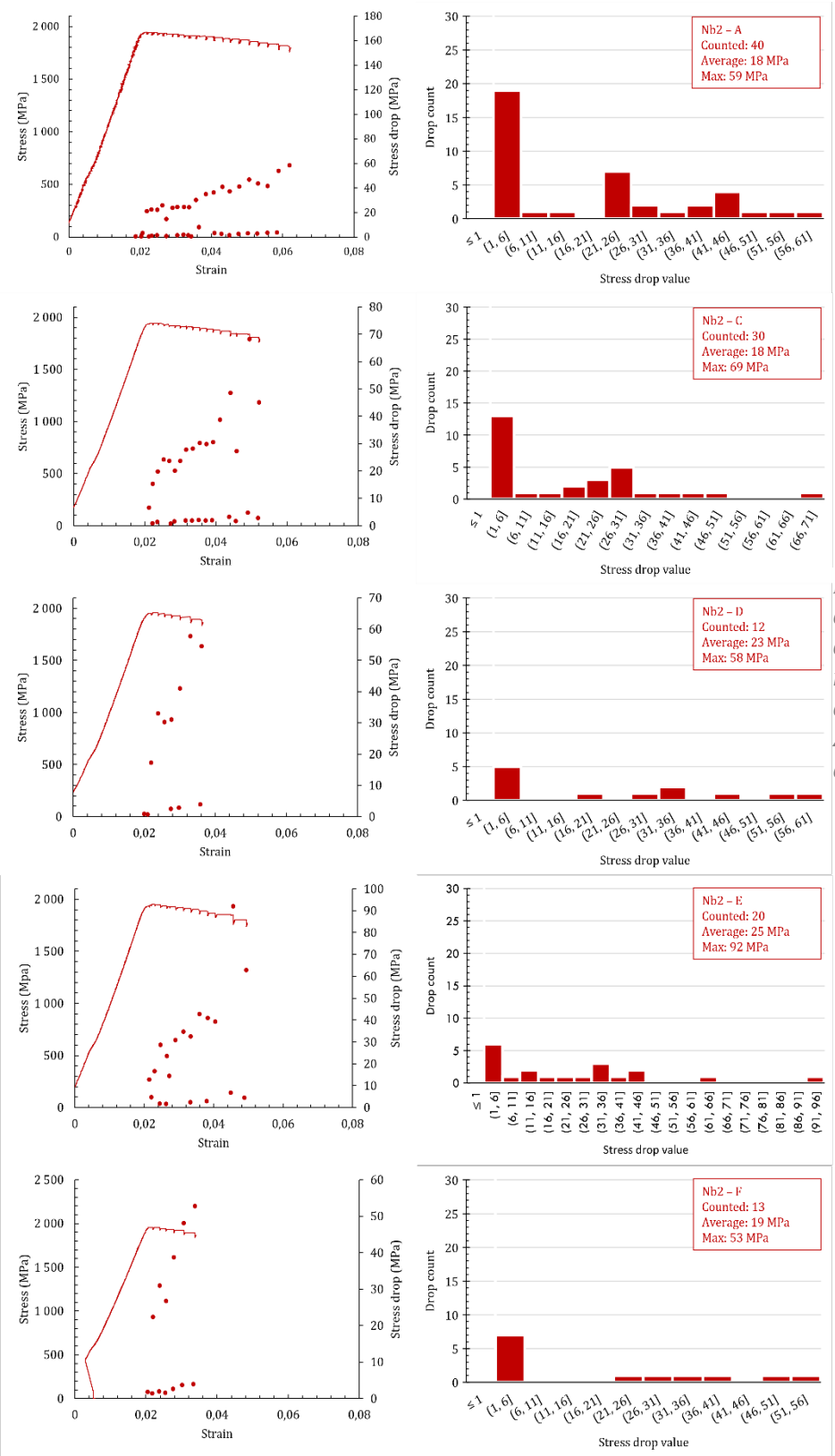

Figure H-3: stress strain curves, stress drop detection and stress drops statistical repartition for each compressive test on $Zr_{54}Co_{28}Al_{16}Nb_2$ used in this chapter.

Abstract

The medical sector is currently facing a challenge regarding the miniaturization of biomedical devices. To allow for less invasive surgeries and safer procedures, there is a need to produce and characterize new materials such as metallic glasses with controlled properties. In this context, a ternary Zr-Co-Al metallic glass is synthesized and structurally characterised. In as-cast conditions, both corrosion and mechanical properties are studied. Thanks to polarisation tests or long-term immersion, it is shown that the studied glass satisfies the medical standards and that cobalt plays a key role in the corrosion mechanism. Thanks to specific fatigue tests, it is demonstrated that the Zr-Co-Al metallic glass meets also the requirements of the medical standard. Compression tests are analysed thanks to a serrated flow analysis considering shear band dynamic in two regimes: a steady propagation regime followed by a catastrophic one. This modified approach to the serrated flow analysis brings interesting information, complementary to the more spread self-ordered criticality approach. Contrasting with the literature, the unusual stability of the glass transition temperature with heating rate, leading to high activation energy toward structural reorganisation, is also reported. Attempts to modify the energy state of the glass are carried out by performing relaxation and rejuvenation treatments. The sensitivity of the studied Zr-Co-Al is compared to the one of Zr-Cu-Al BMGs and the observed differences support the idea of differences in structural heterogeneities between these glasses. Additionally, we demonstrate that rejuvenation by cyclic loading under the yield stress can enhance the plasticity of the Zr-Cu-Al-based BMG. Finally, the effect of minor alloying (substitution of Zr by Nb) on mechanical and corrosion properties is also investigated, underlining the importance of the alloying route.

Résumé en français

Le secteur médical est actuellement confronté à un défi concernant la miniaturisation des dispositifs biomédicaux. Pour permettre des chirurgies moins invasives et des procédures plus sûres, il est nécessaire de produire et de caractériser de nouveaux matériaux tels que des verres métalliques aux propriétés contrôlées. Dans ce contexte, un verre métallique ternaire Zr-Co-Al est synthétisé et caractérisé structurellement. Dans l'état brut de moulage, les propriétés mécaniques et de corrosion sont étudiées. Grâce à des tests de polarisation ou d'immersion à long terme, on démontre que le verre étudié répond aux normes médicales et que le cobalt joue un rôle clé dans le mécanisme de corrosion. Grâce à des tests de fatigue spécifiques, on démontre également que le verre métallique Zr-Co-Al répond aux exigences de la norme médicale. Des essais de compression sont analysés en étudiant les chutes de contraintes en cours de déformation, ce qui permet de proposer une dynamique des bandes de cisaillement en deux régimes : un régime de propagation stable suivi d'un régime catastrophique. Cette approche modifiée de l'analyse des chutes de contraintes apporte des informations intéressantes, complémentaires à l'approche plus répandue de la criticité auto-ordonnée. En contraste avec la littérature, la stabilité de la température de transition vitreuse avec la vitesse de chauffage, conduisant à une énergie d'activation élevée pour la réorganisation structurelle, est également rapportée. Des tentatives de modification de l'état énergétique du verre sont réalisées en mettant en œuvre des traitements de relaxation et de rajeunissement. La sensibilité du verre Zr-Co-Al est comparée à celle de verres Zr-Cu-Al et les différences observées suggèrent des différences en termes d'hétérogénéités structurales entre ces verres. De plus, nous démontrons que le rajeunissement par chargement cyclique sous la limite d'élasticité peut améliorer la plasticité du verre à base de Zr-Cu-Al. Enfin, l'effet d'une modification de composition par l'addition de niobium sur les propriétés mécaniques et de corrosion est également étudié, soulignant l'importance de la stratégie de substitution.